



A University of Sussex PhD thesis

Available online via Sussex Research Online:

<http://sro.sussex.ac.uk/>

This thesis is protected by copyright which belongs to the author.

This thesis cannot be reproduced or quoted extensively from without first obtaining permission in writing from the Author

The content must not be changed in any way or sold commercially in any format or medium without the formal permission of the Author

When referring to this work, full bibliographic details including the author, title, awarding institution and date of the thesis must be given

Please visit Sussex Research Online for more information and further details



**Numerical analysis and simulation of
mathematical models for the rice blast
fungus**

by

James Van Yperen

Supervised by Vanessa Styles

Submitted for the degree of Doctor of Philosophy

University of Sussex

March 2020

Declaration

I hereby declare that this thesis has not been and will not be submitted in whole or in part to another University for the award of any other degree. This thesis is comprised entirely of my own research, conducted under the supervision of Vanessa Styles and Anotida Madzvamuse, unless otherwise stated.

Some of the material in Chapter 3 is taken from [109, 110], publications co-authored with Vanessa Styles. The material in Chapter 4 is heavily reliant on the work conducted in [102]. Otherwise, when applicable, the papers that inspired and informed the work contained in this thesis are referenced.

Signature:

James Van Yperen

UNIVERSITY OF SUSSEX

JAMES VAN YPEREN, DOCTOR OF PHILOSOPHY

NUMERICAL ANALYSIS AND SIMULATION OF MATHEMATICAL MODELSFOR THE RICE BLAST FUNGUSABSTRACT

In this thesis we present numerical analysis and simulations of mathematical models relating to the model for the rice blast fungus proposed in [102]. We begin with a computational study of a diffuse interface approximation of surface advection-diffusion equations on evolving surfaces. We study the experimental order of convergence produced by the finite element approximation presented in [44, 63] with added streamline diffusion from [63] and the stability term introduced in [44]. Furthermore we study the instabilities caused by an advection-dominated advection-diffusion equation and we introduce a finite volume approximation of the diffuse interface approximation. We then extend the computational study to include models in which the velocity law of the surface satisfies curve shortening flow. Next we prove optimal error bounds for a semi-discrete finite element approximation for a system consisting of the evolution of a curve evolving by forced curve shortening flow coupled to a reaction-diffusion equation on the evolving curve, such that the curve evolves in a given domain $\Omega \subset \mathbb{R}^2$ and meets the boundary, $\partial\Omega$, orthogonally. We compliment this analysis with error bounds for a fully discrete finite element approximation of curve shortening flow in the same fixed boundary configuration without the reaction-diffusion coupling. We also present numerical experiments and show the experimental order of convergence of the approximations that we analysed. Finally we derive a diffuse interface approximation to the mathematical model of the rice blast fungus presented in [102] and present numerical simulations that are consistent with the simulations presented in [102].

Acknowledgements

Not often am I lost for words. It feels like yesterday that I started my undergraduate degree at the University of Sussex and this journey began. None of this could have been possible without the unwavering support of my supervisor, my family and my friends, so I leave these messages to you.

To my supervisor Prof. Vanessa Styles. I am hugely grateful for all the opportunities you have given me over the years, starting with our Junior Research Project and finishing with this thesis. This has introduced to me the mathematics I absolutely adore, and for this, I can not be more thankful. Your support, kindness and intelligence has driven me to become the best version of myself. It has been an absolute honour to be your student, I will always be in your debt, and I truly look forward to continuing to work with you in the future.

To the mathematics department at Sussex, specifically to Prof. Anotida Madzvamuse, Dr Omar Lakkis and Dr Chandrasekhar Venkataraman. For all the insightful conversations and the environment to facilitate my growth as a researcher. I want to extend this thanks further to Vanessa, Anotida, Shekar and the group of N. Talbot (TSL, Norwich) for allowing me to use the model you've derived, as well as to the Engineering and Physical Sciences Research Council for funding this project.

To my friends. Your love and support has never gone unnoticed, and I am blessed to have friends like you all. From the feeding sessions on League with Sam and Lizzie, to my trips to Asda with Lam, and inception induced thoughts with Demetris. To travelling around America with Amber. Late nights with John, Jordan and Katie. From reunions back home with Rob and Jason, to reunions with old teammates with Josh and Amber. To many more memories we will all make.

To my family. This thesis is dedicated to you, for the tough road we have been on, to the tough road ahead. I am always thinking of you, and I will always do my best to make you all proud. Lastly, to my future self: never give up.

Contents

List of Tables	x
List of Figures	xiii
1 Introduction	1
1.1 Mean curvature flow	2
1.1.1 Parametric mean curvature flow	3
1.1.2 Phase field approach to mean curvature flow	4
1.1.3 Comments on the discretisation of the mean curvature flow of curves	5
1.2 Surface partial differential equations	6
1.2.1 Parametric representation of SADEs	7
1.2.2 Implicit representation of SADEs	8
1.2.3 Diffuse interface approximation to SADEs	9
1.2.4 Application of SPDEs	10
1.3 Overview of the thesis	11
2 The diffuse interface method for surface advection-diffusion equations	15
2.1 Notation	15
2.2 Phase field approximation of mean curvature flow	17

2.3	The diffuse interface approximation to SADEs on evolving surfaces	23
2.3.1	Computational study of the diffuse interface method for approximating advection-diffusion equations on evolving surfaces by [63]	24
2.3.2	Finite element analysis of the diffuse interface approach for SADEs on evolving surfaces by [44]	25
2.4	Further computational study of the diffuse interface approximation	29
2.4.1	Finite element approximation of a diffuse interface approximation to SADEs on evolving surface, Model: \mathcal{FE}	31
2.4.2	Finite volume approximation of a diffuse interface approximation to SADEs on evolving surfaces, Model: \mathcal{FV}	35
2.4.3	Edge smoothing for Model: \mathcal{FE}	42
2.4.4	Coupling the diffuse interface approximation of a SADE on an evolving surface to the phase field approximation of mean curvature flow	51
2.4.5	Summary of numerical results	59
3	The parametric approach for curve shortening flow	61
3.1	Introduction to Model \mathcal{M}_1 and Model \mathcal{M}_2	61
3.1.1	Notation	62
3.1.2	Useful identities and results	64
3.2	Literature review	65
3.2.1	Curve shortening flow	65
3.2.2	Curve shortening flow coupled to a PDE on the curve	75
3.3	Finite element analysis of Model \mathcal{M}_1	80
3.3.1	Stability bounds for Model \mathcal{M}_1	82
3.3.2	H^1 error bounds for Model \mathcal{M}_1	83
3.3.3	L^2 error bounds for Model \mathcal{M}_1	94

3.4	Finite element analysis of Model \mathcal{M}_2	99
3.4.1	H^1 error bounds for Model \mathcal{M}_2	102
3.5	Numerical results for Model \mathcal{M}_1 and Model \mathcal{M}_2	123
4	Mathematical modelling and numerical discretisation of models focused on the rice blast fungus	137
4.1	Mathematical model introduced in [102]	140
4.2	Parametric formulation of a simplified model for curves	147
4.2.1	Full model from [102] reduced from surfaces in \mathbb{R}^3 to curves in \mathbb{R}^2 .	147
4.2.2	Reduced model of the model presented in Section 4.2.1	158
4.3	The phase field approach to approximating the model for the rice blast fungus	165
4.3.1	Approximation to the curve model in Section 4.2.1	166
4.3.2	Approximation to the three dimensional surface model in [102] . . .	177
5	Conclusion	184
5.1	Summary	184
5.2	Future work	186
	Appendix A Geometric definitions and operators	188
	Appendix B Notable analysis results	190
B.1	Informal derivation of (2.2.9)	190
B.1.1	Derivation of subdifferential B	190
B.1.2	Derivation of variational inequality (2.2.9)	191
B.2	Proof of coarea approximation (2.3.7)	192
B.3	Useful theorems	193

B.4 Fully discrete results 194

Bibliography **197**

List of Tables

2.1	Example 1: Model: \mathcal{FE} , $\gamma = 0$.	34
2.2	Example 1: Model: \mathcal{FE} , $\gamma = 0.01$.	34
2.3	Example 1: Model: \mathcal{FE} , varying γ .	34
2.4	Example 1: Model: \mathcal{FE} , varying r .	34
2.5	Example 1: Model: \mathcal{FV} .	37
2.6	Example 1a: Model: \mathcal{FE} , $\gamma = 0$, varying d .	39
2.7	Example 1a: Model: \mathcal{FE} , $\gamma = 0$, reduced $h_{\mathcal{T}}$, varying d .	39
2.8	Example 1a: Model: \mathcal{FE} , $\gamma = 0.01$, varying d .	40
2.9	Example 1a: Model: \mathcal{FV} , varying d .	40
2.10	Example 1: Model: \mathcal{FEs} , $\gamma = 0$.	45
2.11	Example 1: Model: \mathcal{FEs} , $\gamma = 0.01$.	45
2.12	Example 1a: Model: \mathcal{FEs} , $\gamma = 0$, varying d .	46
2.13	Example 1a: Model: \mathcal{FEs} , $\gamma = 0.01$, varying d .	46
2.14	Example 2: Model: \mathcal{FE} and Model: \mathcal{ACFE} , varying d .	55
2.15	Example 2: Model: \mathcal{FEs} and Model: \mathcal{ACFEs} , varying d .	56
2.16	Example 2: Model: \mathcal{FV} and Model: \mathcal{ACFV} , varying d .	56
3.1	Example 1: Model \mathcal{M}_1 , $\Delta t = h^2$, $\alpha = 1$.	128

3.2	Example 1: Model \mathcal{M}_1 , $\Delta t = h^2$, $\alpha = 0.5$.	128
3.3	Example 1: Model \mathcal{M}_1 , $\Delta t = 0.1h$, $\alpha = 1$.	128
3.4	Example 1: Model \mathcal{M}_1 , $\Delta t = 0.1h$, $\alpha = 0.5$.	128
3.5	Example 1: [42], $\Delta t = h^2$.	129
3.6	Example 1: [42], $\Delta t = 0.1h$.	129
3.7	Example 2: Model \mathcal{M}_1 , $\Delta t = h^2$, $\alpha = 1$.	131
3.8	Example 2: Model \mathcal{M}_1 , $\Delta t = h^2$, $\alpha = 0.5$.	132
3.9	Example 2: Model \mathcal{M}_1 , $\Delta t = 0.1h$, $\alpha = 1$.	132
3.10	Example 2: Model \mathcal{M}_1 , $\Delta t = 0.1h$, $\alpha = 0.5$.	132
3.11	Example 2: [42], $\Delta t = h^2$.	133
3.12	Example 2: [42], $\Delta t = 0.1h$.	133
3.13	Example 2: [42], $\Delta t = h^2$.	133
3.14	Example 2: [42], $\Delta t = 0.1h$.	134
3.15	Example 3: Model \mathcal{M}_2 , $\Delta t = h^2$, $\alpha = 1$.	135
3.16	Example 3: Model \mathcal{M}_2 , $\Delta t = h^2$, $\alpha = 0.5$.	135
3.17	Example 3: Model \mathcal{M}_2 , $\Delta t = 0.1h$, $\alpha = 1$.	136
3.18	Example 3: Model \mathcal{M}_2 , $\Delta t = 0.1h$, $\alpha = 0.5$.	136

List of Figures

1.1	Dumbbell simulation: parametric framework.	6
1.2	Dumbbell simulation: phase field approximation.	6
2.1	Circle simulation: double well potential.	20
2.2	Circle simulation: double obstacle potential.	21
2.3	Circle simulation: profiles.	21
2.4	Different types of potentials.	22
2.5	\mathcal{B}^h for ρ_ε and $\tilde{\rho}_\varepsilon$	30
2.6	Refinement and coarsen procedure with a moving interface.	30
2.7	Finite volume/element dual mesh.	36
2.8	Example 1a: Model: \mathcal{FE} , $\gamma = 0$, varying d	41
2.9	Example 1a: Model: \mathcal{FE} , $\gamma = 0.01$, varying d	41
2.10	Example 1a: Model: \mathcal{FV} , varying d	42
2.11	Edge spiking simulation: Model: \mathcal{FE} , $\gamma = 0$, reducing $h_{\mathcal{T}}$	47
2.12	Edge spiking simulation: Model: \mathcal{FE} , $\gamma = 0$, increasing d	47
2.13	Edge spiking simulation: Model: \mathcal{FE} , $\gamma = 0.01$, reducing $h_{\mathcal{T}}$	48
2.14	Edge spiking simulation: Model: \mathcal{FE} , $\gamma = 0.01$, increasing d	48
2.15	Edge spiking simulation: Model: \mathcal{FV} , reducing $h_{\mathcal{T}}$	49

2.16	Edge spiking simulation: Model: \mathcal{FV} , increasing d .	49
2.17	Example 1a: Model: \mathcal{FEs} , $\gamma = 0$, varying d .	50
2.18	Example 1a: Model: \mathcal{FEs} , $\gamma = 0.01$, varying d .	50
2.19	Example 2: Model: \mathcal{FE} , $\gamma = 0$, varying d .	57
2.20	Example 2: Model: \mathcal{FEs} , $\gamma = 0$, varying d .	57
2.21	Example 2: Model: \mathcal{FV} , varying d .	58
2.22	Example 2: Model: \mathcal{ACFE} , varying d .	58
2.23	Example 2: Model: \mathcal{ACFEs} , varying d .	59
2.24	Example 2: Model: \mathcal{ACFV} , varying d .	59
3.1	Dumbbell simulation: [52].	68
3.2	Dumbbell simulation: [37].	69
3.3	Triple junction attached to a boundary.	71
3.4	Triple junction from collision.	72
3.5	Dumbbell simulation: [11].	74
3.6	Dumbbell simulation: [59].	76
3.7	Dumbbell simulation: final time.	77
3.8	Fixed boundary motivation.	80
3.9	Difference between explicit and implicit boundary conditions.	131
4.1	Life cycle of the rice blast fungus.	139
4.2	Initial rice blast schematic.	148
4.3	Initial conditions for full model simulation in the parametric framework.	154
4.4	Parametric full model: rice blast.	155
4.5	Parametric full model: Melanin and Sln1.	156

4.6	Parametric full model: Septins and F-actin.	157
4.7	Parametric full model: ring structure movement.	158
4.8	Reduced model of the rice blast fungus.	158
4.9	Parametric reduced model: rice blast pore.	163
4.10	Parametric reduced model: Septins and F-actin.	164
4.11	Initial surface for phase field framework.	167
4.12	Initial conditions for curve model in the phase field framework.	173
4.13	Phase field curve model: rice blast.	174
4.14	Phase field curve model: Melanin and Sln1.	175
4.15	Phase field curve model: Septins and F-actin.	176
4.16	Initial conditions for surface model in phase field framework.	178
4.17	Phase field surface model: rice blast.	179
4.18	Phase field surface model: Melanin and Sln1.	180
4.19	Phase field surface model: Septins and F-actin.	181
4.20	Phase field surface model: peg.	182
4.21	Phase field surface model: localisation at $t = 0.35$	183

Chapter 1

Introduction

In this thesis, we study mathematical models relating to the model of the rice blast fungus presented in [102]. Aspects of the models we study are of interest in the surface evolution community. As we progress through the thesis, we will demonstrate how the content we introduce links to the mathematical modelling of the fungus.

The rice blast disease occurs in over 85 countries and accounts for the annual loss of 11-30% of global rice yield [112]. Explicitly, in China between 2001-2005, 5.7 million hectares of rice was destroyed [119], and, in 1995 in Bhutan, more than 700 hectares of rice were affected and led to the losses of 1090 tonnes of rice [114]. It poses a significant threat to global food security. Magnaporthe Oryzae (a.k.a the rice blast fungus) causes this disease.

The study of the fungus itself is prevalent in the biology sector. It has been studied both in-vivo and in-vitro for decades [80, 96, 113, 118]. Gaining a good understanding of the behaviour of fungus is imperative to the success in stopping it. Growing the fungus and studying its behaviour takes time and resources that are often expensive and not available to everyone. This aspect is one of the many reasons why the mathematical community develop mathematical models. Mathematical models have been behind some of the leading research into real-life phenomena. Although simplifications are necessary for forming a model, they offer insight that might not have been obtainable in a laboratory. Multiple simulations with changing parameters can be run in parallel, while mathematical analysis can identify essential parameters and thresholds which can then be interpreted into real-life data and strategy. Indeed, the collaboration between biologists and mathematicians that resulted in the model in [102] that we are using found that a specific molecular species

is the driving force behind the invasion into crops.

In this introduction, we briefly introduce mean curvature flow, one of the central themes in this thesis. We then go on to discuss and compare a parametric formulation of mean curvature flow with a phase field approximation to mean curvature flow. Next, we introduce surface partial differential equations and in particular surface advection-diffusion equations and surface reaction-diffusion equations, the other central theme of this thesis, by considering different frameworks as well as real-life applications. Finally, we give an overview of the whole thesis.

1.1 Mean curvature flow

Definition 1.1 (Mean Curvature Flow).

A family of hypersurfaces $\Gamma(t)$ are said to evolve by *mean curvature flow* if they satisfy the law

$$v = \kappa \quad \text{on } \Gamma(t), t \in (0, T], \quad (1.1.1)$$

where v is the velocity of $\Gamma(t)$ in the normal direction $\vec{\nu}$ and κ is the mean curvature of $\Gamma(t)$.

Remark 1.2. *Often mean curvature flow is described by $v = -\kappa$, we note here that the sign is dependent on the orientation of the surface.*

Remark 1.3. *Forced mean curvature flow is mean curvature flow with a forcing term, that is*

$$v = \kappa + p. \quad (1.1.2)$$

Again we mention that orientation is important for the sign of p .

Remark 1.4. *From [41], mean curvature flow is the result of the L^2 gradient flow of the energy functional*

$$E[\Gamma](t) := \int_{\Gamma(t)} dS. \quad (1.1.3)$$

There are many applications of mean curvature flow, a few of which we list here:

- Grain boundary motion. Grain boundaries in alloys are interfaces which separate bulk crystalline regions of the same phase but with different orientations. Diffusion and surface tension drive the interface which mathematically is modelled by,

some variant of, (1.1.1). Moreover, when the alloyed material is placed in a different material's vapour, the particles from the vapour diffuse through the interfaces, depositing themselves into the bulk exciting the motion of the travelling interface. This deposition can be modelled mathematically by a conservation law that holds on the evolving interface. This process is called diffusion induced grain boundary motion, see [26, 41, 43, 93].

- Image processing. One of the most important aspects of image processing is the detection of edges/contours of an object by reducing the noise of the image. Since (1.1.1) is analogous to the geometric heat equation [41], it poses smoothing properties for curves, and so provides an appropriate model. Several applications come to mind instantly in medicine, such as in magnetic resonance imaging or an ultrasound scan, see [3, 41, 91, 101].
- Cell tracking. Cell migration is a fundamental process in biology; it is one of the factors that explains the process for biological events such as wound healing, inflammation and tumour invasion. Cell tracking is the mathematical process of tracking the cell shape from images. Detecting the geometry of the cell is essential as it provides knowledge of the edges of that cell, and thus (1.1.1) plays an important role. The shape of cells are also affected by their surrounding environment, such as nutrients. Similarly to diffusion induced grain boundary motion, this supplies a conservation law defined on the evolving surface that describes pattern formation on the surface, see [17, 89, 120].

We now closely follow [41] in describing two prevalent forms of mean curvature flow which we consider in this thesis, namely parametric mean curvature flow and the phase field approach to mean curvature flow. Other descriptions are the mean curvature flow of graphs, see [38, 88], and the mean curvature flow of level sets, see [39, 105].

1.1.1 Parametric mean curvature flow

In this thesis we only consider the parametric mean curvature flow of curves in \mathbb{R}^2 , also known as curve shortening flow, whereby, for motivation purposes, we assume the curve $\Gamma(t)$ is closed. We choose to specifically introduce this for curves and not generally for surfaces as the techniques needed are slightly different. Curve shortening flow is a so-called front-tracking method or explicit method. By this we mean that it explicitly tracks the curve

$\Gamma(t)$ and its movement, and the resulting partial differential equation (PDE) essentially provides the coordinates of the curve. To be more precise, let $\Gamma(t) \subset \mathbb{R}^2$ be a family of closed curves parametrised by $\vec{x} : \mathbb{I} \times [0, T] \rightarrow \mathbb{R}^2$, where $\mathbb{I} := \mathbb{R} \setminus \mathbb{Z}$ is the periodic unit interval. Then \vec{x} satisfies the relation

$$\vec{x}_t = \kappa \vec{\nu} = \Delta_{\Gamma(t)} \vec{x}, \quad \text{in } \mathbb{I}, t \in (0, T], \quad (1.1.4)$$

where $\Delta_{\Gamma(t)}$ denotes the Laplace-Beltrami operator on $\Gamma(t)$ defined in Definition A.7. One notices that taking the inner product of (1.1.4) with $\vec{\nu}$, one recovers $v = \kappa$ on \mathbb{I} . By considering textbook results in differential geometry, such as Frenet's formula (3.2.2), (1.1.4) takes the form

$$\vec{x}_t - \vec{x}_{ss} = 0, \quad \text{in } [0, \ell], t \in (0, T], \quad (1.1.5)$$

where s denotes the arc-length parameter associated to $\Gamma(t)$ and ℓ denotes the total arc length of the curve. We go into more detail about curve shortening flow in Section 3.2.1.

1.1.2 Phase field approach to mean curvature flow

Although in this thesis we again only consider the phase field approach to mean curvature flow of curves, we introduce the concept for a general surface since the techniques are the same. The phase field approach is an example of an implicit method in which, for some small positive parameter ε , we assume there exists a function $\varphi : \mathbb{R}^{n+1} \times [0, T] \rightarrow \mathbb{R}$, with $n = 1, 2$, such that

$$\Gamma_\varepsilon(t) := \{\vec{p} \in \mathbb{R}^{n+1} : -1 + C\varepsilon \leq \varphi(\vec{p}, t) \leq 1 - C\varepsilon\},$$

where the constant C depends on the type of potential we use to describe the phases. The phases, $\varphi \approx 1$ and $\varphi \approx -1$, approximate the two sides of the evolving surface and thus φ is consequently described as the phase field function of $\Gamma(t)$. The phase field approximation to (1.1.1) is derived by taking the regularized L^2 gradient flow of the Ginzburg-Landau-Wilson functional

$$E_\varepsilon[\varphi](t) = \int_\Omega \frac{\varepsilon}{2} |\nabla \varphi(\cdot, t)|^2 + \frac{1}{\varepsilon} W(\varphi(\cdot, t)) dx,$$

which results in a function φ that satisfies

$$\varepsilon \varphi_t = \varepsilon \Delta \varphi + \frac{1}{\varepsilon} W'(\varphi), \quad \text{in } \Omega, t \in (0, T], \quad (1.1.6)$$

where W defines the potential and $\Omega \subset \mathbb{R}^{n+1}$ is some set satisfying $\Gamma_\varepsilon(t) \subset \Omega, \forall t \in [0, T]$. The approximation to $\Gamma(t)$ is then $\Gamma_\varepsilon(t)|_{\varphi(\cdot, t)=0}$. Although it is not directly formulated from the definition of $\Gamma(t)$ like (1.1.4), one can note the similarity to (1.1.3). We go into more detail about the phase field approach to mean curvature flow in Section 2.2.

1.1.3 Comments on the discretisation of the mean curvature flow of curves

In this thesis we concentrate mainly on using the finite element method to numerically approximate the mean curvature flow of curves. One can ask the question, how is it known which of the approaches introduced should be used for a given application? For an in-depth analysis and computational study we refer readers to [12] where the authors compare a phase field implementation versus a parametric implementation with emphasis on Stefan problems, such as the Stefan problem for undercooled solidification, see [103]. Here we will highlight some appropriate advantages and disadvantages of the finite element discretisation of the phase field versus the parametric formulations of the mean curvature flow of curves:

- Implementation and simulation. Since curve shortening flow can be parametrised by the arc-length parameter s , a variable in \mathbb{R} , the associated finite element discretisation is easily implementable and does not require the use of specific finite element packages. The phase field approach to curve shortening flow, however, is defined in \mathbb{R}^2 and is thus not as straight forward to implement without the use of finite element packages due to, for example, the need for adaptive mesh refinement. Moreover, since (1.1.6) is defined throughout Ω , the computational domain has significantly more nodes in its triangulation compared to an equivalent partition of $[0, 1]$ for (1.1.5). Thus it is not hard to reason that the computational time needed for phase field approach to mean curvature flow is a lot larger than for a parametric formulation of curve shortening flow.
- Topological changes. Although it is well known that a closed curve evolving under curve shortening flow shrinks to a point [70, 72], under forced curve shortening flow one might expect topological changes to happen, such as self-intersection. Here we consider how the parametric and phase field approaches handle such changes by considering a pinching dumbbell. In Figure 1.1 we demonstrate this problem using a parametric formulation of forced curve shortening flow. As it is an explicit method it has no notion of interior, and so it cannot detect the pinching of the curve. However, the phase field approximation to forced mean curvature flow does have a notion of interior and this allows the phase field function to react to the pinch by splitting into two curves, as seen in Figure 1.2. Thus phase field approximations can provide an important insight for applications in which $\Gamma(t)$ models an evolving boundary that

splits like in cell tracking.

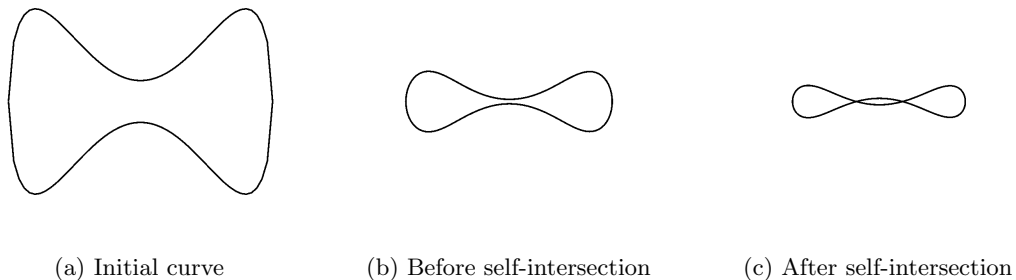


Figure 1.1: Parametric implementation of a pinching dumbbell evolving under forced curve shortening flow.

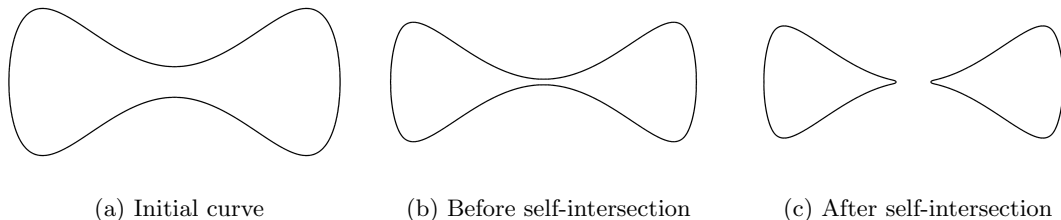


Figure 1.2: Zero level set of the phase field implementation of a pinching dumbbell evolving under forced mean curvature flow.

1.2 Surface partial differential equations

As the name suggests, surface PDEs (SPDEs) are PDEs defined on a surface. More precisely, they are the study of PDEs on manifolds. PDEs themselves have a large number of applications and this extends to SPDEs. Due to the fact that SPDEs are defined on surfaces, one needs to give care not only to how we describe the resulting mathematical operators, but also to the surface. Indeed one has to consider whether the surface is stationary or moving and how this changes the representation of the equations. In addition to this, regularity plays an important factor. In standard PDE theory the relaxation of solutions to weak formulations or even to a distributional setting is well defined, however for surfaces this is not so easily accessible. PDE theory is large and vast, see [68], and is rich in history in comparison to SPDEs. For a review of the finite element analysis for SPDEs we direct readers to the recent review publication [61].

In this thesis we first focus on surface advection-diffusion equations (SADEs) and then

on surface reaction-diffusion equations (SRDEs), more specifically advection-diffusion or reaction-diffusion equations on curves, so in this section we introduce the aspects important for these. Since both SADEs and SRDEs have a similar structure, the main difference in this context of this thesis being the forcing term dependencies, we only refer to advection-diffusion for the remainder of this section. Contextually PDEs are often the result of a conservation law, and an advection-diffusion equation is no different, both in the traditional sense and also on a surface. In the traditional sense, the equation comes about from, for example, the conservation of mass with an advective and diffusive flux. The derivation then comes from the ability to interchange the derivative and integral, as well as the definition of the flux. The same techniques can be applied to surfaces, but we need to consider in addition if the surface evolves. Considering an evolving surface, the interchanging of the derivative and integral becomes more tricky as we need to consider the velocity of the moving surface. In this section we assume that the velocity of the surface is known and takes the form

$$\vec{v} = v \vec{\nu} + \vec{v}_\tau, \quad (1.2.1)$$

where v is the normal velocity of $\Gamma(t)$, $\vec{\nu}$ is the unit normal to $\Gamma(t)$ and \vec{v}_τ is the tangential component of the velocity. However, we note that in many instances the velocity might be defined by a velocity law such as mean curvature flow. We note that in the literature \vec{v} is often called the material velocity.

As precluded to, we will only consider the parametric representation of surface evolution for curves, however we will introduce the notation here for surfaces for completeness and derive the results for curves in a later chapter. Similarly, we introduce the associated equations using an implicit representation even though we only consider the diffuse interface approach, as the concepts are nevertheless important for derivation purposes. Throughout this section we will be following the review publication [58] closely. We start with the parametric representation of a surface.

1.2.1 Parametric representation of SADEs

An advection-diffusion equation on a parametrised surface takes the following form

$$\partial_t^\bullet u + u \operatorname{div}_{\Gamma(t)}(\vec{v}) - \operatorname{div}_{\Gamma(t)}(d \nabla_{\Gamma(t)} u) = f, \quad \text{on } \Gamma(t), t \in (0, T], \quad (1.2.2)$$

where ∂_t^\bullet denotes the material derivative $\partial_t^\bullet u = u_t + \langle \vec{v}, \nabla u \rangle$, with $\langle \cdot, \cdot \rangle$ denoting the standard Euclidean inner product, $\operatorname{div}_{\Gamma(t)}$ is the surface divergence defined in Definition

A.5, $\nabla_{\Gamma(t)}$ is the surface gradient defined in Definition A.4, d denotes a diffusion coefficient and f is a forcing term. If we set $\vec{v}_\tau = 0$ then (1.2.2) is synonymous to

$$u_t + v \langle \nabla u, \vec{\nu} \rangle + \kappa v u - \operatorname{div}_{\Gamma(t)} (d \nabla_{\Gamma(t)} u) = f, \quad \text{on } \Gamma(t), t \in (0, T]. \quad (1.2.3)$$

In order to be able to derive a finite element method for surfaces, we need the weak formulation of a PDE. Traditionally this means multiplying by a test function, integrating, and potentially using integration by parts and Leibniz's rule. One asks, are these techniques extendable to SPDEs and the numerical solution of SPDEs? Only recently has this been the case, by work pioneered by Dziuk and Elliott [53, 54, 55, 56, 57], in which they derived methods for numerically solving SPDEs for the parametric and implicit representations of surfaces. For a review of these techniques see [58]. We briefly mention the numerical techniques for the numerical solution of SPDEs in the parametric representation of surfaces:

- Evolving surface finite element method (ESFEM) [53]. By approximating $\Gamma(t^n)$ with a polyhedral approximation $\Gamma^{h,n}$, one approximates the surface gradient using the approximate normal to $\Gamma^{h,n}$. Then, similar to the traditional finite element method, the matrix contributions are the surface integral of the basis functions over $\Gamma^{h,n}$, using the approximate surface gradient if necessary, in order to obtain a numerical scheme which is similar in structure to a finite element approximation of a standard reaction-diffusion equation. ESFEM is an extension to the originally conceived surface finite element method (SFEM) which is for the finite element approximation of PDEs on stationary surfaces, see [50].
- Arbitrary Lagrangian-Eulerian ESFEM (ALE ESFEM) [67]. In ESFEM only the normal velocity of the surface $\Gamma(t^n)$ is considered when moving the triangulated surface $\Gamma^{h,n}$. There are situations where the evolution of $\Gamma^{h,n}$ causes the clumping of nodes. To prevent this clumping of nodes an artificial tangential motion of the nodes can be introduced. In such instances this adds an extra term to the numerical scheme which is the difference of the introduced advective velocity of the surface and the material velocity of the surface.

1.2.2 Implicit representation of SADEs

When considering $\Gamma(t)$ to be implicitly defined, the resulting SADE will be different to (1.2.2). Indeed, rather than deal with $\Gamma(t)$ explicitly one defines it as the zero level set of

some function ϕ and then defines the SADE in some bounded domain $\Omega \subset \mathbb{R}^{n+1}$, such that $\Gamma(t) \subset \Omega$, $\forall t \in [0, T]$. To be more specific, let $\phi \in C^2(\overline{\Omega})$ be a non-degenerate function, that is $|\nabla\phi(\vec{p}, t)| \neq 0$, for $\vec{p} \in \overline{\Omega}$, and define

$$\Gamma(t) = \{\vec{p} \in \Omega : \phi(\vec{p}, t) = 0\},$$

then the SADE takes the following form

$$\partial_t^\bullet u + u \operatorname{div}_\phi(\vec{v}) - \frac{1}{|\nabla\phi|} \operatorname{div}(d|\nabla\phi| \nabla_\phi u) = f, \quad \text{in } \Omega, t \in (0, T]. \quad (1.2.4)$$

Here div_ϕ can be thought of as the ϕ -extension to $\operatorname{div}_{\Gamma(t)}$, defined as $\operatorname{div}_\phi(\vec{v}) = \operatorname{div}(\vec{v}) - \langle \nabla \langle \vec{v}, \vec{\nu}_\phi \rangle, \vec{\nu}_\phi \rangle$, where $\vec{\nu}_\phi = \frac{\nabla\phi}{|\nabla\phi|}$ which can be thought of as the ϕ -extension to the unit normal $\vec{\nu}$ to $\Gamma(t)$, ∇_ϕ can be thought of as the ϕ -extension to $\nabla_{\Gamma(t)}$, defined as $\nabla_\phi u = \nabla u - \langle \nabla u, \vec{\nu}_\phi \rangle \vec{\nu}_\phi$, and $\partial_t^\bullet u$ is as above. One notes that Ω has a boundary, as opposed to $\Gamma(t)$ which doesn't, and so one can reason that the natural choice for the boundary conditions would be

$$\langle \nabla_\phi u, \vec{n}_\Omega \rangle = 0.$$

An advantage of using the implicit representation of a surface for the finite element approximation of a SADE is that one bypasses the difficulty of approximating $\Gamma(t)$; however, one still needs to choose Ω appropriately. Indeed, if Ω is chosen to be a generic domain, like a square, then the level sets of ϕ will intersect the boundary of Ω , which results in imposing the additional boundary condition above. Alternatively, one can choose Ω in terms of ϕ ; however, this may introduce geometric errors into the scheme if Ω is curved. Considering the implicit surface finite element method, to obtain a numerical scheme the basis functions are integrated over the whole domain Ω rather than over $\Gamma(t^n)$, see [55].

1.2.3 Diffuse interface approximation to SADEs

The diffuse interface approximation to SADEs is based on a phase field approximation of the surface and so, for a non-negative function ρ_ε , which we define shortly, we introduce the diffuse interface approximation to $\Gamma(t)$ as

$$\Gamma_\varepsilon(t) := \{\vec{p} \in \Omega : \rho_\varepsilon(\vec{p}, t) > 0\}.$$

Commonly $\Gamma_\varepsilon(t)$ is called the interfacial region. The derivation of an equivalent equation to (1.2.2) requires a lot more technical detail, which can be found in [44, Lemma 7.1]. We

introduce the necessary details from [44] to state the diffuse interface equivalent of (1.2.2).

Denoting

$$U_\delta(t) := \{\vec{p} \in \Omega : |\phi(\vec{p}, t)| < \delta\},$$

using the extension u^e of u to Ω outlined in [44, Section 2.2], one can show that the suitably extended u^e satisfies

$$\partial_t^\bullet u^e + u^e \operatorname{div}_\phi(\vec{v}^e) - \frac{1}{|\nabla\phi|} \operatorname{div}(d|\nabla\phi| \nabla u^e) = f^e + \phi R, \quad \text{in } U_\delta(t), t \in (0, T],$$

for a suitably chosen δ and suitably extended \vec{v} and f , where R comes from the extension of $\Gamma(t)$ to $U_\delta(t)$ and is a smooth function of ϕ , u and \vec{v} and some of their derivatives, see [44, Lemma 7.1]. By considering a function $g \in C^{1,1}(\mathbb{R})$ such that

$$\rho_\varepsilon(\cdot, t) := g\left(\frac{\phi(\cdot, t)}{\varepsilon}\right), \quad \text{in } \Omega, t \in [0, T],$$

for some $0 < \pi\varepsilon < 2\delta$, the following properties hold, see [44],

$$\phi_t + \langle \vec{v}^e, \nabla\phi \rangle = 0, \quad \partial_t^\bullet \rho_\varepsilon = 0, \quad \langle \nabla u^e, \nabla \rho_\varepsilon \rangle = 0, \quad \text{in } U_\delta(t), t \in (0, T].$$

Thus, as well as noting $\Gamma_\varepsilon(t) \subset U_\delta(t)$, the diffuse interface approximation of (1.2.2) is

$$\begin{aligned} \partial_t^\bullet(\rho_\varepsilon u^e) + \rho_\varepsilon u^e \operatorname{div}_\phi(\vec{v}^e) - \frac{1}{|\nabla\phi|} \operatorname{div}(d|\nabla\phi| \rho_\varepsilon \nabla u^e) \\ = \rho_\varepsilon f^e + \rho_\varepsilon \phi R, \quad \text{in } \Omega, t \in (0, T]. \end{aligned} \quad (1.2.5)$$

A more in-depth review of the diffuse interface approach and the finite element approximation of it is conducted in Section 2.3.

1.2.4 Application of SPDEs

There are many applications to SPDEs, we list a few here:

- **Surfactants.** A surfactant is a mixing agent that is added to a fluid to increase the stability of two or more emulsifying liquids. As the surfactant mixes with the liquids, the tension between the multiple surfaces can cause the surfactant to diffuse along its interface, thus causing a reaction-diffusion effect. This is called the Marangoni effect. Similar to diffusion induced grain boundary motion, the mechanics on the interface changes the boundary layer of the surfactant, leading to a free boundary problem, see [13, 78, 84].

- Turing patterns. It is well known in the literature that reaction-diffusion type mechanics provide a framework for describing pattern formation in biology, such as spots and stripes in skin formation. By adding specific forcing to the reaction-diffusion equation, one can simulate diffusion-driven instabilities, also known as Turing instabilities, and the patterns arising are often called Turing patterns. Focusing on biology it is natural to use the Turing model on evolving surfaces, whereby the instability can be caused by the evolution of the surface, or the instability causes a different evolution of the surface, as described by cell motility, see [4, 5, 95, 117].
- Tumours. Although for the evolution of tumours many different types of models have been derived and used, we specifically mention models that connect the tumour growth and movement to a coupling of a bulk equation for nutrient and necrotic cells to surface equations defining the movement corresponding to the concentrations of nutrients. This application also demonstrates another mathematical use of surface PDEs, namely coupling to interior bulk equations, see [23, 69, 81].

1.3 Overview of the thesis

The main contributions of this thesis are:

- We derive a finite volume approximation to the diffuse interface approximation for SADEs and compare with the errors obtained using the finite element approximation for an advection-dominated problem. To our knowledge, this is the first work that considers the experimental order of convergence of the finite volume approximation to the diffuse interface approximation for SADEs, and the first work which systematically looks at the difference between using the finite element method and the finite volume method for an advection-dominated SADE. Moreover, this is the first work where one considers the finite volume approximation to the diffuse interface approximation for SADEs whereby the velocity law of the evolving surface is a phase field approximation to mean curvature flow. The challenge in this section was that ALBERTA, the software we use to numerically approximate the solution to the SADEs, is a finite element package and therefore generating the resulting linear system required to solve the finite volume approximation had to be developed in the finite element framework.

- We prove fully discrete finite element error bounds for curve shortening flow attached orthogonally to a fixed boundary. This proof uses the typical fully discrete finite element error bound techniques for parabolic PDE problems by bounding the error by the error at the previous time step and the residual, however since curve shortening flow is a non-linear PDE extra care is needed. As in [6], an inductive hypothesis is used to get a stability bound on the length element which enables the typical techniques to be useful. However, unlike in [6] which does not require boundary terms due to the assumption of periodic boundary conditions, the bounds resulting from typical techniques for our problem result in the usual terms and extra terms in the form of L^∞ , L^2 norms and terms with an exponent of 4 rather than 2 which is what is desired. To overcome this we extend the results in [42] from the semi-discrete case to the fully discrete case and propose a strong inductive proof rather than a weak inductive proof as in [6]. Using the concepts presented in [6], the strong inductive hypothesis and the extended results from [42] enable us to complete this proof. To our knowledge, this is the first work which also details fully discrete error bounds in the L^2 norm, work which is the fully discrete extension to the result presented in [42].
- We prove continuous in time finite element error bounds for curve shortening flow attached orthogonally to a fixed boundary with a reaction-diffusion equation on the evolving curve. Similar to above, we use typical semi-discrete finite element error bound techniques for parabolic PDE problems by bounding the time derivative of the error by the error itself and the residual, but extra care has to be taken due to the non-linearity of the problem. Semi-discrete finite element analysis of curve shortening flow can be split into two types. The first involves using a fixed point concept whereby the set of admissible functions is chosen as all possible functions which satisfy the error bound required, using the standard finite element techniques, and then showing there exists a unique fixed point of this set which is the finite element approximation [37, 59]. The other is based upon using the same typical finite element techniques but combined with a contradiction to show that the error bounds must be satisfied for the whole interval $[0, T]$ rather than a subset [40, 42]. Both employ similar techniques, however the latter is used when terms difficult to bound in the traditional sense appear, as in the case of our boundary conditions. In this proof we are considering a coupling of curve shortening flow and a reaction-diffusion equation on the curve, and so we extend the results in [42] using a semi-discrete

version of the analysis presented in [6].

- We derive a diffuse interface approximation to the rice blast model presented in [102] and present simulations that reflect the simulations in [102]. The derivation from the sharp interface description to the phase field setting came with multiple challenges. Firstly, the use of the evolving surface finite element method gives the sharp interface approach a natural way to deal with the small diffusion constants due to its derivation, which is not the case in the phase field setting as demonstrated in Chapter 2. This was overcome by increasing the diffusion constants so that the finite element approximation is stable. Secondly, the sharp interface description makes use of an obstacle potential to stop the two interfaces (the fungus and the leaf) from intersecting until a condition is met. There isn't a clear way of deriving the same obstacle potential in a phase field setting which caused us to try and approximate the obstacle force on the resulting equations by adding an extra term into the Ginzburg-Landau-Wilson function to minimise interaction between the two phases (the fungus and the leaf).

In Chapter 2, we introduce and investigate the phase field approximation of mean curvature flow and then further introduce the diffuse interface approximation to SADEs. We mirror [44, 63] by conducting tests of the experimental order of convergence of the resulting finite element approximation and extend the computational experiments conducted in [44, 63] by considering an advection-dominated simulation. This prompts us to introduce the finite volume method for diffuse interface approximations. Here we demonstrate how the finite volume approximation compares to the equivalent finite element discretisation in advection-dominated simulations. As well as this we discuss the profile spiking due to the evolution of the curve and discuss how one can dampen the effects using the edge smoothing contribution introduced in [63]. We finish off the chapter by considering the diffuse interface approximation of SADEs, both the finite element discretisation and the finite volume discretisation, where the velocity law is a phase field approximation to mean curvature flow.

The main focus of Chapter 3 is the finite element analysis of curve shortening flow for a curve that is attached orthogonally to some defined fixed boundary. We consider a time and space discretisation of this flow as well as a purely spatial discretisation of a model in which this flow is coupled to a SRDE. For the former, we present optimal L^2 and H^1 error estimates. For the later, we present optimal H^1 error estimates for the curve

equation and L^2 error estimates for the SRDE. Finally, we conclude the chapter with some numerical simulations. Namely, we conduct a numerical study of a novel Newton method to discretise the curve shortening flow attached to a fixed boundary. Then we go on to show experimental order of convergence for the coupled scheme.

In Chapter 4, we consider the rice blast model as presented in [102]. We then reduce the model from a surface in \mathbb{R}^3 to a curve in \mathbb{R}^2 and demonstrate a simulation coupling curve shortening flow to a SRDE on the evolving curve. We then derive a diffuse interface approximation to this simplified two dimensional version of the model as well as for the original three dimensional problem and present simulations that compare well to the simulations in [102]. Chapter 5 then concludes the thesis, in it we outline future work as well as possible improvements to the models we derived here. We note here that throughout the thesis we present results proven within the literature which may have edited to provide clarity.

Chapter 2

The diffuse interface method for surface advection-diffusion equations

This chapter is an in-depth investigation and extension of the numerical results presented [44, 63]. To begin, in Section 2.2, we first introduce the phase field approximation to mean curvature flow in more detail. In Section 2.3 we review [44, 63] which analyse the finite element discretisation of diffuse interface approximations of SADEs on evolving surfaces. In Section 2.4 we present an extension to the numerical results presented in [44, 63] by considering an advection-dominated simulation and the introduction of a finite volume discretisation of a diffuse interface approximation to SADEs on evolving surfaces. We also consider the simulation of a diffuse interface approximation to SADEs where the velocity law of the evolving surface is a phase field approximation to mean curvature flow. Before we begin with the content we introduce notation that will be used throughout the chapter.

2.1 Notation

As with standard theory we denote the Euclidean inner product by $\langle \cdot, \cdot \rangle$ associated to the Euclidean norm $|\vec{p}|^2 = \langle \vec{p}, \vec{p} \rangle$.

Since we consider diffuse interface approximations to advection-diffusion on curves, our computational domain Ω is a bounded subset of \mathbb{R}^2 , where we define the closure of a

set, not just Ω , by $\bar{\Omega}$. For some fixed h^* , let $(\mathcal{T}^h)_{0 < h_{\mathcal{T}} \leq h^*}$ be a family of triangulation of Ω with $h_{\mathcal{T}} := \max_{T^h \in \mathcal{T}^h} \text{diam}(T^h)$ being the maximum diameter of each triangle. Furthermore we assume that \mathcal{T}^h is shape regular, as in [44], in the sense that $\forall h_{\mathcal{T}} \in (0, h^*]$ there exists a $\sigma > 0$ with

$$r_{T^h} \geq \sigma h_{T^h}, \quad \forall T^h \in \mathcal{T}^h,$$

where r_{T^h} is the radius of the largest ball contained in T^h and h_{T^h} is the maximum diameter of T^h . Our finite element space is defined as

$$S^h := \left\{ \chi^h \in C(\bar{\Omega}) : \chi^h|_{T^h} \text{ is affine on each triangle } T^h \in \mathcal{T}^h \right\}.$$

We use the notation defined in [63] to further describe the triangulation \mathcal{T}^h as well as sets of nodes of the triangulation relevant to the diffuse interface approach. Let \mathcal{N} be the set of vertex indices of the nodes of the triangulation \mathcal{T}^h with \mathcal{C}^h being the set of coordinates $(\vec{p}_1, \dots, \vec{p}_J)$, $J = |\mathcal{N}|$. For an index $i \in \mathcal{N}$ let ω_i denote the set of nodes in \mathcal{N} that have a triangle edge in common with the node i , let \mathcal{N}_i denote the set of triangles that have the i th node as a vertex and let $\mathcal{N}_{T^h} := \{j \in \mathcal{N} : \vec{p}_j \in T^h\}$ denote the set of vertices belonging to a triangle $T^h \in \mathcal{T}^h$. We define the basis functions of S^h by $\chi_i(\vec{p}_j) = \delta_i^j$ and we set $I^h : C(\bar{\Omega}) \rightarrow S^h$ to be the standard Lagrange interpolation operator defined as $(I^h \eta)(\vec{p}_j) = \eta(\vec{p}_j)$ $j = 1, \dots, J$, and we denote $I^h|_{T^h}$ to be the local interpolation operator. We define the discrete inner product as

$$(\eta_1, \eta_2)^h := \sum_{T^h \in \mathcal{T}^h} \int_{T^h} I^h|_{T^h}(\eta_1 \eta_2) dx.$$

Further to a spatial discretisation, we also discretise in time. Let $0 = t^0 < t^1 < \dots < t^{N-1} < t^N = T$ be a partition of $[0, T]$. We set $\Delta t := \max_{n=1, \dots, N} \Delta t_n$, where $\Delta t_n := t^n - t^{n-1}$ and we define the discrete version of the time derivative as

$$D_t a^n := \frac{a^n - a^{n-1}}{\Delta t_n},$$

where we have denoted the continuous function $a(\cdot, t^n)$ by $a^n(\cdot)$. In this setting we denote fully discretised finite element approximations by capital letters and the continuous solution by lower case letters, e.g. $A^n(\cdot)$ denotes the finite element approximation of the continuous solution $a(\cdot, t^n)$. Similarly, we denote the extension of a continuous function from $\Gamma(t)$ into Ω by a superscript e , e.g. u^e denotes the extension of u .

We adopt standard notation for the Sobolev spaces $W^{l,p}(I)$, where $I \subset \mathbb{R}^2$ is a bounded domain, $l \in \mathbb{N}_0$ and $p \in [1, \infty]$. Here we denote the Sobolev l, p norm of a function f on the interval I to be $\|f\|_{W^{l,p}(I)}$ and its seminorm to be $|f|_{W^{l,p}(I)}$. For the special case of $p = 2$,

we denote $W^{l,2}(I)$ by $H^l(I)$, with the appropriate change to the norm and seminorm. For the special case of $l = 0$, we work within the Lebesgue spaces $L^p(I)$, where the norm has standard notation $\|f\|_{L^p(I)}$. We also denote the L^2 inner product over Ω by (f, g) . Finally, we extend the notation to include time dependent spaces $W^{l,p}(0, T; X)$, where X is a Banach space, with the standard associated norm and seminorm $\|f\|_{W^{l,p}(0,T;X)}$ and $|f|_{W^{l,p}(0,T;X)}$ respectively.

Lastly, C denotes a generic constant that is independent of $h_{\mathcal{T}}$, Δt_n and ε . Multiple occurrences of C will not, in general, take the same value.

2.2 Phase field approximation of mean curvature flow

The phase field approach to approximating the evolution of a surface is derived from taking variational derivatives of energy functionals, which have often come from a physical interpretation of some interface problem. In this thesis we will only be considering the phase field approximation of mean curvature flow, introduced in [2], however other phase field approximations have been introduced for different geometric flows, such as the Cahn-Hilliard equation [27] which has been shown to approximate surface diffusion, see [24].

Mean curvature flow has been formulated as the asymptotic limit of the system that is generated by taking the regularised L^2 gradient flow of the Ginzburg–Landau–Wilson functional, see [25], defined by

$$E_\varepsilon[\varphi](t) := \int_{\Omega} \frac{\varepsilon}{2} |\nabla \varphi(\cdot, t)|^2 + \frac{1}{\varepsilon} W(\varphi(\cdot, t)) dx, \quad \text{for } \varepsilon \ll 1, \quad (2.2.1)$$

where Ω is some set such that $\Gamma(t) \subset \Omega$, $\forall t \in [0, T]$, and W is a potential which defines the phases. We require that the potential $W(\cdot)$ satisfies the following two conditions, namely $W(s) = W(-s)$ and the minima of $W(s)$ are at $s = \pm 1$. Assuming that $\Gamma(t)$ is closed, to give a notion of orientation, we want to describe $\Gamma(t)$ as the zero level set of some function $\varphi(t)$. The region where $\varphi \approx -1$ approximates the interior region enclosed by $\Gamma(t)$ and the region where $\varphi \approx 1$ approximates the exterior region.

We examine how the functional (2.2.1) gives rise to this description. Since we look to minimise (2.2.1), we examine what this means for each term for a suitably small ε . Firstly we consider the potential term, due to the factor of $1/\varepsilon$, if W is not small this contribution will be large. As W is minimised when $s = \pm 1$, this contributes to pushing φ towards ± 1 .

Now, although the small parameter ε multiplies the gradient term, the job of this term is to penalise large jumps in gradients. One can interpret that the job of the gradient term is to regularise φ and to keep it smooth, hence separating the phases, while the job of W is to strongly define the two phases.

On the assumption that $W \in C^2(\mathbb{R})$, utilising Euler-Lagrange theory, see [68], taking the regularised gradient flow of (2.2.1) yields the Allen-Cahn equation

$$\varepsilon\varphi_t = \varepsilon\Delta\varphi - \frac{1}{\varepsilon}W'(\varphi), \quad \text{in } \Omega, t \in (0, T], \quad (2.2.2a)$$

$$\langle \nabla\varphi, \vec{n}_\Omega \rangle = 0, \quad \text{on } \partial\Omega, t \in (0, T], \quad (2.2.2b)$$

$$\varphi(\cdot, 0) = \varphi^0(\cdot), \quad \text{in } \bar{\Omega}, \quad (2.2.2c)$$

where \vec{n}_Ω is the outward pointing unit normal to $\partial\Omega$, [41].

Remark 2.1. *Considering forced mean curvature flow in (1.1.2), (2.2.2a) becomes*

$$\varepsilon\varphi_t = \varepsilon\Delta\varphi - \frac{1}{\varepsilon}W'(\varphi) + c_W p, \quad \text{in } \Omega, t \in (0, T],$$

where c_W takes the form

$$c_W = \frac{1}{\sqrt{2}} \int_{-1}^1 \sqrt{W(s)} ds.$$

This term is derived from the asymptotic analysis of (2.2.2a) so that in the limit as $\varepsilon \rightarrow 0$, (1.1.2) is recovered, see, for example, [20].

There are a variety of choices of W in the literature. We first discuss the use of the so called double well potential, which is depicted by the red line in Figure 2.4. This takes the form

$$W(s) := \frac{1}{4}(s^2 - 1)^2, \quad (2.2.3)$$

and gives rise to the following approximation of $\Gamma(t)$

$$\Gamma_\varepsilon(t) = \{\vec{p} \in \Omega : -1 + C\varepsilon \leq \varphi(\vec{p}, t) \leq 1 - C\varepsilon\}$$

for some $C > 0$. By reducing ε , the width of Γ_ε decreases and $C\varepsilon$ decreases, which can be seen numerically in Figure 2.1 by considering the colour scale of each sub figure. Using (2.2.3), the Allen-Cahn equation (2.2.2a)–(2.2.2c) become

$$\varepsilon\varphi_t = \varepsilon\Delta\varphi - \frac{1}{\varepsilon}\varphi(\varphi^2 - 1), \quad \text{in } \Omega, t \in (0, T], \quad (2.2.4a)$$

$$\langle \nabla\varphi, \vec{n}_\Omega \rangle = 0, \quad \text{on } \partial\Omega, t \in (0, T], \quad (2.2.4b)$$

$$\varphi(\cdot, 0) = \varphi^0(\cdot), \quad \text{in } \bar{\Omega}. \quad (2.2.4c)$$

Remark 2.2. Using (2.2.3) in Remark 2.1, the double well phase field approximation of (1.1.2) takes the form

$$\varepsilon\varphi_t = \varepsilon\Delta\varphi - \frac{1}{\varepsilon}\varphi(\varphi^2 - 1) + \frac{\sqrt{2}}{3}p, \quad \text{in } \Omega, t \in (0, T].$$

Upon multiplying (2.2.4a) by a test function $\xi \in H^1(\Omega)$, and using integration by parts as well as (2.2.4b), the weak form of (2.2.4a)–(2.2.4b) is given by

$$\varepsilon(\varphi_t, \xi) + \varepsilon(\nabla\varphi, \nabla\xi) = \frac{1}{\varepsilon}(\varphi - \varphi^3, \xi), \quad \forall \xi \in H^1(\Omega). \quad (2.2.5)$$

When it comes to discretisation, we could use a fully explicit scheme, such as

$$\varepsilon(D_t\Phi^n, \xi^h)^h + \varepsilon(\nabla\Phi^{n-1}, \nabla\xi^h) = \frac{1}{\varepsilon}(\Phi^{n-1} - (\Phi^{n-1})^3, \xi^h)^h, \quad \forall \xi^h \in S^h, \quad (2.2.6)$$

for which the restrictions on this scheme are the standard parabolic time-step constraint $\Delta t_n \leq C h_{\mathcal{T}}^2$, see [65], or we could use a fully implicit scheme, such as

$$\varepsilon(D_t\Phi^n, \xi^h)^h + \varepsilon(\nabla\Phi^n, \nabla\xi^h) = \frac{1}{\varepsilon}(\Phi^n - (\Phi^n)^3, \xi^h)^h, \quad \forall \xi^h \in S^h.$$

If this is solved using Newton's method, then the time-step constraint is $\Delta t_n \leq C \varepsilon^2$, see [30]. Consulting [48], other methods that have been analysed and used are:

- Crank-Nicolson: this method takes the diffusive and potential terms both implicitly and explicitly;
- IMEX: this method takes the diffusive part to be implicit and the potential terms to be explicit;
- Convex splitting: this method starts by splitting the diffusive and potential terms into convex and concave components, and then taking the convex contribution to be implicit and the concave part to be explicit.

Another choice of potential is the so-called double obstacle potential, depicted by the blue line in Figure 2.4. It was introduced by [15] to give true phase separations in applications such as grain boundary motion. The double obstacle potential takes the form

$$W(s) := \frac{1}{2}(1 - s^2) + I_{[-1,1]}(s) \quad (2.2.7)$$

where

$$I_{[-1,1]}(s) := \begin{cases} 0 & |s| \leq 1, \\ \infty & |s| > 1. \end{cases}$$

This expression is also indeed minimised at $s = \pm 1$ however it is not continuous at these points. Due to this we can't define the derivative formally, instead we define it using the subdifferential, see Section B.1, and label it informally as

$$W'(s) = -s + B(s)$$

where

$$B(s) := \begin{cases} (-\infty, 0] & s = -1, \\ 0 & |s| < 1, \\ [0, \infty) & s = 1. \end{cases}$$

It has been shown, in [29], that under certain conditions of ε , the double obstacle potential gives rise to the following approximation of $\Gamma(t)$

$$\Gamma_\varepsilon(t) = \{\vec{p} \in \Omega : -1 < \varphi(\vec{p}, t) < 1\}. \quad (2.2.8)$$

To compare the effectiveness of the use of the double obstacle potential compared to the double well potential, we present the following simulation. Let $\Gamma(0)$ be a circle of radius 1 defined by

$$\Gamma(0) := \{\vec{p} \in \Omega : |\vec{p}| = 1\}$$

and let it evolve under mean curvature flow, where we define $\Omega := (-1.5, 1.5)^2$. Under mean curvature flow the circle will shrink to a point at a rate inversely proportional to its radius at the current time [41, 72]. Using the relationships $\varepsilon = \frac{320}{3}h_{\mathcal{T}}$ and a uniform time step $\varepsilon = 20\sqrt{10\Delta t}$, Figure 2.1 presents the simulation using (2.2.6) and Figure 2.2 presents the simulation using (2.4.19a)–(2.4.19b) (setting $p^n = 0$), with $T = 0.1$. In Figure 2.3 we show the transition over the line $y = x$ starting at $(-1.5, -1.5)$ of the phases of both the double well, in red, and the double obstacle, in black. It can be seen that, noting (2.2.8), the phases are sharply defined in the case of the double obstacle, and one can also see that as ε decreases, the double well gets closer to attaining values of ± 1 .

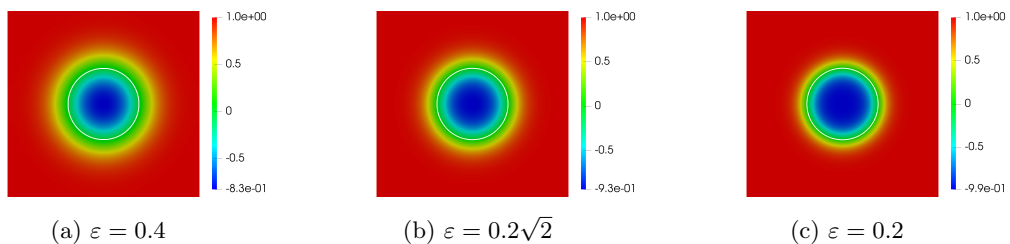


Figure 2.1: Shrinking circle simulation using the double well potential (2.2.3), $T = 0.1$. The white line depicts the $\Phi^N = 0$ level set.

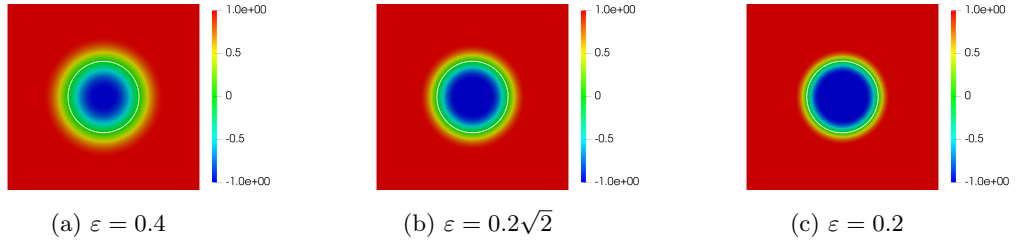


Figure 2.2: Shrinking circle simulation using the double obstacle potential (2.2.7), $T = 0.1$. The white line depicts the $\Phi^N = 0$ level set.

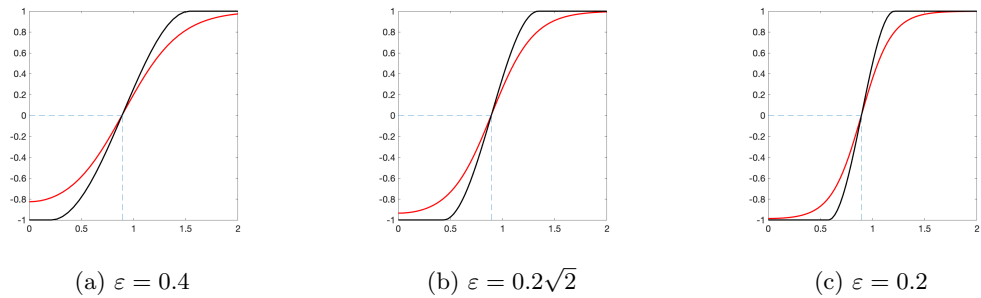


Figure 2.3: Transition over the line $y = x$ of the phases for the shrinking circle simulation, with results obtained using the double obstacle potential (2.2.7), in black, and the double well potential, in red, $T = 0.1$. The dashed line depicts where $\Phi^N = 0$ level set should be to approximate $\Gamma(t^N)$.

Remark 2.3. Following [18], when we set $W(\varphi)$ as (2.2.7), (2.2.2a) is often written as an inclusion

$$\varepsilon\varphi_t - \varepsilon\Delta\varphi - \frac{1}{\varepsilon}\varphi \in B(\varphi), \quad \text{in } \Omega, t \in (0, T],$$

or as a complementary problem

$$\begin{aligned} \left(\varepsilon\varphi_t - \varepsilon\Delta\varphi - \frac{1}{\varepsilon}\varphi \right) (|\varphi| - 1) &= 0, & \text{in } \Omega, t \in (0, T], \\ \left(\varepsilon\varphi_t - \varepsilon\Delta\varphi - \frac{1}{\varepsilon}\varphi \right) \text{sgn}(\varphi) &\leq 0, \quad |\varphi| \leq 1, & \text{in } \Omega, t \in (0, T]. \end{aligned}$$

A weak formulation of (2.2.2a) with (2.2.7) can be obtained by considering the minimisation problem of (2.2.1), we can utilise Euler-Lagrange theory, see [68], to obtain the following variational inequality,

$$\varepsilon(\varphi_t, \xi - \varphi) + \varepsilon(\nabla\varphi, \nabla\xi - \nabla\varphi) - \frac{1}{\varepsilon}(\varphi, \xi - \varphi) \geq 0, \quad \forall \xi \in \mathcal{K}, \quad (2.2.9)$$

where

$$\mathcal{K} := \{\xi \in H^1(\Omega) : |\xi| \leq 1\}.$$

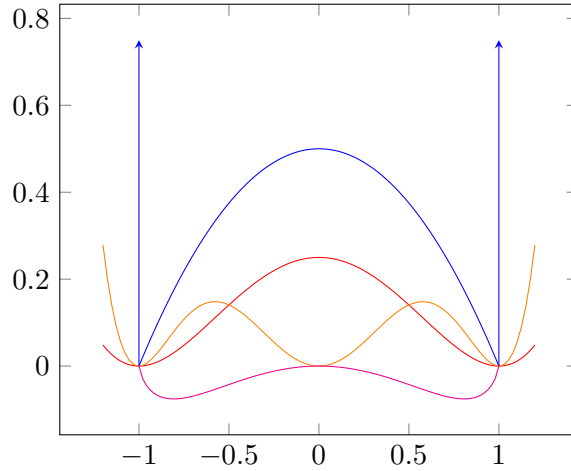


Figure 2.4: Different types of potentials. The red line depicts the double well, the blue line depicts the double obstacle, the orange line depicts the tripe well, and the magenta line depicts the logarithmic.

We also derive (2.2.9) informally in Section B.1.

Remark 2.4. Using (2.2.7) in Remark 2.1, the phase field approximation of (1.1.2) takes the form

$$\varepsilon(\varphi_t, \xi - \varphi) + \varepsilon(\nabla\varphi, \nabla\xi - \nabla\varphi) - \frac{1}{\varepsilon}(\varphi, \xi - \varphi) \geq \frac{\pi}{4}(p, \xi - \varphi), \quad \forall \xi \in \mathcal{K}. \quad (2.2.10)$$

The solution of the system of algebraic equations that result from a standard finite element approximation of (2.2.9) is not standard. In this thesis we use the projected SOR method presented in [60], see Section 2.4.4, however other methods that can be used are presented in [19, 41]. We close this section with some other choices of potential depicted in Figure 2.4:

- The non-convex logarithmic potential $W(s) := \frac{\theta}{2}[(1+s)\ln(1+s) + (1-s)\ln(1-s)] - \frac{\theta_c}{2}s^2$, depicted in magenta, has applications in phase transitions when a binary alloy has its temperature rapidly reduced below some critical temperature θ_c , see [71];
- The triple well potential $W(s) := s^2(s^2 - 1)^2$, depicted in orange, has applications in phase transitions in microemulsions such as oil-water-surfactant systems, see [86].

2.3 The diffuse interface approximation to SADEs on evolving surfaces

The diffuse interface method comes about by using a phase field approximation of an interface problem, and was first introduced by Rätz and Voigt in [99] for the diffusion equation on a fixed surface. In [99] the authors conduct asymptotic analysis and show formal convergence towards the equivalent sharp interface problem as $\varepsilon \rightarrow 0$. This result was then extended to moving surfaces in [87], whereby the authors also demonstrate first order convergence in the L^∞ -norm with $\varepsilon = Ch_{\mathcal{T}}$. In [63] the authors introduced a finite element discretisation of a diffuse interface approximation of a SADE and presented experimental order of convergence of the discretisation as well as the existence of a numerical solution. In [44] the authors prove finite element error estimates for a diffuse interface approximation of a SADE.

Before we begin, we formally define what ρ_ε represents. Considering [44, 63], the concept of ρ_ε is to approximate the delta distribution of $\Gamma(t)$, behaving similarly to a characteristic function for Γ_ε , and is derived with the double obstacle potential in mind. We re-state useful notation we described in the introduction. Considering a bounded domain $\Omega \subset \mathbb{R}^2$ such that $\Gamma(t) \subset \Omega$, $\forall t \in [0, T]$, let $\phi \in C^2(\bar{\Omega})$ be a non-degenerate function such that

$$\Gamma(t) = \{\vec{p} \in \Omega : \phi(\vec{p}, t) = 0\}. \quad (2.3.1)$$

Then we denote the diffuse interface approximation to $\Gamma(t)$ as

$$\Gamma_\varepsilon(t) := \{\vec{p} \in \Omega : \rho_\varepsilon(\vec{p}, t) > 0\}, \quad (2.3.2)$$

where ρ_ε takes the form

$$\rho_\varepsilon(\cdot, t) := g\left(\frac{\phi(\cdot, t)}{\varepsilon}\right), \quad \text{in } \bar{\Omega}, t \in [0, T] \quad (2.3.3)$$

and $g \in C^{1,1}(\mathbb{R})$ is defined as

$$g(r) := \begin{cases} \cos^2(r) & |r| \leq \frac{\pi}{2}, \\ 0 & |r| > \frac{\pi}{2}. \end{cases}$$

This diffuse interface approximation takes advantage of the sharply defined phases produced by the double obstacle potential and is posed in the interfacial region, which is the support of ρ_ε . An advantage of defining ρ_ε in this way is that there is an easy path to couple it to a diffuse interface approximation of a SADE whereby the velocity law is approximated by the double obstacle phase field approximation of mean curvature flow.

In particular this coupling can take place by using $\rho_\varepsilon(\cdot, t) := 1 - \varphi^2(\cdot, t)$. We will discuss this more in Section 2.4.4.

2.3.1 Computational study of the diffuse interface method for approximating advection-diffusion equations on evolving surfaces by [63]

As detailed in Section 1.2.3, the diffuse interface approximation of (1.2.2) is (1.2.5). In [63] the authors set $\phi(\cdot, t) = d_\Gamma(\cdot, t)$, where $d_\Gamma(\cdot, t)$ is the signed distance function

$$d_\Gamma(\vec{p}, t) := \begin{cases} \text{dist}(\vec{p}, \Gamma(t)) & \vec{p} \in \mathbb{R}^{n+1} \setminus \overline{G(t)}, \\ 0 & \vec{p} \in \Gamma(t), \\ -\text{dist}(\vec{p}, \Gamma(t)) & \vec{p} \in G(t), \end{cases}$$

with $\text{dist}(\vec{p}, A)$ being the Hausdorff distance function from a point \vec{p} to a set A , see [100], and $G(t) \subset \Gamma(t)$ such that $\partial G(t) = \Gamma(t)$, which results in $|\nabla \phi(\vec{p}, t)| = 1$ for $\vec{p} \in \overline{\Omega}$. By neglecting R , denoting the extension of u by u_ε to signify we are approximating (1.2.5), and noting $\partial_t^\bullet \rho_\varepsilon = 0$ and $\langle u_\varepsilon, \nabla \rho_\varepsilon \rangle = 0$, see [62], the authors in [63] write (1.2.5) in the following variational form

$$\partial_t(\rho_\varepsilon u_\varepsilon) + \text{div}(\rho_\varepsilon u_\varepsilon \vec{v}^e) - \text{div}(d \rho_\varepsilon \nabla u_\varepsilon) = \rho_\varepsilon f^e, \quad \text{in } \Omega, t \in (0, T], \quad (2.3.4a)$$

$$\langle \nabla u_\varepsilon, \vec{n}_\Omega \rangle = 0, \quad \text{on } \partial\Omega, t \in (0, T], \quad (2.3.4b)$$

$$u_\varepsilon(\cdot, 0) = u^{e,0}(\cdot), \quad \text{in } \overline{\Omega}, \quad (2.3.4c)$$

where $u^{e,0}$ is the extension of $u(\cdot, 0)$ and u_ε is set to zero where $\rho_\varepsilon = 0$. The authors in [63] specify that to generate, for example, f^e , one extends f constantly in the (positive and negative) normal direction to $\Gamma(t)$. Multiplying (2.3.4a) by a smooth test function ξ , using integration by parts and the boundary condition (2.3.4b), the weak form to (2.3.4a)–(2.3.4b) satisfies $u_\varepsilon(\cdot, t) = 0$ in $\Omega \setminus \Gamma_\varepsilon(t)$ and

$$(\partial_t(\rho_\varepsilon u_\varepsilon), \xi) - (\rho_\varepsilon u_\varepsilon \vec{v}^e, \nabla \xi) + (d \rho_\varepsilon \nabla u_\varepsilon, \nabla \xi) = (\rho_\varepsilon f^e, \xi), \quad \text{for all smooth } \xi. \quad (2.3.5)$$

The fully discrete finite element approximation the authors in [63] use then takes the form: given $U^{n-1} \in S^h$, find $U^n \in S^h$ such that

$$\begin{aligned} (D_t[\rho_\varepsilon^n U^n], \xi^h)^h - (\rho_\varepsilon^n U^n \vec{v}^{e,n}, \nabla \xi^h)^h + (d \rho_\varepsilon^n \nabla U^n, \nabla \xi^h)^h \\ = (\rho_\varepsilon^n f^{e,n}, \xi^h)^h, \quad \forall \xi^h \in S^h. \end{aligned} \quad (2.3.6)$$

As can be seen, these integrals are over Ω rather than within $\Gamma_\varepsilon(t)$ and so we need to treat the formulation with care as the equation is degenerate in terms of U^n . More precisely

$\rho_\varepsilon^n = 0$ in $\Omega \setminus \Gamma_\varepsilon(t^n)$ leading us to an ill-posed system, since the values of U^n in $\Omega \setminus \Gamma_\varepsilon(t^n)$ can't be determined. We specify the strategy for solving this, as described by [63], in Section 2.4.1.

In [63] the authors show unique solvability of the finite element approximation (2.3.6) in the following theorem [63, Proposition 2.7, p. 6].

Theorem 2.5 (C. Elliott, B. Stinner, V. Styles & R. Welford, 2010).

Let $\Delta t \|\vec{v}\|_{L^\infty(\Omega)}^2 < 4d$, then the scheme (2.3.6) has a unique solution with initial data

$$U^0(\vec{p}_i) := \begin{cases} u^{e,0}(\vec{p}_i) & i \in \mathcal{N}_h^0, \\ 0 & \text{otherwise,} \end{cases}$$

where

$$\mathcal{N}_h^n := \{i \in \mathcal{N} : \exists j \in \omega_i \text{ such that } \rho_\varepsilon(\vec{p}_j, t^n) > 0\}.$$

In [63] the authors monitor the following errors as part of their computational study

$$\begin{aligned} e[L^\infty, L^2] &:= \max_{n=1, \dots, N} \int_{\Gamma(t^n)} |u(\cdot, t^n) - U^n(\cdot)|^2 dS, \\ e[L^2, H^1] &:= \sum_{n=1}^N \Delta t_n \int_{\Gamma(t^n)} |\nabla_{\Gamma(t^n)} u(\cdot, t^n) - \nabla U^n(\cdot)|^2 dS, \\ e[L^2, H_\nu^1] &:= \sum_{n=1}^N \Delta t_n \int_{\Gamma(t^n)} |\langle \nabla U^n(\cdot), \vec{\nu}(\cdot, t^n) \rangle|^2 dS, \\ e[L^2, H_\tau^1] &:= \sum_{n=1}^N \Delta t_n \int_{\Gamma(t^n)} |\nabla_{\Gamma(t^n)} u(\cdot, t^n) - \nabla_{\Gamma(t^n)} U^n(\cdot)|^2 dS, \end{aligned}$$

for fixed ratios $\varepsilon = C h_\mathcal{T}$ and $h_\mathcal{T} = C \Delta t^2$. They use numerical quadrature to generate the errors and find that they follow the experimental order of convergence

$$e[L^\infty, L^2] \leq C h_\mathcal{T}^4, \quad e[L^2, H^1] \leq C h_\mathcal{T}^2, \quad e[L^2, H_\nu^1] \leq C h_\mathcal{T}^2, \quad e[L^2, H_\tau^1] \leq C h_\mathcal{T}^2.$$

2.3.2 Finite element analysis of the diffuse interface approach for SADEs on evolving surfaces by [44]

In [44] the authors approach the description and approximation of (1.2.2) differently to [63]. With numerics in mind, one of the main arguments supporting the use of the diffuse interface approximation is that it allows us to use a volume integral to approximate a surface integral. For a fixed $t \in [0, T]$ and $\xi \in L^1(\Omega)$, see Section B.2, this can be realised by noting that

$$\frac{2}{\varepsilon\pi} \int_{\Omega} \xi(\cdot) \rho_\varepsilon(\cdot, t) |\nabla \phi(\cdot, t)| dx \approx \int_{\{\phi(\cdot, t)=0\}} \xi(\cdot) dS. \quad (2.3.7)$$

This motivates the consideration that making the restriction $\phi(\cdot, t) = d_\Gamma(\cdot, t)$ is not necessarily helpful for the analysis of the resulting equation. Denoting

$$\mathcal{S}_T := \bigcup_{t \in [0, T]} (\Gamma(t) \times t),$$

in [44] the authors rigorously extend (1.2.2) from being defined on \mathcal{S}_T to $\mathcal{U}_{\delta, T}$ and derive a weak form using an Eulerian transport identity which deals with the $|\nabla\phi|$ term, see Lemma 2.6. To be more specific, noting (2.3.1), the authors in [44] denote

$$U_\delta(t) := \{\vec{p} \in \Omega : |\phi(\vec{p}, t)| < \delta\} \quad \text{and} \quad \mathcal{U}_{\delta, T} := \bigcup_{t \in [0, T]} (U_\delta(t) \times t),$$

where there exists some δ_0 such that $\delta < \delta_0$, $\overline{U_{\delta_0}(t)} \subset \Omega$, $\forall t \in [0, T]$, and the following stability bounds hold

$$c_0 \leq |\nabla\phi(\vec{p}, t)| \leq c_1, \quad |D^2\phi(\vec{p}, t)|, |\phi_t(\vec{p}, t)|, |\phi_{tt}(\vec{p}, t)| \leq c_2, \quad (\vec{p}, t) \in \mathcal{U}_{\delta_0, T}, \quad (2.3.8)$$

for some $0 < c_0 \leq c_1$ and $c_2 > 0$. Although we won't describe the extension used by the authors in [44], we will state useful properties derived from it. Namely for some function $z : \overline{\mathcal{S}_T} \rightarrow \mathbb{R}$, the extension $z^e : \mathcal{U}_{\delta, T} \rightarrow \mathbb{R}$ satisfies

$$\langle \nabla z^e(\vec{p}, t), \nabla\phi(\vec{p}, t) \rangle = 0, \quad (\vec{p}, t) \in \mathcal{U}_{\delta, T}. \quad (2.3.9)$$

Considering the extension of the velocity, the authors in [44] go on to describe that \vec{v} can be extended to $\vec{v}^e = v^e \vec{\nu}^e + \vec{v}_{\tau^e}^e$, where

$$\vec{v}_{\tau^e}^e := \vec{v}_\tau^e - \langle \vec{v}_\tau^e, \vec{\nu}^e \rangle \vec{\nu}^e \quad \text{in } \mathcal{U}_{\delta, T},$$

and

$$v^e := -\frac{\phi_t}{|\nabla\phi|}, \quad \vec{\nu}^e := \frac{\nabla\phi}{|\nabla\phi|}, \quad \langle \vec{v}_{\tau^e}^e, \vec{\nu}^e \rangle = 0, \quad \text{in } \mathcal{U}_{\delta, T}. \quad (2.3.10)$$

A simple calculation gives us

$$\langle \vec{v}^e, \vec{\nu}^e \rangle = v^e = -\frac{\phi_t}{|\nabla\phi|} \quad \text{in } \mathcal{U}_{\delta, T},$$

which implies that, for some $0 < \pi\varepsilon < 2\delta$,

$$\partial_t^\bullet \rho_\varepsilon = \frac{1}{\varepsilon} g' \left(\frac{\phi}{\varepsilon} \right) \partial_t^\bullet \phi = \frac{1}{\varepsilon} g' \left(\frac{\phi}{\varepsilon} \right) (\phi_t + \langle \vec{v}^e, \nabla\phi \rangle) = 0. \quad (2.3.11)$$

Using these properties the authors in [44] present (1.2.5), the extension of (1.2.2) from \mathcal{S}_T to $\mathcal{U}_{\delta, T}$, which we state again for the ease of the reader

$$\partial_t^\bullet u^e + u^e \operatorname{div}_\phi(\vec{v}^e) - \frac{1}{|\nabla\phi|} \operatorname{div}(|\nabla\phi| \nabla u^e) = f^e + \phi R, \quad \text{in } \mathcal{U}_{\delta, T}, \quad (2.3.12a)$$

$$u^\varepsilon(\cdot, 0) = u^{\varepsilon, 0}(\cdot), \quad \text{in } U_\delta(0), \quad (2.3.12b)$$

where R is as described in Section 1.2.3. We note that $U_\delta(t)$ is without boundary, hence the lack of boundary conditions. We first introduce the Eulerian transport formula, which will be used to generate the weak formulation of (2.3.12a).

Lemma 2.6 (Eulerian transport formula, [56]).

For some functions $g : \Omega \times [0, T] \rightarrow \mathbb{R}$ and $\vec{v} : \Omega \times [0, T] \rightarrow \mathbb{R}^{n+1}$ defined as $\vec{v} = v\vec{\nu} + \vec{v}_\tau$, where \vec{v} is material velocity of some hypersurface $\Gamma(t)$, noting (2.3.1), the Eulerian transport formula is defined as

$$\frac{d}{dt} \int_{\Omega} g |\nabla \phi| dx = \int_{\Omega} (\partial_t^\bullet g + g \operatorname{div}_\phi(\vec{v})) |\nabla \phi| dx - \int_{\partial\Omega} g \langle \nu, \vec{n}_\Omega \rangle |\nabla \phi| dS,$$

where \vec{n}_Ω is the outward pointing unit normal to Ω .

Using Lemma 2.6, taking $g = \rho_\varepsilon u^\varepsilon$, $\xi \in H^1(\Omega)$ and noting (2.3.3), the authors in [44] present the following weak formulation of (2.3.12a) as

$$\begin{aligned} & \frac{d}{dt} (\rho_\varepsilon u^\varepsilon |\nabla \phi|, \xi) + (\rho_\varepsilon \nabla u^\varepsilon |\nabla \phi|, \nabla \xi) - (\rho_\varepsilon u^\varepsilon \vec{v}^e |\nabla \phi|, \nabla \xi) \\ & = (\rho_\varepsilon f^e |\nabla \phi|, \xi) + (\rho_\varepsilon \phi R |\nabla \phi|, \xi), \quad \forall \xi \in H^1(\Omega), \end{aligned} \quad (2.3.13)$$

where the boundary conditions from the Eulerian transport formula and integration by parts disappear due to the support of ρ_ε . Rather than considering a finite element space throughout the domain Ω , the authors in [44] consider a finite element space that is defined on a diffuse interface domain with a slightly larger support than ρ_ε for analysis purposes. Namely, the authors define $\tilde{\rho}_\varepsilon$ by

$$\tilde{\rho}_\varepsilon(\cdot, t) := g \left(\frac{\phi(\cdot, t)}{r\varepsilon} \right), \quad \text{in } \bar{\Omega}, t \in [0, T]$$

with $r = 2$, see Figure 2.5, and describe an evolving triangulation, for $n = 0, \dots, N$, as

$$\mathcal{T}_h^n := \{T^h \in \mathcal{T}^h : \tilde{\rho}_\varepsilon(\vec{p}, t^n) > 0 \text{ for some } \vec{p} \in T^h \cap \mathcal{C}^h\}, \quad \text{and} \quad D_h^n := \bigcup_{T^h \in \mathcal{T}_h^n} T^h,$$

as well as an evolving finite element space

$$V_h^n := \{\xi^h \in C^0(D_h^n) : \xi^h|_{T^h} \text{ is affine on each triangle } T^h \in \mathcal{T}_h^n\},$$

with corresponding Lagrangian interpolant operator $I_h^n : C^0(D_h^n) \rightarrow V_h^n$. By neglecting the term containing R , the fully discrete finite element approximation presented in [44] is then as follows: given $U^{n-1} \in V_h^{n-1}$, find $U^n \in V_h^n$ such that

$$D_t \left[\left(\rho_\varepsilon^n U^n |\nabla \phi^n|, \xi^h \right) \right] + \left(\rho_\varepsilon^n \nabla U^n |\nabla \phi^n|, \nabla \xi^h \right) - \left(\rho_\varepsilon^n U^n \vec{v}^{e,n} |\nabla \phi^n|, \nabla \xi^h \right)$$

$$+ \gamma \Delta t_n \left(I_h^n(\tilde{\rho}_\varepsilon^n) \nabla U^n, \nabla \xi^h \right) = \left(\rho_\varepsilon^n f^{e,n} |\nabla \phi^n|, \xi^h \right), \quad \forall \xi^h \in V_h^n. \quad (2.3.14)$$

Here the additional term acts as artificial diffusion and is the crucial term that allows the finite element analysis. Indeed, $\gamma > 0$ is chosen suitably to ensure existence and stability of the scheme.

Remark 2.7. *We notice that (2.3.14) is not fully practical, in the sense of computations, since the integrals are to be evaluated exactly. The analysis of a fully practical scheme involving mass lumping would result in the interpolation of ρ_ε and, using interpolations estimates, would introduce a term of the form*

$$\|(I - I^h)\rho_\varepsilon^n\|_{L^2(\Omega)} \leq C h^2 \|\rho_\varepsilon^n\|_{H^2(\Omega)} \leq C \frac{h^2}{\varepsilon^2}$$

into the analysis, for which it is not obvious how to deal with, [44]. However, for a stationary surface, recent work has been conducted to rectify this for a fully practical finite element approximation to the diffuse interface approximation of an elliptic SPDE, [7].

In [44] the authors go on to show existence and stability bounds as well as the finite element error bounds for (2.3.14) in the following theorem [44, Theorem 5.2, p. 15].

Theorem 2.8 (K. Deckelnick & V. Styles, 2018).

Suppose that a solution of (1.2.2) satisfies

$$\max_{t \in [0, T]} \|u(\cdot, t)\|_{H^2(\Gamma(t))}^2 + \int_0^T \left(\|u(\cdot, t)\|_{H^3(\Gamma(t))}^2 + \|\partial_t^\bullet u(\cdot, t)\|_{H^2(\Gamma(t))}^2 \right) dt < \infty.$$

Then there exist $0 < \Delta t_2 \leq \Delta t_1$ and a constant $C > 0$ such that

$$\begin{aligned} & \max_{n=1, \dots, N} \frac{2}{\varepsilon \pi} \int_{\Omega} \rho_\varepsilon(\cdot, t^n) |\nabla \phi(\cdot, t^n)| |u^e(\cdot, t^n) - U^n(\cdot)|^2 dx \\ & + \sum_{n=1}^N \Delta t_n \frac{2}{\varepsilon \pi} \int_{\Omega} \rho_\varepsilon(\cdot, t^n) |\nabla \phi(\cdot, t^n)| |\nabla u^e(\cdot, t^n) - \nabla U^n(\cdot)|^2 dx \leq C \varepsilon^2 \end{aligned}$$

provided that (2.3.8) holds, $\Delta t \leq \max(\varepsilon^2, \Delta t_2)$, $\gamma \geq \gamma_1 := 1 + C$ and

$$h \leq \frac{\cos^2(\frac{3\pi}{8})}{2c_1} \varepsilon, \quad \Delta t \leq \frac{\cos^2(\frac{3\pi}{8})}{2c_2} \varepsilon.$$

Remark 2.9. *Noting the approximation in (2.3.7), one can see that the error results in Theorem 2.8 are the diffuse interface approximations to the equivalent errors on the surface $\Gamma(t)$. This allowed the authors in [44] to derive formal error bounds on the surface $\Gamma(t)$ in the form of*

$$\max_{n=1, \dots, N} \|u(\cdot, t^n) - U^n(\cdot)\|_{L^2(\Gamma(t^n))}^2$$

$$+ \sum_{n=1}^N \Delta t_n \|\nabla_{\Gamma(t^n)} u(\cdot, t^n) - \nabla_{\Gamma(t^n)} U^n(\cdot)\|_{L^2(\Gamma(t^n))}^2 \leq C\varepsilon^2.$$

This motivates the computational bounds found in [63] by monitoring $e[L^\infty, L^2]$ and $e[L^2, H_\tau^1]$.

Remark 2.10. *As with all existence and uniqueness results for PDEs and the finite element approximation to the solutions of PDEs in bounded domains, one would expect some sort of regularity on the boundary of the domain Ω [32, 68]. A benefit of using the diffuse interface approach is that Ω is defined large enough so that $\Gamma_\varepsilon(t) \subset \Omega$, $\forall t \in [0, T]$ and thus there is no interaction between Γ_ε and $\partial\Omega$, which is why $\partial\Omega$ doesn't appear in the analysis. The same can't be said for other implicit methods of approximating moving surfaces, such as the implicit surface finite element method [58].*

2.4 Further computational study of the diffuse interface approximation

As mentioned in Section 1.1.3, one major disadvantage of using the phase field approach and the diffuse interface approach is that the entire domain Ω has to be triangulated rather than just the surface $\Gamma(t)$, and if we require a fine mesh on the whole of Ω this will greatly increase the computational time. However, as defined in [58, 63], the so-called narrow band implementation can be adopted in which the triangulation is refined in the interfacial region where $\rho_\varepsilon > 0$ and coarsened elsewhere. Recalling (2.3.14) we denote

$$\begin{aligned} \mathcal{N}_h^n &:= \{i \in \mathcal{N} : \exists j \in \omega_i \text{ such that } \rho_\varepsilon(\vec{p}_j, t^n) > 0\}, \\ \tilde{\mathcal{N}}_h^n &:= \{i \in \mathcal{N} : \exists j \in \omega_i \text{ such that } \tilde{\rho}_\varepsilon(\vec{p}_j, t^n) > 0\} \end{aligned}$$

and set

$$\Gamma_\varepsilon^{h,n} := \begin{cases} \{T^h \in \mathcal{T}^h : \mathcal{N}_{T^h} \subset \mathcal{N}_h^n\} & \text{if } \gamma = 0, \\ \{T^h \in \mathcal{T}^h : \mathcal{N}_{T^h} \subset \tilde{\mathcal{N}}_h^n\} & \text{if } \gamma > 0. \end{cases}$$

Taking the restriction that $\Delta t \|\vec{v}\|_{L^\infty(\Omega)}^2 \leq Ch\mathcal{T}$ ensures that the approximations $\Gamma_\varepsilon^{h,n+1}$ and $\Gamma_\varepsilon^{h,n}$ only differ by at most a single layer of elements. Using this the following refinement procedure can be adopted. At each time level, taking \mathcal{B}^h such that $\Gamma_\varepsilon^{h,n} \cup \Gamma_\varepsilon^{h,n+1} \subset \mathcal{B}^h$, the refinement procedure can be set up to refine in \mathcal{B}^h to the necessary level and coarsen everywhere else. Considering this we continue to denote \mathcal{T}^h by the evolving triangulation with corresponding interpolant operator I^h as well as redefining the mesh size as $h_{\mathcal{T}} := \max_{T^h \in \mathcal{B}^h} \text{diam}(T^h)$. We demonstrate this procedure in Figures 2.5 and 2.6. Figure 2.5a

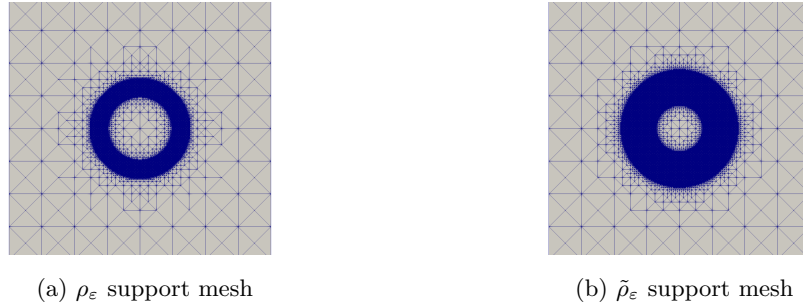


Figure 2.5: Comparison of \mathcal{B}^h for **Model: \mathcal{FE}** (2.4.2) with $\gamma = 0$ (a) and $\gamma > 0$ (b).

shows \mathcal{B}^h for $\gamma = 0$ and Figure 2.5b shows \mathcal{B}^h for $\gamma > 0$. Figure 2.6 shows the refinement and coarsen procedure happening throughout a simulation of an expanding circle.

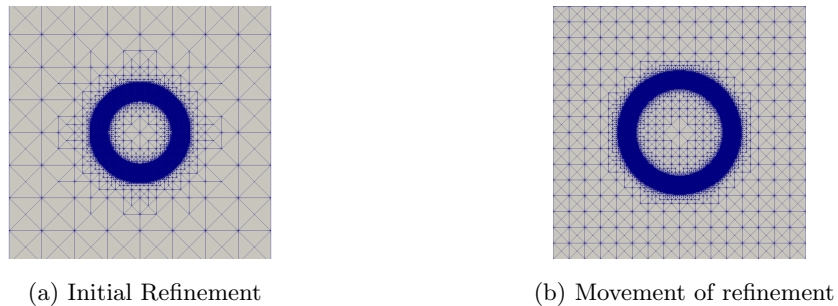


Figure 2.6: Refinement and coarsen procedure with a moving interface.

Another aspect of the scheme that needs to be considered is that the scheme is degenerate in terms of U^n , as mentioned in Section 2.3.1, since we are solving over the whole of Ω . For simplicity of notation we only consider the situation when $\gamma = 0$. In order to combat the degeneracy we define the coefficients of our numerical solution to be zero when $\rho_\varepsilon = 0$, namely we decompose

$$U^n = \sum_{j \in \mathcal{N}_h^n} U_j^n \chi_j + \sum_{j \in \mathcal{N} \setminus \mathcal{N}_h^n} \bar{U}_j^n \chi_j = \sum_{j \in \mathcal{N}_h^{n+1}} \tilde{U}_j^n \chi_j + \sum_{j \in \mathcal{N}_h^n \setminus \mathcal{N}_h^{n+1}} U_j^n \chi_j, \quad (2.4.1)$$

where one notes that if $i \in \mathcal{N}_h^n \setminus \mathcal{N}_h^{n+1}$ then $\rho_\varepsilon^n(\vec{p}_i) = 0$, which can be guaranteed using the narrow band implementation. This is called the discrete interface assumption, see [63, Assumption 2.3, p. 5]. We also note that, from Theorem 2.5, $\bar{U}_j^n = 0$ for $j \notin \mathcal{N}_h^n$.

2.4.1 Finite element approximation of a diffuse interface approximation to SADEs on evolving surface, Model: \mathcal{FE}

Model: \mathcal{FE}

The fully practical finite element scheme we will be using for our numerical computations takes the form of

$$\bar{U}^n(\vec{p}_i) = 0 \quad \text{for} \quad \begin{cases} i \notin \mathcal{N}_h^n & \text{if } \gamma = 0, \\ i \notin \tilde{\mathcal{N}}_h^n & \text{if } \gamma > 0, \end{cases}$$

and

$$\begin{aligned} D_t \left[\left(\rho_\varepsilon^n U^n |\nabla \phi^n|, \xi^h \right)^h \right] + d \left(\rho_\varepsilon^n \nabla U^n |\nabla \phi^n|, \nabla \xi^h \right)^h - \left(\rho_\varepsilon^n U^n \vec{v}^{e,n} |\nabla \phi^n|, \nabla \xi^h \right)^h \\ + \gamma \Delta t_n \left(I^h(\rho_\varepsilon^n) \nabla U^n, \nabla \xi^h \right) = \left(\rho_\varepsilon^n f^{e,n} |\nabla \phi^n|, \xi^h \right)^h, \quad \forall \xi^h \in S^h. \end{aligned} \quad (2.4.2)$$

Remark 2.11. *In the derivation of (2.4.2) we have implicitly set the functions to ξ^h to only depend on space and not time, which is why we can interchange the integration and the discrete time derivative. For analytic purposes one would need to keep the D_t inside the integration, but since we only look at simulations in this section we are justified in making this restriction in view of taking ξ^h as basis functions.*

Similarly to [44, 63] we look to test **Model: \mathcal{FE}** (2.4.2) against the convergence results predicted by the theorems. We look to monitor the following errors

$$\mathcal{E}_1 := \sup_{n=0, \dots, N} \frac{2}{\varepsilon \pi} \int_{\Omega} I^h(\rho_\varepsilon(\cdot, t^n)) |I^h u^e(\cdot, t^n) - U^n(\cdot)|^2 |\nabla I^h \phi(\cdot, t^n)| dx, \quad (2.4.3a)$$

$$\mathcal{E}_2 := \sum_{n=1}^N \frac{2}{\varepsilon \pi} \Delta t_n \int_{\Omega} I^h(\rho_\varepsilon(\cdot, t^n)) |\nabla I^h u^e(\cdot, t^n) - \nabla U^n(\cdot)|^2 |\nabla I^h \phi(\cdot, t^n)| dx, \quad (2.4.3b)$$

as well as the equivalent versions of $e[L^\infty, L^2]$ and $e[L^2, H_\tau^1]$ over the surface $\Gamma(t)$. Following [44, 63], in all the examples presented $\Gamma(t)$ will be a circle, with radius $R(t)$ and centre $\vec{c}_0(t)$, to be defined in the example. Given this, the quadrature approximations of $e[L^\infty, L^2]$ and $e[L^2, H_\tau^1]$ take the form

$$\mathcal{E}_3 := \sup_{n=0, \dots, N} \sum_{l=0}^{L-1} \frac{2\pi}{L} |u(x_l(t^n), t^n) - U^n(x_l(t^n))|^2, \quad (2.4.3c)$$

$$\mathcal{E}_4 := \sum_{n=1}^M \Delta t_n \sum_{l=0}^{L-1} \frac{2\pi}{L} |\nabla_{\Gamma(t^n)} u(x_l(t^n), t^n) - \nabla_{\Gamma(t^n)} U^n(x_l(t^n))|^2, \quad (2.4.3d)$$

where,

$$x_l(t) := c_0(t) + \left(\cos\left(\frac{2\pi l}{L}\right), \sin\left(\frac{2\pi l}{L}\right) \right)^T, \quad l = 0, \dots, L-1,$$

and, noting [44, 63], we set $L = 200$. We quantify the errors by calculating the estimated order of convergence (eoc)

$$eoc_{i,j} := \frac{\ln(\mathcal{E}_{i,j+1}) - \ln(\mathcal{E}_{i,j})}{\ln(h_{\mathcal{T}_{j+1}}) - \ln(h_{\mathcal{T}_j})} \quad (2.4.4)$$

where i corresponds to the error measurement, j corresponds to the relative mesh size $h_{\mathcal{T}_j}$ and $\mathcal{E}_{i,j}$ corresponds to the error of the error measurement i at the j level. Upon setting up the initial refinement using the refinement procedure, we note the refinement and coarsening will maintain the shape regular properties with $h_{\mathcal{T}}$ fixed throughout the simulation. The computational domain we consider is $\Omega = (-2.4, 2.4)^2$ and the computational end time is taken to be $T = 0.1$. We solve the linear system appearing at each time step using GMRES, since the resulting system matrix is not symmetric, together with diagonal preconditioning.

Example 1

For our first example we use a translating circle, which is the same as Example 3 in [44] and Example 1 in Section 3.1 in [63]. Consider $R(t) := 1$ and $\vec{c}_0(t) := (\frac{1}{2} - 2t, 0)^T$, with $d = 1$, $\vec{v}(\vec{p}, t) = (2, 0)^T$ and $f(\vec{p}, t) = 0$ for $\vec{p} \in \Gamma(t)$. Then, the solution to (1.2.2) is

$$u(\vec{p}, t) = e^{-4t} \left(\vec{p}_1 + \frac{1}{2} - 2t \right) \vec{p}_2, \quad \vec{p} \in \Gamma(t), t \in [0, T].$$

The following results in Tables 2.1–2.4 were produced using the finite element toolbox ALBERTA 2.0 [104] implemented on the University of Sussex High Performance Computer cluster (HPC) which uses Scientific Linux as its operating system [111]. Each result used one core, a core is a processor in the Central Processing Unit (CPU) which is the hardware that executes the software commands, of an AMD 64 bit CPU which typically has between 8 to 64 cores. Given the HPC infrastructure, we have no way of using a specific core to enable us to compare execution times reliably. There are many factors that may effect execution time that we can't foresee or manipulate, such as the current number of different codes being executed on a core or the age of a CPU, especially when simulations last at least an hour.

We first demonstrate the experimental order of convergence of **Model: \mathcal{FE}** (2.4.2) with $\gamma = 0$ in Table 2.1 and $\gamma = 0.01$ in Table 2.2. We use the same relationship in [44], that is $\varepsilon = \frac{256}{3}h_{\mathcal{T}}$ and $\varepsilon = 20\sqrt{\Delta t}$, where a uniform time step was chosen, $T = 0.1$ and we define $\phi(\vec{p}, t) = |\vec{p} - \vec{c}_0(t)|^2 - R^2(t)$, for $\vec{p} \in \bar{\Omega}$. We see very similar results to the equivalent error results in [44], that is \mathcal{E}_1 is approaching an eoc of 4, \mathcal{E}_2 and \mathcal{E}_3 have eocs close to 4, and \mathcal{E}_4 has an eoc between 2 and 3. \mathcal{E}_1 and \mathcal{E}_3 have eocs that are larger than what

is proven in the theorem, but they do have the correct order expected from the general literature of numerical solution to PDEs [22, 32, 115], since they are L^2 type errors. \mathcal{E}_2 has an eoc which is larger than the theory predicts and larger than we would expect from the general literature which, since it is an H^1 type error, is an eoc of 2 and is thus exhibits superconvergence. Superconvergence is a phenomenon which occurs when the computable error, that is $\nabla I^h u(\cdot, t^n) - \nabla U^n(\cdot)$, is a higher order than that of the total error, that is $\nabla u(\cdot, t^n) - \nabla U^n(\cdot)$. In other words, $\nabla U^n(\cdot)$ is a better approximation to $\nabla I^h u(\cdot, t^n)$ than to $\nabla u(\cdot, t^n)$ [115]. One often notices superconvergence in one spatial variable problems and we speculate that, since we are approximating advection-diffusion on a curve, this is why we see this here. \mathcal{E}_4 has an eoc which is slightly larger than what the theory predicts, but one expects that this eoc will reduce towards 2 as ε decreases.

Next we test how the value of γ affects the errors. In the proof of Theorem 2.8 in [44] the authors require $\gamma \geq 1 + C$, so in Table 2.3 we present the errors for $\varepsilon = 0.4$ with $\gamma = 0, 0.01, 0.1, 1, 2$. As can be seen the errors are very similar. We stick with the choice of $\gamma = 0.01$ from here onwards.

Next we demonstrate that choosing $r = 2$ for $\tilde{\rho}_\varepsilon$ computationally is just a formality. In Table 2.4 we present the errors for $\varepsilon = 0.4$ with $\gamma = 0.01$ and $r = 1, 1.2, 1.5, 2$. As can be seen the errors are practically identical. The important result we can extract here is that, comparing $r = 2$ to $r = 1.2$, we can reduce the amount of degrees of freedom in the mesh since the interfacial region of $\tilde{\rho}_\varepsilon$ is smaller. From here onwards we will take $r = 1.2$.

Finally, we look at the computational time of some of the results. Considering the standard setting of $\gamma = 0$, taking $\varepsilon = 0.4$, which noting the narrow band implementation equates initially to 370727 degrees of freedom (DOFs), results in approximately 140 minutes of execution whilst $\varepsilon = 0.1\sqrt{2}$, which equates initially to 1047848 DOFs, results in approximately 2760 minutes (1 day, 22 hours) of execution time. In the setting of $\gamma > 0$ and $r = 1.2$, taking $\varepsilon = 0.4$, which equates initially to 442139 DOFs, results in approximately 240 minutes of execution whilst $\varepsilon = 0.1\sqrt{2}$, which equates initially to 1250991 DOFs, results in approximately 3960 minutes (2 days, 18 hours) of execution time. Lastly, in the setting of $\gamma > 0$ and $r = 2$, taking $\varepsilon = 0.4$, which equates initially to 654423 DOFs, results in approximately 1220 minutes of execution time whilst $\varepsilon = 0.1\sqrt{2}$, which equates initially to 2063849 DOFs, results in approximately 10800 minutes (7 days, 12 hours) of execution time. As one can readily see, the computational time gained from taking $r = 1.2$ rather than $r = 2$ is massive. Similarly, taking $r = 1$ rather than $r = 1.2$ gains computational

time but you lose the guaranteed convergence from the theory.

ε	$\mathcal{E}_1 \times 10^4$	eoc_1	$\mathcal{E}_2 \times 10^4$	eoc_2	$\mathcal{E}_3 \times 10^5$	eoc_3	$\mathcal{E}_4 \times 10^6$	eoc_4
0.4	1.056	-	5.959	-	2.764	-	4.770	-
$0.2\sqrt{2}$	0.1602	5.44	1.484	4.01	0.8114	3.54	1.812	2.79
0.2	0.03097	4.74	0.3736	3.98	0.2193	3.76	0.6371	3.02
$0.1\sqrt{2}$	0.006715	4.41	0.09462	3.96	0.05703	3.89	0.2383	2.84

Table 2.1: Errors for **Model: \mathcal{FE}** (2.4.2), with $\gamma = 0$, for Example 1.

ε	$\mathcal{E}_1 \times 10^4$	eoc_1	$\mathcal{E}_2 \times 10^4$	eoc_2	$\mathcal{E}_3 \times 10^5$	eoc_3	$\mathcal{E}_4 \times 10^6$	eoc_4
0.4	1.056	-	5.952	-	2.764	-	4.770	-
$0.2\sqrt{2}$	0.1602	5.44	1.481	4.01	0.8110	3.54	1.811	2.79
0.2	0.03092	4.74	0.3723	3.98	0.2188	3.78	0.6363	3.02
$0.1\sqrt{2}$	0.006691	4.42	0.09390	3.98	0.05679	3.89	0.2379	2.84

Table 2.2: Errors for **Model: \mathcal{FE}** (2.4.2), with $\gamma = 0.01$, for Example 1.

γ	$\mathcal{E}_1 \times 10^4$	$\mathcal{E}_2 \times 10^4$	$\mathcal{E}_3 \times 10^5$	$\mathcal{E}_4 \times 10^6$
0	1.056	5.959	2.764	4.770
0.01	1.056	5.952	2.764	4.770
0.1	1.057	5.954	2.774	4.785
1	1.065	5.982	2.877	4.936
2	1.074	6.013	2.994	5.107

Table 2.3: Errors for **Model: \mathcal{FE}** (2.4.2), with varying γ and fixed $\varepsilon = 0.4$, for Example 1.

r	$\mathcal{E}_1 \times 10^4$	$\mathcal{E}_2 \times 10^4$	$\mathcal{E}_3 \times 10^5$	$\mathcal{E}_4 \times 10^6$
1	1.056	5.959	2.764	4.770
1.2	1.056	5.952	2.764	4.769
1.5	1.056	5.952	2.764	4.770
2	1.056	5.952	2.764	4.770

Table 2.4: Errors for **Model: \mathcal{FE}** (2.4.2), with varying r , and fixed $\gamma = 0.01$ and $\varepsilon = 0.4$, for Example 1.

2.4.2 Finite volume approximation of a diffuse interface approximation to SADEs on evolving surfaces, Model: \mathcal{FV}

In this section we present a finite volume discretisation of (2.3.12a), for which we closely follow the finite volume/element discretisation in [66]. Before we derive a scheme, we set up the appropriate dual mesh. Here we follow the set up from [66] adopting our notation for clarity.

Given a quasi-uniform triangulation \mathcal{T}^h , of a bounded, polygonal domain $\Omega \subset \mathbb{R}^2$, we construct the following dual mesh: we denote each cell of the dual mesh by V_i and associate it with a node \vec{p}_i of \mathcal{T}^h . Each V_i is bounded by the lines that bisect and are perpendicular to the edge emanating from its associated node, see Figure 2.7. When the mesh is acute the dual cell associated with a particular node can also be characterised as the set of points in Ω that are closer to the node than any others. The perpendicular bisectors will meet at the circumcentres of the triangles of \mathcal{T}^h which form the nodes of the complementary mesh. We refer to the edges and nodes of the dual mesh as co-nodes and co-edges and we restrict ourselves to triangulations whose interior angles are no greater than $\frac{\pi}{2}$ as this guarantees that the circumcentre of a triangle will be contained within the triangle and co-edges intersect only at co-nodes. We denote the edge of \mathcal{T}^h connecting the i th node to the j th node by σ_{ij} and its length by h_{ij} . Similarly, σ'_{ij} will denote the co-edge that is perpendicular to σ_{ij} and h'_{ij} will denote its length and we denote the portion of h'_{ij} that is in T^h by $(h'_{ij})_{T^h}$. We set ξ_{ij} to be the set of triangles in \mathcal{T}^h having σ_{ij} as an edge: $\xi_{ij} = \{T^h \in \mathcal{T}^h : \sigma_{ij} \subset T^h\}$ and we note in general ξ_{ij} contains two triangles; the exception being when σ_{ij} is a boundary edge which only meets one triangle.

Using the notation defined in [66] we can now derive a finite volume scheme for (2.3.12a), which follows a similar derivation to the finite element approximation to (2.3.12a) in [63]. We multiply (2.3.12a) by $\rho_\varepsilon |\nabla \phi|$, noting (2.3.9) and (2.3.11), and integrate over each volume cell V_j , where $j \in \mathcal{N}$ such that $\vec{p}_j \notin \partial\Omega$, to obtain

$$\begin{aligned} \int_{V_j} [\partial_t^\bullet(\rho_\varepsilon u^e) + \rho_\varepsilon u^e \operatorname{div}_\phi(\vec{v}^e)] |\nabla \phi| dx - d \int_{V_j} \operatorname{div}(\rho_\varepsilon |\nabla \phi| \nabla u^e) dx \\ = \int_{V_j} \rho_\varepsilon f^e |\nabla \phi| dx + \int_{V_j} \phi \rho_\varepsilon R |\nabla \phi| dx. \end{aligned}$$

Using the classical divergence theorem and Lemma 2.6, we obtain the weak form

$$\frac{d}{dt} \int_{V_j} \rho_\varepsilon u^e |\nabla \phi| dx + \int_{\partial V_j} \rho_\varepsilon u^e \langle \vec{v}^e, \vec{n}_{V_j} \rangle |\nabla \phi| dS - d \int_{\partial V_j} \rho_\varepsilon \langle \nabla u^e, \vec{n}_{V_j} \rangle |\nabla \phi| dS$$

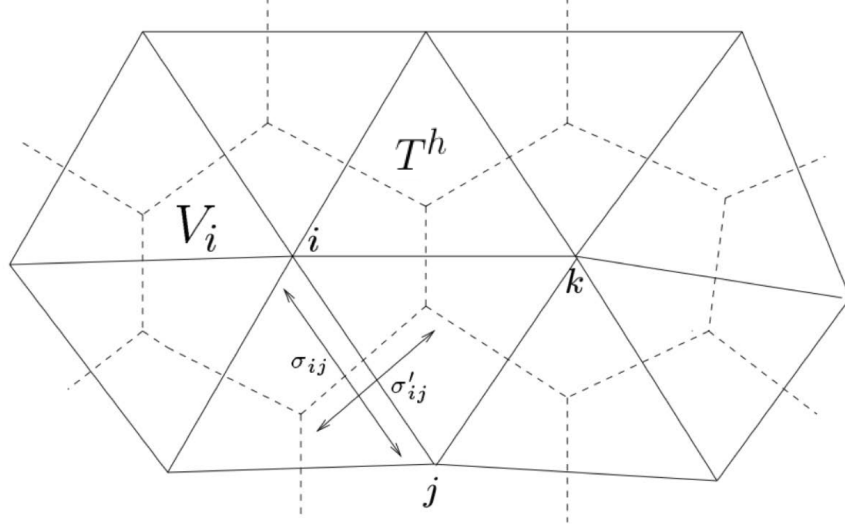


Figure 2.7: The basic structure of the dual mesh considered in Section 2.4.2. Here T^h denotes a triangle in the triangulation \mathcal{T}^h and V_i denotes the volume cell corresponding to the node \vec{p}_i at index i . Inspiration from [66].

$$= \int_{V_j} \rho_\varepsilon f^e |\nabla \phi| dx + \int_{V_j} \phi \rho_\varepsilon R |\nabla \phi| dx, \quad (2.4.5)$$

where $n_{\vec{V}_j}$ is the outward pointing unit normal to ∂V_j .

Model: \mathcal{FV}

In a similar manner to (2.3.14), we neglect the remainder term involving R . To approximate (2.4.5) for U^n in the form of (2.4.1) we set $U_j^n = 0$ for $j \notin \mathcal{N}_h^n$ together with the following upwinding scheme

$$\begin{aligned} & \frac{1}{\Delta t_n} (\rho_\varepsilon^n)_j U_j^n m_j^n - d \sum_{k \in \omega_j} \left(\frac{U_k^n - U_j^n}{h_{jk}} \right) (\rho_\varepsilon^n)_{jk} p_{jk}^n \\ & + \sum_{k \in \omega_j} \left(U_j^n \left[\langle (\rho_\varepsilon^n \vec{v}^{e,n})_{jk}, \vec{n}_{\sigma'_{jk}} \rangle \right]_+ + U_k^n \left[\langle (\rho_\varepsilon^n \vec{v}^{e,n})_{jk}, \vec{n}_{\sigma'_{jk}} \rangle \right]_- \right) p_{jk}^n \\ & = \frac{1}{\Delta t_n} (\rho_\varepsilon^{n,n-1})_j U_j^{n-1} m_j^{n-1} + (\rho_\varepsilon^n)_j f_j^{e,n} m_j^n, \quad \forall j \in \mathcal{N}_h^n, \end{aligned} \quad (2.4.6)$$

where $[s]_+ = \max\{s, 0\}$, $[s]_- = \min\{s, 0\}$, $(g)_{jk} = \frac{1}{2} (g_j + g_k)$ with $g_j = g(\vec{p}_j)$ and

$$m_j^n := \sum_{T^h \in \mathcal{N}_j} |\nabla I^h \phi|_{T^h}^n \int_{T^h|_{V_j}} dx, \quad p_{jk}^n := \sum_{T^h \in \xi_{jk}} (h'_{jk})_{T^h} |\nabla I^h \phi|_{T^h}^n,$$

with

$$(\rho_\varepsilon^{n,n-1})_j := \begin{cases} (\rho_\varepsilon^{n-1})_j & \text{if } j \in \mathcal{N}_h^n, \\ 0 & \text{otherwise.} \end{cases} \quad (2.4.7)$$

The discretisation method we employ here to derive (2.4.6) from (2.4.5) is similar to the so called Finite Volume Element method [28, 85, 94]. This method sets up the weak form

of the equation we want to approximate in a finite volume style, i.e. integrals over volume cells, and then approximates the integrals in a finite element style by using the nodal values of the functions within the integrals. This enables us to use the finite element framework set up in ALBERTA. We include upwinding in **Model: \mathcal{FV}** (2.4.6) as a tool used to dampen oscillations by introducing some form of numerical diffusion [74]. Given this setup, and how similar the resulting nodal scheme is to the one derived for the finite element approximation, one would expect the same rates of convergence for the conventional advection-diffusion equation, even with the addition of upwinding [46, 47, 85].

Table 2.5 demonstrates the errors and eocs using **Model: \mathcal{FV}** (2.4.6) applied to Example 1 with the same parameter choices and relationships, and the same implementation using ALBERTA with access to one core of computational power on the HPC. By comparing Table 2.5 to Table 2.1 we see that the eocs for the errors \mathcal{E}_3 and \mathcal{E}_4 , the errors restricted to the interface, follow a similar trend and the error values themselves are quite similar. The diffuse interface type error \mathcal{E}_1 also follows the eoc trend of the finite element results in Table 2.1 and the error values are quite similar to the finite element error values. The diffuse interface type error \mathcal{E}_2 is however not converging. We speculate this is due to the large profile spikes which can be seen in Figure 2.10.

Taking $\varepsilon = 0.4$ results in approximately 130 minutes of execution time, which is slightly shorter than using **Model: \mathcal{FE}** (2.4.2) with $\gamma = 0$. Taking $\varepsilon = 0.1\sqrt{2}$ results in approximately 3180 minutes (2 days, 15 hours) of execution time. Finally, taking $\varepsilon = 0.05\sqrt{2}$, which is the smallest value of ε we take in this section and leads initially to 2123063 DOFs, results in approximately 16530 minutes (11 days, 11.5 hours) of execution time. Given the difference in computational time needed for $\varepsilon = 0.05\sqrt{2}$ compared to $\varepsilon = 0.1\sqrt{2}$, one can see that using a finer mesh would almost be intractable.

ε	$\mathcal{E}_1 \times 10^4$	eoc_1	$\mathcal{E}_2 \times 10^4$	eoc_2	$\mathcal{E}_3 \times 10^5$	eoc_3	$\mathcal{E}_4 \times 10^6$	eoc_4
0.4	1.084	-	6.641	-	3.385	-	5.778	-
$0.2\sqrt{2}$	0.1778	5.22	7.887	-0.50	0.9801	3.58	2.102	2.92
0.2	0.04000	4.30	2.453	3.37	0.3086	3.33	0.7812	2.86
$0.1\sqrt{2}$	0.009010	4.30	22.36	-6.38	0.07977	3.90	0.2919	2.84
0.1	0.002729	3.45	7.756	3.06	0.02630	3.20	0.1176	2.62
$0.05\sqrt{2}$	0.0006637	4.08	85.79	-6.93	0.006390	4.08	0.04221	2.82

Table 2.5: Errors for **Model: \mathcal{FV}** (2.4.6), for Example 1.

With the rice blast model in mind, we notice the molecular species equations (4.1.2a)–(4.1.2b) each have a small, if not zero, diffusion constant. This leads us to investigating how **Model: \mathcal{FE}** (2.4.2) and **Model: \mathcal{FV}** (2.4.6) fare when small diffusion constants are used. To solve the algebraic system of equations resulting from **Model: \mathcal{FV}** (2.4.6) we use GMRES but without diagonal preconditioning.

Example 1a

We consider a slightly perturbed version of Example 1. Considering $R(t) = 1$ and $\vec{c}_0(t) = (\frac{1}{2} - 2t, 0)^T$, with $\vec{v}(\vec{p}, t) = (2, 0)^T$, $f(\vec{p}, t) = 4(d - 1)e^{-4t} (\vec{p}_1 + \frac{1}{2} - 2t) \vec{p}_2$ for $\vec{p} \in \Gamma(t)$, the solution to (1.2.2) is

$$u(\vec{p}, t) = e^{-4t} \left(\vec{p}_1 + \frac{1}{2} - 2t \right) \vec{p}_2, \quad \vec{p} \in \Gamma(t), t \in [0, T].$$

Similarly to Example 1, we produce the results in Tables 2.6–2.9 using ALBERTA with access to one core of computational power on the HPC. Figures 2.8–2.10 are produced using MATLAB (R2019a) [92].

Tables 2.6–2.9 depict the errors of Example 1a whilst Figures 2.8–2.10 depict the profile of U^N on the line $y = x$ starting at $(0, 0)$. Table 2.6 demonstrates how **Model: \mathcal{FE}** (2.4.2), with $\gamma = 0$, performs when d is reduced, for $\varepsilon = \frac{32}{3}h_{\mathcal{T}}$, $\varepsilon = 20\sqrt{\Delta t}$ and $\varepsilon = 0.1\sqrt{2}$, $T = 0.1$ and $\phi(\vec{p}, t) = |\vec{p} - \vec{c}_0(t)| - R(t)$ for $\vec{p} \in \bar{\Omega}$. This value of ε results initially in 19997 DOFs. We display the profile of U^N in Figure 2.8, in which we see that there seems to be an appearance of instabilities over the interfacial region as d reduces. One may expect that this could be due to the CFL type condition in Theorem 2.5, however the instabilities appear magnitudes of d before this condition is not met since $\Delta t = 5 \times 10^{-5}$ and $\|v\|_{L^\infty(\Omega)} = 2$. Moreover we also see large peaks close to the edge of the interfacial region, we will discuss these peaks in Section 2.4.3. We reduced $h_{\mathcal{T}}$ by a factor of 2 and Δt by a factor of 4 and saw no major improvements, as shown in Table 2.7. In Figure 2.9 we see a similar profile for **Model: \mathcal{FE}** (2.4.2) with $\gamma = 0.01$. In Table 2.6 we display the errors for **Model: \mathcal{FE}** (2.4.2) with $\gamma = 0.01$ and we see that \mathcal{E}_1 and \mathcal{E}_2 are significantly better than the errors for $\gamma = 0$ in Table 2.6 even though this is not evident from Figure 2.9. This improvement of the errors for $\gamma > 0$ can be expected due to the added diffusion the stabilisation term gives. Table 2.9 demonstrates how **Model: \mathcal{FV}** (2.4.6) performs when d is reduced. With the exception of \mathcal{E}_2 we see that **Model: \mathcal{FV}** (2.4.6) performs well even for very small values of d . Figure 2.10 displays the profile of U^N obtained using **Model: \mathcal{FV}** (2.4.6), in it we see that, as d is reducing, no instabilities

appear, however there also seems to be sharp peaks close to the edge of the interfacial region. Taking $d = 1$, the computational time solving Example 1a using **Model: \mathcal{FE}** (2.4.2) with $\gamma = 0$ was approximately 80 minutes of execution time whilst using **Model: \mathcal{FV}** (2.4.6) was approximately 120 minutes of execution time, a similar difference in times compared to Example 1. Taking $d = 0$, the computational time solving Example 1a using **Model: \mathcal{FE}** (2.4.2) with $\gamma = 0$ was approximately 690 minutes of execution time whilst using **Model: \mathcal{FV}** (2.4.6) was approximately 390 minutes of execution time. We expect that the instabilities caused by $d = 0$ whilst using **Model: \mathcal{FE}** (2.4.2) caused an increased number of iterations of the GMRES solver at each time step, hence the longer computational time.

d	$\mathcal{E}_1 \times 10^5$	$\mathcal{E}_2 \times 10^4$	$\mathcal{E}_3 \times 10^6$	$\mathcal{E}_4 \times 10^5$
1	1.18	1.479	2.348	1.741
10^{-1}	4.022	48.33	0.1356	2.484
10^{-2}	1967	29711	0.2266	74.95
10^{-3}	22202	610920	9.488	6465
10^{-4}	167224	3865034	175.9	117704
10^{-5}	289409	6447880	368.2	232113
0	310241	6941655	405.3	254757

Table 2.6: Errors for **Model: \mathcal{FE}** (2.4.2), with varying d , and fixed $\gamma = 0$ and $\varepsilon = 0.1\sqrt{2}$, for Example 1a.

d	$\mathcal{E}_1 \times 10^5$	$\mathcal{E}_2 \times 10^4$	$\mathcal{E}_3 \times 10^6$	$\mathcal{E}_4 \times 10^5$
1	1.1166	1.375	2.204	0.4382
10^{-1}	0.5351	1.910	0.06514	0.5861
10^{-2}	25.82	1983	0.01511	18.42
10^{-3}	544.0	63230	0.7940	1767
10^{-4}	2299	564966	48.46	113730
10^{-5}	8144	2230500	289.7	674849
0	10750	3235908	387.7	931739

Table 2.7: Errors for **Model: \mathcal{FE}** (2.4.2), with varying d , and fixed $\gamma = 0$ and $\varepsilon = 0.1\sqrt{2}$ but with a smaller $h_{\mathcal{T}}$ and Δt , for Example 1a.

d	$\mathcal{E}_1 \times 10^5$	$\mathcal{E}_2 \times 10^4$	$\mathcal{E}_3 \times 10^6$	$\mathcal{E}_4 \times 10^5$
1	1.18	1.478	2.348	1.741
10^{-1}	0.5559	5.752	0.1355	2.484
10^{-2}	8.061	616.2	0.2267	74.94
10^{-3}	29.52	5690	9.48	6459
10^{-4}	49.95	51727	174.2	117200
10^{-5}	109.7	117598	362.9	230440
0	124.7	131751	399.2	252775

Table 2.8: Errors for **Model: \mathcal{FE}** (2.4.2), with varying d , and fixed $\gamma = 0.01$ and $\varepsilon = 0.1\sqrt{2}$, for Example 1a.

d	$\mathcal{E}_1 \times 10^5$	$\mathcal{E}_2 \times 10^4$	$\mathcal{E}_3 \times 10^6$	$\mathcal{E}_4 \times 10^5$
1	2.390	14.48	17.68	1.952
10^{-1}	2.367	65.07	12.50	2.486
10^{-2}	4.106	535.8	9.776	21.19
10^{-3}	50.21	10417	9.891	67.34
10^{-4}	63.52	15934	9.920	80.75
10^{-5}	63.36	15934	9.923	82.24
0	63.99	15988	9.924	82.40

Table 2.9: Errors for **Model: \mathcal{FV}** (2.4.6), with varying d and fixed $\varepsilon = 0.1\sqrt{2}$, for Example 1a.

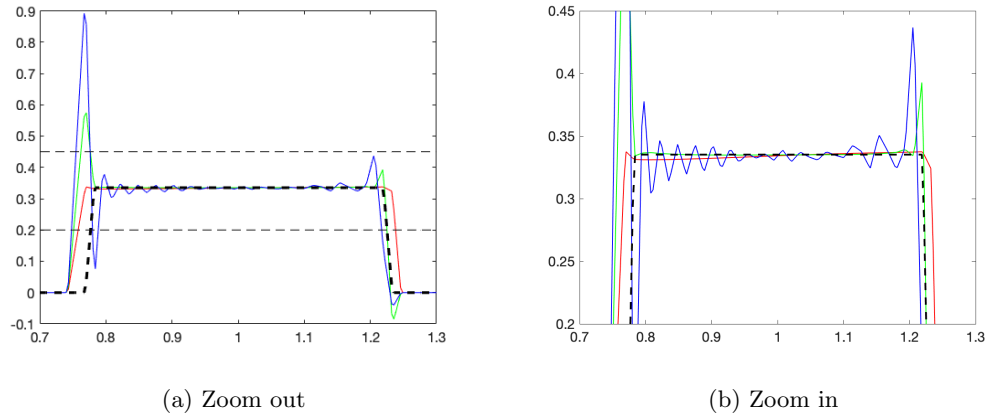


Figure 2.8: Profile of U^N demonstrating appearance of instabilities when reducing d using **Model: \mathcal{FE}** (2.4.2) with fixed $\gamma = 0$ and $\varepsilon = \frac{32}{3}h_{\mathcal{T}}$, $\varepsilon = 20\sqrt{\Delta t}$ and $\varepsilon = 0.1\sqrt{2}$, for Example 1a. The red line is $d = 1$, the green line is $d = 10^{-2}$ and the blue line is $d = 10^{-4}$, with the black dashed line being the profile of the true solution. The grey dashed lines in (a) represents the zone that (b) is demonstrating.

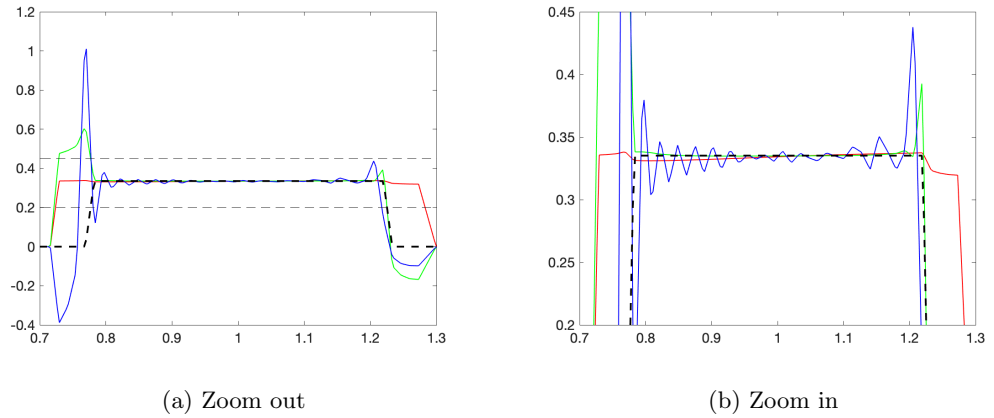


Figure 2.9: Profile of U^N demonstrating appearance of instabilities when reducing d using **Model: \mathcal{FE}** (2.4.2) with fixed $\gamma = 0.01$ and $\varepsilon = \frac{32}{3}h_{\mathcal{T}}$, $\varepsilon = 20\sqrt{\Delta t}$ and $\varepsilon = 0.1\sqrt{2}$, for Example 1a. The red line is $d = 1$, the green line is $d = 10^{-2}$ and the blue line is $d = 10^{-4}$, with the black dashed line being the profile of the true solution. The grey dashed lines in (a) represents the zone that (b) is demonstrating.

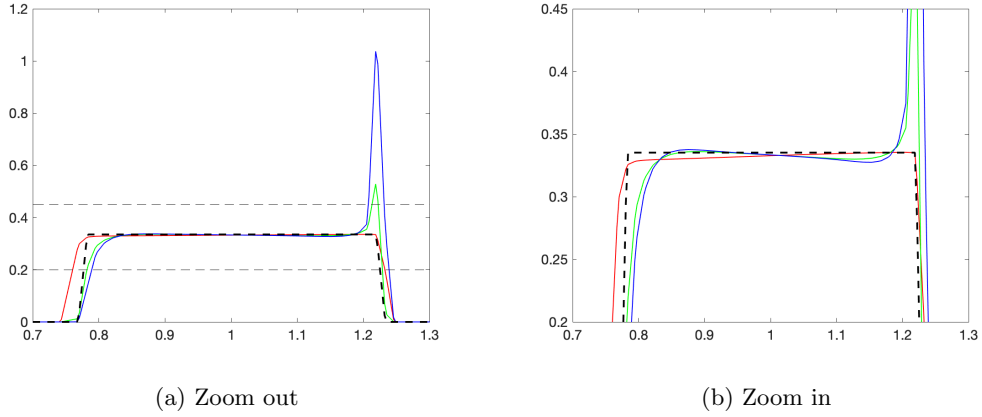


Figure 2.10: Profile of U^N demonstrating appearance no instabilities when reducing d using **Model: \mathcal{FV}** (2.4.6) with fixed $\varepsilon = \frac{32}{3}h_{\mathcal{T}}$, $\varepsilon = 20\sqrt{\Delta t}$ and $\varepsilon = 0.1\sqrt{2}$, for Example 1a. The red line is $d = 1$, the green line is $d = 10^{-2}$ and the blue line is $d = 10^{-4}$, with the black dashed line being the profile of the true solution. The grey dashed lines in (a) represents the zone that (b) is demonstrating.

2.4.3 Edge smoothing for Model: \mathcal{FE}

Studying Figures 2.8–2.10 we notice spikes at the edge of the profiles of U^N for large h and small d . The authors in [63] note that this could be the result of the surface evolving and subsequently investigate how to remedy it by considering the one dimensional problem with $\Omega \subset \mathbb{R}$. We reiterate their calculations with the inclusion of the diffusion constant.

Let $\Omega \subset \mathbb{R}$, and $\mathcal{T}^h = \cup_{j=1}^J \sigma_j$, where $\sigma_j = (p_{j-1}, p_j)$ and $|\sigma_j| = h_j$. By denoting $v_i = v(p_i)$, let $i \in \mathcal{N}_h^n$ be a node index such that $(\rho_\varepsilon^n)_i = 0$ but $(\rho_\varepsilon^n)_{i-1} > 0$ and $(\rho_\varepsilon^{n-1})_i > 0$. Then, considering σ_i in **Model: \mathcal{FE}** (2.4.2), whereby for simplicity we set $\gamma = 0$, with $(\rho_\varepsilon^n)_{i+1} = 0$ by default, one has

$$\begin{aligned}
 -\frac{1}{\Delta t_n} \left(\frac{h_i q_i^{n-1} + h_{i+1} q_{i+1}^{n-1}}{2} \right) (\rho_\varepsilon^{n-1})_i U_i^{n-1} - \frac{1}{2} (\rho_\varepsilon^n)_{i-1} U_{i-1}^n \vec{v}_{i-1}^{e,n} q_i^n \\
 + \frac{d}{2} \frac{q_i^n}{h_i} (\rho_\varepsilon^n)_{i-1} (U_i^n - U_{i-1}^n) = 0, \quad (2.4.8)
 \end{aligned}$$

where $q_i^n = |(\phi_{|\sigma_i}^n)_x|$. It is easy to see that, in general, U_i^n will be different from U_{i-1}^n , thus resulting in peaks. Considering a uniform mesh size h and a uniform time step Δt , it can be verified that $\rho_\varepsilon^{n-1}(a_i) = \mathcal{O}(\Delta t^2)$ as $\Delta t \rightarrow 0$ and $\rho_\varepsilon^n(a_{i-1}) = \mathcal{O}(h^2)$, from [62]. Thus, the authors in [63] conclude that

$$|U_i^n - U_{i-1}^n| = \mathcal{O}(h), \quad \text{as } h \rightarrow 0.$$

We can see this behaviour in Figure 2.11. Here, we also add that the peaks scale linearly in d^{-1} , which can be seen in Figure 2.12. Indeed we speculate that as d gets smaller, this forces $|U_i^n - U_{i-1}^n|$ to get larger, thus creating the larger peaks. By including γ in the expansion (2.4.8), this also heuristically shows why the errors \mathcal{E}_1 and \mathcal{E}_2 obtained from **Model: \mathcal{FE}** (2.4.2) with $\gamma > 0$ are smaller when d is reducing compared to the errors with $\gamma = 0$. Nevertheless taking $\gamma > 0$ doesn't actually help with the peaks in the interface, as demonstrated by Figures 2.13 and 2.14.

Model: \mathcal{FEs}

Although these spikes occur close to the boundary of the interfacial region, this can still have an effect on the overall solution given enough time, especially in situations when the scalar quantity is used in other equations, such as for our application of the rice blast. To reduce the size of the peaks, in [63] the authors present a streamline diffusion term in the form of

$$\int_{\Omega} I^h(g_e^n) \langle \vec{v}_{\vec{v},h}^{e,n}, \nabla \chi_i \rangle \langle \vec{v}_{\vec{v},h}^{e,n}, \nabla \chi_j \rangle |\nabla \phi^n| dx, \quad i, j \in \mathcal{N}_h^n \quad (2.4.9)$$

where, for $\vec{p} \in \Omega$,

$$g_e(\vec{p}, t) := \begin{cases} 0 & \text{if } \frac{|d_{\Gamma}(\vec{p}, t)|}{\varepsilon} \leq \frac{\pi}{4} \text{ or } \frac{|d_{\Gamma}(\vec{p}, t)|}{\varepsilon} \geq \frac{\pi}{2}, \\ \frac{h}{d} \frac{4}{\pi} \left(\frac{|d_{\Gamma}(\vec{p}, t)|}{\varepsilon} - \frac{\pi}{4} \right) & \text{otherwise,} \end{cases} \quad (2.4.10)$$

and $\vec{v}_{\vec{v},h}^{e,n}$ is an approximate projection of $\vec{v}^{e,n}$ in the normal direction, which is approximately orthogonal to the boundary of Γ_{ε}^n . The role of g_e is to add small levels of diffusion close to the boundary in the approximate normal direction, hence the given description of streamline diffusion. The addition of (2.4.9) to (2.4.2), with $\bar{U}^n(\vec{p}_i) = 0$ for $i \notin \mathcal{N}_h^n$, yields the following scheme

$$\begin{aligned} D_t \left[\left(\rho_{\varepsilon}^n U^n |\nabla \phi^n|, \xi^h \right)^h \right] + d \left(\rho_{\varepsilon}^n \nabla U^n |\nabla \phi^n|, \nabla \xi^h \right)^h - \left(\rho_{\varepsilon}^n U^n \vec{v}^{e,n} |\nabla \phi^n|, \nabla \xi^h \right)^h \\ + \gamma \Delta t_n \left(I^h(\tilde{\rho}_{\varepsilon}^n) \nabla U^n, \nabla \xi^h \right) + \left(g_e^n \langle \vec{v}_{\vec{v},h}^{e,n}, \nabla U^n \rangle \vec{v}_{\vec{v},h}^{e,n} |\nabla \phi^n|, \nabla \xi^h \right)^h \\ = \left(\rho_{\varepsilon}^n f^{e,n} |\nabla \phi^n|, \xi^h \right)^h, \quad \forall \xi^h \in S^h. \end{aligned} \quad (2.4.11)$$

With the addition of (2.4.9) into **Model: \mathcal{FE}** (2.4.2), continuing from (2.4.8), noting that $(g_e^n)_i = (g_e^n)_{i+1} = 0$, the authors in [63] yield

$$\begin{aligned} - \frac{1}{\Delta t_n} \left(\frac{h_i q_i^{n-1} + h_{i+1} q_{i+1}^{n-1}}{2} \right) (\rho_{\varepsilon}^{n-1})_i U_i^{n-1} - \frac{1}{2} (\rho_{\varepsilon}^n)_{i-1} U_{i-1}^n \vec{v}_{i-1}^{e,n} q_{i-1}^n \\ + \frac{d}{2} \frac{q_i^n}{h_i} (\rho_{\varepsilon}^n)_{i-1} (U_i^n - U_{i-1}^n) + \frac{1}{2} \frac{q_i^n}{h_i} (g_e^n)_{i-1} |(\vec{v}_{\vec{v},h}^{e,n})_{i-1}|^2 (U_i^n - U_{i-1}^n) = 0. \end{aligned} \quad (2.4.12)$$

Thus, since $g_e = \mathcal{O}(h)$ as $h \rightarrow 0$, the authors in [63] conclude that with the addition of (2.4.9) one has

$$|U_i^n - U_{i-1}^n| = \mathcal{O}(h^2), \quad \text{as } h \rightarrow 0.$$

Since $g_e \leq Cd^{-1}$, as opposed to in (2.4.8), where d getting smaller makes $|U_i^n - U_{i-1}^n|$ get larger, d getting smaller implies the contribution from g_e gets larger, thus forcing $|U_i^n - U_{i-1}^n|$ to stay small, dampening the spikes. In [63] the authors extend their uniqueness result Theorem 2.5 to include (2.4.9) with $d = 1$.

Remark 2.12. *We note that the same edge spiking phenomena happens for **Model: \mathcal{FV}** (2.4.6), see Figures 2.15 and 2.16; however, we leave the edge smoothing for **Model: \mathcal{FV}** for future research.*

Tables 2.10 and 2.11 depicts the errors resulting from Example 1 using **Model: \mathcal{FEs}** (2.4.11) with $\gamma = 0$ and $\gamma = 0.01$ respectively, whilst Tables 2.12 and 2.13 depict the errors resulting from Example 1a using **Model: \mathcal{FEs}** (2.4.11) with $\gamma = 0$ and $\gamma = 0.01$ respectively. Figures 2.11–2.14 depict the profile of U^N resulting from a reduction in $h_{\mathcal{T}}$ and d using **Model: \mathcal{FE}** (2.4.2) with $\gamma = 0$ and $\gamma = 0.01$ on the line $y = x$ starting at $(0, 0)$, whilst Figures 2.15 and 2.16 depict the same except using **Model: \mathcal{FV}** (2.4.6). Figures 2.17 and 2.18 depict the profile of U^N resulting from Example 1a using **Model: \mathcal{FEs}** (2.4.11) with $\gamma = 0$ and $\gamma = 0.01$ on the line $y = x$ starting at $(0, 0)$.

In terms of errors, it is reported in [63] that using **Model: \mathcal{FEs}** (2.4.11) rather than **Model: \mathcal{FE}** (2.4.2) doesn't largely affect the errors since it is only present close to the boundary of the interfacial region, we see this in Tables 2.10 and 2.11. In Table 2.10 we see the errors for Example 1 obtained using **Model: \mathcal{FEs}** (2.4.11) with $\gamma = 0$, while Table 2.11 shows the errors for **Model: \mathcal{FEs}** (2.4.11) with $\gamma = 0.01$. Considering the setting of $\gamma = 0$, taking $\varepsilon = 0.4$ resulted in approximately 150 minutes of execution time whilst taking $\varepsilon = 0.1\sqrt{2}$ resulted in approximately 2880 minutes (2 days) of execution time. Considering the setting of $\gamma = 0.01$, taking $\varepsilon = 0.4$ resulted in approximately 270 minutes of execution time whilst taking $\varepsilon = 0.1\sqrt{2}$ resulted in approximately 4380 minutes (3 days, 1 hour) of execution time. As one can see, adding the edge smoothing term only adds a small amount of computational time which is probably due to the assembling of an extra matrix. Even though the addition of the edge smoothing term gives stabilisation and thus should improve the solving time for each linear system, the choices of h and Δt in Example 1 are suitably small and so the edge spiking has a relatively small impact. Tables 2.12 and 2.13 display the errors for Example 1a for **Model: \mathcal{FEs}** (2.4.11) with

$\gamma = 0$ and $\gamma = 0.01$ respectively. Considering Table 2.12 first, comparing to Table 2.6 we can see that initially the addition of (2.4.9) has a positive effect on the errors, however as d reduces it has a negative effect. Although we can see from Figure 2.17 that the profile is a lot smoother at the edges, even when d is small, wiggles still appear in regions where there is no edge smoothing, but the edge smoothing results in a jump of the profile. We speculate that this is caused by a combination of the instabilities outside the region of edge smoothing and the fact that the finite element approximation is continuous. We see a similar behaviour for **Model: \mathcal{FE}_5** (2.4.11) when $\gamma > 0$ in Table 2.13 and in Figure 2.18. Taking $d = 1$ resulted in approximately 45 minutes of execution time whilst taking $d = 10^{-8}$ resulted in approximately 510 minutes of execution time. Here we can see that reducing the effects of the edge spikes enables a faster solving time as one expects the solver converges quicker. For the comparison of Figures 2.11–2.16 we note here to be wary of the different scaling used for the y -axis. In these simulations we have used the same implementation in ALBERTA with one core of power on the HPC but used GMRES with diagonal preconditioning for the solution to the algebraic system resulting from **Model: \mathcal{FE}_5** (2.4.11).

ε	$\mathcal{E}_1 \times 10^4$	eoc_1	$\mathcal{E}_2 \times 10^4$	eoc_2	$\mathcal{E}_3 \times 10^5$	eoc_3	$\mathcal{E}_4 \times 10^6$	eoc_4
0.4	1.056	-	5.950	-	2.763	-	4.769	-
$0.2\sqrt{2}$	0.1601	5.44	1.481	4.01	0.8102	3.54	1.810	2.80
0.2	0.03085	4.75	0.3719	3.99	0.2182	3.79	0.6353	3.02
$0.1\sqrt{2}$	0.006634	4.43	0.09384	3.97	0.05621	3.91	0.2369	2.84

Table 2.10: Errors for **Model: \mathcal{FE}_5** (2.4.11) with $\gamma = 0$, for Example 1.

ε	$\mathcal{E}_1 \times 10^4$	eoc_1	$\mathcal{E}_2 \times 10^4$	eoc_2	$\mathcal{E}_3 \times 10^5$	eoc_3	$\mathcal{E}_4 \times 10^6$	eoc_4
0.4	1.056	-	5.950	-	2.764	-	4.770	-
$0.2\sqrt{2}$	0.1601	5.44	1.481	4.01	0.8108	3.54	1.811	2.79
0.2	0.03092	4.74	0.3719	3.99	0.2188	3.78	0.6363	3.02
$0.1\sqrt{2}$	0.006691	4.42	0.09385	3.97	0.05679	3.89	0.2379	2.84

Table 2.11: Errors for **Model: \mathcal{FE}_5** (2.4.11) with $\gamma = 0.01$, for Example 1

d	$\mathcal{E}_1 \times 10^5$	$\mathcal{E}_2 \times 10^4$	$\mathcal{E}_3 \times 10^6$	$\mathcal{E}_4 \times 10^5$
1	1.176	1.404	2.351	1.741
10^{-1}	5.108	0.6212	0.124	2.484
10^{-2}	0.04293	11.47	0.223	74.94
10^{-3}	0.6292	890.7	9.441	6329
10^{-4}	15.13	12642	95.64	68726
10^{-5}	75.48	23889	155.9	112827
10^{-8}	19668	8562119	33420	1960620

Table 2.12: Errors for **Model: $\mathcal{FE}\varepsilon$** (2.4.11), with varying d , and fixed $\gamma = 0$ and $\varepsilon = 0.1\sqrt{2}$, for Example 1a.

d	$\mathcal{E}_1 \times 10^5$	$\mathcal{E}_2 \times 10^4$	$\mathcal{E}_3 \times 10^6$	$\mathcal{E}_4 \times 10^5$
1	1.176	1.404	2.351	1.741
10^{-1}	0.5108	0.6213	0.124	2.484
10^{-2}	0.04293	11.46	0.223	74.94
10^{-3}	0.6286	890.0	9.433	6323
10^{-4}	15.12	12607	95.44	68575
10^{-5}	75.50	23811	155.5	112535
10^{-8}	19665	853545	33315	1949437

Table 2.13: Errors for **Model: $\mathcal{FE}\varepsilon$** (2.4.11), with varying d , and fixed $\gamma = 0.01$ and $\varepsilon = 0.1\sqrt{2}$, for Example 1a.

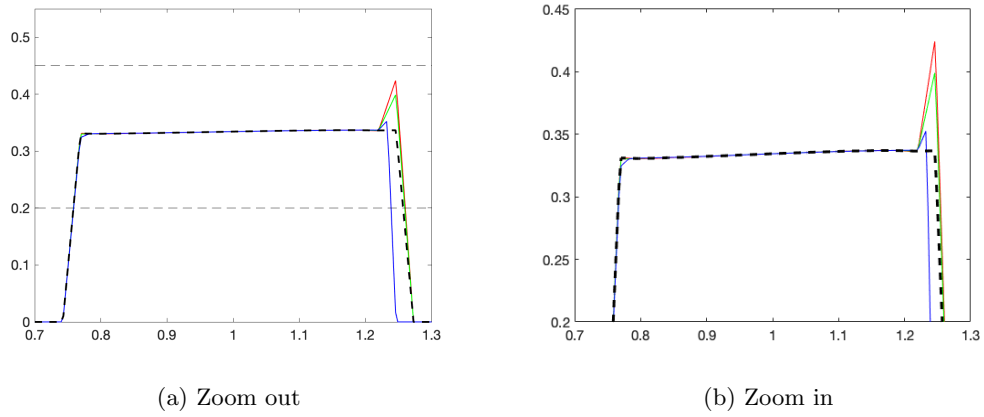


Figure 2.11: Profile of U^N demonstrating profile spiking when reducing $h_{\mathcal{T}}$ using **Model: \mathcal{FE}** (2.4.2) with $\gamma = 0$, for Example 1a. The red line is $h_{\mathcal{T}} = 2.4 \times 2^{-6.5}$, the green line is $h_{\mathcal{T}} = 2.4 \times 2^{-7}$ and the blue line is $h_{\mathcal{T}} = 2.4 \times 2^{-7.5}$, where ε is fixed and $\Delta t = \frac{8}{15}(h_{\mathcal{T}})^2$. The black line depicts the profile of $U^n(\cdot)$ using **Model: $\mathcal{FE}\varepsilon$** (2.4.11) with $\gamma = 0$ and $h_{\mathcal{T}} = 2.4 \times 2^{-6.5}$. The grey dashed lines in (a) represents the zone that (b) is demonstrating.

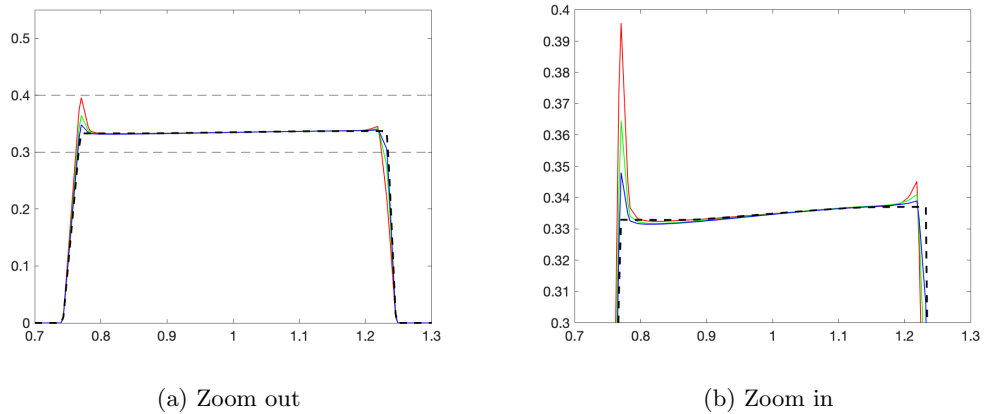


Figure 2.12: Profile of U^N demonstrating profile spiking when increasing d using **Model: \mathcal{FE}** (2.4.2) with $\gamma = 0$, for Example 1a. The red line is $d = 0.1$, the green line is $d = 0.2$ and the blue line is $d = 0.4$, where $\varepsilon = 0.1\sqrt{2}$, $\varepsilon = \frac{32}{3}h_{\mathcal{T}}$ and $\varepsilon = 20\sqrt{\Delta t}$ are fixed. The black line depicts the profile of $U^n(\cdot)$ using **Model: $\mathcal{FE}\varepsilon$** (2.4.11) with $\gamma = 0$ and $d = 0.1$. The grey dashed lines in (a) represents the zone that (b) is demonstrating.

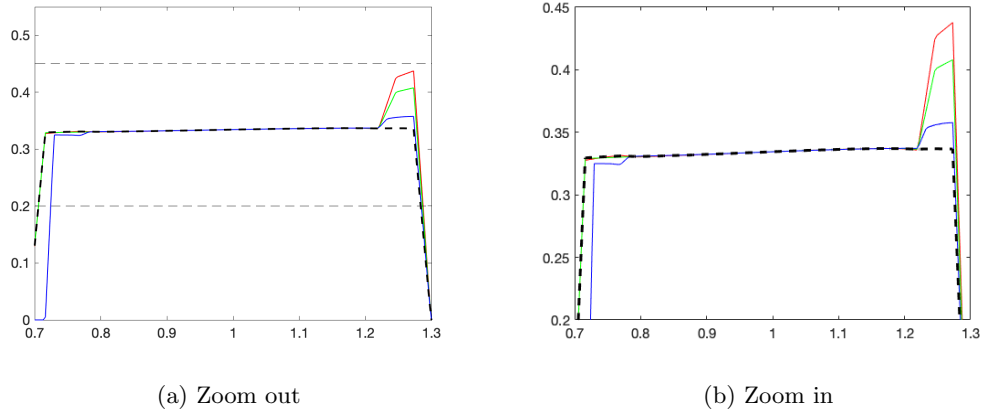


Figure 2.13: Profile of U^N demonstrating profile spiking when reducing $h_{\mathcal{T}}$ using **Model: \mathcal{FE}** (2.4.2) with $\gamma = 0.01$, for Example 1a. The red line is $h_{\mathcal{T}} = 2.4 \times 2^{-6.5}$, the green line is $h_{\mathcal{T}} = 2.4 \times 2^{-7}$ and the blue line is $h_{\mathcal{T}} = 2.4 \times 2^{-7.5}$, where ε is fixed and $\Delta t = \frac{8}{15}(h_{\mathcal{T}})^2$. The black line depicts the profile of $U^n(\cdot)$ using **Model: $\mathcal{FE}\varepsilon$** (2.4.11) with $\gamma = 0.01$ and $h_{\mathcal{T}} = 2.4 \times 2^{-7.5}$. The grey dashed lines in (a) represents the zone that (b) is demonstrating.

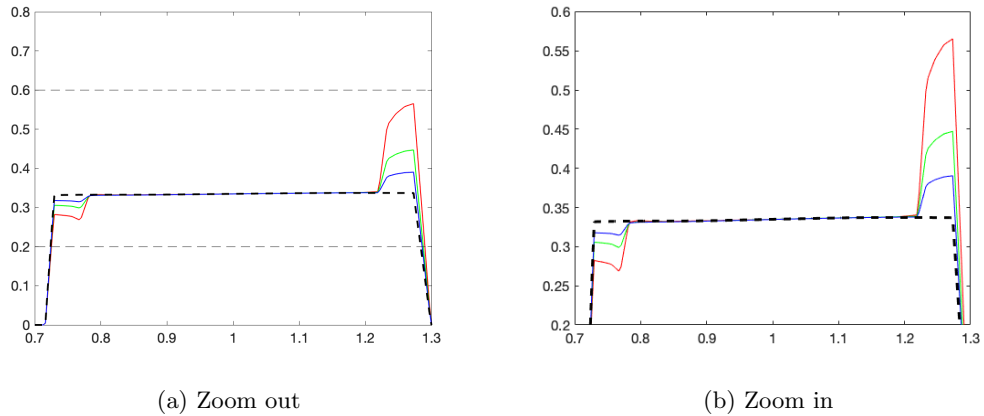


Figure 2.14: Profile of U^N demonstrating profile spiking when increasing d using **Model: \mathcal{FE}** (2.4.2) with $\gamma = 0.01$, for Example 1a. The red line is $d = 0.1$, the green line is $d = 0.2$ and the blue line is $d = 0.4$, where $\varepsilon = 0.1\sqrt{2}$, $\varepsilon = \frac{32}{3}h_{\mathcal{T}}$ and $\varepsilon = 20\sqrt{\Delta t}$ are fixed. The black line depicts the profile of $U^n(\cdot)$ using **Model: $\mathcal{FE}\varepsilon$** (2.4.11) with $\gamma = 0.01$ and $d = 0.1$. The grey dashed lines in (a) represents the zone that (b) is demonstrating.

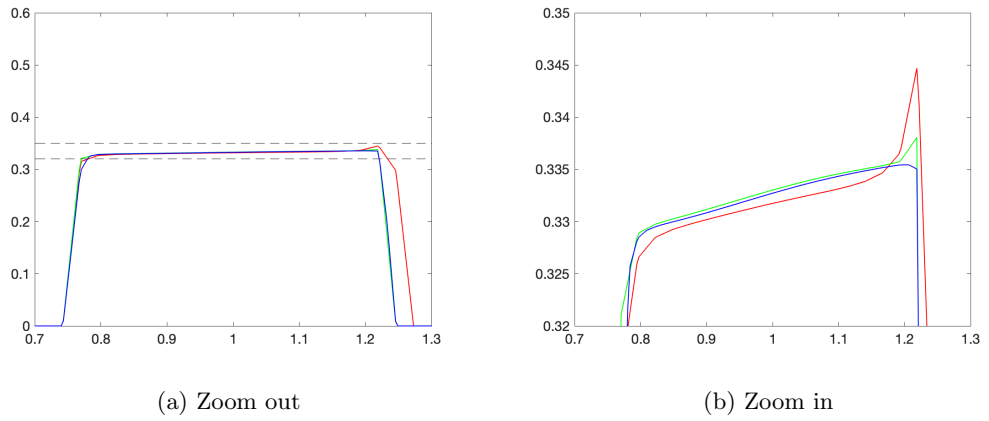


Figure 2.15: Profile of U^N demonstrating the profile spiking when reducing $h_{\mathcal{T}}$ using **Model: \mathcal{FV}** (2.4.6), for Example 1a. The red line is $h_{\mathcal{T}} = 2.4 \times 2^{-6.5}$, the green line is $h_{\mathcal{T}} = 2.4 \times 2^{-7}$ and the blue line is $h_{\mathcal{T}} = 2.4 \times 2^{-7.5}$, where ε is fixed and $\Delta t = \frac{8}{15}(h_{\mathcal{T}})^2$. The grey dashed lines in (a) represents the zone that (b) is demonstrating.

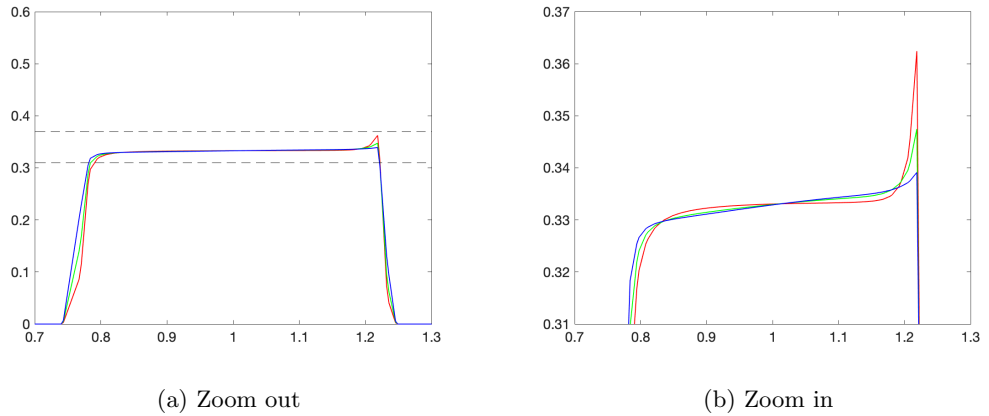


Figure 2.16: Profile of U^N demonstrating the profile spiking when reducing d using **Model: \mathcal{FV}** (2.4.6), for Example 1a. The red line is $d = 0.1$, the green line is $d = 0.2$ and the blue line is $d = 0.4$, where $\varepsilon = 0.1\sqrt{2}$, $\varepsilon = \frac{32}{3}h_{\mathcal{T}}$ and $\varepsilon = 20\sqrt{\Delta t}$ are fixed. The grey dashed lines in (a) represents the zone that (b) is demonstrating.

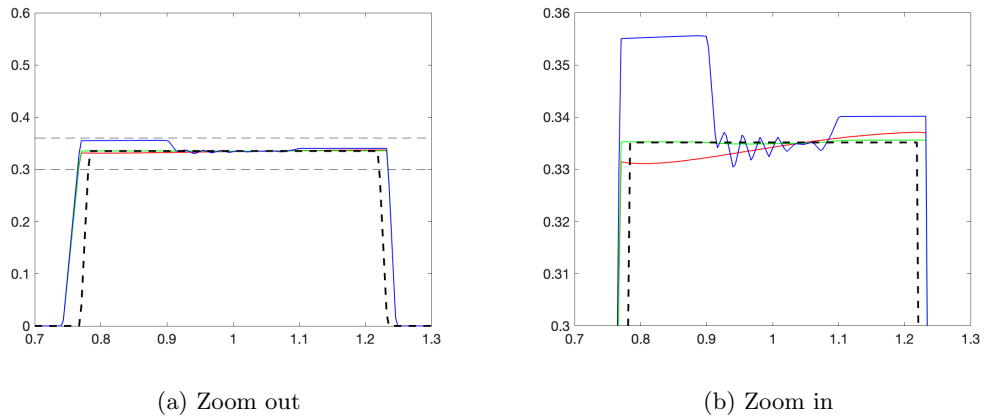


Figure 2.17: Profile of U^N demonstrating the appearance of instabilities when reducing d using **Model: $\mathcal{FE}\mathfrak{s}$** (2.4.11) with fixed $\gamma = 0$ and $\varepsilon = \frac{32}{3}h_{\mathcal{T}}$, $\varepsilon = 20\sqrt{\Delta t}$ and $\varepsilon = 0.1\sqrt{2}$, for Example 1a. The red line is $d = 1$, the green line is $d = 10^{-2}$ and the blue line is $d = 10^{-4}$, with the black dashed line being the profile of the true solution. The grey dashed lines in (a) represents the zone that (b) is demonstrating.

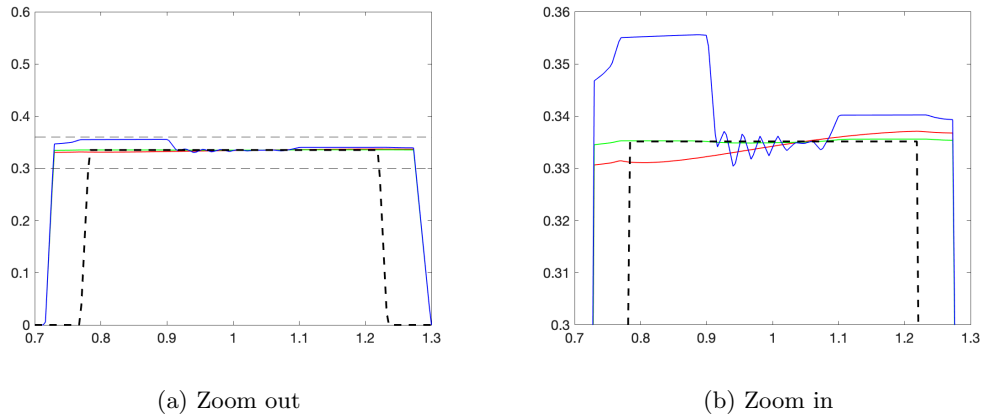


Figure 2.18: Profile of U^N demonstrating the appearance of instabilities when reducing d using **Model: $\mathcal{FE}\mathfrak{s}$** (2.4.11) with fixed $\gamma = 0.01$ and $\varepsilon = \frac{32}{3}h_{\mathcal{T}}$, $\varepsilon = 20\sqrt{\Delta t}$ and $\varepsilon = 0.1\sqrt{2}$, for Example 1a. The red line is $d = 1$, the green line is $d = 10^{-2}$ and the blue line is $d = 10^{-4}$, with the black dashed line being the profile of the true solution. The grey dashed lines in (a) represents the zone that (b) is demonstrating.

2.4.4 Coupling the diffuse interface approximation of a SADE on an evolving surface to the phase field approximation of mean curvature flow

Following [63, Section 4.1], we now look to extend **Model: \mathcal{FE}** , **Model: \mathcal{FEs}** and **Model: \mathcal{FV}** to the case where the velocity \vec{v} isn't a given function but instead is the solution of an equation that approximates mean curvature flow. As in [63] we set

$$\rho_\varphi(\vec{p}, t) := 1 - \varphi^2(\vec{p}, t), \quad \vec{p} \in \bar{\Omega}, t \in [0, T] \quad (2.4.13)$$

where φ is the solution to (2.2.9). In essence, this means that all appearances of ϕ in (2.3.12a), subsequent weak formulations and finite element and finite volume approximations will be replaced by φ . In particular, this means that the phase field approximation to the normal velocity of $\Gamma(t)$ and the unit normal vector of $\Gamma(t)$ in (2.3.10) are respectively

$$v_\varphi(\cdot, t) := -\frac{\varphi_t(\cdot, t)}{|\nabla\varphi(\cdot, t)|}, \quad \vec{v}_\varphi(\cdot, t) := \frac{\nabla\varphi(\cdot, t)}{|\nabla\varphi(\cdot, t)|}, \quad \text{in } \bar{\Omega}, t \in [0, T]. \quad (2.4.14)$$

Moreover, since we consider mean curvature flow, we note that $\vec{v}_\tau = 0$. Denoting the approximation of ρ_φ and \vec{v}_φ as

$$\rho_\Phi^n(\cdot) := 1 - (\Phi^n(\cdot))^2, \quad \vec{v}_\Phi^n(\cdot) := -\frac{D_t\Phi^n(\cdot)}{|\nabla\Phi^n(\cdot)|} \frac{\nabla\Phi^n(\cdot)}{|\nabla\Phi^n(\cdot)|}, \quad \text{in } \bar{\Omega},$$

with an abuse of notation we redefine

$$\mathcal{N}_h^n := \{i \in \mathcal{N} : \exists j \in \omega_i \text{ such that } \rho_\Phi^n(\vec{p}_j) > 0\}$$

and set

$$\Gamma_\varepsilon^{h,n} := \{T^h \in \mathcal{T}^h : \mathcal{N}_{T^h} \subset \mathcal{N}_h^n\}. \quad (2.4.15)$$

Model: \mathcal{ACFE}

With the velocity of the surface given by (2.4.14), the coupling of the finite element approximation to the diffuse interface approximation to SADEs to the finite element approximation to the phase field approximation of mean curvature flow takes the form of $\bar{U}^n(\vec{p}_i) = 0$ for $i \notin \mathcal{N}_h^n$ and

$$D_t \left[\left(\rho_\Phi^n U^n |\nabla\Phi^n|, \xi^h \right)^h \right] + d \left(\rho_\Phi^n \nabla U^n |\nabla\Phi^n|, \nabla\xi^h \right)^h - \left(\rho_\Phi^n U^n \vec{v}_\Phi^n |\nabla\Phi^n|, \nabla\xi^h \right)^h = \left(\rho_\Phi^n f^{e,n} |\nabla\Phi^n|, \xi^h \right)^h, \quad \forall \xi^h \in S^h, \quad (2.4.16a)$$

$$\varepsilon \left(D_t \Phi^n, \eta^h - \Phi^n \right)^h + \varepsilon \left(\nabla\Phi^n, \nabla\eta^h - \nabla\Phi^n \right) - \frac{1}{\varepsilon} \left(\Phi^n, \eta^h - \Phi^n \right)^h - \frac{\pi}{4} \left(p^n, \eta^h - \Phi^n \right)^h \geq 0, \quad \forall \eta^h \in \mathcal{K}^h, \quad (2.4.16b)$$

where

$$\mathcal{K}^h := \{\eta^h \in S^h : |\eta^h| \leq 1\}.$$

Model: \mathcal{ACFEs}

Similarly, the coupling of the finite element approximation to the diffuse interface approximation to SADEs with edge smoothing to the finite element approximation to the phase field approximation of mean curvature flow takes the form of $\bar{U}^n(\vec{p}_i) = 0$ for $i \notin \mathcal{N}_h^n$ and

$$\begin{aligned} & D_t \left[\left(\rho_{\Phi}^n U^n |\nabla \Phi^n|, \xi^h \right)^h \right] + d \left(\rho_{\Phi}^n \nabla U^n |\nabla \Phi^n|, \nabla \xi^h \right)^h - \left(\rho_{\Phi}^n U^n \vec{v}_{\Phi}^n |\nabla \Phi^n|, \nabla \xi^h \right)^h \\ & + \left(g_{e,\Phi}^n \langle \vec{v}_{\vec{v},\Phi}^{e,n}, \nabla U^n \rangle \vec{v}_{\vec{v},\Phi}^{e,n} |\nabla \Phi^n|, \nabla \xi^h \right)^h = \left(\rho_{\Phi}^n f^{e,n} |\nabla \Phi^n|, \xi^h \right)^h, \quad \forall \xi^h \in S^h, \quad (2.4.17a) \\ & \varepsilon \left(D_t \Phi^n, \eta^h - \Phi^n \right)^h + \varepsilon \left(\nabla \Phi^n, \nabla \eta^h - \nabla \Phi^n \right) \\ & - \frac{1}{\varepsilon} \left(\Phi^n, \eta^h - \Phi^n \right)^h - \frac{\pi}{4} \left(p^n, \eta^h - \Phi^n \right)^h \geq 0, \quad \forall \eta^h \in \mathcal{K}^h, \quad (2.4.17b) \end{aligned}$$

with $\vec{v}_{\vec{v},\Phi}^n$ being the approximate projection of \vec{v}_{Φ}^n in the approximate normal direction \vec{v}_{Φ} . Given the form of g_e in (2.4.10), we can approximate $d_{\Gamma}(\cdot, t^n)$ by using $\Phi^n(\cdot)$, noting (2.4.20) and see [41], which is how we calculate $g_{e,\Phi}$.

Remark 2.13. *One notices that **Model: \mathcal{ACFE}** and **Model: \mathcal{ACFEs}** do not have the added streamline diffusion term from [44]. This is because we could not find a way to define $\tilde{\rho}_{\varepsilon}$ for any time without the explicit knowledge of the curve, and hence we could not extend the term to this coupled case where the approximation of the curve satisfies its own velocity law.*

Model: \mathcal{ACFV}

The coupling of the finite volume approximation to the diffuse interface approximation to SADEs to the finite element approximation to the phase field approximation of mean curvature flow takes the form of $\bar{U}^n(\vec{p}_i) = 0$ for $i \notin \mathcal{N}_h^n$ and

$$\begin{aligned} & \frac{1}{\Delta t_n} (\rho_{\Phi}^n)_j U_j^n (m_{\Phi}^n)_j - d \sum_{k \in \omega_j} \left(\frac{U_k^n - U_j^n}{h_{jk}} \right) (\rho_{\Phi}^n)_{jk} (p_{\Phi}^n)_{jk} \\ & + \sum_{k \in \omega_j} \left(U_j^n \left[\langle (\rho_{\Phi}^n \vec{v}_{\Phi}^{e,n})_{jk}, \vec{n}_{\sigma'_{jk}} \rangle \right]_+ + U_k^n \left[\langle (\rho_{\Phi}^n \vec{v}_{\Phi}^{e,n})_{jk}, \vec{n}_{\sigma'_{jk}} \rangle \right]_- \right) (p_{\Phi}^n)_{jk} \\ & = \frac{1}{\Delta t_n} (\rho_{\Phi}^{n,n-1})_j U_j^{n-1} (m_{\Phi}^{n-1})_j + (\rho_{\Phi}^n)_j f_j^{e,n} (m_{\Phi}^n)_j, \quad \forall j \in \mathcal{N}_h^n, \quad (2.4.18a) \\ & \varepsilon \left(D_t \Phi^n, \eta^h - \Phi^n \right)^h + \varepsilon \left(\nabla \Phi^n, \nabla \eta^h - \nabla \Phi^n \right) \\ & - \frac{1}{\varepsilon} \left(\Phi^n, \eta^h - \Phi^n \right)^h - \frac{\pi}{4} \left(p^n, \eta^h - \Phi^n \right)^h \geq 0, \quad \forall \eta^h \in \mathcal{K}^h, \quad (2.4.18b) \end{aligned}$$

where $(\rho_\Phi^{n,n-1})_j$ as defined in (2.4.7), and

$$(m_\Phi^n)_j := \sum_{T^h \in \mathcal{N}_j} |\nabla \Phi_{|T^h}^n| \int_{T^h} dx, \quad (p_\Phi^n)_{jk} := \sum_{T^h \in \xi_{jk}} (h'_{jk})_{T^h} |\nabla \Phi_{|T^h}^n|.$$

Example 2

For our second example we use an expanding circle, which is the same as Example 2 in Section 3.2 in [63], whereby we want to see how **Model: \mathcal{ACFE}** (2.4.16a)–(2.4.16b), **Model: \mathcal{ACFEs}** (2.4.17a)–(2.4.17b) and **Model: \mathcal{ACFV}** (2.4.18a)–(2.4.18b) react to a small diffusion constant. Consider $R(t) = 0.75 + 5t$ and $\vec{c}_0(t) = (0, 0)^T$, with $\vec{v}(\vec{p}, t) = \frac{5\vec{p}}{|\vec{p}|}$, and $f(\vec{p}, t) = 4(d-1)e^{\frac{4}{5R(t)}} \frac{\vec{p}_1 \vec{p}_2}{R^3(t)|\vec{p}|^2}$ for $\vec{p} \in \Gamma(t)$. Then, the solution to (1.2.2) is

$$u(\vec{p}, t) = e^{\frac{4}{5R(t)}} \frac{\vec{p}_1 \vec{p}_2}{R(t)|\vec{p}|^2}, \quad \vec{p} \in \Gamma(t), t \in [0, T].$$

One notices that the velocity in Example 1 was not in the normal direction; however, for this example it is which allows us to compare the errors from diffuse interface approach to the errors from the coupled Allen-Cahn diffuse interface approach. As $\Gamma(t)$ is a circle, this implies that $v = R'(t)$ and $\kappa = -R(t)^{-1}$, and hence we take the forcing for the Allen-Cahn equation, noting (1.1.2), to be

$$p = v - \kappa = 5 + \frac{1}{0.75 + 5t}.$$

We solve the algebraic system of equations resulting from the diffuse interface approximation of the SADEs using GMRES with diagonal preconditioning only for the finite element approximations (2.4.16a) and (2.4.17a), we do not use diagonal preconditioning for (2.4.18a). For the solution of algebraic system resulting from (2.4.16b), (2.4.17b) and (2.4.18b) we use the projective SOR method presented in [60], which, $\forall j \in \mathcal{N}$, gives

$$\frac{\varepsilon}{\Delta t_n} (\Phi^{n'}, \chi_j)^h + \varepsilon (\nabla \Phi^{n'}, \nabla \chi_j) = \left(\frac{\varepsilon}{\Delta t_n} + \frac{1}{\varepsilon} \right) (\Phi^{n-1}, \chi_j)^h + \frac{\pi}{4} (p^n, \chi_j)^h, \quad (2.4.19a)$$

$$\Phi^n = \mathcal{P} \Phi^{n'}, \quad (2.4.19b)$$

where, as in [41], \mathcal{P} is defined as the component-wise projection

$$(\mathcal{P}x)_j := \max\{-1, \min\{1, x_j\}\}, \quad j \in \mathcal{N}.$$

Simplistically this can be thought of as the semi-implicit finite element approximation to the ‘equivalent’ variational equality to (2.2.9) whereby if a nodal value goes above 1 or below -1 it gets truncated to make sure that $\Phi^n \in \mathcal{K}^h$. Initially, see [41], we consider the

profiles for (2.4.16b), (2.4.17b) and (2.4.18b), for $\vec{p} \in \bar{\Omega}$, to be $\Phi^0 := I^h \varphi^0$, where

$$\varphi^0(\vec{p}) := \begin{cases} 1 & \text{if } d_\Gamma(\vec{p}, 0) > \frac{\pi\varepsilon}{2}, \\ \sin\left(\frac{d_\Gamma(\vec{p}, 0)}{\varepsilon}\right) & \text{if } |d_\Gamma(\vec{p}, 0)| \leq \frac{\pi\varepsilon}{2}, \\ -1 & \text{if } d_\Gamma(\vec{p}, 0) < -\frac{\pi\varepsilon}{2}. \end{cases} \quad (2.4.20)$$

As before, the following results were produced using ALBERTA using one core of processing power on the HPC whilst the visualisations were produced in MATLAB. To quantify how each system is reacting we consider \mathcal{E}_3 and \mathcal{E}_4 in (2.4.3c) and (2.4.3d) respectively. We take $\phi(\vec{p}, t) = |\vec{p} - c_0(t)| - R(t)$, for $\vec{p} \in \bar{\Omega}$, and set $\varepsilon = 0.1$, $h_T = \frac{3\varepsilon}{32}$, $\Delta t = \frac{\varepsilon^2}{400}$, and $T = 0.1$. This value of ε results initially in 21221 DOFs. Table 2.14 depicts the errors resulting from Example 2 comparing **Model: \mathcal{FE}** (2.4.2) and **Model: \mathcal{ACFE}** (2.4.16a)–(2.4.16b), Table 2.15 depicts the errors resulting from Example 2 comparing **Model: \mathcal{FE}_ε** (2.4.11) with **Model: $\mathcal{ACFE}_\varepsilon$** (2.4.17a)–(2.4.17b), and Table 2.16 depicts the errors resulting from Example 2 comparing **Model: \mathcal{FV}** (2.4.6) with **Model: \mathcal{ACFV}** (2.4.18a)–(2.4.18b). Figures 2.19–2.21 depict the profile of U^N resulting from Example 2 using **Model: \mathcal{FE}** (2.4.2), **Model: \mathcal{FE}_ε** (2.4.11) and **Model: \mathcal{FV}** (2.4.6) respectively on the line $y = x$ starting at $(0, 0)$, whilst Figures 2.22–2.24 depict the same profiles but resulting from the Allen-Cahn variants of the schemes.

Table 2.19b demonstrates how **Model: \mathcal{ACFE}** (2.4.16a)–(2.4.16b) performs when d is reduced, while for comparison Table 2.19a demonstrates how **Model: \mathcal{FE}** (2.4.2), with $\gamma = 0$, performs when d is reduced. We display the profiles of U^N resulting from **Model: \mathcal{FE}** (2.4.2) and **Model: \mathcal{ACFE}** (2.4.16a)–(2.4.16b) in Figures 2.19 and 2.22 respectively. Unlike in Figure 2.8 for Example 1a where we saw the appearance of instabilities, albeit for smaller values of d than here, the edge spikes are causing a much larger problem, especially for **Model: \mathcal{ACFE}** (2.4.16a)–(2.4.16b). Taking $d = 1$, the computational time solving Example 2 using **Model: \mathcal{FE}** (2.4.2) was approximately 120 minutes of execution time whilst using **Model: \mathcal{ACFE}** (2.4.16a)–(2.4.16b) was approximately 70 minutes of execution time. As one can see the simulation using **Model: \mathcal{ACFE}** (2.4.16a)–(2.4.16b) is faster, which is somewhat surprising. Taking $d = 0$, the computational time solving Example 2 using **Model: \mathcal{FE}** (2.4.2) was approximately 720 minutes of execution time whilst using **Model: \mathcal{ACFE}** (2.4.16a)–(2.4.16b) was approximately 620 minutes of execution time. In Table 2.19b we display the errors for **Model: $\mathcal{ACFE}_\varepsilon$** (2.4.17a)–(2.4.17b) and Table 2.19a displays the errors for **Model: \mathcal{FE}_ε** (2.4.11) for comparison. Figure 2.20 depicts the profile of U^N resulting from **Model: \mathcal{FE}_ε** (2.4.11) while Figure 2.23 depicts the profile of U^N resulting from **Model: $\mathcal{ACFE}_\varepsilon$** (2.4.17a)–(2.4.17b). In a sim-

ilar fashion to Example 1a, the edge smoothing contributions affect the errors when d is small but largely improve the profile of U^N , as we see from comparing Figure 2.23 to Figure 2.22. Taking $d = 1$, the computational time solving Example 2 using **Model: $\mathcal{FE}\varepsilon$** (2.4.11) was approximately 150 minutes of execution time whilst using **Model: $\mathcal{ACFE}\varepsilon$** (2.4.17a)–(2.4.17b) was approximately 120 minutes of execution time. Taking $d = 10^{-8}$, the computational time solving Example 2 using **Model: $\mathcal{FE}\varepsilon$** (2.4.11) was approximately 405 minutes of execution time whilst using **Model: $\mathcal{ACFE}\varepsilon$** (2.4.17a)–(2.4.17b) was approximately 510 minutes of execution time. Table 2.19a displays the errors for **Model: \mathcal{FV}** (2.4.6) for the comparison to **Model: \mathcal{ACFV}** (2.4.18a)–(2.4.18b) whose errors are displayed in Table 2.19b. As in Example 1a the interface errors using **Model: \mathcal{ACFV}** are significantly better than the respective errors of **Model: \mathcal{ACFE}** (2.4.16a)–(2.4.16b) and **Model: $\mathcal{ACFE}\varepsilon$** (2.4.17a)–(2.4.17b); however, like in Example 1a, the profile of U^N resulting from **Model: \mathcal{FV}** (2.4.6) and **Model: \mathcal{ACFV}** (2.4.18a)–(2.4.18b) both suffer from large edge spikes, which for **Model: \mathcal{FV}** (2.4.6) can be seen in Figure 2.21 and in Figure 2.24 for **Model: \mathcal{ACFV}** (2.4.18a)–(2.4.18b). Taking $d = 1$, the computational time solving Example 2 using **Model: \mathcal{FV}** (2.4.6) was approximately 80 minutes of execution time whilst using **Model: \mathcal{ACFV}** (2.4.18a)–(2.4.18b) was approximately 45 minutes of execution time. Taking $d = 0$, the computational time solving Example 2 using **Model: \mathcal{FV}** (2.4.6) was approximately 300 minutes of execution time whilst using **Model: \mathcal{ACFV}** (2.4.18a)–(2.4.18b) was approximately 240 minutes of execution time. For the comparison of Figures 2.19–2.24 we note here to be wary of the different scaling used for the y -axis.

d	$\mathcal{E}_3 \times 10^6$	$\mathcal{E}_4 \times 10^4$	d	$\mathcal{E}_3 \times 10^6$	$\mathcal{E}_4 \times 10^4$
1	6.368	1.316	1	295.0	2.202
10^{-1}	10.40	9.876	10^{-1}	727.4	19.37
10^{-2}	72.40	808.9	10^{-2}	770.5	2822
10^{-3}	1390	58593	10^{-3}	6466	344237
10^{-4}	7138	372797	10^{-4}	22130	1334963
10^{-5}	9538	484733	10^{-5}	25552	1559463
0	9871	499776	0	25930	1559463

(a) **Model: \mathcal{FE}** (b) **Model: \mathcal{ACFE}**

Table 2.14: Errors comparing **Model: \mathcal{FE}** (2.4.2) to **Model: \mathcal{ACFE}** (2.4.16a)–(2.4.16b), with varying d , and fixed $\varepsilon = 0.1$, for Example 2.

d	$\mathcal{E}_3 \times 10^6$	$\mathcal{E}_4 \times 10^4$	d	$\mathcal{E}_3 \times 10^6$	$\mathcal{E}_4 \times 10^4$
1	6.327	1.315	1	302.7	2.224
10^{-1}	7.423	9.859	10^{-1}	838.8	21.02
10^{-2}	59.69	808.7	10^{-2}	2230	2865
10^{-3}	1288	50174	10^{-3}	45293	279309
10^{-4}	5275	195772	10^{-4}	192630	955223
10^{-5}	961604	3969932	10^{-5}	201504	992176
10^{-8}	996891	4178887	10^{-8}	224957	1164530

(a) **Model:** \mathcal{FE}_ε (b) **Model:** $\mathcal{ACFE}_\varepsilon$

Table 2.15: Errors comparing **Model:** \mathcal{FE}_ε (2.4.11) to **Model:** $\mathcal{ACFE}_\varepsilon$ (2.4.17a)–(2.4.17b), with varying d , and fixed $\varepsilon = 0.1$, for Example 2.

d	$\mathcal{E}_3 \times 10^6$	$\mathcal{E}_4 \times 10^4$	d	$\mathcal{E}_3 \times 10^6$	$\mathcal{E}_4 \times 10^4$
1	38.23	1.585	1	442.2	3.476
10^{-1}	93.56	11.17	10^{-1}	1125	42.24
10^{-2}	132.1	175	10^{-2}	1754	802.5
10^{-3}	146.0	402.3	10^{-3}	1790	1956
10^{-4}	146.7	451.6	10^{-4}	1789	2197
10^{-5}	146.8	457.4	10^{-5}	1789	2224
0	146.8	458.0	0	1790	2227

(a) **Model:** \mathcal{FV} (b) **Model:** \mathcal{ACFV}

Table 2.16: Errors comparing **Model:** \mathcal{FV} (2.4.6) to **Model:** \mathcal{ACFV} (2.4.18a)–(2.4.18b), with varying d , and fixed $\varepsilon = 0.1$, for Example 2.

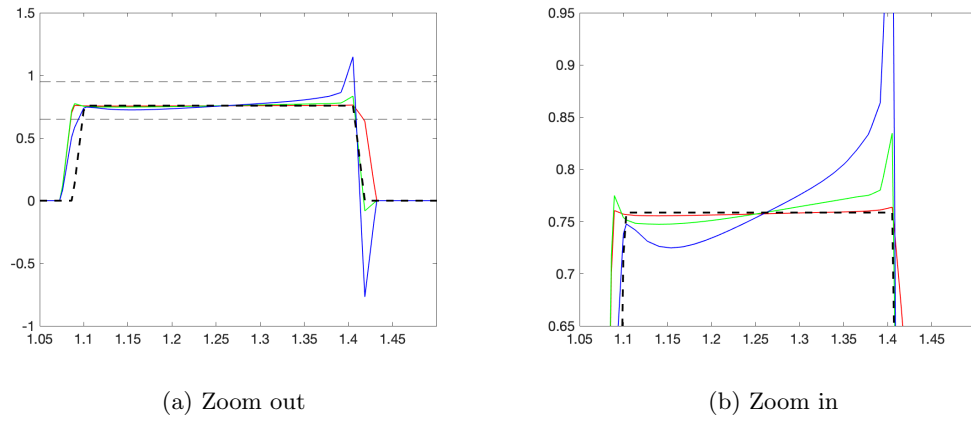


Figure 2.19: Profile of U^N when reducing d using **Model: \mathcal{FE}** (2.4.2) with fixed $\gamma = 0$, $\varepsilon = \frac{32}{3}h_{\mathcal{T}}$, $\varepsilon = 20\sqrt{\Delta t}$ and $\varepsilon = 0.1$, for Example 2. The red line is $d = 1$, the green line is $d = 10^{-1}$ and the blue line is $d = 10^{-2}$, with the black dashed line being the profile of the true solution. The grey dashed lines in (a) represents the zone that (b) is demonstrating.

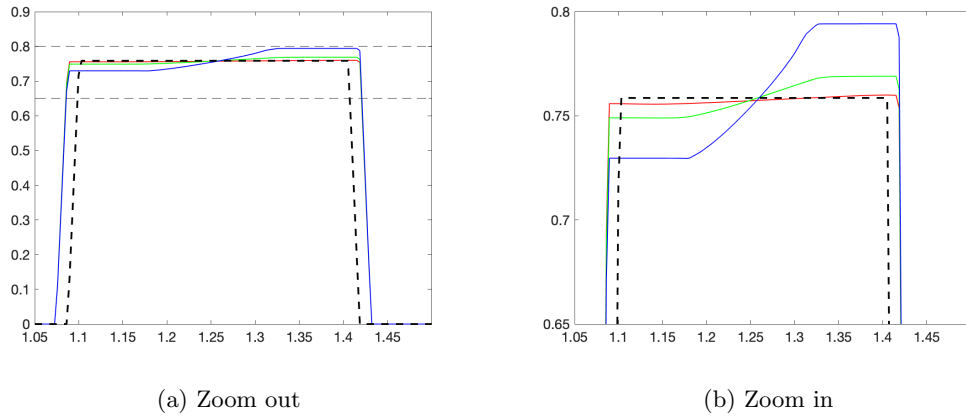


Figure 2.20: Profile of U^N when reducing d using **Model: $\mathcal{FE}\varepsilon$** (2.4.11) with fixed $\gamma = 0$, $\varepsilon = \frac{32}{3}h_{\mathcal{T}}$, $\varepsilon = 20\sqrt{\Delta t}$ and $\varepsilon = 0.1$, for Example 2. The red line is $d = 1$, the green line is $d = 10^{-1}$ and the blue line is $d = 10^{-2}$, with the black dashed line being the profile of the true solution. The grey dashed lines in (a) represents the zone that (b) is demonstrating.

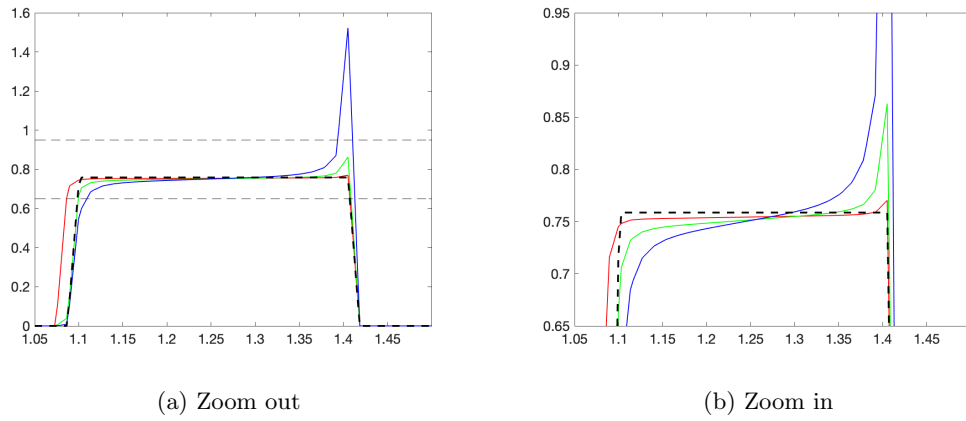


Figure 2.21: Profile of U^N when reducing d using **Model: \mathcal{FV}** (2.4.6) with fixed $\varepsilon = \frac{32}{3}h_{\mathcal{T}}$, $\varepsilon = 20\sqrt{\Delta t}$ and $\varepsilon = 0.1$, for Example 2. The red line is $d = 1$, the green line is $d = 10^{-1}$ and the blue line is $d = 10^{-2}$, with the black dashed line being the profile of the true solution. The grey dashed lines in (a) represents the zone that (b) is demonstrating.

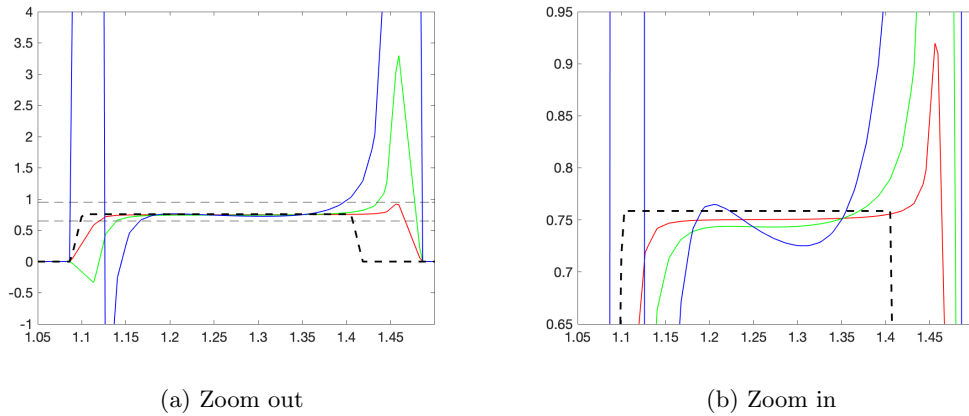


Figure 2.22: Profile of U^N when reducing d using **Model: \mathcal{ACFE}** (2.4.16a)–(2.4.16b) with fixed $\varepsilon = \frac{32}{3}h_{\mathcal{T}}$, $\varepsilon = 20\sqrt{\Delta t}$ and $\varepsilon = 0.1$, for Example 2. The red line is $d = 1$, the green line is $d = 10^{-1}$ and the blue line is $d = 10^{-2}$, with the black dashed line being the profile of the true solution. The grey dashed lines in (a) represents the zone that (b) is demonstrating. *The blue line goes up to approximately 100 and down to approximately -4.*

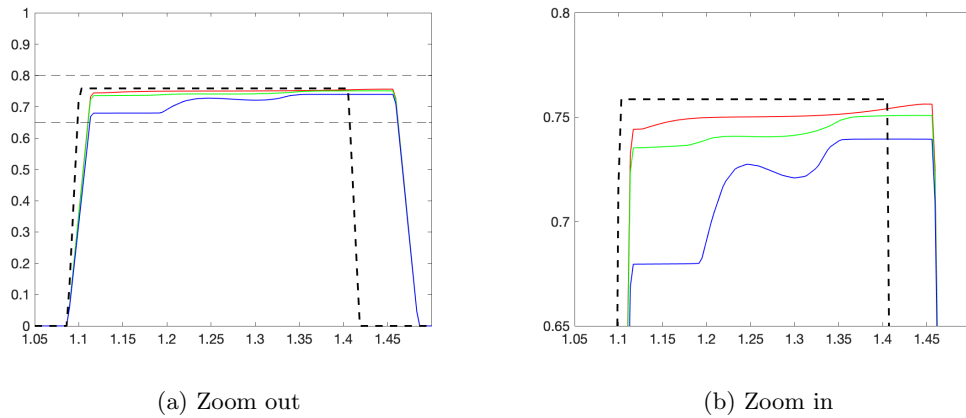


Figure 2.23: Profile of U^N when reducing d using **Model: \mathcal{ACFEs}** (2.4.17a)–(2.4.17b) with fixed $\varepsilon = \frac{32}{3}h_{\mathcal{T}}$, $\varepsilon = 20\sqrt{\Delta t}$ and $\varepsilon = 0.1$, for Example 2. The red line is $d = 1$, the green line is $d = 10^{-1}$ and the blue line is $d = 10^{-2}$, with the black dashed line being the profile of the true solution. The grey dashed lines in (a) represents the zone that (b) is demonstrating.

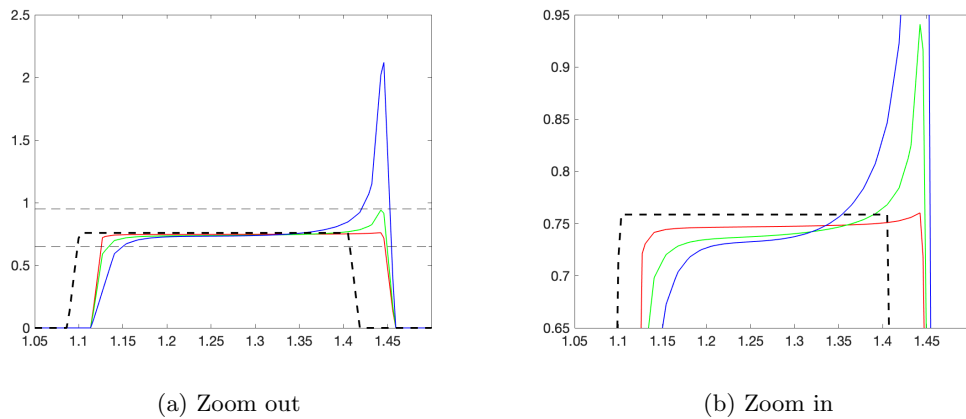


Figure 2.24: Profile of U^N when reducing d using **Model: \mathcal{ACfV}** (2.4.18a)–(2.4.18b) with fixed $\varepsilon = \frac{32}{3}h_{\mathcal{T}}$, $\varepsilon = 20\sqrt{\Delta t}$ and $\varepsilon = 0.1$, for Example 2. The red line is $d = 1$, the green line is $d = 10^{-1}$ and the blue line is $d = 10^{-2}$, with the black dashed line being the profile of the true solution. The grey dashed lines in (a) represents the zone that (b) is demonstrating.

2.4.5 Summary of numerical results

In this section we have introduced a finite element approximation of the diffuse interface approximation to SADEs without edge smoothing **Model: \mathcal{FE}** (2.4.2) and with edge smoothing **Model: \mathcal{FEs}** (2.4.11), as well introduced a finite volume approximation of

the diffuse interface approximation to SADEs **Model: \mathcal{FV}** (2.4.6). We mirrored the error results and estimated orders of convergence found in the literature for **Model: \mathcal{FE}** (2.4.2) and **Model: \mathcal{FEs}** (2.4.11) and we demonstrated that **Model: \mathcal{FV}** (2.4.6) has similar errors as well as follows a similar experimental order of convergence, except for \mathcal{E}_2 . We then showed that for an advection-dominated simulation **Model: \mathcal{FV}** (2.4.6) has significantly better errors for a small diffusion constant d ; however, like **Model: \mathcal{FE}** (2.4.2), it suffers from large spikes in the profile of the approximate solution near the edge of the interface. The edge smoothing term (2.4.9) was introduced by [63] to dampen these profile spikes which we demonstrated for **Model: \mathcal{FE}** (2.4.2), but we are currently unable to show a similar feature for **Model: \mathcal{FV}** (2.4.6). We then coupled these approximations to the finite element approximation to the phase field approximation of mean curvature flow, whereby the velocity of the SADE satisfied mean curvature flow. We demonstrated errors for the systems **Model: \mathcal{ACFE}** (2.4.16a)–(2.4.16b), **Model: \mathcal{ACFEs}** (2.4.17a)–(2.4.17b) and **Model: \mathcal{ACFV}** (2.4.18a)–(2.4.18b) and showed that, in terms of errors, **Model: \mathcal{ACFV}** (2.4.18a)–(2.4.18b) was still superior; however, in terms of profile, still suffered from edge spiking.

We finish this section off with some general observations. Considering **Model: \mathcal{FE}** (2.4.2), judging from the errors in Table 2.6 and the plot in Figure 2.8, it seems that the approximate solution U^n is only meaningful for $d \geq 10^{-3}$, whereas one can argue that **Model: \mathcal{FV}** (2.4.6) is meaningful for all values of d judging by the errors but, due to the spiking, is ineffective for $d \leq 10^{-5}$. The addition of edge smoothing in **Model: \mathcal{FEs}** (2.4.11) improves the profile massively but is heavily affected by the instabilities caused for small d , as can be seen for $d = 1 \times 10^{-5}$ in Figure 2.17, as the smoothing is not near the true solution but rather whatever the nodal value of U^n is when it reaches the smoothing zone. Each of the schemes maintain these properties upon the coupling to the Allen-Cahn equation, and all are more susceptible to profile spiking for even larger values of d . Again, **Model: \mathcal{ACFV}** (2.4.18a)–(2.4.18b) provides much better errors compared to **Model: \mathcal{ACFE}** (2.4.16a)–(2.4.16b) and **Model: \mathcal{ACFEs}** (2.4.17a)–(2.4.17b) but still suffers from large profile spiking. We conclude that, for a small d , one should consider **Model: \mathcal{FV}** (2.4.6) and **Model: \mathcal{ACFV}** (2.4.18a)–(2.4.18b) for good accuracy, but should consider **Model: \mathcal{FEs}** (2.4.11) and **Model: \mathcal{ACFEs}** (2.4.17a)–(2.4.17b) if the pointwise value of the approximate solution U^n is needed as, for example, forcing for another equation as part of a system.

Chapter 3

The parametric approach for curve shortening flow

3.1 Introduction to Model \mathcal{M}_1 and Model \mathcal{M}_2

This chapter concerns itself with the derivation and finite element error analysis of the parametric setting of curve shortening flow attached to a fixed boundary. In this chapter we consider two models. The first is simply curve shortening flow for a curve attached to some prescribed boundary under an orthogonal contact condition. To be more specific, let the curve $\Gamma(t)$ move inside some domain $\Omega \subset \mathbb{R}^2$ such that we can describe the boundary, $\partial\Omega$, as

$$\partial\Omega := \{\vec{p} \in \mathbb{R}^2 : F(\vec{p}) = 0\} \quad \text{with} \quad |\nabla F(\vec{p})| = 1 \quad \text{for } \vec{p} \in \partial\Omega,$$

for some function $F \in C^{2,1}(\mathbb{R}^2)$. Relating to this setup, we introduce **Model \mathcal{M}_1** , which takes the following form, find $\vec{x} : [0, 1] \times [0, T] \rightarrow \mathbb{R}^2$ such that

$$\vec{x}_t - \frac{\vec{x}_{\rho\rho}}{|\vec{x}_\rho|^2} = 0, \quad (\rho, t) \in \mathcal{I} \times (0, T], \quad (3.1.1a)$$

$$F(\vec{x}(\rho, t)) = 0, \quad (\rho, t) \in \{0, 1\} \times (0, T], \quad (3.1.1b)$$

$$\langle \vec{x}_\rho(\rho, t), \nabla^\perp F(\vec{x}(\rho, t)) \rangle = 0, \quad (\rho, t) \in \{0, 1\} \times (0, T], \quad (3.1.1c)$$

$$\vec{x}(\rho, 0) = \vec{x}^0(\rho), \quad \rho \in [0, 1]. \quad (3.1.1d)$$

Here ρ denotes the parametrisation of \vec{x} associated to \mathcal{I} , \vec{x}^0 denotes the given parametrisation of $\Gamma(0)$ and $\vec{p}^\perp = (p_0, p_1)^\perp := (-p_1, p_0)$. We denote $\mathcal{I} := (0, 1)$ for ease of notation, but will refer to the closure as $[0, 1]$ rather than $\bar{\mathcal{I}}$ and refer to the boundary elements as

$\{0, 1\}$ rather than $\partial\mathcal{I}$. In Section 3.3 we motivate **Model** \mathcal{M}_1 and prove discrete in time and space finite element error bounds. The second model concerns itself with a coupling of **Model** \mathcal{M}_1 with a reaction-diffusion equation on the curve $\Gamma(t)$. For this setup we introduce **Model** \mathcal{M}_2 , which takes the following form, find $\vec{x} : [0, 1] \times [0, T] \rightarrow \mathbb{R}^2$ and $\tilde{w} : [0, 1] \times [0, T] \rightarrow \mathbb{R}$ such that

$$\alpha \vec{x}_t + (1 - \alpha) \langle \vec{x}_t, \vec{\nu} \rangle \vec{\nu} - \frac{\vec{x}_{\rho\rho}}{|\vec{x}_\rho|^2} = f(\tilde{w}) \vec{\nu}, \quad (\rho, t) \in \mathcal{I} \times (0, T], \quad (3.1.2a)$$

$$(|\vec{x}_\rho| \tilde{w})_t - (\psi \tilde{w})_\rho - d \left(\frac{\tilde{w}_\rho}{|\vec{x}_\rho|} \right)_\rho = |\vec{x}_\rho| g(v, \tilde{w}), \quad (\rho, t) \in \mathcal{I} \times (0, T], \quad (3.1.2b)$$

$$F(\vec{x}(\rho, t)) = 0, \quad (\rho, t) \in \{0, 1\} \times (0, T], \quad (3.1.2c)$$

$$\langle \vec{x}_\rho(\rho, t), \nabla^\perp F(\vec{x}(\rho, t)) \rangle = 0, \quad (\rho, t) \in \{0, 1\} \times (0, T], \quad (3.1.2d)$$

$$\tilde{w}(\rho, t) = w_b, \quad (\rho, t) \in \{0, 1\} \times (0, T], \quad (3.1.2e)$$

$$\vec{x}(\rho, 0) = \vec{x}^0(\rho), \quad \tilde{w}(\rho, 0) = \tilde{w}^0(\rho) \quad \rho \in [0, 1]. \quad (3.1.2f)$$

Here $\alpha \in (0, 1]$, $w_b \in \mathbb{R}$, f, g are given functions and $\psi(\cdot, t)$ and $v(\cdot, t)$ define the tangential and normal velocity of $\Gamma(t)$ respectively. Moreover we denote $\tilde{w}(\cdot, t) := w(\vec{x}(\cdot, t), t)$ such that $w(\cdot, t) : \Gamma(t) \rightarrow \mathbb{R}$ and w^0 is a given function defined on $\Gamma(0)$. In Section 3.4 we motivate the reaction-diffusion equation contribution in terms of this thesis and prove continuous in time finite element error bounds. We next introduce notation that is used throughout this chapter.

3.1.1 Notation

We repeat some of the same notation used in Chapter 2 for the ease of the reader. As with standard theory we denote the Euclidean inner product by $\langle \cdot, \cdot \rangle$ associated to the Euclidean norm $|\vec{p}|^2 = \langle \vec{p}, \vec{p} \rangle$. We let \otimes denote the outer product defined as

$$\left(\vec{a} \otimes \vec{b} \right)_{ij} := \vec{a}_i \vec{b}_j, \quad \text{for } \vec{a} \in \mathbb{R}^m \text{ and } \vec{b} \in \mathbb{R}^n, \quad m, n \in \mathbb{N}.$$

Let us define a partition of our interval $[0, 1] = \cup_{j=1}^J \bar{\sigma}_j$, where $\sigma_j = (\rho_{j-1}, \rho_j)$. We set $h := \max_{j=1, \dots, J} h_j$, where $h_j = \rho_j - \rho_{j-1}$. Our finite element spaces are defined as

$$S^h := \{\chi^h \in C([0, 1]) : \chi^h|_{\sigma_j} \text{ is affine for each } j = 1, \dots, J\} \subset H^1(\mathcal{I})$$

$$S_0^h := \{\chi^h \in S^h : \chi^h(\rho_j) = 0, \text{ for } j \in \{0, J\}\}$$

$$S_{per}^h := \{\chi^h \in S^h : \chi^h(0) = \chi^h(1)\}.$$

We define the basis functions of S^h to be defined as $\chi_i(\rho_j) = \delta_i^j$ and we set $I^h : C([0, 1]) \rightarrow S^h$ to be the standard Lagrange interpolation operator defined as

$$(I^h \eta)(\rho_j) = \eta(\rho_j), \quad j = 0, \dots, J, \quad (3.1.3)$$

and we denote $I_j^h := I_{|\sigma_j}^h$ to be the local interpolation operator. We define the discrete inner product and the resultant induced norm as

$$(\eta_1, \eta_2)^h := \sum_{j=1}^J \int_{\sigma_j} I_j^h(\eta_1 \eta_2) d\rho, \quad \|\eta\|_h^2 := (\eta, \eta)^h.$$

Further to a spatial discretisation, we also discretise in time. Let $0 = t_0 < t_1 < \dots < t_{N-1} < t_N = T$ be a partition of $[0, T]$. We set $\Delta t := \max_{n=1, \dots, N} \Delta t_n$, where $\Delta t_n := t_n - t_{n-1}$. We define the discrete time derivative as

$$D_t a^n := \frac{a^n - a^{n-1}}{\Delta t_n},$$

where we have denoted the continuous function $a(\cdot, t^n)$ by $a^n(\cdot)$. In this setting, with the exception of F , we use capital letters to denote fully discretised finite element approximations and lower case letters to denote the continuous solution, e.g. $A^n(\cdot)$ denotes the finite element approximation to $a(\cdot, t^n)$. We add a superscript h to a lower case letter to denote a continuous in time finite element function, e.g. $a^h(\cdot, t^n)$ denotes the semi-discrete finite element approximation to $a(\cdot, t^n)$.

We adopt standard notation for Sobolev spaces $W^{l,p}(I)$, where $I \subset \mathbb{R}$ is a bounded interval, $l \in \mathbb{N}_0$ and $p \in [1, \infty]$. Unless stated otherwise we will be considering only $I = \mathcal{I}$ and so omit this dependency from the standard Sobolev notation. We denote the Sobolev l, p norm of a function f to be $\|f\|_{l,p}$ and its associated seminorm to be $|f|_{l,p}$. For the special case of $p = 2$, we denote $W^{l,2}(\mathcal{I})$ by $H^l(\mathcal{I})$ and denote the associated norm and seminorm to be $\|f\|_l$ and $|f|_l$ respectively. For the special case of $l = 0$, we work within the Lebesgue spaces $L^p(\mathcal{I})$, where the norm has its standard notation $\|f\|_{L^p(\mathcal{I})}$ with the $L^2(\mathcal{I})$ inner product denoted as (f, g) . When the function is vector valued, the function spaces are naturally extended to $[W^{l,p}(\mathcal{I})]^n$ and $[H^l(\mathcal{I})]^n$ with appropriately defined norms and seminorms, we however leave the notation for the norms unchanged. We extend the notation to include time dependent spaces $W^{l,p}(0, T; X)$, where $[0, T] \subset \mathbb{R}$ is the time domain and X a Banach Space, with the standard associated norm and seminorm $\|f\|_{W^{l,p}(0,T;X)}$ and $|f|_{W^{l,p}(0,T;X)}$.

Lastly, C denotes a generic constant that is independent of h and Δt_n . Multiple occurrences of C will not, in general, take the same value.

3.1.2 Useful identities and results

Using the notation defined above, we now state the approximation identities we plan on using throughout our analysis in this chapter. Firstly, we assume for some $C > 0$ that

$$h \leq C h_j, \quad j = 1, \dots, J, \quad (3.1.4a)$$

as well as

$$\Delta t \leq C \Delta t_n, \quad n = 1, \dots, N. \quad (3.1.4b)$$

In our notation, the standard interpolation results, see [32], are as follows, for $p \in (1, \infty]$, $k \in \{0, 1\}$, $l \in \{1, 2\}$, $s \in \{0, 1, 2\}$ and $j = 1, \dots, J$

$$h_j^{\frac{1}{p}} |\eta^h|_{0, \infty, \sigma_j} + h_j |\eta^h|_{1, p, \sigma_j} \leq C |\eta^h|_{0, p, \sigma_j} \quad \forall \eta^h \in S^h, \quad (3.1.5a)$$

$$|(I - I_j^h)\eta|_{k, p, \sigma_j} \leq C h_j^{\ell-k} |\eta|_{\ell, p, \sigma_j} \quad \forall \eta \in W^{\ell, p}(\sigma_j), \quad (3.1.5b)$$

$$|(I - I_j^h)\eta|_{\ell-1, \infty, \sigma_j} \leq C h_j^{\frac{1}{2}} |\eta|_{\ell, \sigma_j} \quad \forall \eta \in H^{\ell}(\sigma_j), \quad (3.1.5c)$$

$$|I_j^h \eta|_{s, p, \sigma_j} \leq C |\eta|_{s, p, \sigma_j} \quad \forall \eta \in W^{s, p}(\sigma_j), \quad (3.1.5d)$$

where $|\eta|_{\ell, p, \sigma_j}$ is the seminorm of the space $W^{\ell, p}(\sigma_j)$. We also have that for $j = 1, \dots, J$, and for all $\eta^h, \chi^h \in S^h$ that

$$\int_{\sigma_j} |\eta^h|^2 \, d\rho \leq \int_{\sigma_j} I_j^h [|\eta^h|^2] \, d\rho \leq 3 \int_{\sigma_j} |\eta^h|^2 \, d\rho, \quad (3.1.6a)$$

$$\left| \int_{\sigma_j} (I - I_j^h)(\eta^h \chi^h) \, d\rho \right| \leq C h_j^2 |\eta^h|_{1, \sigma_j} |\chi^h|_{1, \sigma_j} \leq C h_j |\eta^h|_{1, \sigma_j} |\chi^h|_{0, \sigma_j}. \quad (3.1.6b)$$

We also state explicitly that from the definition of the interpolant operator (3.1.3) we have

$$I^h \bar{x}^n(\rho) = \bar{x}^n(\rho), \quad \rho \in \{0, 1\}. \quad (3.1.7)$$

We note two inequalities that we will be using a lot in this chapter. First we have Young's inequality, which states that, for $a, b \in \mathbb{R}$ and $\delta > 0$,

$$|a||b| \leq \frac{\delta}{2} |a|^2 + \frac{2}{\delta} |b|^2. \quad (3.1.8)$$

Secondly we have the Gagliardo–Nirenberg inequality, which states that for $\eta \in H^1(\mathcal{I})$,

$$|\eta|_{0, \infty}^2 \leq C |\eta|_0 \|\eta\|_1 \quad (3.1.9a)$$

$$\leq \varepsilon |\eta|_1^2 + C(\varepsilon) |\eta|_0^2. \quad (3.1.9b)$$

Another identity we look to use, for $a, b \in \mathbb{R}$, is

$$b^2 - a^2 = (a - b)^2 - 2a(a - b). \quad (3.1.10)$$

Using Theorem B.6 we have that $H^1(\mathcal{I}) \hookrightarrow L^\infty(\mathcal{I})$. Namely, for $u \in H^1(\mathcal{I})$, we have

$$\|u\|_{0,\infty} \leq C_{emb} \|u\|_1. \quad (3.1.11)$$

We also use the following Taylor's expansions

$$\begin{aligned} F(\vec{p}) - F(\vec{q}) &= \langle \vec{p} - \vec{q}, \nabla F(\vec{p}) \rangle \\ &+ \int_0^1 \langle \nabla F(s\vec{p} + (1-s)\vec{q}) - \nabla F(\vec{p}), \vec{p} - \vec{q} \rangle ds, \end{aligned} \quad (3.1.12)$$

for $\vec{p}, \vec{q} \in \mathbb{R}^2$, as well as

$$\begin{aligned} \nabla F(\vec{p}) - \nabla F(\vec{q}) &= D^2 F(\vec{p})(\vec{p} - \vec{q}) \\ &+ \int_0^1 (D^2 F(s\vec{p} + (1-s)\vec{q}) - D^2 F(\vec{p}))(\vec{p} - \vec{q}) ds, \end{aligned} \quad (3.1.13)$$

Finally we introduce the discrete version of Gronwall's Lemma.

Lemma 3.1 (Discrete Gronwall's Lemma, [75]).

Let y_n , f_n and g_n be non-negative sequences and

$$y_n \leq f_n + \sum_{k=0}^n g_k y_k, \quad \text{for } n \geq 0,$$

then

$$y_n \leq f_n + \sum_{k=0}^n f_k g_k \exp\left(\sum_{j=k}^n g_j\right), \quad \text{for } n \geq 0.$$

3.2 Literature review

In Section 3.2.1 we present established results relating to the finite element approximation and analysis of curve shortening flow whilst in Section 3.2.2 we present results relating to the finite element approximation and analysis of curve shortening flow coupled to a reaction-diffusion equation on the curve.

3.2.1 Curve shortening flow

We begin with the seminal work produced by Dziuk in [52] who proposed a finite element approximation to curve shortening flow for a closed curve in \mathbb{R}^2 . Details of the derivation are standard and found in a differential geometry textbook such as [116]. Namely, let $s(\rho)$

define the arc-length of \vec{x} , then $\vec{x}(s)$ defines the arc-length parameterisation. Thus, the unit tangential and normal vectors of \vec{x} respectively are

$$\vec{\tau} = \vec{x}_s = \frac{\vec{x}_\rho}{|\vec{x}_\rho|}, \quad \vec{\nu} = \vec{\tau}^\perp. \quad (3.2.1)$$

Moreover, we have Frenet's formula, see [42, 107], which relates the tangent vector to the normal vector and the mean curvature

$$\vec{\tau}_s = \kappa \vec{\nu}. \quad (3.2.2)$$

Using (3.2.1) and (3.2.2) we see that the curvature in the normal direction is

$$\Delta_{\Gamma(t)} \vec{x} = \vec{\kappa} = \kappa \vec{\nu} = \vec{\tau}_s = \vec{x}_{ss}. \quad (3.2.3)$$

We also detail the tangential and normal velocities of \vec{x} , namely

$$\psi = \langle \vec{x}_t, \vec{\tau} \rangle, \quad v = \langle \vec{x}_t, \vec{\nu} \rangle. \quad (3.2.4)$$

Hence, as introduced in [52], we see that (1.1.5) can be rewritten as

$$\vec{x}_t - \frac{1}{|\vec{x}_\rho|} \left(\frac{\vec{x}_\rho}{|\vec{x}_\rho|} \right)_\rho = 0, \quad (\rho, t) \in \mathbb{I} \times (0, T), \quad (3.2.5a)$$

$$\vec{x}(0, t) = \vec{x}(1, t), \quad t \in (0, T], \quad (3.2.5b)$$

$$\vec{x}(\rho, 0) = \vec{x}^0(\rho), \quad \rho \in \mathbb{I}. \quad (3.2.5c)$$

Here we define $\mathbb{I} := \mathbb{R}/\mathbb{Z}$ to be the periodic unit interval and ρ is the parameter associated to it. In an abuse of notation we use ρ as the parameter associated to \mathbb{I} and also to \mathcal{I} . Multiplying (3.2.5a) by $|\vec{x}_\rho|$ and a smooth periodic test function $\vec{\xi}$, using integration by parts and the boundary conditions (3.2.5b), the weak form of (3.2.5a)–(3.2.5b) is given by

$$\left(|\vec{x}_\rho| \vec{x}_t, \vec{\xi} \right) + \left(\frac{\vec{x}_\rho}{|\vec{x}_\rho|}, \vec{\xi}_\rho \right) = 0, \quad \text{for all smooth periodic } \vec{\xi}, \quad (3.2.6)$$

and the associated semi-discrete finite element approximation presented in [52] takes the form

$$\left(|\vec{x}_\rho^h| \vec{x}_t^h, \vec{\xi}^h \right) + \left(\frac{\vec{x}_\rho^h}{|\vec{x}_\rho^h|}, \vec{\xi}_\rho^h \right) = 0, \quad \forall \vec{\xi}^h \in [S_{\text{per}}^h]^2. \quad (3.2.7)$$

Dziuk in [52] proves the following theorem which provides finite element error estimates for curve shortening flow [52, Theorem 2, p. 591].

Theorem 3.2 (G. Dziuk, 1994).

Let $\vec{x} = \vec{x}(\rho, t)$, $(\rho, t) \in \mathbb{I} \times [0, T]$, be a smooth solution of the curve shortening flow (3.2.5a)–(3.2.5c) with $|\vec{x}_\rho| \geq c_0 > 0$. Then there exists an h_0 depending on \vec{x} and T such

that for every $h \in (0, h_0]$ there exists a unique solution \vec{x}^h of (3.2.7) with initial data $\vec{x}^h(\rho_j, 0) = \vec{x}^0(\rho_j)$, for $j = 0, \dots, J$, and

$$\begin{aligned} \max_{t \in [0, T]} |\vec{x} - \vec{x}^h|_0^2 + \int_0^T |\vec{x} - \vec{x}^h|_1^2 dt &\leq Ch^2, \\ \max_{t \in [0, T]} |\vec{x}_t - \vec{x}_t^h|_0^2 + \int_0^T |\vec{x}_t - \vec{x}_t^h|_1^2 dt &\leq Ch^2, \end{aligned}$$

where C depends on \vec{x} , T and \mathbb{I} .

This realisation of curve shortening flow is prescribed purely in the normal direction. For the continuous solution, this is not a problem; however, for numerical simulation, this could lead to problems such as the nodes of the finite element approximation clumping together since they do not have any tangential motion, see Figure 3.1. Not only can one see the nodes clump together, but in turn this means that the distribution of the values of the length elements is poor as well. Heuristically we can see this occurs because in the continuous setting we have

$$\psi = \langle \vec{x}_t, \vec{\tau} \rangle = \frac{1}{|\vec{x}_\rho|} \langle \vec{\tau}_\rho, \vec{\tau} \rangle = \frac{1}{2} \frac{1}{|\vec{x}_\rho|} \frac{d}{d\rho} |\vec{\tau}|^2 = 0. \quad (3.2.8)$$

In [37], Deckelnick and Dziuk replaced the parametrisation of (3.2.5a) by

$$\vec{x}_t - \frac{\vec{x}_{\rho\rho}}{|\vec{x}_\rho|^2} = 0, \quad (\rho, t) \in \mathbb{I} \times (0, T), \quad (3.2.9a)$$

$$\vec{x}(0, t) = \vec{x}(1, t), \quad t \in (0, T], \quad (3.2.9b)$$

$$\vec{x}(\rho, 0) = \vec{x}^0(\rho), \quad \rho \in \mathbb{I}, \quad (3.2.9c)$$

where here we note that

$$\frac{1}{|\vec{x}_\rho|} \left(\frac{\vec{x}_\rho}{|\vec{x}_\rho|} \right)_\rho = \frac{\vec{x}_{\rho\rho}}{|\vec{x}_\rho|^2} - \frac{\langle \vec{x}_{\rho\rho}, \vec{\tau} \rangle}{|\vec{x}_\rho|^2} \vec{\tau} = (I - \vec{\tau} \otimes \vec{\tau}) \frac{\vec{x}_{\rho\rho}}{|\vec{x}_\rho|^2} \quad (3.2.10)$$

such that removing the term containing $\langle \vec{x}_{\rho\rho}, \vec{\tau} \rangle$ in (3.2.10) consequentially adds a tangential component to the parametrisation. We importantly stress that neglecting the term containing $\langle \vec{x}_{\rho\rho}, \vec{\tau} \rangle$ in (3.2.10) only changes the parametrisation tangentially and thus has no effect on the desired movement of the curve. Multiplying (3.2.9a) by $|\vec{x}_\rho|^2$ and a test function $\vec{\xi} \in [H_{\text{per}}^1(\mathbb{I})]^2$, using integration by parts and the boundary conditions (3.2.9b), the weak form of (3.2.9a)–(3.2.9b) is given by

$$\left(|\vec{x}_\rho|^2 \vec{x}_t, \vec{\xi} \right) + \left(\vec{x}_\rho, \vec{\xi}_\rho \right) = 0, \quad \forall \vec{\xi} \in [H_{\text{per}}^1(\mathbb{I})]^2, \quad (3.2.11)$$

and the associated semi-discrete finite element approximation presented in [37] takes the form

$$\left(|\vec{x}_\rho^h|^2 \vec{x}_t^h, \vec{\xi}^h \right) + \left(\vec{x}_\rho^h, \vec{\xi}_\rho^h \right) = 0, \quad \forall \vec{\xi}^h \in [S_{\text{per}}^h]^2. \quad (3.2.12)$$

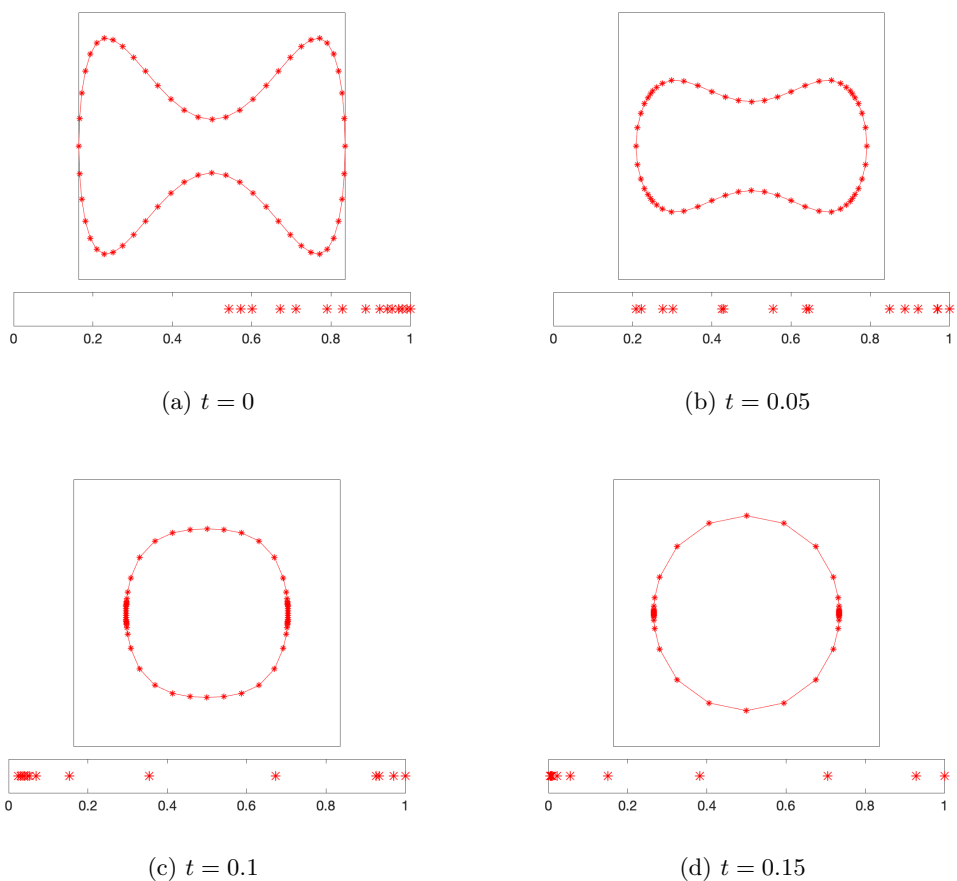


Figure 3.1: Simulation of a dumbbell moving under curve shortening flow using the numerical scheme presented in [52]. The top plot is the finite element approximation \vec{X}^n and the bottom is the distribution of the (normalised) length elements $|\vec{X}_\rho^n|$. $T = 0.15$.

Here we denote $H_{\text{per}}^1(\mathbb{I}) := \{f \in H^1(\mathbb{I}) : f(\rho) = f(\rho + z), \rho \in \mathbb{I}, \forall z \in \mathbb{Z}\}$. In [37] the authors prove the following theorem which provides finite element error estimates for this new parametrisation of curve shortening flow [37, Theorem 3.1, p. 4].

Theorem 3.3 (K. Deckelnick & G. Dziuk, 1995).

Let $\vec{x} \in C^{2,1}(\mathbb{I} \times [0, T])$ be a solution of (3.2.9a)–(3.2.9c) with $|\vec{x}_\rho| \geq c_0 > 0$ and

$$\vec{x}_t \in L^\infty(0, T; [H_{\text{per}}^1(\mathbb{I})]^2) \cap L^2(0, T; [H_{\text{per}}^2(\mathbb{I})]^2).$$

Then there exists an h_0 depending on \vec{x} and T such that for every $h \in (0, h_0]$ there exists a unique solution $\vec{x}^h \in H^1(0, T; [S_{\text{per}}^h]^2)$ of (3.2.12) and

$$\max_{t \in [0, T]} |\vec{x} - \vec{x}^h|_1^2 + \int_0^T |\vec{x}_t - \vec{x}_t^h|_0^2 \leq Ch^2$$

where C depends on \vec{x} and T .

One thing to note about (3.2.11) in comparison to (3.2.6) is that there is no division by the length element in the weak form. Furthermore, there is an improvement in the distribution of the length elements of the finite element approximation by comparing Figure 3.2 to Figure 3.1, which is due to the added tangential motion.

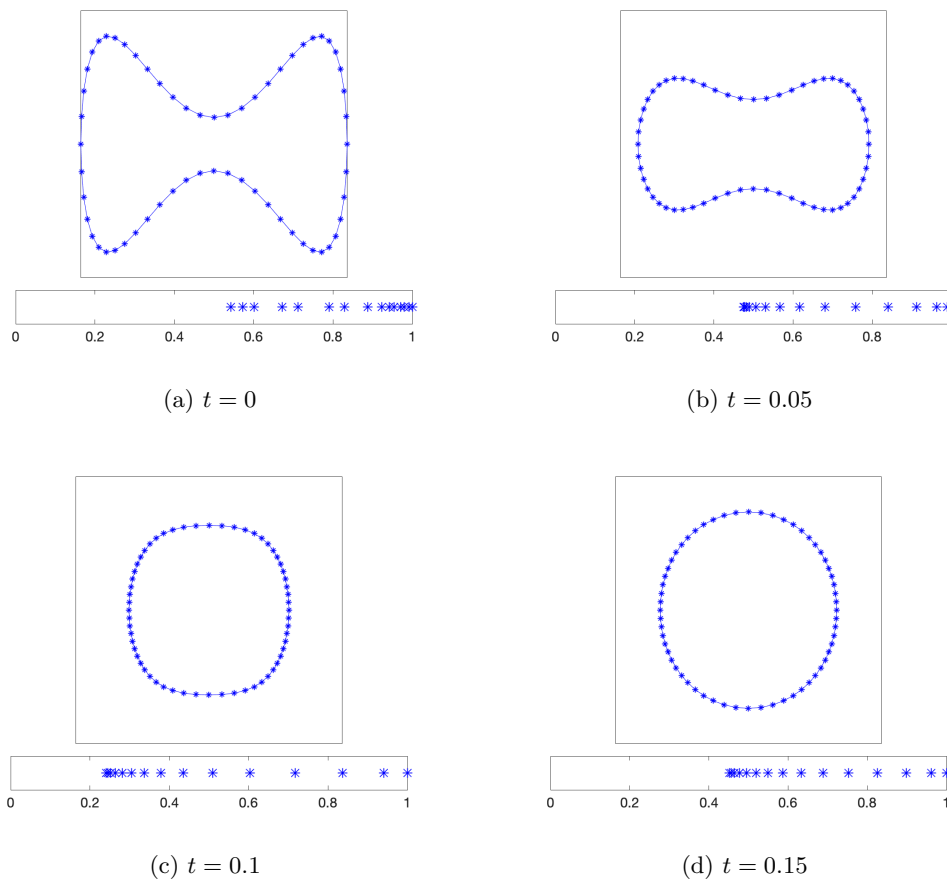


Figure 3.2: Simulation of a dumbbell moving under curve shortening flow using the numerical scheme presented in [37]. The top plot is the finite element approximation \vec{X}^n and the bottom is the distribution of the (normalised) length elements $|\vec{X}_\rho^n|$. $T = 0.15$.

In [37, 52] the numerical analysis of curve shortening flow was only concerned with closed curves. In [42] the authors consider curve shortening flow fixed to a boundary under a normal contact condition, as in **Model** \mathcal{M}_1 , which we restate for clarity

$$\vec{x}_t - \frac{\vec{x}_{\rho\rho}}{|\vec{x}_\rho|^2} = 0, \quad (\rho, t) \in \mathcal{I} \times (0, T], \quad (3.2.13a)$$

$$F(\vec{x}(\rho, t)) = 0, \quad (\rho, t) \in \{0, 1\} \times (0, T], \quad (3.2.13b)$$

$$\langle \vec{x}_\rho(\rho, t), \nabla^\perp F(\vec{x}(\rho, t)) \rangle = 0, \quad (\rho, t) \in \{0, 1\} \times (0, T], \quad (3.2.13c)$$

$$\vec{x}(\rho, 0) = \vec{x}^0(\rho), \quad \rho \in \mathcal{I}. \quad (3.2.13d)$$

The weak form for (3.2.13a)–(3.2.13c) will differ to that of (3.2.9a)–(3.2.9b) due to the

boundary conditions, we derive the weak form formally in Section 3.3. Multiplying (3.2.13a) by $|\vec{x}_\rho|^2$ and a test function $\vec{\xi} \in [H^1(\mathcal{I})]^2$, using integration by parts and noting (3.2.13c), the weak form of (3.2.13a)–(3.2.13c) is given by

$$\left(|\vec{x}_\rho|^2 \vec{x}_t, \vec{\xi}\right) + \left(\vec{x}_\rho, \vec{\xi}_\rho\right) = \left[\langle \vec{x}_\rho, \nabla F(\vec{x}) \rangle \langle \vec{\xi}, \nabla F(\vec{x}) \rangle\right]_{\rho=0}^{\rho=1}, \quad \forall \vec{\xi} \in [H^1(\mathcal{I})]^2. \quad (3.2.14)$$

and the associated semi-discrete finite element approximation presented in [42] takes the form

$$\left(|\vec{x}_\rho^h|^2 \vec{x}_t^h, \vec{\xi}^h\right)^h + \left(\vec{x}_\rho^h, \vec{\xi}_\rho^h\right) = \left[\langle \vec{x}_\rho^h, \nabla F(\vec{x}^h) \rangle \langle \vec{\xi}^h, \nabla F(\vec{x}^h) \rangle\right]_{\rho=0}^{\rho=1}, \quad \forall \vec{\xi}^h \in [S^h]^2. \quad (3.2.15)$$

In [42] the authors prove the following theorem which provides finite element error estimates for curve shortening flow attached normally to a fixed boundary [42, Theorem 2.1, p. 639]. We see that the authors of [42] have improved on the L^2 -error estimates originally derived by Theorem 3.2 and have made them optimal.

Theorem 3.4 (K. Deckelnick & C. M. Elliott, 1998).

Let $\vec{x} \in W^{2+\alpha, 1+\frac{\alpha}{2}}([0, 1] \times [0, T])$ be a solution of (3.2.13a)–(3.2.13d) with initial data $\vec{x}^0 \in C^{2+\alpha}([0, 1], \mathbb{R}^2)$ satisfying compatibility conditions for $\rho \in \{0, 1\}$

$$F(\vec{x}^0(\rho)) = 0, \quad \langle \nabla F(\vec{x}^0(\rho)), (\vec{x}^0(\rho))_{\rho\rho} \rangle = 0, \quad \langle (\vec{x}^0(\rho))_\rho, \nabla^\perp F(\vec{x}^0(\rho)) \rangle = 0$$

and boundary $\partial\Omega \in C^{2+\alpha}$ where $\alpha \in (0, 1)$, $0 < c_0 \leq |\vec{x}_\rho|^2 \leq c_1$ and

$$\vec{x}_t \in L^\infty(0, T; [H^1(\mathcal{I})]^2) \cap L^2(0, T; [H^2(\mathcal{I})]^2).$$

Then there exists an h_0 depending on \vec{x} and T such that for every $h \in (0, h_0]$ there exists a unique solution $\vec{x}^h \in H^1(0, T; [S^h]^2)$ of (3.2.15) and

$$\begin{aligned} \max_{t \in [0, T]} |\vec{x} - \vec{x}^h|_1^2 + \int_0^T |\vec{x}_t - \vec{x}_t^h|_0^2 dt &\leq Ch^2, \\ \max_{t \in [0, T]} |\vec{x} - \vec{x}^h|_0^2 &\leq Ch^4, \end{aligned}$$

where C depends on \vec{x} and T .

A further study of curve shortening flow is the study of triple junctions which has applications in material science such as grain boundary motion, for example, where grains meet at junctions with angle conditions. Publications concerning mathematical models involving triple junctions typically consider two different formulations. The first formulation considers three curves attached to a fixed boundary and meeting at a triple junction, see Figure 3.3. This setup requires following the boundary and triple junction conditions

$$F(\vec{x}^i(1, t)) = 0, \quad \langle \vec{x}_\rho^i(1, t), \nabla^\perp F(\vec{x}^i(1, t)) \rangle = 0, \quad \text{for } t \in [0, T], \quad i = 1, 2, 3,$$

$$\begin{aligned}\vec{x}^1(0, t) &= \vec{x}^2(0, t) = \vec{x}^3(0, t), \quad \text{for } t \in [0, T], \\ \langle \vec{\tau}^1(0, t), \vec{\tau}^2(0, t) \rangle &= \cos \theta^1, \quad \langle \vec{\tau}^2(0, t), \vec{\tau}^3(0, t) \rangle = \cos \theta^2, \quad \text{for } t \in [0, T],\end{aligned}$$

where \vec{x}^i denotes the i -th curve with $\vec{\tau}^i$ being the unit tangent vector of curve \vec{x}^i , and θ^i denotes the angle between \vec{x}^i and \vec{x}^{i+1} , see [8, 42].

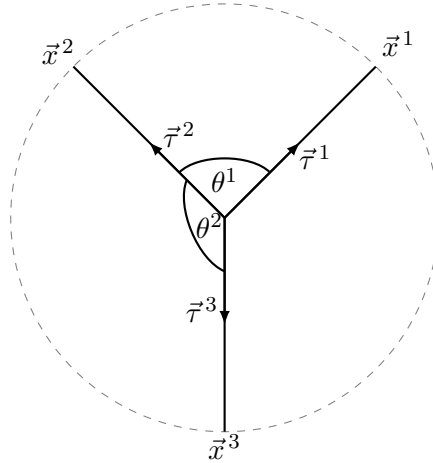


Figure 3.3: Triple junction attached to a boundary. The grey dashed line depicts $\partial\Omega$, each black line depicts a curve \vec{x}^i with an arrow which depicts the corresponding tangential vector $\vec{\tau}^i$. The orientation of each vector is corresponding to the angle condition. Inspiration from [8].

The other formulation, which is considered in [9, 98], is a closed curve formulation with two triple junctions. The assumption that the tangent vectors of each of the curves point away from one of the triple junctions and towards the other, see Figure 3.4, results in the following conditions at the triple junctions

$$\begin{aligned}\vec{x}^1(0, t) &= \vec{x}^2(0, t) = \vec{x}^3(0, t), \quad \vec{x}^1(1, t) = \vec{x}^2(1, t) = \vec{x}^3(1, t), \quad \text{for } t \in [0, T], \\ \vec{\tau}^1(\rho, t) + \vec{\tau}^2(\rho, t) + \vec{\tau}^3(\rho, t) &= 0, \quad \text{for } (\rho, t) \in \{0, 1\} \times [0, T].\end{aligned}$$

For the second motivated formulation, finite element analysis has only recently been conducted, in [98], for a regularised version, regularised in the sense of adding artificial tangential motion, due to the difficulty of using (3.2.5a) as the basis for the curve shortening flow.

Even though introducing a reparametrisation was designed to give the numerical scheme tangential movement, it still did not solve the problem entirely, as demonstrated by Figure 3.2c, because the redistribution timescale is much larger than that of the simulation timescale, see [59]. In a series of papers, including but not limited to [8, 9, 10],

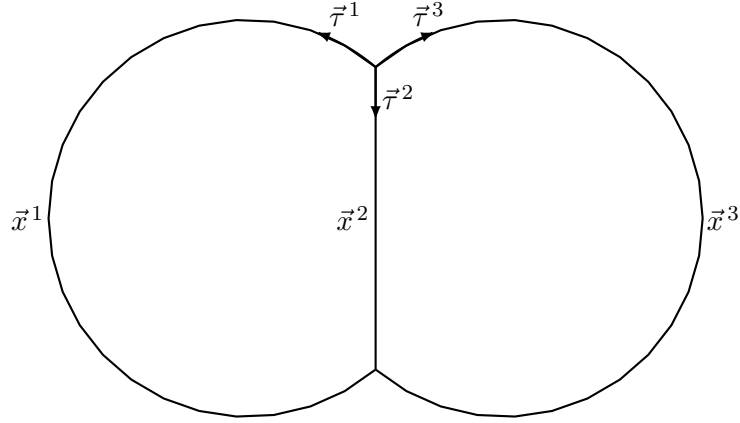


Figure 3.4: Triple junction occurring from collision of closed curves. Each black line depicts a curve \vec{x}^i with an arrow which depicts the corresponding tangential vector \vec{r}^i . Inspiration from [8].

about geometric evolution equations, such as mean curvature flow and surface diffusion, Barrett, Garcke and Nürnberg introduced a scheme that equidistributes the nodes of the finite element approximation to curve shortening flow. Shown in [11], the derivation of the scheme differs slightly from the original version that Dziuk proposed. Namely in [11] the authors couple (1.1.1), using $v := \langle \vec{x}_t, \vec{\nu} \rangle$, to (3.2.3), using $\vec{\kappa} = \kappa \vec{\nu}$, to result in a coupled system for κ and \vec{x} . Furthermore they assume that the parametrisation of $\Gamma(t)$ is equidistributed, i.e.

$$|\Gamma(t)| := \int_{\Gamma(t)} 1 ds = \int_{\mathbb{I}} |\vec{x}_\rho(\cdot, t)| d\rho = |\vec{x}_\rho(\rho, t)| \quad \forall \rho \in \mathbb{I}.$$

Multiplying (1.1.1) by $\xi \in H^1_{\text{per}}(\mathbb{I})$ and multiplying (3.2.3) by $\vec{\xi} \in [H^1_{\text{per}}(\mathbb{I})]^2$, integrating and using integration by parts in the second case, yields the following weak form

$$\left(\langle \vec{x}_t, \vec{\nu} \rangle, \xi \right)_{\Gamma(t)} - (\kappa, \xi)_{\Gamma(t)} = 0, \quad \forall \xi \in H^1_{\text{per}}(\mathbb{I}), \quad (3.2.16a)$$

$$\left(\kappa \vec{\nu}, \vec{\xi} \right)_{\Gamma(t)} + \left(\vec{x}_s, \vec{\xi}_s \right)_{\Gamma(t)} = 0, \quad \forall \vec{\xi} \in [H^1_{\text{per}}(\mathbb{I})]^2. \quad (3.2.16b)$$

We note here that in fact one can eliminate κ from the above coupling to obtain

$$\left(\langle \vec{x}_t, \vec{\nu} \rangle \vec{\nu}, \vec{\xi} \right)_{\Gamma(t)} + \left(\vec{x}_s, \vec{\xi}_s \right)_{\Gamma(t)} = 0, \quad \forall \vec{\xi} \in [H^1_{\text{per}}(\mathbb{I})]^2. \quad (3.2.17)$$

To be consistent with the weak forms derived for curve shortening flow that we presented earlier, the authors in [11] also present (3.2.16a)–(3.2.16b) using the normalised parametrisation in the following way

$$\left(\langle \vec{x}_t, \vec{x}_\rho^\perp \rangle, \xi \right) - |\Gamma(t)| (\kappa, \xi) = 0, \quad \forall \xi \in H^1_{\text{per}}(\mathbb{I}), \quad (3.2.18a)$$

$$\left(\kappa \vec{x}_\rho^\perp, \vec{\xi} \right) + \frac{1}{|\Gamma(t)|} \left(\vec{x}_\rho, \vec{\xi}_\rho \right) = 0, \quad \forall \vec{\xi} \in [H^1_{\text{per}}(\mathbb{I})]^2. \quad (3.2.18b)$$

In [11] the authors present a fully discrete finite element approximation of (3.2.16a)–(3.2.16b) however for consistency purposes we will state the equivalent formulations of the finite element approximation associated to (3.2.18a)–(3.2.18b)

$$\frac{1}{\Delta t_n} \left(\langle \vec{X}^n - \vec{X}^{n-1}, (\vec{X}_\rho^n)^\perp, \xi^h \rangle^h - |\Gamma^n| \left(K^n, \xi^h \right)^h = 0, \quad \forall \xi^h \in S_{\text{per}}^h, \quad (3.2.19a)$$

$$\left(K^n (\vec{X}_\rho^n)^\perp, \vec{\xi}^h \right)^h + \frac{1}{|\Gamma^n|} \left(\vec{X}_\rho^n, \vec{\xi}_\rho^h \right) = 0, \quad \forall \vec{\xi}^h \in [S_{\text{per}}^h]^2. \quad (3.2.19b)$$

In [11] the authors prove the following equidistributing property described in [11, Theorem 2.3, p. 9]. Figure 3.5 demonstrates this equidistributing property, whereby we can see that all the normalised length elements are equal to 1.

Theorem 3.5 (J. W. Barrett, H. Garcke & R. Nürnberg, 2011).

Let $(\vec{X}^n, K^n)_{n=0}^N$ denote a solution to (3.2.19a)–(3.2.19b). Then it holds that

$$|\vec{X}_{j+1}^n - \vec{X}_j^n| = |\vec{X}_j^n - \vec{X}_{j-1}^n|, \quad j = 1, \dots, J-1, \quad n = 1, \dots, N.$$

In addition, $(\vec{X}^n, K^n)_{n=0}^N$ is a solution to the associated fully discrete finite element form of (3.2.16a)–(3.2.17). In particular the following stability result holds for all $k = 1, \dots, N$

$$|\Gamma^k| + \sum_{n=0}^{k-1} \Delta t_n \left(K^{n+1}, K^{n+1} \right)_{\Gamma^{n+1}}^h \leq |\Gamma^0|.$$

In [59] Elliott and Fritz derived a finite element approximation to curve shortening flow that results in a good distribution of the nodes as well as allowing for analysis of finite element error estimates. In [59] the authors reparametrise (3.2.5a) using a well-known instrument in differential geometry called the De-Turck trick, [45]. The De-Turck trick reparametrises the curve (or surface) by using the inverse of the solution to the harmonic heat flow map. This introduces a constant $\alpha \in (0, 1]$ that provides a linear combination between (3.2.9a) and (3.2.17). Namely, the authors in [59] present a parametrisation of the form

$$\alpha \vec{x}_t + (1 - \alpha) \langle \vec{x}_t, \vec{\nu} \rangle \vec{\nu} - \frac{\vec{x}_{\rho\rho}}{|\vec{x}_\rho|^2} = 0, \quad (\rho, t) \in \mathbb{I} \times (0, T], \quad (3.2.20a)$$

$$\vec{x}(0, t) = \vec{x}(1, t), \quad t \in (0, T], \quad (3.2.20b)$$

$$\vec{x}(\rho, 0) = \vec{x}^0(\rho), \quad \rho \in \mathbb{I}. \quad (3.2.20c)$$

Multiplying (3.2.20a) by $|\vec{x}_\rho|^2$ and a test function $\vec{\xi} \in [H_{\text{per}}^1(\mathbb{I})]^2$, using integration by parts as well as the boundary condition (3.2.20b), the weak form of (3.2.20a)–(3.2.20b) is given by

$$\left(|\vec{x}_\rho|^2 [\alpha \vec{x}_t + (1 - \alpha) \langle \vec{x}_t, \vec{\nu} \rangle \vec{\nu}], \vec{\xi} \right) + \left(\vec{x}_\rho, \vec{\xi}_\rho \right) = 0, \quad \forall \vec{\xi} \in [H_{\text{per}}^1(\mathbb{I})]^2, \quad (3.2.21)$$

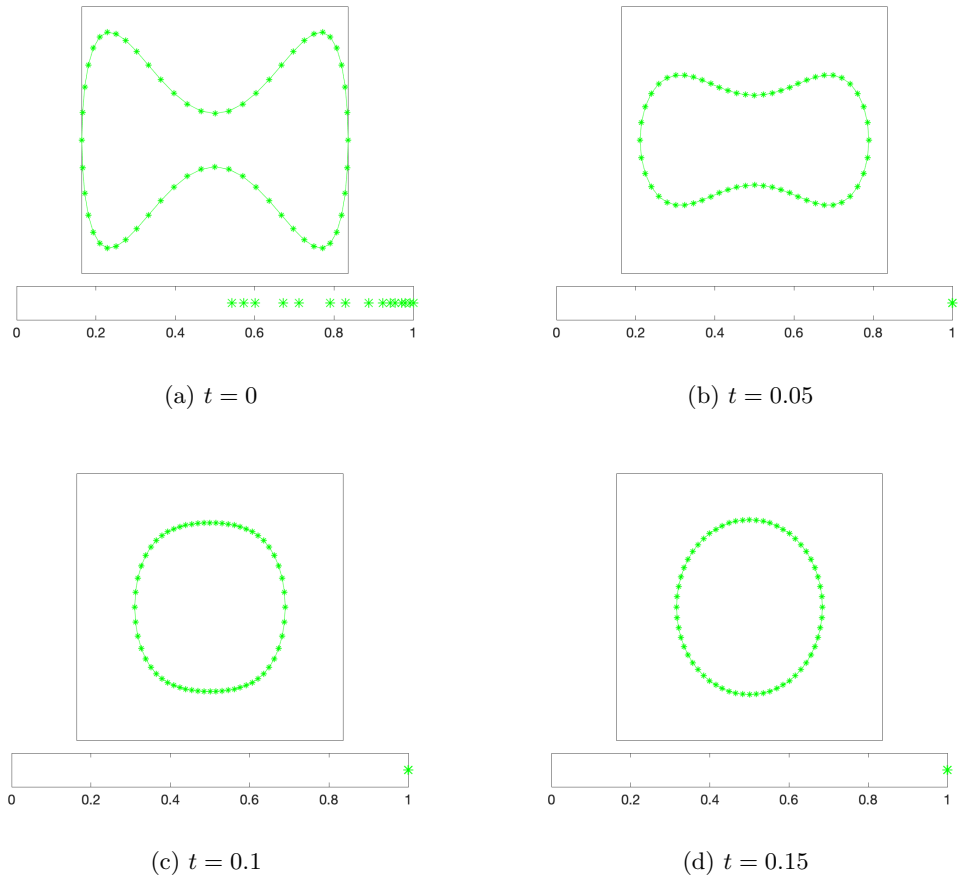


Figure 3.5: Simulation of a dumbbell moving under curve shortening flow using the numerical scheme presented in [11]. The top plot is the finite element approximation \vec{X}^n and the bottom is the distribution of the (normalised) length elements $|\vec{X}_\rho^n|$. $T = 0.15$.

and the associated semi-discrete finite element approximation presented in [59] takes the form

$$\left(|\vec{x}_\rho^h|^2 \left[\alpha \vec{x}_t^h + (1 - \alpha) \langle \vec{x}_t^h, \vec{\nu}^h \rangle \vec{\nu}^h \right], \vec{\xi}^h \right) + \left(\vec{x}_\rho^h, \vec{\xi}_\rho^h \right) = 0, \quad \forall \vec{\xi}^h \in [S_{\text{per}}^h]^2. \quad (3.2.22)$$

In [59] the authors prove Theorem 3.6, [59, Theorem 3.5, p. 11], which provides finite element error estimates for this new parametrisation of curve shortening flow.

Theorem 3.6 (C. M. Elliott & H. Fritz, 2016).

Let $\alpha \in (0, 1]$ and suppose that $\vec{x} \in C^{2,1}(\mathbb{I} \times [0, T], \mathbb{R}^2)$ is a solution of (3.2.20a)–(3.2.20c) with

$$\begin{aligned} \vec{x}_t &\in L^\infty(0, T; [H_{\text{per}}^1(\mathbb{I})]^2) \cap L^2(0, T; [H_{\text{per}}^2(\mathbb{I})]^2), \\ |\vec{x}_\rho| &\geq c_0 > 0, \quad \text{in } \mathbb{I} \times [0, T]. \end{aligned}$$

Then there exists a constant $h_0 > 0$ depending on \vec{x} and T such that for every $h \in (0, h_0]$ there is a unique solution $\vec{x}^h \in H^1(0, T; [S_{\text{per}}^h(\mathbb{I})]^2)$ of the non-linear, semi-discrete problem

(3.2.22) for all $\vec{\xi}^h \in [S_{per}^h(\mathbb{I})]^2$, $t \in (0, T)$, with initial data $\vec{x}^h(\cdot, 0) = (I^h \vec{x}^0)(\cdot)$ on \mathbb{I} , and

$$\max_{t \in [0, T]} |\vec{x} - \vec{x}_h|_1^2 + \alpha \int_0^T |\vec{x}_t - \vec{x}_t^h|_0^2 dt + (1 - \alpha) \int_0^T |\langle \vec{x}_t - \vec{x}_t^h, \vec{v}^h \rangle|_0^2 dt \leq C e^{\frac{M}{\alpha} T} h^2.$$

The constants C and M depend on the continuous solution \vec{x} and T .

The proof of Theorem 3.6 shows that one obtains convergence for α non zero. We can see this numerically by looking at Figure 3.7, although the numerical scheme presented in [11] has the equidistribution property, see Figure 3.7d, the numerical scheme presented in [59] is closer to the “true” solution, see Figure 3.7c. Here we mean that the “true” solution, depicted by the black line, is the numerical solution from the numerical scheme presented in [37] using a significantly smaller value of h and Δt . Although formally choosing $\alpha = 0$ will result in (3.2.17), the numerical scheme presented in [59] will not equidistribute with $\alpha = 0$ since, unlike the numerical scheme presented in [11], it is not fully implicit; however, choosing α small does lead to a good distribution of the nodes of the finite element approximation, as can be seen in Figure 3.6.

Briefly turning our attention to surfaces, Dziuk in [51] derived a finite element algorithm for the mean curvature flow of surfaces. There has been no proof of error convergence for this scheme due to the difficulty of the strong form equation, as explained in [83]. The authors in [83] managed to prove convergence for the evolution of a surface but used Huisken’s formulation of parametric mean curvature flow, see [77], rather than Dziuk’s, and used higher order finite elements, not just linear finite elements.

3.2.2 Curve shortening flow coupled to a PDE on the curve

In studying the rice blast fungus we want to simulate a system consisting of a moving curve coupled to a reaction-diffusion equation defined on the curve. Noting Definitions A.4–A.7 such a system takes the form

$$v = \kappa + f, \quad \text{on } \Gamma(t), t \in (0, T] \quad (3.2.23a)$$

$$\partial_t^\bullet w - \kappa v w - dw_{ss} = g, \quad \text{on } \Gamma(t), t \in (0, T], \quad (3.2.23b)$$

where f and g are (coupling) functions and $\partial_t^\bullet w = w_t + v \langle \nabla w, \vec{v} \rangle$, since $\vec{v}_\tau = 0$.

In [97], Pozzi and Stinner produced the first finite element error analysis for such a coupling. By considering Dziuk’s original method (3.2.5a) for closed curves and labelling

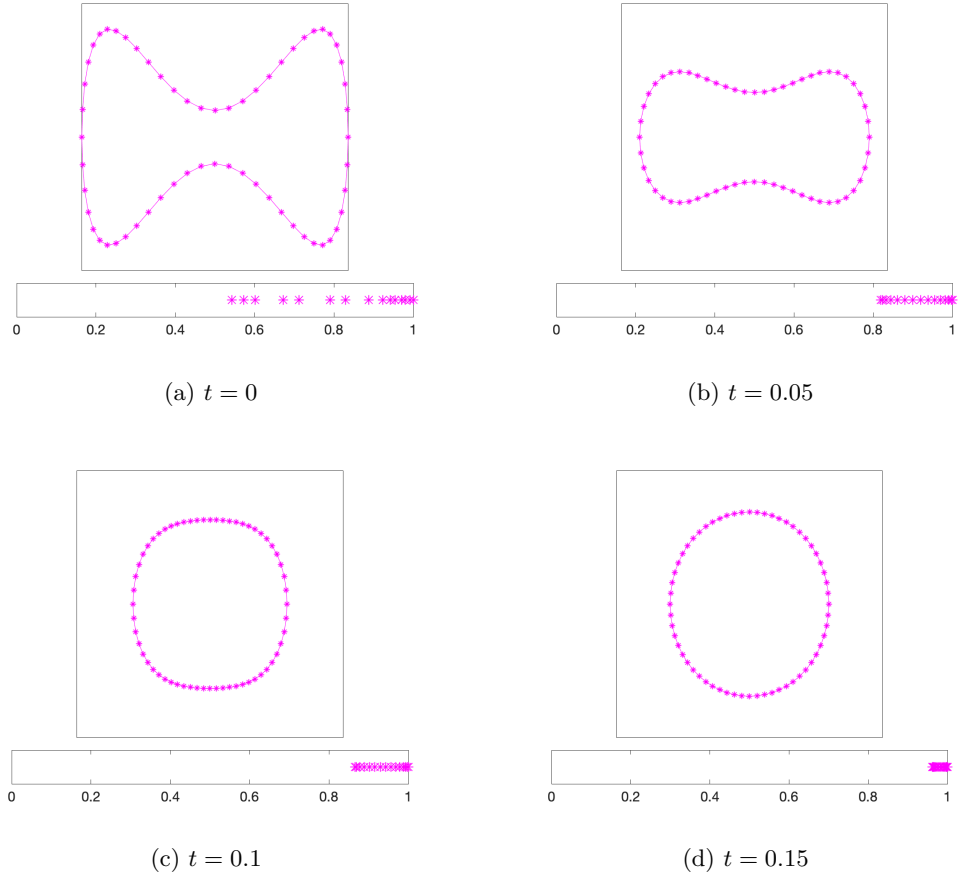


Figure 3.6: Simulation of a dumbbell moving under curve shortening flow using the numerical scheme presented in [59] with $\alpha = 0.1$. The top plot is the finite element approximation \vec{X}^n and the bottom is the distribution of the (normalised) length elements $|\vec{X}_\rho^n|$. $T = 0.15$.

$\tilde{w}(\rho, t) = w(\vec{x}(\rho, t), t)$, taking $d = 1$ and $g = 0$, the system (3.2.23a)–(3.2.23b) becomes

$$\vec{x}_t - \frac{1}{|\vec{x}_\rho|} \left(\frac{\vec{x}_\rho}{|\vec{x}_\rho|} \right)_\rho = f(\tilde{w}) \vec{\nu}, \quad (\rho, t) \in \mathbb{I} \times (0, T], \quad (3.2.24a)$$

$$\tilde{w}_t + \tilde{w} \frac{|\vec{x}_\rho|_t}{|\vec{x}_\rho|} - \frac{1}{|\vec{x}_\rho|} \left(\frac{\tilde{w}_\rho}{|\vec{x}_\rho|} \right)_\rho = 0, \quad (\rho, t) \in \mathbb{I} \times (0, T], \quad (3.2.24b)$$

$$\vec{x}(0, t) = \vec{x}(1, t), \quad \tilde{w}(0, t) = \tilde{w}(1, t), \quad t \in (0, T], \quad (3.2.24c)$$

$$\vec{x}(\rho, 0) = \vec{x}^0(\rho), \quad \tilde{w}(\rho, 0) = \tilde{w}^0(\rho), \quad \rho \in \mathbb{I}. \quad (3.2.24d)$$

The derivation of (3.2.24b) from (3.2.23b) is discussed in Section 3.4. Multiplying (3.2.24a) by $|\vec{x}_\rho|$ and a smooth periodic test function $\vec{\xi}$ as well as multiplying (3.2.24b) by $|\vec{x}_\rho|$ and a smooth periodic test function η constant in time, using integration by parts and boundary conditions (3.2.24c), the weak form of (3.2.24a)–(3.2.24c) is given by

$$\left(|\vec{x}_\rho| \vec{x}_t, \vec{\xi} \right) + \left(\frac{\vec{x}_\rho}{|\vec{x}_\rho|}, \vec{\xi}_\rho \right) = \left(|\vec{x}_\rho| f(\tilde{w}) \vec{\nu}, \vec{\xi} \right), \quad \text{for all smooth periodic } \vec{\xi}, \quad (3.2.25a)$$

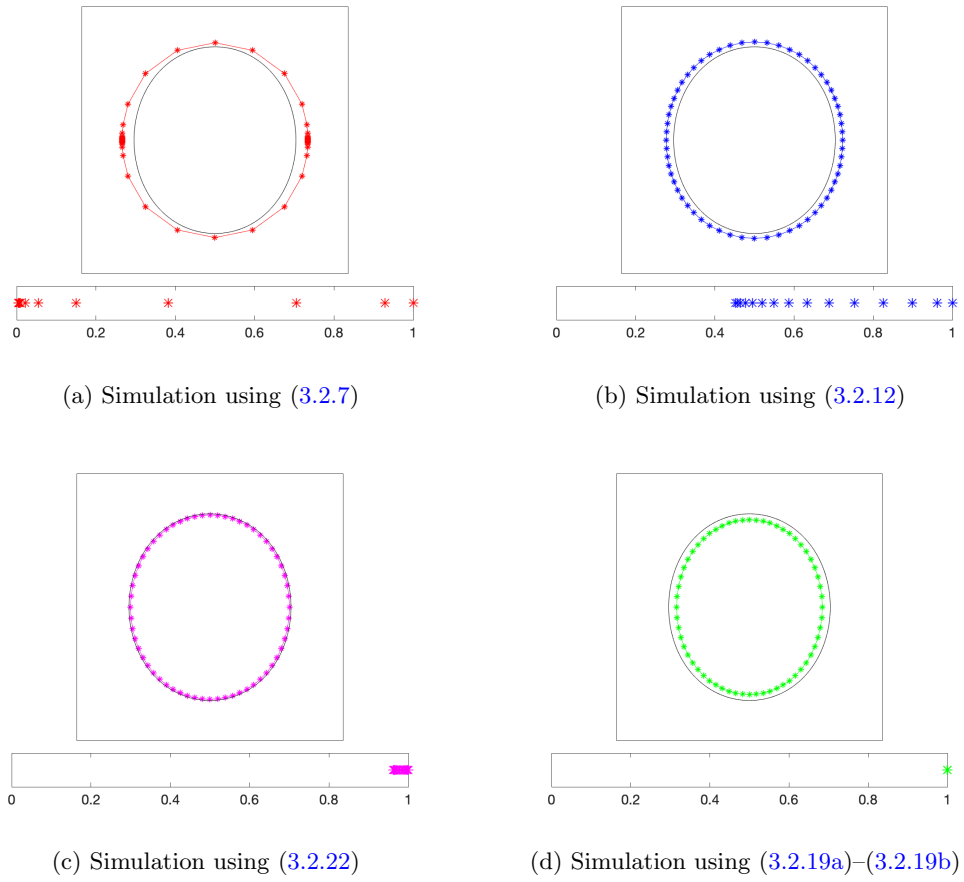


Figure 3.7: Simulation of a dumbbell moving under curve shortening flow using the numerical schemes presented in [52] in red, [37] in blue, [59] with $\alpha = 0.1$ in pink, [11] in green and the “true” solution in black, at $T = 0.15$. The top plot is the finite element approximation \vec{X}^N and the bottom is the distribution of the (normalised) length elements $|\vec{X}_\rho^N|$.

$$\frac{d}{dt} (|\vec{x}_\rho| \tilde{w}, \eta) + \left(\frac{\tilde{w}_\rho}{|\vec{x}_\rho|}, \eta_\rho \right) = 0, \quad \text{for all smooth periodic } \eta, \quad (3.2.25b)$$

and the associated semi-discrete finite element approximation presented in [97] takes the form

$$\left(|\vec{x}_\rho^h| \vec{x}_t^h, \vec{\xi}^h \right)^h + \left(\frac{\vec{x}_\rho^h}{|\vec{x}_\rho^h|}, \vec{\xi}_\rho^h \right) = \left(|\vec{x}_\rho^h| f(\tilde{w}^h) \vec{\nu}^h, \vec{\xi}^h \right)^h, \quad \forall \vec{\xi}^h \in [S_{\text{per}}^h]^2, \quad (3.2.26a)$$

$$\frac{d}{dt} \left(|\vec{x}_\rho^h| \tilde{w}^h, \eta^h \right) + \left(\frac{\tilde{w}_\rho^h}{|\vec{x}_\rho^h|}, \eta_\rho^h \right) = 0, \quad \forall \eta^h \in S_{\text{per}}^h. \quad (3.2.26b)$$

In [97] the authors prove the following theorem which consists of semi-discrete finite element error estimates for the system consisting of curve shortening flow coupled to lateral diffusion on the curve [97, Theorem 1.1, p. 2].

Theorem 3.7 (P. Pozzi & B. Stinner, 2015).

Under the assumptions that

$$\begin{aligned} \|f\|_{W^{1,\infty}(\mathbb{R})} &\leq C, \\ |\vec{x}_\rho| &\geq C > 0, \\ \vec{x} &\in W^{1,\infty}(0, T; [H_{per}^2(\mathbb{I})]^2), \\ w &\in W^{1,\infty}(0, T; H_{per}^1(\mathbb{I})) \cap L^\infty(0, T; H_{per}^2(\mathbb{I})), \end{aligned}$$

there exist $h_0 > 0$ such that for all $h \in (0, h_0]$ there exists a unique solution to (3.2.26a)–(3.2.26b), and the error between the smooth solution and the discrete solutions can be estimated as follows:

$$\begin{aligned} \int_0^T |\vec{x}_t - \vec{x}_t^h|_0^2 + |w - w^h|_1^2 &\leq Ch^2, \\ \sup_{t \in [0, T]} \left[|\vec{\tau} - \vec{\tau}^h|_0^2 + |w - w^h|_0^2 + \|\vec{x}_\rho\| - |\vec{x}_\rho^h|_0^2 \right] &\leq Ch^2, \end{aligned}$$

with constant $C > 0$. The constant C depends on the final time T , on the bounds $\|f\|_{W^{1,\infty}(\mathbb{R})}$ of the coupling function, on the regularity and bounds $\|\vec{x}\|_{W^{1,\infty}(0, T; [H_{per}^2(\mathbb{I})]^2)}$, $\|w\|_{W^{1,\infty}(0, T; H_{per}^1(\mathbb{I}))}$ and $\|w\|_{L^\infty(0, T; H_{per}^2(\mathbb{I}))}$ of the solution (which include the bounds $\|\vec{x}^0\|_2$ and $\|w^0\|_1$ of the initial values), on the bound from below of the length element, and on the grid regularity.

In [6] Barrett, Deckelnick and Styles derive a fully practical scheme and present fully discrete error estimates to a coupled system similar to that considered by Pozzi and Stinner. Rather than using (3.2.5a) for closed curves, the authors used (3.2.20a) to introduce tangential motion to the nodes of the finite element approximation, resulting in the following slightly different formulation compared to (3.2.24a)–(3.2.24d)

$$\alpha \vec{x}_t + (1 - \alpha) \langle \vec{x}_t, \vec{\nu} \rangle \vec{\nu} = \frac{\vec{x}_{\rho\rho}}{|\vec{x}_\rho|^2} + f(\tilde{w}) \vec{\nu}, \quad (\rho, t) \in \mathbb{I} \times (0, T], \quad (3.2.27a)$$

$$\tilde{w}_t - \frac{1}{|\vec{x}_\rho|} \psi \tilde{w}_\rho - \frac{d}{|\vec{x}_\rho|} \left(\frac{\tilde{w}_\rho}{|\vec{x}_\rho|} \right)_\rho - \kappa v \tilde{w} = g(v, \tilde{w}), \quad (\rho, t) \in \mathbb{I} \times (0, T], \quad (3.2.27b)$$

$$\vec{x}(0, t) = \vec{x}(1, t), \quad \tilde{w}(0, t) = \tilde{w}(1, t), \quad t \in (0, T], \quad (3.2.27c)$$

$$\vec{x}(\rho, 0) = \vec{x}^0(\rho), \quad \tilde{w}(\rho, 0) = \tilde{w}^0(\rho), \quad \rho \in \mathbb{I}. \quad (3.2.27d)$$

By multiplying (3.2.27a) by $|\vec{x}_\rho|^2$ and a test function $\vec{\xi} \in [H_{per}^1(\mathbb{I})]^2$ as well as multiplying (3.2.27b) by $|\vec{x}_\rho|$ and a test function $\eta \in H_{per}^1(\mathbb{I})$ constant in time, using integration by parts and (3.2.27c), the weak form of (3.2.27a)–(3.2.27c) is given by

$$\left(|\vec{x}_\rho|^2 [\alpha \vec{x}_t + (1 - \alpha) \langle \vec{x}_t, \vec{\nu} \rangle \vec{\nu}], \vec{\xi} \right) + \left(\vec{x}_\rho, \vec{\xi}_\rho \right)$$

$$= \left(|\vec{x}_\rho|^2 f(\tilde{w}) \vec{v}, \vec{\xi} \right), \quad \forall \vec{\xi} \in [H^1_{\text{per}}(\mathbb{I})]^2, \quad (3.2.28a)$$

$$\frac{d}{dt} (|\vec{x}_\rho| \tilde{w}, \eta) + (\psi \tilde{w}, \eta_\rho) + d \left(\frac{\tilde{w}_\rho}{|\vec{x}_\rho|}, \eta_\rho \right) = (|\vec{x}_\rho| g(v, \tilde{w}), \eta), \quad \forall \eta \in H^1_{\text{per}}(\mathbb{I}), \quad (3.2.28b)$$

and the associated fully discrete finite element approximation presented in [6] takes the form

$$\begin{aligned} & \left(|\vec{X}_\rho^{n-1}|^2 \left[\alpha D_t \vec{X}^n + (1 - \alpha) \langle D_t \vec{X}^n, \vec{\mathcal{V}}^{n-1} \rangle \vec{\mathcal{V}}^{n-1} \right], \vec{\xi}^h \right)^h \\ & + \left(\vec{X}_\rho^n, \vec{\xi}_\rho^h \right) = \left(|\vec{X}_\rho^{n-1}|^2 f(W^{n-1}) \vec{\mathcal{V}}^{n-1}, \vec{\xi}^h \right), \quad \forall \vec{\xi}^h \in [S^h_{\text{per}}]^2, \end{aligned} \quad (3.2.29a)$$

$$\begin{aligned} D_t \left[\left(|\vec{X}_\rho^n| W^n, \eta^h \right)^h \right] + \left(\Psi^n W^n, \eta_\rho^h \right)^h + d \left(\frac{W_\rho^n}{|\vec{X}_\rho^n|}, \eta_\rho^h \right) \\ = \left(|\vec{X}_\rho^n| g(V^n, W^{n-1}), \eta^h \right)^h, \quad \forall \eta^h \in S^h_{\text{per}}. \end{aligned} \quad (3.2.29b)$$

In [6] the authors prove the following theorem which is the fully discrete finite element error estimates for the coupled system of curve shortening flow with a reaction-diffusion equation on the curve [6, Theorem 2.1, p. 5].

Theorem 3.8 (J. W. Barrett, K. Deckelnick & V. Styles, 2017).

Let $\vec{x}^0 = I^h \tilde{x}^0 \in [S^h_{\text{per}}]^2$ and $W^0 = I^h \tilde{w}^0 \in S^h_{\text{per}}$. Under the assumptions that

$$\begin{aligned} & f \in C^{1,1}(\mathbb{R}), \\ & g \in C^{1,1}(\mathbb{R}^2), \\ & \vec{x} \in W^{1,\infty}(0, T; [H^2_{\text{per}}(\mathbb{I})]^2) \cap H^2(0, T; [H^1_{\text{per}}(\mathbb{I})]^2) \cap W^{2,\infty}(0, T; [L^2_{\text{per}}(\mathbb{I})]^2), \\ & w \in C([0, T]; H^2_{\text{per}}(\mathbb{I})) \cap W^{1,\infty}(0, T; H^1_{\text{per}}(\mathbb{I})) \cap H^2(0, T; L^2_{\text{per}}(\mathbb{I})), \\ & 0 < m \leq |\vec{x}_\rho| \leq M, \quad \text{on } \mathbb{I} \times [0, T], \end{aligned}$$

then there exists $h^* > 0$ such that for all $h \in (0, h^*]$ and $\Delta t \leq C h$ the discrete problem (3.2.29a)–(3.2.29b) has a unique solution $(\vec{X}^n, W^n) \in [S^h_{\text{per}}]^2 \times S^h_{\text{per}}$, $n = 1, \dots, N$, and the following error bounds hold:

$$\begin{aligned} & \sup_{n=0, \dots, N} \left[|\vec{x}^n - \vec{X}^n|_1^2 + |w^n - W^n|_0^2 \right] \\ & + \sum_{n=1}^N \Delta t_n \left[|\vec{x}_t^n - D_t \vec{X}^n|_0^2 + |w^n - W^n|_1^2 \right] \leq C h^2, \end{aligned}$$

where $\vec{x}^n := \vec{x}(\cdot, t_n)$, $w^n := w(\cdot, t_n)$, $\vec{x}_t^n := \vec{x}_t(\cdot, t_n)$, $n = 0, \dots, N$.

Briefly turning our attention to surfaces, the authors of [83] have extended their result of the convergence of the finite element approximation of mean curvature flow for surfaces to a coupled system consisting of the mean curvature of surfaces coupled to a reaction-diffusion equation on the surface in [82].

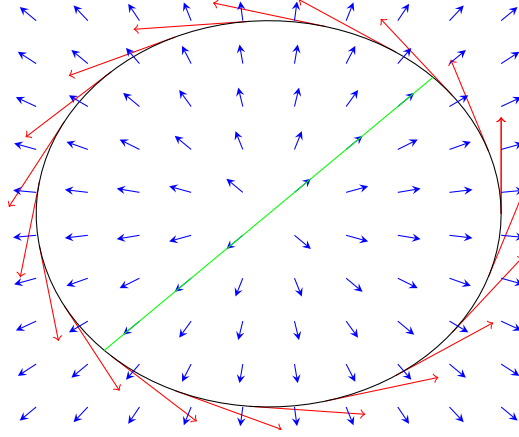


Figure 3.8: Fixed Boundary Motivation. The green line represents \vec{x} , in this instance the line $y = x$, the black line describes F , in this instance the circle $F(\vec{p}) = \sqrt{p_0^2 + p_1^2} - 1$, the blue arrows describe ∇F and the red arrows describe $\nabla^\perp F$ on $\partial\Omega$, where here Ω is the disk of radius 1. Hence, we can see that the blue arrows on the green line and red arrows are orthogonal.

3.3 Finite element analysis of Model \mathcal{M}_1

In this section we look at **Model** \mathcal{M}_1 in more detail. We have supplied Figure 3.8 as motivation for the condition (3.1.1c). To derive the weak form of **Model** \mathcal{M}_1 we multiply (3.1.1a) by $|\vec{x}_\rho|^2$ and a test function $\vec{\xi} \in [H^1(\mathcal{I})]^2$, using integration by parts, we arrive at the form

$$\left(|\vec{x}_\rho|^2 \vec{x}_t, \vec{\xi}\right) + \left(\vec{x}_\rho, \vec{\xi}_\rho\right) = \left[\langle \vec{x}_\rho, \vec{\xi} \rangle\right]_{\rho=0}^{\rho=1}.$$

Since $F \in C^{2,1}(\mathbb{R}^2)$, using a standard basis expansion in \mathbb{R}^2 , we have that

$$\vec{\xi} = \langle \vec{\xi}, \nabla F(\vec{x}) \rangle \nabla F(\vec{x}) + \langle \vec{\xi}, \nabla^\perp F(\vec{x}) \rangle \nabla^\perp F(\vec{x})$$

and, using (3.1.1c), we have

$$\vec{x}_\rho = \langle \vec{x}_\rho, \nabla F(\vec{x}) \rangle \nabla F(\vec{x}).$$

Thus, noting (3.1.1b) and (3.3.4d), we obtain the weak form of (3.1.1a)–(3.1.1c)

$$\left(|\vec{x}_\rho|^2 \vec{x}_t, \vec{\xi}\right) + \left(\vec{x}_\rho, \vec{\xi}_\rho\right) = \left[\langle \vec{x}_\rho, \nabla F(\vec{x}) \rangle \langle \vec{\xi}, \nabla F(\vec{x}) \rangle\right]_{\rho=0}^{\rho=1} \quad \forall \vec{\xi} \in [H^1(\mathcal{I})]^2. \quad (3.3.1)$$

Alternatively, one can express the weak form as

$$\left(|\vec{x}_\rho|^2 \vec{x}_t, \vec{\xi}\right) + \left(\vec{x}_\rho, \vec{\xi}_\rho\right) = 0, \quad \forall \vec{\xi} \in [H^1(\mathcal{I})]^2, \quad (3.3.2)$$

with the additional property that $\langle \vec{\xi}(\rho), \nabla F(\vec{x}(\rho, t)) \rangle = 0$ for $\rho \in \{0, 1\}$. Using (3.1.1b), we notice that this property is similar to

$$0 = \frac{d}{dt} F(\vec{x}(\rho, t)) = \langle \vec{x}_t(\rho, t), \nabla F(\vec{x}(\rho, t)) \rangle, \quad \text{for } \rho \in \{0, 1\}. \quad (3.3.3)$$

We pursue the analysis using (3.3.1) since we do not want to restrict the test functions on the boundary. Before introducing the finite element formulation we detail the assumptions we need for the analysis.

Assumptions 3.9.

We assume that there is a unique solution \vec{x} of **Model** \mathcal{M}_1 on the time interval $[0, T]$. Furthermore we assume this unique solution and specified data satisfies

$$\vec{x} \in W^{1,\infty}(0, T; [H^2(\mathcal{I})]^2) \cap W^{2,\infty}(0, T; [L^2(\mathcal{I})]^2), \quad (3.3.4a)$$

$$m \leq |\vec{x}_\rho| \leq M \quad \text{on } [0, 1] \times [0, T], \text{ for some } m, M \in \mathbb{R}_{>0}, \quad (3.3.4b)$$

$$F \in C^{2,1}(\mathbb{R}^2), \quad (3.3.4c)$$

$$|\nabla F(\vec{p})| = 1, \quad \text{for } \vec{p} \in \{\vec{p} \in \mathbb{R}^2 : F(\vec{p}) = 0\}. \quad (3.3.4d)$$

We assign each element $\vec{X}^n \in [S^h]^2$ a piecewise constant discrete unit tangent and normal, denoted respectively by $\vec{\mathcal{T}}^n$ and $\vec{\mathcal{V}}^n$, approximating $\vec{\tau}(\cdot, t^n)$ and $\vec{\nu}(\cdot, t^n)$ respectively, which take the form

$$\vec{\mathcal{T}}^n := \frac{\vec{X}_\rho^n}{|\vec{X}_\rho^n|}, \quad \vec{\mathcal{V}}^n := (\vec{\mathcal{T}}^n)^\perp, \quad \text{on } \sigma_j, j = 1, \dots, J.$$

We are now in a position to introduce the fully discrete finite element form. Setting $\vec{X}^0(\cdot) := I^h \vec{x}^0(\cdot)$ in $[0, 1]$ and given $\vec{X}^{n-1} \in [S^h]^2$, find $\vec{X}^n \in [S^h]^2$ such that for every $\vec{\xi}^h \in [S^h]^2$ we have

$$\left(|\vec{X}_\rho^{n-1}|^2 D_t \vec{X}^n, \vec{\xi}^h \right)^h + \left(\vec{X}_\rho^n, \vec{\xi}_\rho^h \right) = \left[\langle \vec{X}_\rho^n, \nabla F(\vec{X}^n) \rangle \langle \vec{\xi}^h, \nabla F(\vec{X}^n) \rangle \right]_0^1, \quad (3.3.5a)$$

as well as the discrete equivalent of (3.1.1b)

$$F(\vec{X}^n(\rho)) = 0, \quad \text{for } \rho \in \{0, 1\}. \quad (3.3.5b)$$

A consequence of (3.3.5b) is that, in view of (3.3.4d), we have

$$|\nabla F(\vec{X}^n(\rho))| = 1, \quad \text{for } \rho \in \{0, 1\}, \quad (3.3.6)$$

and therefore, by taking $\vec{\xi}^h = \nabla F(\vec{X}_j^n) \chi_j$ in (3.3.5a), for $j = 0, J$, we have

$$\langle D_t \vec{X}^n, \nabla F(\vec{X}^n) \rangle = 0, \quad \text{for } \rho \in \{0, 1\}, \quad (3.3.7)$$

which is the discrete equivalent of (3.3.3). Throughout the remainder of Section 3.3 we make the assumption that a unique solution to (3.3.5a)–(3.3.5b) exists on the bounded time interval $[0, T]$.

Remark 3.10. *Existence of a solution can be proven relatively trivially for (3.3.5a) using standard techniques but with a harsh constraint of $\Delta t_n \leq Ch^{\frac{5}{2}}$. To date we are unable to improve this due to the non-linear boundary conditions; we note this is a similar problem found in [11, Remark 2.4, p. 9].*

Remark 3.11. *We remark that the property (3.3.7) is vital for the analysis, specifically for deriving the bound for T_2 in (3.3.49). Indeed we hoped to generalise (3.3.5a) to use the corresponding α -scheme from the De-Turck trick as in [59]. However this changes (3.3.7) to*

$$\langle D_t \vec{X}^n, \nabla F(\vec{X}^n) \rangle = \frac{\alpha - 1}{\alpha} \langle D_t \vec{X}^n, \vec{\mathcal{V}}^{n-1} \rangle \langle \vec{\mathcal{V}}^{n-1}, \nabla F(\vec{X}^n) \rangle, \quad \text{for } \rho \in \{0, 1\}.$$

In the continuous and semi-discrete setting, the equivalents of $\langle \vec{\mathcal{V}}^{n-1}, \nabla F(\vec{X}^n) \rangle$ are zero due to (3.1.1c); however, in the fully discrete setting, (3.1.1c) is in fact approximated, see [42, Remark 3.2, p. 642]. In order to bound this new term using the current techniques we would require a bound of the form $|D_t \vec{X}^n|_{0, \infty} \leq C$. A similar problem occurs in the case of forced curve shortening flow.

3.3.1 Stability bounds for Model \mathcal{M}_1

In this section we prove stability bounds for **Model \mathcal{M}_1** . Indeed, we look to prove the following lemma.

Lemma 3.12.

Let $h \in (0, h^*]$. Assuming h^* is chosen appropriately so that $0 < c_m \leq |\vec{X}_\rho^{n-1}|$, for all $n - 1 = 0, \dots, N - 1$, then we have

$$\max_{n=1, \dots, N} |\vec{X}^n|_1^2 + \sum_{n=1}^N \left[|\vec{X}^n - \vec{X}^{n-1}|_1^2 \right] + 2c_m^2 \sum_{n=1}^N \Delta t_n |D_t \vec{X}^n|_0^2 \leq |\vec{X}^0|_1^2.$$

Proof: Setting $\xi^h = D_t \vec{X}^n$ in (3.3.5a), and noting (3.3.7), gives

$$\left(|\vec{X}_\rho^{n-1}|^2 D_t \vec{X}^n, D_t \vec{X}^n \right)^h + (\vec{X}_\rho^n, D_t \vec{X}_\rho^n) = \left[\langle \vec{X}_\rho^n, \nabla F(\vec{X}^n) \rangle \langle D_t \vec{X}^n, \nabla F(\vec{X}^n) \rangle \right]_0^1 = 0.$$

Using a simple calculation, we can see that

$$2\Delta t_n (\vec{X}_\rho^n, D_t \vec{X}_\rho^n) = |\vec{X}^n|_1^2 + |\vec{X}^n - \vec{X}^{n-1}|_1^2 - |\vec{X}^{n-1}|_1^2, \quad (3.3.8)$$

and hence, using (3.1.6a), we have

$$\frac{1}{2}|\vec{X}^n|_1^2 + \frac{1}{2}|\vec{X}^n - \vec{X}^{n-1}|_1^2 + c_m^2 \Delta t_n |D_t \vec{X}^n|_0^2 \leq \frac{1}{2}|\vec{X}^{n-1}|_1^2.$$

The bound follows by summing from $n = 1, \dots, N$. \square

3.3.2 H^1 error bounds for Model \mathcal{M}_1

In this section we prove optimal H^1 error bounds for **Model \mathcal{M}_1** . Indeed, we look to prove the following theorem.

Theorem 3.13.

Let $\vec{X}^0 = I^h \vec{x}^0 \in [S^h]^2$. There exists $h^* > 0$ and $\Delta t^* > 0$ such that for all $h \in (0, h^*]$ and $\Delta t \in (0, \Delta t^*]$, with $\Delta t \leq Ch^2$, the fully-discrete problem (3.3.5a)–(3.3.5b) has the following error bound

$$\sup_{n=0, \dots, N} |\vec{x}^n - \vec{X}^n|_1^2 + \sum_{n=1}^N \Delta t_n |\vec{x}_t^n - D_t \vec{X}^n|_0^2 \leq Ch^2,$$

for some $C > 0$ independent of h and Δt .

The proof of this theorem combines some of the techniques presented in [6] with a fully discrete version of the analysis presented in [42]. Before we begin the proof of the Theorem 3.13 we introduce some notation and the induction hypothesis that underpins the proof.

We define

$$\vec{x}^n - \vec{X}^n = (\vec{x}^n - I^h \vec{x}^n) + (I^h \vec{x}^n - \vec{X}^n) =: (I - I^h) \vec{x}^n + \vec{E}^n,$$

and assume for $n - 1 \in \{1, \dots, N - 1\}$ that

$$\sup_{m=1, \dots, n-1} e^{-\mu t_m} |\vec{E}^m|_1^2 + \sum_{m=1}^{n-1} \Delta t_m e^{-\mu t_m} |D_t \vec{E}^m|_0^2 \leq C_1 h^2 \quad \text{for } h \in (0, h^*]. \quad (3.3.9)$$

In order for the inductive proof to work the parameters need to be chosen carefully so that there are no hidden relations. For example, if C_1 depended on n , then as N became large, the error bound in (3.3.9) would also become large defeating the point of the actual bound. First, it is assumed that h^* and Δt^* can be chosen appropriately small enough independently of n , for the bounds in (3.3.10) and (3.3.55) respectively, which put inherent bounds on h and Δt . We first choose μ independent of n , h and Δt , which depends only on Δt^* , bounds on the true solution \vec{x} and the function F , inverse estimates and interpolation results, and T . We then find C_1 independent of n , h and Δt , which depends only on μ ,

Grönwall's inequality, and the aforementioned bounds and results. With the appropriate bound on h^* , this then finishes the proof.

The main part of the proof of Theorem 3.13 is split into the following two lemmas:

Lemma 3.14.

Let $h \in (0, h^*]$. Then we have

$$\begin{aligned} & \frac{1}{2} |\vec{E}^n|_1^2 + \frac{1}{4} |\vec{E}^n - \vec{E}^{n-1}|_1^2 + \Delta t_n \left(\frac{m^2}{8} - C \Delta t_n \right) |D_t \vec{E}^n|_0^2 \\ & \leq \frac{1}{2} |\vec{E}^{n-1}|_1^2 + \frac{\Delta t_n}{2} D_t \left[\langle \vec{x}_\rho^n, \nabla F(\vec{x}^n) \rangle \langle \vec{E}^n, D^2 F(\vec{x}^n) \vec{E}^n \rangle \right]_0^1 \\ & \quad + C \Delta t_n \left[h^2 + \Delta t_n + |\vec{E}^{n-1}|_0^2 + |\vec{E}^n|_0^2 + |\vec{E}^{n-1}|_1^2 + |\vec{E}^n|_1^2 + h^{-1} |\vec{E}^{n-1}|_{0,\infty}^4 \right]. \end{aligned}$$

Lemma 3.15.

Let $h \in (0, h^*]$ and $\Delta t \in (0, \Delta t^*]$. Then for small enough h^* and Δt^* , with

$$\mu \Delta t^* \leq \frac{1}{2}, \quad \text{and} \quad \mu \geq \max \left\{ \frac{14 C_\star}{m^2}, 1 \right\}, \quad (3.3.10)$$

where C_\star is the constant in (3.3.53), we have

$$\sup_{m=1,\dots,n} e^{-\mu t_m} |\vec{E}^m|_1^2 + \sum_{m=1}^n \Delta t_m e^{-\mu t_m} |D_t \vec{E}^m|_0^2 \leq C_1 h^2.$$

Before proving Lemmas 3.14 and 3.15 and subsequently Theorem 3.13 we note some useful results. Using (3.1.5a), (3.1.5d), (3.1.4a), (3.3.4a) and (3.3.9) we have that

$$\begin{aligned} |\vec{x}^{n-1} - \vec{X}^{n-1}|_{1,\infty} & \leq |(I - I^h) \vec{x}^{n-1}|_{1,\infty} + |\vec{E}^{n-1}|_{1,\infty} \\ & \leq C h^{\frac{1}{2}} |\vec{x}^{n-1}|_2 + C h^{-\frac{1}{2}} |\vec{E}^{n-1}|_1 \\ & \leq C h^{\frac{1}{2}} \left(\|\vec{x}\|_{W^{0,\infty}(0,T;[H^2(X)]^2)} + e^{\frac{\mu}{2} t_{n-1}} \right) \leq \frac{m}{2}, \end{aligned}$$

provided h^* is chosen small enough. Thus we have

$$|\vec{X}_\rho^{n-1}| \leq |\vec{x}_\rho^{n-1} - \vec{X}_\rho^{n-1}| + |\vec{x}_\rho^{n-1}| \leq M + \frac{m}{2} \leq 2M,$$

and

$$|\vec{X}_\rho^{n-1}| \geq |\vec{x}_\rho^{n-1}| - |\vec{x}_\rho^{n-1} - \vec{X}_\rho^{n-1}| \geq m - \frac{m}{2} \geq \frac{m}{2},$$

which combine to give

$$0 < \frac{m}{2} \leq |\vec{X}_\rho^{n-1}| \leq 2M. \quad (3.3.11)$$

From (3.1.5b) and (3.3.4a), we see that

$$|\vec{x}^{n-1} - \vec{X}^{n-1}|_1 \leq |(I - I^h) \vec{x}^{n-1}|_1 + |\vec{E}^{n-1}|_1$$

$$\begin{aligned}
&\leq C h |\bar{x}^{n-1}|_2 + |\bar{E}^{n-1}|_1 \\
&\leq C h \|\bar{x}\|_{W^{0,\infty}(0,T;[H^2(\mathcal{I})]^2)} + |\bar{E}^{n-1}|_1 \leq C \left[h + |\bar{E}^{n-1}|_1 \right], \quad (3.3.12)
\end{aligned}$$

and, with (3.3.12),

$$\begin{aligned}
|\bar{x}^n - \bar{X}^{n-1}|_1 &\leq |\bar{x}^n - \bar{x}^{n-1}|_1 + |\bar{x}^{n-1} - \bar{X}^{n-1}|_1 \\
&\leq \Delta t_n |D_t \bar{x}^n|_1 + C \left[h + |\bar{E}^{n-1}|_1 \right] \\
&\leq \Delta t_n \|\bar{x}\|_{W^{1,\infty}(0,T;[H^1(\mathcal{I})]^2)} + C \left[h + |\bar{E}^{n-1}|_1 \right] \\
&\leq C \left[h + \Delta t_n + |\bar{E}^{n-1}|_1 \right]. \quad (3.3.13)
\end{aligned}$$

Using (3.3.11), (3.3.4b) and (3.3.12), we see that

$$\begin{aligned}
\left| \frac{1}{|\bar{x}_\rho^{n-1}|} - \frac{1}{|\bar{X}_\rho^{n-1}|} \right|_0 &= \left| \frac{|\bar{x}_\rho^{n-1}| - |\bar{X}_\rho^{n-1}|}{|\bar{x}_\rho^{n-1}| |\bar{X}_\rho^{n-1}|} \right|_0 \\
&\leq \frac{2}{m^2} |\bar{x}^{n-1} - \bar{X}^{n-1}|_1 \leq C \left[h + |\bar{E}^{n-1}|_1 \right], \quad (3.3.14)
\end{aligned}$$

and

$$\begin{aligned}
|\bar{\tau}^{n-1} - \bar{\mathcal{T}}^{n-1}|_0 &\leq \left| \frac{1}{|\bar{x}_\rho^{n-1}|} (\bar{x}_\rho^{n-1} - \bar{X}_\rho^{n-1}) \right|_0 + \left| \bar{X}_\rho^{n-1} \left(\frac{1}{|\bar{x}_\rho^{n-1}|} - \frac{1}{|\bar{X}_\rho^{n-1}|} \right) \right|_0 \\
&\leq \frac{1}{m} |\bar{x}^{n-1} - \bar{X}^{n-1}|_1 + \left| \frac{\bar{X}_\rho^{n-1} (\bar{X}_\rho^{n-1} - \bar{x}_\rho^{n-1})}{|\bar{x}_\rho^{n-1}| |\bar{X}_\rho^{n-1}|} \right|_0 \\
&\leq \frac{2}{m} |\bar{x}^{n-1} - \bar{X}^{n-1}|_1 \leq C \left[h + |\bar{E}^{n-1}|_1 \right],
\end{aligned}$$

which gives

$$|\bar{\tau}^{n-1} - \bar{\mathcal{T}}^{n-1}|_0 + |\bar{\nu}^{n-1} - \bar{\mathcal{V}}^{n-1}|_0 \leq C \left[h + |\bar{E}^{n-1}|_1 \right]. \quad (3.3.15)$$

A Taylor's expansion together with (3.3.4a) yields

$$|D_t \bar{x}^n - \bar{x}_t^n|_0 \leq \Delta t_n \sup_{s \in [t_{n-1}, t_n]} |\bar{x}_{tt}(\cdot, s)|_0 \leq \Delta t_n \|\bar{x}\|_{W^{2,\infty}(0,T;[L^2(\mathcal{I})]^2)} \leq C \Delta t_n, \quad (3.3.16)$$

and, using (3.3.4d), (3.1.11) and (3.3.4a), for $\rho \in \{0, 1\}$, we have

$$\begin{aligned}
&\frac{1}{\Delta t_n} \int_{t_{n-1}}^{t_n} \langle x_{tt}(\rho, s), \nabla F(\bar{x}(\rho, s)) \rangle (t_{n-1} - s) ds \\
&\leq \frac{1}{\Delta t_n} \left(\int_{t_{n-1}}^{t_n} |\langle x_{tt}(\rho, s), \nabla F(\bar{x}(\rho, s)) \rangle|^2 ds \right)^{\frac{1}{2}} \left(\int_{t_{n-1}}^{t_n} (t_{n-1} - s)^2 ds \right)^{\frac{1}{2}} \\
&\leq \left(\Delta t_n \int_{t_{n-1}}^{t_n} |\bar{x}_{tt}(\rho, s)|^2 ds \right)^{\frac{1}{2}} \\
&\leq \left(\Delta t_n \int_{t_{n-1}}^{t_n} |\bar{x}_{tt}(\cdot, s)|_{0,\infty}^2 ds \right)^{\frac{1}{2}} \leq C \Delta t_n \|\bar{x}\|_{W^{2,\infty}(0,T;[H^1(\mathcal{I})]^2)} \leq C \Delta t_n. \quad (3.3.17)
\end{aligned}$$

Using [B.4.1](#) and the inductive hypothesis [\(3.3.9\)](#), for $\mu > 0$, we have that

$$|\vec{E}^{n-1}|_0^2 e^{-\mu t_{n-1}} \leq \sum_{m=1}^{n-1} \left(\mu(\Delta t_m)^2 + \frac{4}{\mu} \right) \Delta t_m e^{-\mu t_m} |D_t \vec{E}^m|_0^2 \leq C_1 \left(\mu(\Delta t)^2 + \frac{4}{\mu} \right) h^2,$$

and so, using [\(3.1.9b\)](#) and choosing $\varepsilon = 1$, we see that

$$\begin{aligned} |\vec{E}^{n-1}|_{0,\infty}^2 e^{-\mu t_{n-1}} &\leq \varepsilon |\vec{E}^{n-1}|_1^2 e^{-\mu t_{n-1}} + C(\varepsilon) |\vec{E}^{n-1}|_0^2 e^{-\mu t_{n-1}} \\ &\leq C C_1 \left(1 + \mu(\Delta t)^2 + \frac{4}{\mu} \right) h^2. \end{aligned} \quad (3.3.18)$$

Proof of Lemma 3.14: Taking $\vec{\xi} = \vec{\xi}^h$ in [\(3.3.1\)](#) and subtracting the resulting equation from [\(3.3.5a\)](#) we have

$$\begin{aligned} &\left[\left(|\vec{x}_\rho^n|^2 \vec{x}_t^n, \vec{\xi}^h \right) - \left(|\vec{X}_\rho^{n-1}|^2 D_t \vec{X}^n, \vec{\xi}^h \right)^h \right] + \left[\left(\vec{x}_\rho^n, \vec{\xi}_\rho^h \right) - \left(\vec{X}_\rho^n, \vec{\xi}_\rho^h \right) \right] \\ &= \left[\langle \vec{x}_\rho^n, \nabla F(\vec{x}^n) \rangle \langle \vec{\xi}^h, \nabla F(\vec{x}^n) \rangle - \langle \vec{X}_\rho^n, \nabla F(\vec{X}^n) \rangle \langle \vec{\xi}^h, \nabla F(\vec{X}^n) \rangle \right]_0^1. \end{aligned} \quad (3.3.19)$$

First we note that, since $\vec{\xi}^h \in [S^h]^2$, we have that $\vec{\xi}_\rho^h$ is constant on each interval σ_j , and so, by the fundamental theorem of calculus and [\(3.1.3\)](#), we have

$$\left(\vec{x}_\rho^n - I^h \vec{x}_\rho^n, \vec{\xi}_\rho^h \right) = \sum_{j=1}^J \int_{\sigma_j} \langle \vec{x}_\rho^n - I_j^h \vec{x}_\rho^n, \vec{\xi}_\rho^h \rangle d\rho = \sum_{j=1}^J \left[\langle \vec{x}_\rho^n - I_j^h \vec{x}_\rho^n, \vec{\xi}_\rho^h \rangle \right]_{\rho_{j-1}}^{\rho_j} = 0. \quad (3.3.20)$$

Hence, setting $\vec{\xi}^h = \Delta t_n D_t \vec{E}^n$ in [\(3.3.19\)](#), we see that

$$\begin{aligned} &\Delta t_n \left(|\vec{X}_\rho^{n-1}|^2 D_t \vec{E}^n, D_t \vec{E}^n \right)^h + \Delta t_n \left(\vec{E}_\rho^n, D_t \vec{E}_\rho^n \right) \\ &= \Delta t_n \left[\left(|\vec{X}_\rho^{n-1}|^2 D_t [I^h \vec{x}^n], D_t \vec{E}^n \right)^h - \left(|\vec{x}_\rho^n|^2 \vec{x}_t^n, D_t \vec{E}^n \right) \right] \\ &\quad + \Delta t_n \left[\langle \vec{x}_\rho^n, \nabla F(\vec{x}^n) \rangle \langle D_t \vec{E}^n, \nabla F(\vec{x}^n) \rangle - \langle \vec{X}_\rho^n, \nabla F(\vec{X}^n) \rangle \langle D_t \vec{E}^n, \nabla F(\vec{X}^n) \rangle \right]_0^1 \\ &=: \Delta t_n (S_1 + S_2). \end{aligned} \quad (3.3.21)$$

It is easy to see that, using [\(3.3.11\)](#) and [\(3.1.6a\)](#), we have

$$\left(|\vec{X}_\rho^{n-1}|^2 D_t \vec{E}^n, D_t \vec{E}^n \right)^h \geq \frac{m^2}{4} |D_t \vec{E}^n|_0^2.$$

Hence, noting [\(3.3.8\)](#), we have

$$\begin{aligned} &\Delta t_n \left(|\vec{X}_\rho^{n-1}|^2 D_t \vec{E}^n, D_t \vec{E}^n \right)^h + \Delta t_n \left(\vec{E}_\rho^n, D_t \vec{E}_\rho^n \right) \\ &\geq \Delta t_n \frac{m^2}{4} |D_t \vec{E}^n|_0^2 + \frac{1}{2} \left[|\vec{E}^n|_1^2 + |\vec{E}^n - \vec{E}^{n-1}|_1^2 - |\vec{E}^{n-1}|_1^2 \right]. \end{aligned} \quad (3.3.22)$$

We now bound S_1 and S_2 in [\(3.3.21\)](#). We begin with S_1 in which we closely follow some of the techniques presented in [\[6\]](#).

$$S_1 = \left[\left(|\vec{X}_\rho^{n-1}|^2 D_t [I^h \vec{x}^n], D_t \vec{E}^n \right)^h - \left(|\vec{x}_\rho^n|^2 \vec{x}_t^n, D_t \vec{E}^n \right) \right]$$

$$\begin{aligned}
&= \left(\left[|\vec{X}_\rho^{n-1}|^2 - |\vec{x}_\rho^n|^2 \right] \vec{x}_t^n, D_t \vec{E}^n \right) + \left(|\vec{X}_\rho^{n-1}|^2 \left[D_t [I^h \vec{x}^n] - \vec{x}_t^n \right], D_t \vec{E}^n \right) \\
&\quad + \left[\left(|\vec{X}_\rho^{n-1}|^2 D_t [I^h \vec{x}^n], D_t \vec{E}^n \right)^h - \left(|\vec{X}_\rho^{n-1}|^2 D_t [I^h \vec{x}^n], D_t \vec{E}^n \right) \right] =: \sum_{i=1}^3 S_{1,i}. \quad (3.3.23)
\end{aligned}$$

Using (3.3.11), (3.3.4b), (3.1.11), (3.3.13) and (3.3.4a), we see that

$$\begin{aligned}
S_{1,1} &= \left(\left[|\vec{X}_\rho^{n-1}|^2 - |\vec{x}_\rho^n|^2 \right] \vec{x}_t^n, D_t \vec{E}^n \right) \\
&\leq |\vec{x}_t^n|_{0,\infty} \left[|\vec{X}_\rho^{n-1}| + |\vec{x}_\rho^n| \right]_{0,\infty} |\vec{x}^n - \vec{X}^{n-1}|_1 |D_t \vec{E}^n|_0 \\
&\leq C \|\vec{x}\|_{W^{1,\infty}(0,T;[H^1(\mathcal{I})]^2)} |\vec{x}^n - \vec{X}^{n-1}|_1 |D_t \vec{E}^n|_0 \\
&\leq C \left[h + \Delta t_n + |\vec{E}^{n-1}|_1 \right] |D_t \vec{E}^n|_0. \quad (3.3.24)
\end{aligned}$$

From (3.3.11), (3.1.5b), (3.3.13), (3.3.16) and (3.3.4a), we have

$$\begin{aligned}
S_{1,2} &= \left(|\vec{X}_\rho^{n-1}|^2 \left[D_t [I^h \vec{x}^n] - \vec{x}_t^n \right], D_t \vec{E}^n \right) \\
&\leq 4M^2 |D_t [I^h \vec{x}^n] - \vec{x}_t^n|_0 |D_t \vec{E}^n|_0 \\
&\leq 4M^2 \left[|(I - I^h) D_t \vec{x}^n|_0 + |D_t \vec{x}^n - \vec{x}_t^n|_0 \right] |D_t \vec{E}^n|_0 \\
&\leq C [h |D_t \vec{x}^n|_1 + \Delta t_n] |D_t \vec{E}^n|_0 \\
&\leq C [h \|\vec{x}\|_{W^{1,\infty}(0,T;[H^1(\mathcal{I})]^2)} + \Delta t_n] |D_t \vec{E}^n|_0 \leq C [h + \Delta t_n] |D_t \vec{E}^n|_0. \quad (3.3.25)
\end{aligned}$$

Using (3.1.6b), (3.3.11), (3.1.5d) and (3.3.4a), we see that

$$\begin{aligned}
S_{1,3} &= \left(|\vec{X}_\rho^{n-1}|^2 D_t [I^h \vec{x}^n], D_t \vec{E}^n \right)^h - \left(|\vec{X}_\rho^{n-1}|^2 D_t [I^h \vec{x}^n], D_t \vec{E}^n \right) \\
&\leq C h \sum_{j=1}^J |D_t [I^h \vec{x}^n]|_{1,\sigma_j} \|\vec{X}_\rho^{n-1}\|^2 |D_t \vec{E}^n|_{0,\sigma_j} \\
&\leq C h |D_t \vec{x}^n|_1 |D_t \vec{E}^n|_0 \leq C h \|\vec{x}\|_{W^{1,\infty}(0,T;[H^1(\mathcal{I})]^2)} |D_t \vec{E}^n|_0 \leq C h |D_t \vec{E}^n|_0, \quad (3.3.26)
\end{aligned}$$

where $|\eta|_{1,\sigma_j}$ is the seminorm of the space $H^1(\sigma_j)$. Combining (3.3.23)–(3.3.26) and using (3.1.8), we have

$$|S_1| \leq \frac{m^2}{16} |D_t \vec{E}^n|_0^2 + C \left[h^2 + (\Delta t_n)^2 + |\vec{E}^{n-1}|_1^2 \right]. \quad (3.3.27)$$

To bound S_2 we present a fully discrete version of the techniques presented in [42] for a semi-discrete approximation. To this end we set

$$b^n := \langle \vec{x}_\rho^n, \nabla F(\vec{x}^n) \rangle \quad \text{and} \quad b_h^n := \langle \vec{X}_\rho^n, \nabla F(\vec{X}^n) \rangle. \quad (3.3.28)$$

Using (3.3.7) and (3.1.7), we have

$$\begin{aligned}
S_2 &= \left[\langle \vec{x}_\rho^n, \nabla F(\vec{x}^n) \rangle \langle D_t \vec{E}^n, \nabla F(\vec{x}^n) \rangle - \langle \vec{X}_\rho^n, \nabla F(\vec{X}^n) \rangle \langle D_t \vec{E}^n, \nabla F(\vec{X}^n) \rangle \right]_0^1 \\
&= \left[b^n \langle D_t \vec{E}^n, \nabla F(\vec{x}^n) - \nabla F(\vec{X}^n) \rangle \right]_0^1 + \left[(b^n - b_h^n) \langle D_t \vec{x}^n, \nabla F(\vec{X}^n) - \nabla F(\vec{x}^n) \rangle \right]_0^1
\end{aligned}$$

$$+ \left[(b^n - b_h^n) \langle D_t \bar{x}^n, \nabla F(\bar{x}^n) \rangle \right]_0^1 =: \sum_{i=1}^3 S_{2,i}. \quad (3.3.29)$$

We now note some not so obvious stability bounds useful for the analysis. Using (3.3.4a)–(3.3.4d), and noting (3.1.7), for $\rho \in \{0, 1\}$, we have

$$|b^n(\rho)| \leq M, \quad (3.3.30a)$$

$$|D_t[\nabla F(\bar{x}^n(\rho))]| \leq L_{\nabla F} |D_t \bar{x}^n(\rho)| \leq C \|\bar{x}\|_{W^{1,\infty}(0,T;[H^1(\mathcal{I})]^2)} \leq C, \quad (3.3.30b)$$

$$|D_t[D^2 F(\bar{x}^n(\rho))]| \leq L_{D^2 F} |D_t \bar{x}^n(\rho)| \leq C \|\bar{x}\|_{W^{1,\infty}(0,T;[H^1(\mathcal{I})]^2)} \leq C. \quad (3.3.30c)$$

With the addition of (3.1.7) we have

$$\begin{aligned} |D_t[\nabla F(\bar{X}^n(\rho))]| &\leq L_{\nabla F} |D_t \bar{X}^n(\rho)| \\ &\leq C \left[\|\bar{x}\|_{W^{1,\infty}(0,T;[H^1(\mathcal{I})]^2)} + |D_t \bar{E}^n|_{0,\infty} \right] \\ &\leq C \left[1 + |D_t \bar{E}^n|_{0,\infty} \right], \end{aligned} \quad (3.3.30d)$$

as well as

$$|\nabla F(\bar{x}^n(\rho)) - \nabla F(\bar{X}^n(\rho))| \leq L_{\nabla F} |\bar{x}^n(\rho) - \bar{X}^n(\rho)| \leq C |\bar{E}^n|_{0,\infty}. \quad (3.3.30e)$$

Moreover we have

$$\begin{aligned} |D_t b^n(\rho)| &= \frac{1}{\Delta t_n} |\langle \bar{x}_\rho^n(\rho), \nabla F(\bar{x}^n(\rho)) \rangle - \langle \bar{x}_\rho^{n-1}(\rho), \nabla F(\bar{x}^{n-1}(\rho)) \rangle| \\ &\leq |\langle D_t \bar{x}_\rho^n(\rho), \nabla F(\bar{x}^n(\rho)) \rangle| + |\langle \bar{x}_\rho^{n-1}(\rho), D_t[\nabla F(\bar{x}^n(\rho))] \rangle| \\ &\leq C \|\bar{x}\|_{W^{1,\infty}(0,T;[H^2(\mathcal{I})]^2)} + M |D_t[\nabla F(\bar{x}^n(\rho))]| \leq C. \end{aligned} \quad (3.3.30f)$$

We now bound $S_{2,i}$, $i = 1, 2, 3$. First, we split up $S_{2,1}$ such that

$$\begin{aligned} S_{2,1} &= \left[b^n \langle D_t \bar{E}^n, \nabla F(\bar{x}^n) - \nabla F(\bar{X}^n) \rangle \right]_0^1 \\ &= \left[b^n \langle D_t \bar{E}^n, \nabla F(\bar{x}^n) - \nabla F(\bar{x}^{n-1}) \rangle \right]_0^1 + \left[b^n \langle D_t \bar{E}^n, \nabla F(\bar{X}^{n-1}) - \nabla F(\bar{X}^n) \rangle \right]_0^1 \\ &\quad + \left[b^n \langle D_t \bar{E}^n, \nabla F(\bar{x}^{n-1}) - \nabla F(\bar{X}^{n-1}) \rangle \right]_0^1 =: \sum_{i=1}^3 S_{2,1,i}. \end{aligned} \quad (3.3.31)$$

Using (3.3.30a) and (3.3.30b), we have

$$|S_{2,1,1}| = \left| \left[b^n \langle D_t \bar{E}^n, \nabla F(\bar{x}^n) - \nabla F(\bar{x}^{n-1}) \rangle \right]_0^1 \right| \leq C \Delta t_n |D_t \bar{E}^n|_{0,\infty}. \quad (3.3.32)$$

Similarly, using (3.3.30d), we have

$$\begin{aligned} |S_{2,1,2}| &= \left| \left[b^n \langle D_t \bar{E}^n, \nabla F(\bar{X}^{n-1}) - \nabla F(\bar{X}^n) \rangle \right]_0^1 \right| \\ &\leq C \Delta t_n |D_t \bar{E}^n|_{0,\infty} \left[1 + |D_t \bar{E}^n|_{0,\infty} \right]. \end{aligned} \quad (3.3.33)$$

Using (3.1.13), (3.1.7), (3.3.4c), (3.3.30f), (3.3.30c), (3.1.5a), (3.1.4a) and noting

$$\begin{aligned}
D_t \left[b^n \langle \vec{E}^n, D^2 F(\vec{x}^n) \vec{E}^n \rangle \right] &= \frac{1}{\Delta t_n} \left[b^n \langle \vec{E}^n, D^2 F(\vec{x}^n) \vec{E}^n \rangle - b^{n-1} \langle \vec{E}^{n-1}, D^2 F(\vec{x}^{n-1}) \vec{E}^{n-1} \rangle \right] \\
&= \Delta t_n b^n \langle D_t \vec{E}^n, D^2 F(\vec{x}^{n-1}) D_t \vec{E}^n \rangle \\
&\quad + 2 b^n \langle D_t \vec{E}^n, D^2 F(\vec{x}^{n-1}) \vec{E}^{n-1} \rangle \\
&\quad + b^n \langle E^n, D_t [D^2 F(\vec{x}^n)] E^n \rangle \\
&\quad + D_t [b^n] \langle \vec{E}^{n-1}, D^2 F(\vec{x}^{n-1}) \vec{E}^{n-1} \rangle,
\end{aligned}$$

we have

$$\begin{aligned}
S_{2,1,3} &= \left[b^n \langle D_t \vec{E}^n, \nabla F(\vec{x}^{n-1}) - \nabla F(\vec{X}^{n-1}) \rangle \right]_0^1 \\
&= \left[b^n \langle D_t E^n, D^2 F(\vec{x}^{n-1}) \vec{E}^{n-1} \rangle \right. \\
&\quad \left. + b^n \int_0^1 \langle D_t \vec{E}^n, (D^2 F(s\vec{x}^{n-1} + (1-s)\vec{X}^{n-1}) - D^2 F(\vec{x}^{n-1})) \vec{E}^{n-1} \rangle ds \right]_0^1 \\
&= \left[\frac{1}{2} D_t \left[b^n \langle \vec{E}^n, D^2 F(\vec{x}^n) \vec{E}^n \rangle \right] - \frac{1}{2} D_t [b^n] \langle \vec{E}^{n-1}, D^2 F(\vec{x}^{n-1}) \vec{E}^{n-1} \rangle \right. \\
&\quad \left. - \frac{1}{2} b^n \langle \vec{E}^n, D_t [D^2 F(\vec{x}^n)] \vec{E}^n \rangle - \frac{1}{2} \Delta t_n b^n \langle D_t \vec{E}^n, D^2 F(\vec{x}^{n-1}) D_t \vec{E}^n \rangle \right. \\
&\quad \left. + b^n \int_0^1 \langle D_t \vec{E}^n, (D^2 F(s\vec{x}^{n-1} + (1-s)\vec{X}^{n-1}) - D^2 F(\vec{x}^{n-1})) \vec{E}^{n-1} \rangle ds \right]_0^1 \\
&\leq \frac{1}{2} D_t \left[b^n \langle \vec{E}^n, D^2 F(\vec{x}^n) \vec{E}^n \rangle \right]_0^1 \\
&\quad + C \left[|\vec{E}^{n-1}|_{0,\infty}^2 + |\vec{E}^n|_{0,\infty}^2 + \Delta t_n |D_t \vec{E}^n|_{0,\infty}^2 \right] \\
&\quad + C |D_t \vec{E}^n|_{0,\infty} |\vec{E}^{n-1}|_{0,\infty}^2 \int_0^1 |s-1| ds \\
&\leq \frac{1}{2} D_t \left[b^n \langle \vec{E}^n, D^2 F(\vec{x}^n) \vec{E}^n \rangle \right]_0^1 \\
&\quad + C \left[\left(1 + h^{-\frac{1}{2}} |D_t \vec{E}^n|_0 \right) |\vec{E}^{n-1}|_{0,\infty}^2 + |\vec{E}^n|_{0,\infty}^2 + \Delta t_n |D_t \vec{E}^n|_{0,\infty}^2 \right]. \tag{3.3.34}
\end{aligned}$$

Combining (3.3.31) with (3.3.32)–(3.3.34), and using (3.1.9b) and (3.1.8), we have

$$\begin{aligned}
|S_{2,1}| &\leq \frac{1}{2} D_t \left[b^n \langle \vec{E}^n, D^2 F(\vec{x}^n) \vec{E}^n \rangle \right]_0^1 \\
&\quad + C \left[\left(1 + h^{-\frac{1}{2}} |D_t \vec{E}^n|_0 \right) |\vec{E}^{n-1}|_{0,\infty}^2 + |\vec{E}^n|_{0,\infty}^2 + \Delta t_n \left(1 + |D_t \vec{E}^n|_{0,\infty}\right) |D_t \vec{E}^n|_{0,\infty} \right] \\
&\leq \frac{1}{2} D_t \left[b^n \langle \vec{E}^n, D^2 F(\vec{x}^n) \vec{E}^n \rangle \right]_0^1 + \frac{1}{4\Delta t_n} |\vec{E}^n - \vec{E}^{n-1}|_1^2 + \frac{m^2}{24} |D_t \vec{E}^n|_0^2 \\
&\quad + C \left[\Delta t_n + |\vec{E}^{n-1}|_{0,\infty}^2 + |\vec{E}^n|_{0,\infty}^2 + \Delta t_n |D_t \vec{E}^n|_0^2 + h^{-1} |\vec{E}^{n-1}|_{0,\infty}^4 \right]. \tag{3.3.35}
\end{aligned}$$

Taking $\vec{\xi} = (1 - \rho) \nabla F(\vec{x}^n(0))$ in (3.3.1), and noting (3.3.4d), we see that

$$\begin{aligned}
&(|\vec{x}_\rho^n|^2 \vec{x}_t^n, (1 - \rho) \nabla F(\vec{x}^n(0))) - (\vec{x}_\rho^n, \nabla F(\vec{x}^n(0))) \\
&= \left[\langle \vec{x}_\rho^n, \nabla F(\vec{x}^n) \rangle \langle (1 - \rho) \nabla F(\vec{x}^n(0)), \nabla F(\vec{x}^n) \rangle \right]_0^1 = -b^n(0).
\end{aligned}$$

Hence,

$$b^n(0) = (\vec{x}_\rho^n, \nabla F(\vec{x}^n(0))) - (|\vec{x}_\rho^n|^2 \vec{x}_t^n, (1-\rho)\nabla F(\vec{x}^n(0))). \quad (3.3.36)$$

Similarly, taking $\xi^h = (1-\rho)\nabla F(\vec{X}^n(0))$ in (3.3.5a), noting (3.3.6), we have

$$b_h^n(0) = (\vec{X}_\rho^n, \nabla F(\vec{X}^n(0))) - (|\vec{X}_\rho^{n-1}|^2 D_t \vec{X}^n, (1-\rho)\nabla F(\vec{X}^n(0)))^h. \quad (3.3.37)$$

Denoting $\vec{x}^n(0)$ by \vec{x}_0^n and $\vec{X}^n(0)$ by \vec{X}_0^n , subtracting (3.3.37) from (3.3.36), we have

$$\begin{aligned} b^n(0) - b_h^n(0) &= [(\vec{x}_\rho^n, \nabla F(\vec{x}_0^n)) - (\vec{X}_\rho^n, \nabla F(\vec{X}_0^n))] \\ &\quad + \left[(|\vec{X}_\rho^{n-1}|^2 D_t \vec{X}^n, (1-\rho)\nabla F(\vec{X}_0^n))^h - (|\vec{x}_\rho^n|^2 \vec{x}_t^n, (1-\rho)\nabla F(\vec{x}_0^n)) \right] \\ &=: A_1 + A_2. \end{aligned} \quad (3.3.38)$$

We first bound A_1 . Using (3.3.20), (3.3.4b), (3.3.30e) and (3.3.6), we have

$$\begin{aligned} A_1 &= (\vec{x}_\rho^n, \nabla F(\vec{x}_0^n)) - (\vec{X}_\rho^n, \nabla F(\vec{X}_0^n)) \\ &= (\vec{x}_\rho^n, \nabla F(\vec{x}_0^n) - \nabla F(\vec{X}_0^n)) + (\vec{E}_\rho^n, \nabla F(\vec{X}_0^n)) \\ &\leq ML_{\nabla F} |\vec{E}_0^n|_0 + |\vec{E}^n|_1 |\nabla F(\vec{X}_0^n)|_0 \leq C |\vec{E}^n|_{0,\infty} + |\vec{E}^n|_1. \end{aligned} \quad (3.3.39)$$

We now bound A_2

$$\begin{aligned} A_2 &= (|\vec{X}_\rho^{n-1}|^2 D_t \vec{X}^n, (1-\rho)\nabla F(\vec{X}_0^n))^h - (|\vec{x}_\rho^n|^2 \vec{x}_t^n, (1-\rho)\nabla F(\vec{x}_0^n)) \\ &= (|\vec{x}_\rho^n|^2 \vec{x}_t^n, (1-\rho) [\nabla F(\vec{X}_0^n) - \nabla F(\vec{x}_0^n)]) \\ &\quad + \left([|\vec{X}_\rho^{n-1}|^2 - |\vec{x}_\rho^n|^2] \vec{x}_t^n, (1-\rho)\nabla F(\vec{X}_0^n) \right) \\ &\quad + (|\vec{X}_\rho^{n-1}|^2 (I^h - I) \vec{x}_t^n, (1-\rho)\nabla F(\vec{X}_0^n)) \\ &\quad + (|\vec{X}_\rho^{n-1}|^2 [D_t \vec{X}^n - I^h \vec{x}_t^n], (1-\rho)\nabla F(\vec{X}_0^n))^h \\ &\quad + \left[(|\vec{X}_\rho^{n-1}|^2 I^h \vec{x}_t^n, (1-\rho)\nabla F(\vec{X}_0^n))^h - (|\vec{X}_\rho^{n-1}|^2 I^h \vec{x}_t^n, (1-\rho)\nabla F(\vec{X}_0^n)) \right] \\ &=: \sum_{i=1}^5 A_{2,i}. \end{aligned} \quad (3.3.40)$$

Using (3.3.4b), (3.3.30e), (3.1.11) and (3.3.4a), we have

$$\begin{aligned} A_{2,1} &= (|\vec{x}_\rho^n|^2 \vec{x}_t^n, (1-\rho) [\nabla F(\vec{X}_0^n) - \nabla F(\vec{x}_0^n)]) \\ &\leq C \|\vec{x}\|_{W^{1,\infty}(0,T;[L^2(\mathcal{I})]^2)} |1-\rho|_0 |\vec{E}^n|_{0,\infty} \leq C |\vec{E}^n|_{0,\infty}. \end{aligned} \quad (3.3.41)$$

Using (3.1.11), (3.3.4b), (3.3.11), (3.3.4c) and (3.3.13), we have

$$A_{2,2} = \left([|\vec{X}_\rho^{n-1}|^2 - |\vec{x}_\rho^n|^2] \vec{x}_t^n, (1-\rho)\nabla F(\vec{X}_0^n) \right)$$

$$\begin{aligned}
&\leq |\bar{x}_t^n|_{0,\infty} \left[|\bar{X}_\rho^{n-1}| + \|\bar{x}_\rho^n\|_{0,\infty} |\nabla F(\bar{X}_0^n)| |1 - \rho|_0 |\bar{x}^n - \bar{X}^{n-1}|_1 \right. \\
&\leq C \|\bar{x}\|_{W^{1,\infty}(0,T;[H^1(\mathcal{I})]^2)} |\bar{x}^n - \bar{X}^{n-1}|_1 \leq C \left[h + \Delta t_n + |\bar{E}^{n-1}|_1 \right]. \tag{3.3.42}
\end{aligned}$$

Using (3.3.11), (3.3.6), (3.1.5b) and (3.3.4a), we see that

$$\begin{aligned}
A_{2,3} &= \left(|\bar{X}_\rho^{n-1}|^2 (I^h - I) \bar{x}_t^n, (1 - \rho) \nabla F(\bar{X}_0^n) \right) \\
&\leq 4M^2 |\nabla F(\bar{X}_0^{n-1})| |(1 - \rho)|_0 \|(I - I^h) \bar{x}_t^n\|_0 \\
&\leq C h |\bar{x}_t^n|_1 \leq C h \|\bar{x}\|_{W^{1,\infty}(0,T;[H^1(\mathcal{I})]^2)} \leq Ch, \tag{3.3.43}
\end{aligned}$$

and from (3.1.6a), (3.3.11), (3.3.6), (3.1.5d) and (3.3.16), we have

$$\begin{aligned}
A_{2,4} &= \left(|\bar{X}_\rho^{n-1}|^2 \left[D_t \bar{X}^n - I^h \bar{x}_t^n \right], (1 - \rho) \nabla F(\bar{X}_0^n) \right)^h \\
&\leq 4M^2 |\nabla F(\bar{X}_0^n)| \|(1 - \rho)\|_h \|I^h \bar{x}_t^n - D_t \bar{X}^n\|_h \\
&\leq C \left[|I^h(\bar{x}_t^n - D_t \bar{x}^n)|_0 + |D_t \bar{E}^n|_0 \right] \leq C \left[\Delta t_n + |D_t \bar{E}^n|_0 \right]. \tag{3.3.44}
\end{aligned}$$

Using the bound on (3.3.26) as well as (3.3.6) yields

$$\begin{aligned}
A_{2,5} &= \left(|\bar{X}_\rho^{n-1}|^2 I^h \bar{x}_t^n, (1 - \rho) \nabla F(\bar{X}_0^n) \right)^h - \left(|\bar{X}_\rho^{n-1}|^2 I^h \bar{x}_t^n, (1 - \rho) \nabla F(\bar{X}_0^n) \right) \\
&\leq C h \sum_{j=1}^J |I^h \bar{x}_t^n|_{1,\sigma_j} \|\bar{X}_\rho^{n-1}\|^2 (1 - \rho) \nabla F(\bar{X}_0^n)|_{0,\sigma_j} \\
&\leq C h |\bar{x}_t^n|_1 \leq C h \|\bar{x}\|_{W^{1,\infty}(0,T;[H^1(\mathcal{I})]^2)} \leq Ch. \tag{3.3.45}
\end{aligned}$$

Combining (3.3.38) with (3.3.39)–(3.3.45), we see that

$$|b^n(0) - b_h^n(0)| \leq C \left[h + \Delta t_n + |\bar{E}^n|_{0,\infty} + |D_t \bar{E}^n|_0 + |\bar{E}^{n-1}|_1 + |\bar{E}^n|_1 \right].$$

We remark that this bound does not depend on ρ and so also holds for $\rho = 1$. Thus we have

$$|[b^n(\rho) - b_h^n(\rho)]_0^1| \leq C \left[h + \Delta t_n + |\bar{E}^n|_{0,\infty} + |D_t \bar{E}^n|_0 + |\bar{E}^{n-1}|_1 + |\bar{E}^n|_1 \right]. \tag{3.3.46}$$

Hence, using (3.1.11), (3.3.30e), (3.3.46), (3.3.4a), and (3.1.8), we have

$$\begin{aligned}
|S_{2,2}| &= \left| \left[(b^n - b_h^n) \langle (D_t \bar{x}^n, \nabla F(\bar{X}^n) - \nabla F(\bar{x}^n)) \rangle \right]_0^1 \right| \\
&\leq C \|\bar{x}\|_{W^{1,\infty}(0,T;[H^1(\mathcal{I})]^2)} |\bar{E}^n|_{0,\infty} [|b^n(0) - b_h^n(0)| + |b^n(1) - b_h^n(1)|] \\
&\leq C |\bar{E}^n|_{0,\infty} \left[h + \Delta t_n + |\bar{E}^n|_{0,\infty} + |D_t \bar{E}^n|_0 + |\bar{E}^{n-1}|_1 + |\bar{E}^n|_1 \right] \\
&\leq \frac{m^2}{32} |D_t \bar{E}^n|_0^2 + C \left[h^2 + (\Delta t_n)^2 + |\bar{E}^n|_{0,\infty}^2 + |\bar{E}^{n-1}|_1^2 + |\bar{E}^n|_1^2 \right]. \tag{3.3.47}
\end{aligned}$$

Using the integral remainder of the Taylor's expansion, (3.3.3), (3.3.17) and (3.3.46), we have

$$|S_{2,3}| = \left| \left[(b^n - b_h^n) \langle D_t \bar{x}^n, \nabla F(\bar{x}^n) \rangle \right]_0^1 \right|$$

$$\begin{aligned}
&= \frac{1}{\Delta t_n} \left| \left[(b^n - b_h^n) \int_{t_{n-1}}^{t_n} \langle \vec{x}_{tt}(\cdot, s), \nabla F(\vec{x}^n(\cdot)) \rangle (t_{n-1} - s) ds \right]_0^1 \right| \\
&\leq C \Delta t_n [|b^n(0) - b_h^n(0)| + |b^n(1) - b_h^n(1)|] \\
&\leq C \Delta t_n [h + \Delta t_n + |\vec{E}^n|_{0,\infty} + |D_t \vec{E}^n|_0 + |\vec{E}^{n-1}|_1 + |\vec{E}^n|_1] \\
&\leq \frac{m^2}{32} |D_t \vec{E}^n|_0^2 + C [h^2 + (\Delta t_n)^2 + |\vec{E}^n|_{0,\infty}^2 + |\vec{E}^{n-1}|_1^2 + |\vec{E}^n|_1^2]. \tag{3.3.48}
\end{aligned}$$

Combining (3.3.35), (3.3.47) and (3.3.48), and using (3.1.9b), we see that

$$\begin{aligned}
S_2 &\leq \frac{1}{2} D_t [b^n \langle \vec{E}^n, D^2 F(\vec{x}^n) \vec{E}^n \rangle]_0^1 + \frac{1}{4\Delta t_n} |\vec{E}^n - \vec{E}^{n-1}|_1^2 + \frac{m^2}{16} |D_t \vec{E}^n|_0^2 + C \Delta t_n |D_t \vec{E}^n|_0^2 \\
&\quad + C [h^2 + \Delta t_n + |\vec{E}^{n-1}|_0^2 + |\vec{E}^n|_0^2 + |\vec{E}^{n-1}|_1^2 + |\vec{E}^n|_1^2 + h^{-1} |\vec{E}^{n-1}|_{0,\infty}^4]. \tag{3.3.49}
\end{aligned}$$

Combining (3.3.21), (3.3.22), (3.3.27) and (3.3.49) yields the desired result. \square

Proof of Lemma 3.15: Multiplying the result in Lemma 3.14 by $e^{-\mu t_n}$, for some $\mu > 1$, and summing from 1 to n , noting the fact that $|\vec{E}^0| = 0$, gives

$$\begin{aligned}
&\frac{1}{2} \sum_{m=1}^n e^{-\mu t_m} |\vec{E}^m|_1^2 + \frac{1}{4} \sum_{m=1}^n e^{-\mu t_m} |\vec{E}^m - \vec{E}^{m-1}|_1^2 + \left(\frac{m^2}{8} - C \Delta t \right) \sum_{m=1}^n \Delta t_m e^{-\mu t_m} |D_t \vec{E}^m|_0^2 \\
&\leq \frac{1}{2} \sum_{m=1}^n e^{-\mu t_m} |\vec{E}^{m-1}|_1^2 + \frac{1}{2} \sum_{m=1}^n \Delta t_m e^{-\mu t_m} D_t [\langle \vec{x}_\rho^m, \nabla F(\vec{x}^m) \rangle \langle \vec{E}^m, D^2 F(\vec{x}^m) \vec{E}^m \rangle]_0^1 \\
&\quad + C \sum_{m=1}^n \Delta t_m e^{-\mu t_m} [|\vec{E}^{m-1}|_0^2 + |\vec{E}^m|_0^2 + |\vec{E}^{m-1}|_1^2 + |\vec{E}^m|_1^2] \\
&\quad + C \sum_{m=1}^n \Delta t_m e^{-\mu t_m} [h^2 + \Delta t_m + h^{-1} |\vec{E}^{m-1}|_{0,\infty}^4] \\
&\leq \frac{1}{2} \sum_{m=1}^n e^{-\mu t_{m-1}} |\vec{E}^{m-1}|_1^2 + \frac{1}{2} e^{-\mu t_n} [\langle \vec{x}_\rho^n, \nabla F(\vec{x}^n) \rangle \langle \vec{E}^n, D^2 F(\vec{x}^n) \vec{E}^n \rangle]_0^1 \\
&\quad - \frac{1}{2} \sum_{m=1}^n \Delta t_m [\langle \vec{x}_\rho^{m-1}, \nabla F(\vec{x}^{m-1}) \rangle \langle \vec{E}^{m-1}, D^2 F(\vec{x}^{m-1}) \vec{E}^{m-1} \rangle]_0^1 D_t e^{-\mu t_m} \\
&\quad + C \sum_{m=1}^n \Delta t_m e^{-\mu t_m} [|\vec{E}^{m-1}|_0^2 + |\vec{E}^m|_0^2 + |\vec{E}^{m-1}|_1^2 + |\vec{E}^m|_1^2] \\
&\quad + C \sum_{m=1}^n \Delta t_m e^{-\mu t_m} [h^2 + \Delta t_m + h^{-1} |\vec{E}^{m-1}|_{0,\infty}^4]. \tag{3.3.50}
\end{aligned}$$

Using (3.3.30a), (3.3.4c), (3.1.9b), (B.4.1) and the fact that $\mu > 1$, we see that

$$\begin{aligned}
&\frac{1}{2} e^{-\mu t_n} [\langle \vec{x}_\rho^n, \nabla F(\vec{x}^n) \rangle \langle \vec{E}^n, D^2 F(\vec{x}^n) \vec{E}^n \rangle]_0^1 \leq C e^{-\mu t_n} |\vec{E}^n|_{0,\infty}^2 \\
&\leq \frac{1}{4} e^{-\mu t_n} |\vec{E}^n|_1^2 + C e^{-\mu t_n} |\vec{E}^n|_0^2 \\
&\leq \frac{1}{4} e^{-\mu t_n} |\vec{E}^n|_1^2 + C \sum_{m=1}^n \left(\mu (\Delta t_m)^2 + \frac{4}{\mu} \right) \Delta t_m e^{-\mu t_m} |D_t \vec{E}^m|_0^2. \tag{3.3.51}
\end{aligned}$$

Using (3.3.30a), (3.3.4c), (B.4.4), (B.4.2) and (3.1.4b), we have that

$$\begin{aligned}
& -\frac{1}{2} \sum_{m=1}^n \Delta t_m \left[\langle \vec{x}_\rho^{n-1}, \nabla F(\vec{x}^{n-1}) \rangle \langle \vec{E}^{m-1}, D^2 F(\vec{x}^{m-1}) \vec{E}^{m-1} \rangle \right]_0^1 D_t e^{-\mu t_m} \\
& \leq \frac{1}{2} \sum_{m=1}^n \Delta t_m \left| \left[\langle \vec{x}_\rho^{n-1}, \nabla F(\vec{x}^{n-1}) \rangle \langle \vec{E}^{m-1}, D^2 F(\vec{x}^{m-1}) \vec{E}^{m-1} \rangle \right]_0^1 \right| \mu e^{-\mu t_{m-1}} \\
& \leq C\mu \sum_{m=1}^n \Delta t_m e^{-\mu t_{m-1}} \left[|\vec{E}^{m-1}|_1^2 + |\vec{E}^{m-1}|_0^2 \right] \\
& \leq C\mu \sum_{m=1}^n \Delta t_m e^{-\mu t_m} |\vec{E}^m|_1^2 + C \sum_{m=1}^n \left(\mu(\Delta t_m)^2 + \frac{4}{\mu} \right) \Delta t_m e^{-\mu t_m} |D_t \vec{E}^m|_0^2. \quad (3.3.52)
\end{aligned}$$

Hence, combining (3.3.50)–(3.3.52) and using B.4.1, we have that

$$\begin{aligned}
& \frac{1}{4} e^{-\mu t_n} |\vec{E}^n|_1^2 + \left(\frac{m^2}{8} - C_\star [\Delta t + \mu(\Delta t)^2 + \mu^{-1}] \right) \sum_{m=1}^n \Delta t_m e^{-\mu t_m} |D_t \vec{E}^m|_0^2 \\
& \leq C\mu \sum_{m=1}^n \Delta t_m e^{-\mu t_m} |\vec{E}^m|_1^2 + C \sum_{m=1}^n \Delta t_m e^{-\mu t_m} \left[h^2 + \Delta t_m + h^{-1} |\vec{E}^{m-1}|_{0,\infty}^4 \right]. \quad (3.3.53)
\end{aligned}$$

Setting $\bar{C} = \frac{m^2}{8} - C_\star [\Delta t + \mu(\Delta t)^2 + \mu^{-1}]$, whereby $\bar{C} > 0$ by (3.3.10), and using Lemma 3.1, we have

$$\begin{aligned}
& \frac{1}{4} \sup_{m=0,\dots,n} e^{-\mu t_m} |\vec{E}^m|_1^2 + \bar{C} \sum_{m=1}^n \Delta t_m e^{-\mu t_m} |D_t \vec{E}^m|_0^2 \\
& \leq C \sum_{m=1}^n \Delta t_m e^{-\mu t_m} \left[h^2 + \Delta t_m + h^{-1} |\vec{E}^{m-1}|_{0,\infty}^4 \right] \\
& \quad + \sum_{k=1}^n C\mu \sum_{m=1}^k \Delta t_m e^{-\mu t_m} \left[h^2 + \Delta t_m + h^{-1} |\vec{E}^{m-1}|_{0,\infty}^4 \right] \Delta t_m \exp \left(C\mu \sum_{m=k}^n \Delta t_m \right) \\
& \leq C(1 + \mu T e^{C\mu T}) \sum_{m=1}^n \Delta t_m e^{-\mu t_m} \left[h^2 + \Delta t_m + h^{-1} |\vec{E}^{m-1}|_{0,\infty}^4 \right].
\end{aligned}$$

By dividing both sides by $\min\{\bar{C}, \frac{1}{4}\}$, we have that

$$\begin{aligned}
& \sup_{m=0,\dots,n} e^{-\mu t_m} |\vec{E}^m|_1^2 + \sum_{m=1}^n \Delta t_m e^{-\mu t_m} |D_t \vec{E}^m|_0^2 \\
& \leq \frac{C_1}{2} h^2 + Ch^{-1} \sum_{m=1}^n \Delta t_m e^{-\mu t_m} |\vec{E}^{m-1}|_{0,\infty}^4 \quad (3.3.54)
\end{aligned}$$

for $C_1 \geq 2CT$ and $\Delta t \leq Ch^2$. Using (3.3.18), for some small $h^\star > 0$, we have

$$\begin{aligned}
Ch^{-1} \sum_{m=1}^n \Delta t_m e^{-\mu t_{m-1}} |\vec{E}^{m-1}|_{0,\infty}^4 & = Ch^{-1} \sum_{m=1}^n \Delta t_m (e^{-\mu t_{m-1}} |\vec{E}^{m-1}|_{0,\infty}^2)^2 e^{\mu t_{m-1}} \\
& \leq CC_1 \left(1 + \mu(\Delta t)^2 + \frac{1}{\mu} \right)^2 h^3 e^{\mu T} \sum_{m=1}^n \Delta t_m \\
& \leq Ch^3 \leq \frac{C_1}{2} h^2. \quad (3.3.55)
\end{aligned}$$

Hence, combining (3.3.54) and (3.3.55), we have the desired result. \square

Proof of Theorem 3.13: Using (3.1.5b), (3.3.4a), Lemma 3.15 and (3.1.8), simple calculations give us

$$\begin{aligned} \sup_{n=0,\dots,N} |\bar{x}^n - \bar{X}^n|_1^2 &\leq 2 \sup_{n=0,\dots,N} \left[|(I - I^h)\bar{x}^n|_1^2 + |\bar{E}^n|_1^2 \right] \\ &\leq Ch^2 \|\bar{x}\|_{W^{0,\infty}(0,T;[H^2(\mathcal{I})]^2)}^2 + 2C_1 h^2 e^{\mu T} \leq Ch^2, \end{aligned}$$

and, in addition with (3.1.5d) and (3.3.16) whilst noting $\Delta t \leq Ch^2$,

$$\begin{aligned} \sum_{n=1}^N \Delta t_n |\bar{x}_t^n - D_t \bar{X}^n|_0^2 &\leq 3 \sum_{n=1}^N \Delta t_n \left[|(I - I^h)\bar{x}_t^n|_0^2 + |I^h(\bar{x}_t^n - D_t \bar{x}^n)|_0^2 + |D_t \bar{E}^n|_0^2 \right] \\ &\leq CT h^2 \|\bar{x}\|_{W^{0,\infty}(0,T;[H^2(\mathcal{I})]^2)}^2 + CT(\Delta t)^2 + 2C_1 h^2 e^{\mu T} \leq Ch^2. \end{aligned}$$

\square

Remark 3.16. We note that if we did not rewrite the term $S_{2,1}$ in (3.3.31) into three parts, $S_{2,1}$ would yield a term of the form $|\bar{E}^n|_{0,\infty}^4$ in (3.3.34), which we could not find a way to bound. Rewriting $S_{2,1}$ as we do results in the time step restriction $\Delta t \leq Ch^2$ rather than $\Delta t \leq Ch$.

Remark 3.17. We note here the unconventional approach we use to obtain the bound, (3.3.46), on $|b^n(\rho) - b_h^n(\rho)|$. Indeed, approaching such a bound conventionally, by subtracting b_h^n from b^n , and noting (3.1.7), would give

$$b^n - b_h^n = \langle \bar{x}_\rho^n, \nabla F(\bar{x}^n) - \nabla F(\bar{X}^n) \rangle + \langle \bar{E}_\rho^n, \nabla F(\bar{X}^n) \rangle$$

and hence, using (3.3.4b), (3.3.4c), (3.3.6) and (3.3.4a), we would have

$$S_{2,2} = \left[(b^n - b_h^n) \langle D_t \bar{x}^n, \nabla F(\bar{x}^n) - \nabla F(\bar{X}^n) \rangle \right]_0^1 \leq C \left[|\bar{E}^n|_{0,\infty} + |\bar{E}^n|_{1,\infty} \right] |\bar{E}^n|_{0,\infty}.$$

This estimate is not desirable as an inverse estimate would be required that would not result in the desired power of h we require for the result.

3.3.3 L^2 error bounds for Model \mathcal{M}_1

In this section we present a fully discrete version of the arguments used in [42] to prove optimal L^2 error bounds for the scheme (3.3.5a). We look to prove the following theorem.

Theorem 3.18.

Let $\bar{X}^0 = I^h \bar{x}^0 \in [S^h]^2$. There exists $h^* > 0$ and $\Delta t^* > 0$ such that for all $h \in (0, h^*)$

and $\Delta t \in (0, \Delta t^*]$, with $\Delta t \leq Ch^2$, the fully-discrete problem (3.3.5a)–(3.3.5b) has the following error bound

$$\sup_{n=0, \dots, N} |\bar{x}^n - \bar{X}^n|_0^2 \leq Ch^4,$$

for some $C > 0$ independent of h and Δt , where $\bar{x}^n := \bar{x}(\cdot, t^n)$.

Before proving Theorem 3.18 we note some useful results. Using (3.3.4b), (3.1.5a), (3.1.4a) and Theorem 3.13, we see that

$$|\bar{X}_\rho^n|_{0, \infty} \leq |\bar{x}^n|_{1, \infty} + |\bar{x}^n - \bar{X}^n|_{1, \infty} \leq M + Ch^{-\frac{1}{2}} |\bar{x}^n - \bar{X}^n|_1 \leq M + Ch^{\frac{1}{2}} \leq 2M$$

and similarly

$$|\bar{X}_\rho^n|_{0, \infty} \geq |\bar{x}^n|_{1, \infty} - |\bar{x}^n - \bar{X}^n|_{1, \infty} \geq m - Ch^{-\frac{1}{2}} |\bar{x}^n - \bar{X}^n|_1 \geq m - Ch^{\frac{1}{2}} \geq \frac{m}{2},$$

provided h^* is chosen small enough, which combine to give

$$\frac{m}{2} \leq |\bar{X}_\rho^n| \leq 2M. \quad (3.3.56)$$

Using (3.3.4a), (3.1.5a), (3.1.4a), and Theorem 3.13, we see that

$$\begin{aligned} \sum_{m=1}^n \Delta t_n |D_t \bar{X}^n|_1^2 &\leq 2 \sum_{m=1}^n \left[\Delta t_n |\bar{x}_t^m|_1^2 + \Delta t_n |\bar{x}_t^m - D_t \bar{X}^n|_1^2 \right] \\ &\leq C \|\bar{x}\|_{W^{1, \infty}(0, T; [H^1(\mathcal{I})]^2)}^2 + Ch^{-2} \sum_{m=1}^n \Delta t_n |\bar{x}_t^m - D_t \bar{X}^n|_0^2 \leq C. \end{aligned} \quad (3.3.57)$$

Recalling the definition of \bar{E}^n , using (3.1.5b) and (3.3.4a), we have

$$\begin{aligned} |\bar{x}^n - \bar{X}^n|_0 &\leq |(I - I^h)\bar{x}^n|_0 + |\bar{E}^n|_0 \\ &\leq Ch^2 |\bar{x}^n|_2 + |\bar{E}^n|_0 \\ &\leq Ch^2 \|\bar{x}\|_{W^{0, \infty}(0, T; [H^2(\mathcal{I})]^2)} + |\bar{E}^n|_0 \leq C \left[h^2 + |\bar{E}^n|_0 \right]. \end{aligned} \quad (3.3.58)$$

We restate (3.3.16) for the ease of the reader, namely we have

$$|D_t \bar{x}^n - \bar{x}_t^n|_0 \leq \Delta t_n \sup_{s \in [t_{n-1}, t_n]} |\bar{x}_{tt}(\cdot, s)|_0 \leq \Delta t_n \|\bar{x}\|_{W^{2, \infty}(0, T; [L^2(\mathcal{I})]^2)} \leq C \Delta t_n. \quad (3.3.59)$$

Proof of Theorem 3.18: Noting (3.3.19) and (3.3.20), we have

$$\begin{aligned} &\left(|\bar{X}_\rho^{n-1}|^2 D_t \bar{E}^n, \bar{\xi}^h \right)^h + \left(\bar{E}_\rho^n, \bar{\xi}_\rho^h \right) \\ &= \left[\left(|\bar{X}_\rho^{n-1}|^2 D_t [I^h \bar{x}^n], \bar{\xi}^h \right)^h - \left(|\bar{x}_\rho^n|^2 \bar{x}_t^n, \bar{\xi}^h \right) \right] \\ &\quad + \left[\langle \bar{x}_\rho^n, \nabla F(\bar{x}^n) \rangle \langle \bar{\xi}^h, \nabla F(\bar{x}^n) \rangle - \langle \bar{X}_\rho^n, \nabla F(\bar{X}^n) \rangle \langle \bar{\xi}^h, \nabla F(\bar{X}^n) \rangle \right]_0^1. \end{aligned} \quad (3.3.60)$$

A simple calculation gives

$$\begin{aligned} D_t \left[\left(|\vec{X}_\rho^n|^2 \vec{E}^n, \vec{E}^n \right)^h \right] &= \left(D_t \left[|\vec{X}_\rho^n|^2 \right] \vec{E}^n, \vec{E}^n \right)^h + 2 \left(|\vec{X}_\rho^{n-1}|^2 D_t \vec{E}^n, \vec{E}^n \right)^h \\ &\quad - \Delta t_n \left(|\vec{X}_\rho^{n-1}|^2 D_t \vec{E}^n, D_t \vec{E}^n \right)^h \end{aligned}$$

and hence, taking $\xi^h = \Delta t_n \vec{E}^n$ in (3.3.60), we see that

$$\begin{aligned} &\frac{\Delta t_n}{2} D_t \left[\left(|\vec{X}_\rho^n|^2 \vec{E}^n, \vec{E}^n \right)^h \right] + \Delta t_n \left(\vec{E}_\rho^n, \vec{E}_\rho^n \right) \\ &\leq \Delta t_n \left[\left(|\vec{X}_\rho^{n-1}|^2 D_t [I^h \vec{x}^n], \vec{E}^n \right)^h - \left(|\vec{x}_\rho^n|^2 \vec{x}_t^n, \vec{E}^n \right) \right] + \frac{\Delta t_n}{2} \left(D_t \left[|\vec{X}_\rho^n|^2 \right] \vec{E}^n, \vec{E}^n \right)^h \\ &\quad + \Delta t_n \left[\langle \vec{x}_\rho^n, \nabla F(\vec{x}^n) \rangle \langle \vec{E}^n, \nabla F(\vec{x}^n) \rangle - \langle \vec{X}_\rho^n, \nabla F(\vec{X}^n) \rangle \langle \vec{E}^n, \nabla F(\vec{X}^n) \rangle \right]_0^1 \\ &=: \Delta t_n \sum_{i=3}^5 S_i. \end{aligned} \tag{3.3.61}$$

We first bound S_3

$$\begin{aligned} S_3 &= \Delta t_n \left[\left(|\vec{X}_\rho^{n-1}|^2 D_t [I^h \vec{x}^n], \vec{E}^n \right)^h - \left(|\vec{x}_\rho^n|^2 \vec{x}_t^n, \vec{E}^n \right) \right] \\ &= \left[\left(|\vec{X}_\rho^{n-1}|^2 D_t [I^h \vec{x}^n], \vec{E}^n \right)^h - \left(|\vec{X}_\rho^{n-1}|^2 D_t [I^h \vec{x}^n], \vec{E}^n \right) \right] \\ &\quad + \left(|\vec{x}_\rho^n|^2 \left[D_t [I^h \vec{x}^n] - \vec{x}_t^n \right], \vec{E}^n \right) + \left(\left[|\vec{X}_\rho^n|^2 - |\vec{x}_\rho^n|^2 \right] D_t [I^h \vec{x}^n], \vec{E}^n \right) \\ &\quad + \left(\left[|\vec{X}_\rho^{n-1}|^2 - |\vec{X}_\rho^n|^2 \right] D_t [I^h \vec{x}^n], \vec{E}^n \right) =: \sum_{i=1}^4 S_{3,i}. \end{aligned} \tag{3.3.62}$$

Using (3.1.6b), (3.3.56), (3.1.5d) and (3.3.4a), we see that

$$\begin{aligned} S_{3,1} &= \left(|\vec{X}_\rho^{n-1}|^2 D_t [I^h \vec{x}^n], \vec{E}^n \right)^h - \left(|\vec{X}_\rho^{n-1}|^2 D_t [I^h \vec{x}^n], \vec{E}^n \right) \\ &\leq C h^2 \sum_{j=1}^J |D_t [I^h \vec{x}^n]|_{1,\sigma_j} |\vec{E}^n|_{1,\sigma_j} \\ &\leq C h^2 |D_t [I^h \vec{x}^n]|_1 |\vec{E}^n|_1 \\ &\leq C h^2 \|\vec{x}\|_{W^{1,\infty}(0,T;[H^1(\mathcal{I})]^2)} |\vec{E}^n|_1 \leq C h^2 |\vec{E}^n|_1, \end{aligned} \tag{3.3.63}$$

where $|\eta|_{1,\sigma_j}$ is the seminorm of the space $H^1(\sigma_j)$, and from (3.3.4b), (3.1.5b), (3.3.59) and (3.3.4a), we have

$$\begin{aligned} S_{3,2} &= \left(|\vec{x}_\rho^n|^2 \left[D_t [I^h \vec{x}^n] - \vec{x}_t^n \right], \vec{E}^n \right) \\ &\leq 4M^2 \left[|(I - I^h) D_t \vec{x}^n|_0 + |D_t \vec{x}^n - \vec{x}_t^n|_0 \right] |\vec{E}^n|_0 \\ &\leq C \left[h^2 |D_t \vec{x}^n|_2 + \Delta t_n \right] |\vec{E}^n|_0 \\ &\leq C \left[h^2 \|\vec{x}\|_{W^{1,\infty}(0,T;[H^2(\mathcal{I})]^2)} + \Delta t_n \right] \leq C \left[h^2 + \Delta t_n \right] |\vec{E}^n|_0. \end{aligned} \tag{3.3.64}$$

Integration by parts and (3.1.10) yield

$$\begin{aligned}
S_{3,3} &= \left(\left[|\vec{X}_\rho^n|^2 - |\vec{x}_\rho^n|^2 \right] D_t[I^h \vec{x}^n], \vec{E}^n \right) \\
&= \left(|\vec{X}_\rho^n - \vec{x}_\rho^n|^2 D_t[I^h \vec{x}^n], \vec{E}^n \right) - 2 \left(\langle \vec{x}_\rho^n, \vec{x}_\rho^n - \vec{X}_\rho^n \rangle D_t[I^h \vec{x}^n], \vec{E}^n \right) \\
&= \left(|\vec{X}_\rho^n - \vec{x}_\rho^n|^2 D_t[I^h \vec{x}^n], \vec{E}^n \right) + 2 \left(\langle \vec{x}_\rho^n, \vec{x}^n - \vec{X}^n \rangle D_t[I^h \vec{x}^n], \vec{E}^n \right) \\
&\quad + \left[2 \left(\langle \vec{x}_{\rho\rho}^n, \vec{x}^n - \vec{X}^n \rangle D_t[I^h \vec{x}^n], \vec{E}^n \right) + 2 \left(\langle \vec{x}_\rho^n, \vec{x}^n - \vec{X}^n \rangle D_t[I^h \vec{x}_\rho^n], \vec{E}^n \right) \right] \\
&\quad + 2 \left[\langle \vec{x}_\rho^n, \vec{X}^n - \vec{x}^n \rangle \langle D_t[I^h \vec{x}^n], \vec{E}^n \rangle \right]_0^1 =: \sum_{i=1}^4 S_{3,3,i}. \tag{3.3.65}
\end{aligned}$$

From (3.1.11), (3.3.4a) and Theorem 3.13, we have

$$\begin{aligned}
S_{3,3,1} &= \left(|\vec{X}_\rho^n - \vec{x}_\rho^n|^2 D_t[I^h \vec{x}^n], \vec{E}^n \right) \\
&\leq |D_t[I^h \vec{x}^n]|_{0,\infty} |\vec{E}^n|_{0,\infty} |\vec{x}^n - \vec{X}^n|_1^2 \\
&\leq C \|\vec{x}\|_{W^{1,\infty}(0,T;[H^1(\mathcal{I})]^2)} |\vec{E}^n|_{0,\infty} |\vec{x}^n - \vec{X}^n|_1^2 \leq C h^2 |\vec{E}^n|_{0,\infty}, \tag{3.3.66}
\end{aligned}$$

and using (3.1.5d), (3.3.58) and (3.3.4a), we have

$$\begin{aligned}
S_{3,3,2} &= 2 \left(\langle \vec{x}_\rho^n, \vec{x}^n - \vec{X}^n \rangle D_t[I^h \vec{x}^n], \vec{E}^n \right) \\
&\leq 2 |\vec{x}^n|_{1,\infty} |D_t I^h \vec{x}^n|_{0,\infty} |\vec{E}^n|_1 |\vec{x}^n - \vec{X}^n|_0 \\
&\leq C \|\vec{x}\|_{W^{0,\infty}(0,T;[H^2(\mathcal{I})]^2)} \|\vec{x}\|_{W^{1,\infty}(0,T;[H^1(\mathcal{I})]^2)} |\vec{E}^n|_1 |\vec{x}^n - \vec{X}^n|_0 \\
&\leq C |\vec{E}^n|_1 \left[h^2 + |\vec{E}^n|_0 \right]. \tag{3.3.67}
\end{aligned}$$

Similarly we have

$$\begin{aligned}
S_{3,3,3} &= 2 \left(\langle \vec{x}_{\rho\rho}^n, \vec{x}^n - \vec{X}^n \rangle D_t[I^h \vec{x}^n], \vec{E}^n \right) + 2 \left[\langle \vec{x}_\rho^n, \vec{x}^n - \vec{X}^n \rangle D_t[I^h \vec{x}_\rho^n], \vec{E}^n \right] \\
&\leq 2 |\vec{x}^n|_2 |D_t[I^h \vec{x}^n]|_{0,\infty} |\vec{E}^n|_{0,\infty} |\vec{x}^n - \vec{X}^n|_0 + 2 |\vec{x}^n|_{1,\infty} |D_t I^h \vec{x}^n|_{1,\infty} |\vec{E}^n|_0 |\vec{x}^n - \vec{X}^n|_0 \\
&\leq C \|\vec{x}\|_{W^{0,\infty}(0,T;[H^2(\mathcal{I})]^2)} \|\vec{x}\|_{W^{1,\infty}(0,T;[H^2(\mathcal{I})]^2)} \left[|\vec{E}^n|_{0,\infty} + |\vec{E}^n|_0 \right] |\vec{x}^n - \vec{X}^n|_0 \\
&\leq C \left[|\vec{E}^n|_{0,\infty} + |\vec{E}^n|_0 \right] \left[h^2 + |\vec{E}^n|_0 \right]. \tag{3.3.68}
\end{aligned}$$

Using (3.1.7), (3.3.4b), (3.1.5d), (3.1.11) and (3.3.4a), we see that

$$\begin{aligned}
S_{3,3,4} &= 2 \left[\langle \vec{x}_\rho^n, \vec{X}^n - \vec{x}^n \rangle \langle D_t[I^h \vec{x}^n], \vec{E}^n \rangle \right]_0^1 \\
&\leq 2M |D_t[I^h \vec{x}^n]|_{0,\infty} |\vec{E}^n|_{0,\infty}^2 \\
&\leq C \|\vec{x}\|_{W^{1,\infty}(0,T;[H^1(\mathcal{I})]^2)} |\vec{E}^n|_{0,\infty}^2 \leq C |\vec{E}^n|_{0,\infty}^2. \tag{3.3.69}
\end{aligned}$$

Hence, combining (3.3.65)–(3.3.69), we see that

$$S_{3,3} \leq C \left[|\vec{E}^n|_0 + |\vec{E}^n|_1 + |\vec{E}^n|_{0,\infty} \right] \left[h^2 + |\vec{E}^n|_0 + |\vec{E}^n|_{0,\infty} \right]. \tag{3.3.70}$$

Using (3.1.5d), (3.3.56) and (3.3.4a), we see that

$$\begin{aligned}
S_{3,4} &= \left(\left[|\vec{X}_\rho^{n-1}|^2 - |\vec{X}_\rho^n|^2 \right] D_t [I^h \vec{x}^n], \vec{E}^n \right) \\
&\leq |D_t [I^h \vec{x}^n]|_{0,\infty} \left| |\vec{X}_\rho^n| + |\vec{X}_\rho^{n-1}| \right|_{0,\infty} |\vec{E}^n|_0 |\vec{X}^n - \vec{X}^{n-1}|_1 \\
&\leq C \|\vec{x}\|_{W^{1,\infty}(0,T;[H^1(\mathcal{X})]^2)} |\vec{E}^n|_0 |\vec{X}^n - \vec{X}^{n-1}|_1 \leq C \Delta t_n |\vec{E}^n|_0 |D_t \vec{X}^n|_1. \quad (3.3.71)
\end{aligned}$$

Hence, combining (3.3.62) with (3.3.63), (3.3.64), (3.3.70) and (3.3.71), as well as using (3.1.8) and (3.1.9b), we have

$$S_3 \leq \frac{1}{6} |\vec{E}^n|_1^2 + C \left[h^4 + (\Delta t_n)^2 + \left(1 + |D_t \vec{X}^n|_1^2 \right) |\vec{E}^n|_0^2 \right]. \quad (3.3.72)$$

We now bound S_4 . Using (3.1.6a), (3.3.56), (3.1.8) and (3.1.9b), we have

$$\begin{aligned}
S_4 &= \frac{1}{2} \left(D_t \left[|\vec{X}_\rho^n|^2 \right] \vec{E}^n, \vec{E}^n \right)^h \\
&\leq C \left| |\vec{X}_\rho^n| + |\vec{X}_\rho^{n-1}| \right|_{0,\infty} |\vec{E}^n|_{0,\infty} |D_t \vec{X}^n|_1 |\vec{E}^n|_0 \\
&\leq \frac{1}{6} |\vec{E}^n|_1^2 + C \left[1 + |D_t \vec{X}^n|_1^2 \right] |\vec{E}^n|_0^2. \quad (3.3.73)
\end{aligned}$$

Now we bound S_5 . Denoting

$$b^n := \langle \vec{x}^n, \nabla F(\vec{x}^n) \rangle \quad \text{and} \quad b_h^n := \langle \vec{X}_\rho^n, \nabla F(\vec{X}^n) \rangle,$$

and using (3.3.4b), (3.3.4d), (3.3.56) and (3.3.6) yields

$$|b^n(\rho)| \leq M, \quad \text{and} \quad |b_h^n(\rho)| \leq 2M, \quad \text{for } \rho \in \{0, 1\}. \quad (3.3.74)$$

Using (3.1.12), (3.1.1b), (3.3.5b) and (3.1.7), we have

$$\begin{aligned}
0 &= \left[F(\vec{x}^n) - F(\vec{X}^n) \right]_0^1 = \left[\langle \vec{E}^n, \nabla F(\vec{x}^n) \rangle \right]_0^1 \\
&\quad + \left[\int_0^1 \langle \nabla F(s\vec{x}^n + (1-s)\vec{X}^n) - \nabla F(\vec{x}^n), \vec{E}^n \rangle ds \right]_0^1
\end{aligned}$$

and

$$\begin{aligned}
0 &= \left[F(\vec{x}^n) - F(\vec{X}^n) \right]_0^1 = \left[\langle \vec{E}^n, \nabla F(\vec{X}^n) \rangle \right]_0^1 \\
&\quad + \left[\int_0^1 \langle \nabla F(s\vec{X}^n + (1-s)\vec{x}^n) - \nabla F(\vec{X}^n), \vec{E}^n \rangle ds \right]_0^1.
\end{aligned}$$

Hence, using (3.3.4c), we have

$$\left| \left[\langle \vec{E}^n, \nabla F(\vec{x}^n) \rangle \right]_0^1 \right| \leq L_{\nabla F} |\vec{E}^n|_{0,\infty}^2 \int_0^1 |1-s| ds \leq C |\vec{E}^n|_{0,\infty}^2 \quad (3.3.75)$$

and

$$\left| \left[\langle \vec{E}^n, \nabla F(\vec{X}^n) \rangle \right]_0^1 \right| \leq L_{\nabla F} |\vec{E}^n|_{0,\infty}^2 \int_0^1 |1-s| ds \leq C |\vec{E}^n|_{0,\infty}^2. \quad (3.3.76)$$

Thus, using (3.3.30a), (3.3.74), (3.3.75), (3.3.76) and (3.1.9b), we have that

$$\begin{aligned} |S_5| &= \left| \left[b^n \langle \vec{E}^n, \nabla F(\vec{x}^n) \rangle - b_h^n \langle \vec{E}^n, \nabla F(\vec{X}^n) \rangle \right]_0^1 \right| \\ &\leq C |\vec{E}^n|_{0,\infty}^2 \leq \frac{1}{6} |\vec{E}^n|_1^2 + C |\vec{E}^n|_0^2. \end{aligned} \quad (3.3.77)$$

Combining (3.3.61) with (3.3.72), (3.3.73) and (3.3.77) gives

$$\frac{\Delta t_n}{2} D_t \left[\left(|\vec{X}_\rho^n|^2 \vec{E}^n, \vec{E}^n \right)^h \right] + \frac{\Delta t_n}{2} |\vec{E}^n|_1^2 \leq C \Delta t_n \left[h^4 + (\Delta t_n)^2 + (1 + |D_t \vec{X}^n|_1^2) |\vec{E}^n|_0^2 \right].$$

Summing from $n = 1, \dots, N$, noting the fact that $|\vec{E}^0| = 0$, and using (3.1.6b) and (3.3.56), we have

$$\begin{aligned} &\frac{m^2}{8} |\vec{E}^N|_0^2 + \frac{1}{2} \sum_{n=1}^N \Delta t_n |\vec{E}^n|_1^2 \\ &\leq C \sum_{n=1}^N \Delta t_n [h^4 + (\Delta t_n)^2] + C \sum_{n=1}^N \Delta t_n \left(1 + |D_t \vec{X}^n|_1^2 \right) |\vec{E}^n|_0^2. \end{aligned}$$

Next, using Lemma 3.1 and (3.3.57), and noting $\Delta t \leq Ch^2$, we see that

$$\sup_{n=0,\dots,N} |\vec{E}^n|_0^2 + \sum_{n=1}^N \Delta t_n |\vec{E}^n|_1^2 \leq Ch^4. \quad (3.3.78)$$

Finally, using (3.1.5b) and (3.3.4a), a simple calculation gives us

$$\begin{aligned} &\sup_{n=0,\dots,N} |\vec{x}^n - \vec{X}^n|_0^2 \\ &\leq 2 \sup_{n=0,\dots,N} \left[|(I - I^h) \vec{x}^n|_0^2 + |\vec{E}^n|_0^2 \right] \leq Ch^4 \|\vec{x}\|_{W^{0,\infty}(0,T;[H^2(\mathcal{I})]^2)}^2 + Ch^4 \leq Ch^4 \end{aligned}$$

as desired. \square

3.4 Finite element analysis of Model \mathcal{M}_2

In this section we look at **Model \mathcal{M}_2** in more detail. We first discuss the De-Turck trick. The author in [108] derives the reparametrised curve shortening flow using an Euler-Lagrange formulation rather than the use of charts used by [59]; however, as mentioned in [59], the formulation in [108] falls short to be able to discretise directly in space. We refer readers to either [108] or [59] for the derivation of the reparametrised curve shortening flow, and simply state the result they show. Namely, that the reparametrisation of (3.2.5a) using the De-Turck trick is as follows

$$\vec{x}_t = \left(I + \left(\frac{1}{\alpha} - 1 \right) \vec{\tau} \otimes \vec{\tau} \right) \frac{\vec{x}_{\rho\rho}}{|\vec{x}_\rho|^2}. \quad (3.4.1)$$

Remark 3.19. In [59, 108] the authors consider a closed curve to derive the reparametrisation. The objective of this thesis was not to rigorously extend the result to the orthogonal boundary conditions (3.1.2c) and (3.1.2d), rather just to use it under the assumption that it does extend to this situation and to show analytical and numerical results using it. Given that the transition from [37] to [42] was a simple change of boundary conditions, we speculate this would be the same in our case of extending [59] to **Model** \mathcal{M}_2 .

Using Theorem B.4, since $\det(\vec{\tau} \otimes \vec{\tau}) = 0$ and $\text{Tr}(\vec{\tau} \otimes \vec{\tau}) = 1$, we have that $\vec{\tau} \otimes \vec{\tau}$ is idempotent. Hence, using Theorem B.5, taking $T = \vec{\tau} \otimes \vec{\tau}$ and $\beta = \frac{1-\alpha}{\alpha}$, we see that

$$\left(I + \left(\frac{1}{\alpha} - 1 \right) \vec{\tau} \otimes \vec{\tau} \right)^{-1} = I - (1 - \alpha) \vec{\tau} \otimes \vec{\tau}$$

and hence, noting that $\vec{\tau} \otimes \vec{\tau} = I - \vec{\nu} \otimes \vec{\nu}$, we have (3.2.20a). Simply adding a forcing term gives us (3.1.2a). We now turn our attention to (3.1.2b). Labelling $\tilde{w}(\rho, t) = w(\vec{x}(\rho, t), t)$, we see that

$$\begin{aligned} \tilde{w}_t(\rho, t) &= w_t(\vec{x}, t) + \langle \nabla w(\vec{x}, t), \vec{x}_t \rangle \\ &= w_t(\vec{x}, t) + \langle \nabla w(\vec{x}, t), \vec{\tau} \rangle \langle \vec{\tau}, \vec{x}_t \rangle + \langle \nabla w(\vec{x}, t), \vec{\nu} \rangle \langle \vec{\nu}, \vec{x}_t \rangle \\ &= \partial_t^\bullet w(\vec{x}, t) + \psi w_s(\vec{x}, t) = \partial_t^\bullet w(\vec{x}, t) + \psi \frac{w_\rho(\vec{x}, t)}{|\vec{x}_\rho|}. \end{aligned}$$

Noting (3.2.8) and (3.2.2), we have

$$|\vec{x}_\rho|_t = \langle \vec{\tau}, (\vec{x}_t)_\rho \rangle = (\langle \vec{\tau}, \vec{x}_t \rangle)_\rho - \langle \vec{\tau}_\rho, \vec{x}_t \rangle = \psi_\rho - |\vec{x}_\rho| \kappa v$$

and hence we can write (3.2.23b) as

$$(|\vec{x}_\rho| \tilde{w})_t - (\psi \tilde{w})_\rho - d \left(\frac{\tilde{w}_\rho}{|\vec{x}_\rho|} \right)_\rho = |\vec{x}_\rho| g(v, \tilde{w}),$$

which is (3.2.27b) in variational form.

Remark 3.20. In the case of [97], since they are using (3.2.5a), the authors have the property that $\psi = 0$, which leads them to the slightly different formulation (3.2.24b).

We drop the tilde over the w now for ease of notation. We refer the readers to (3.3.1) for the derivation of the weak formulation of (3.1.2a) and instead look to derive the weak formulation of (3.1.2b). By multiplying (3.1.2b) by a test function $\eta \in H_0^1(\mathcal{I})$, using integration by parts and (3.1.2e), we have

$$((|\vec{x}_\rho| w)_t, \eta) + (\psi w, \eta_\rho) + d \left(\frac{w_\rho}{|\vec{x}_\rho|}, \eta_\rho \right) = \left[\left(\frac{w_\rho}{|\vec{x}_\rho|} + \psi w \right) \eta \right]_0^1 + (|\vec{x}_\rho| g(v, w), \eta)$$

$$= (|\vec{x}_\rho| g(v, w), \eta).$$

Thus, we have the following weak form of (3.1.2a)–(3.1.2e)

$$\begin{aligned} & \left(|\vec{x}_\rho|^2 [\alpha \vec{x}_t + (1 - \alpha) \langle \vec{x}_t, \vec{\nu} \rangle \vec{\nu}], \vec{\xi} \right) + \left(\vec{x}_\rho, \vec{\xi}_\rho \right) \\ & = \left(|\vec{x}_\rho|^2 f(w) \vec{\nu}, \vec{\xi} \right) + \left[\langle \vec{x}_\rho, \nabla F(\vec{x}) \rangle \langle \vec{\xi}, \nabla F(\vec{x}) \rangle \right]_0^1, \quad \forall \vec{\xi} \in [H^1(\mathcal{I})]^2, \end{aligned} \quad (3.4.2a)$$

$$\left((|\vec{x}_\rho| w)_t, \eta \right) + d \left(\frac{w_\rho}{|\vec{x}_\rho|}, \eta_\rho \right) + (\psi w, \eta_\rho) = (|\vec{x}_\rho| g(v, w), \eta), \quad \forall \eta \in H_0^1(\mathcal{I}). \quad (3.4.2b)$$

We also restate the property derived from (3.1.2c) for the ease of the reader, that is (3.3.3)

$$\langle \vec{x}_t(\rho, t), \nabla F(\vec{x}(\rho, t)) \rangle = 0, \quad \text{for } \rho \in \{0, 1\}. \quad (3.4.3)$$

We note that, unlike in the fully discrete case, (3.4.3) is independent of α and f . Before introducing the finite element formulation we detail the assumptions we will need for the analysis.

Assumptions 3.21.

We assume that there is a unique solution (\vec{x}, w) of **Model** \mathcal{M}_2 on the time interval $[0, T]$.

Furthermore we assume this unique solution and specified data satisfies

$$\vec{x} \in W^{1,\infty}(0, T; [H^2(\mathcal{I})]^2) \cap W^{2,\infty}(0, T; [L^2(\mathcal{I})]^2), \quad (3.4.4a)$$

$$w \in C([0, T]; H^2(\mathcal{I})) \cap W^{1,\infty}(0, T; H^1(\mathcal{I})), \quad (3.4.4b)$$

$$f \in C^{1,1}(\mathbb{R}), \quad (3.4.4c)$$

$$g \in C^{1,1}(\mathbb{R}^2), \quad (3.4.4d)$$

$$m \leq |\vec{x}_\rho| \leq M \quad \text{in } [0, 1] \times [0, T], \quad \text{for some } m, M \in \mathbb{R}_{>0}, \quad (3.4.4e)$$

$$F \in C^{2,1}(\mathbb{R}^2), \quad (3.4.4f)$$

$$|\nabla F(\vec{p})| = 1, \quad \text{for } \vec{p} \in \{\vec{p} \in \mathbb{R}^2 : F(\vec{p}) = 0\}. \quad (3.4.4g)$$

We assign each element $\vec{x}^h \in [S^h]^2$ a piecewise constant discrete unit tangent and normal, denoted respectively by $\vec{\tau}^h$ and $\vec{\nu}^h$, approximating $\vec{\tau}$ and $\vec{\nu}$ respectively, and on each σ_j we approximate the tangential velocity and the normal velocity, denoted respectively by ψ^h and v^h , approximating ψ and v respectively, which take the form

$$\vec{\tau}^h := \frac{\vec{x}_\rho^h}{|\vec{x}_\rho^h|}, \quad \vec{\nu}^h := (\vec{\tau}^h)^\perp, \quad \psi^h := \langle \vec{x}_t^h, \vec{\tau}^h \rangle, \quad v^h := \langle \vec{x}_t^h, \vec{\nu}^h \rangle, \quad \text{on } \sigma_j, \quad j = 1, \dots, J.$$

We are now in a position to introduce the semi-discrete finite element form of (3.4.2a)–(3.4.2b). Find $\vec{x}^h : [0, 1] \times [0, T] \rightarrow \mathbb{R}^2$ and $w^h : [0, 1] \times [0, T] \rightarrow \mathbb{R}$ such that $\vec{x}^h(\cdot, t) \in [S^h]^2$ and $w^h(\cdot, t) - w_b \in S_0^h$, for $t \in [0, T]$, and

$$\left(|\vec{x}_\rho^h|^2 \left[\alpha \vec{x}_t^h + (1 - \alpha) \langle \vec{x}_t^h, \vec{\nu}^h \rangle \vec{\nu}^h \right], \vec{\xi}^h \right)^h + \left(\vec{x}_\rho^h, \vec{\xi}_\rho^h \right)$$

$$= \left(|\bar{x}_\rho^h|^2 f(w^h) \bar{v}^h, \bar{\xi}^h \right)^h + \left[\langle \bar{x}_\rho^h, \nabla F(\bar{x}^h) \rangle \langle \bar{\xi}^h, \nabla F(\bar{x}^h) \rangle \right]_0^1, \quad \forall \bar{\xi}^h \in [S^h]^2, \quad (3.4.5a)$$

$$\begin{aligned} & \left((|\bar{x}_\rho^h| w^h)_t, \eta^h \right)^h + d \left(\frac{w_\rho^h}{|\bar{x}_\rho^h|}, \eta_\rho^h \right) + \left(\psi^h w^h, \eta_\rho^h \right)^h \\ & = \left(|\bar{x}_\rho^h| g(v^h, w^h), \eta^h \right)^h, \quad \forall \eta^h \in S_0^h, \end{aligned} \quad (3.4.5b)$$

as well as the semi-discrete equivalent of (3.1.2c)

$$F(\bar{x}^h(\rho, t)) = 0, \quad \text{for } \rho \in \{0, 1\}, t \in [0, T]. \quad (3.4.5c)$$

Similar to **Model** \mathcal{M}_1 , a consequence of (3.4.5c) is that, in view of (3.4.4g), we have

$$|\nabla F(\bar{x}^h(\rho, t))| = 1, \quad \text{for } \rho \in \{0, 1\}, t \in [0, T] \quad (3.4.6)$$

and, by taking the time derivative of (3.4.5c), we have

$$\langle \bar{x}_t^h(\rho, t), \nabla F(\bar{x}^h(\rho, t)) \rangle = 0, \quad \text{for } \rho \in \{0, 1\}, t \in [0, T] \quad (3.4.7)$$

which is the semi-discrete equivalent of (3.4.3).

Remark 3.22. *Standard ODE theory implies that there exists a unique solution (\bar{x}^h, w^h) of (3.4.5a)–(3.4.5b) on some time interval $[0, T_h]$, $T_h > 0$, [42, 97].*

3.4.1 H^1 error bounds for **Model** \mathcal{M}_2

In this section we will prove the H^1 error bounds for **Model** \mathcal{M}_2 . We look to prove the following theorem.

Theorem 3.23.

Let $\bar{x}^h(\cdot, 0) = I^h \bar{x}^0(\cdot) \in [S^h]^2$ and $w^h(\cdot, 0) = I^h w^0(\cdot) \in S^h$. There exists $h^ > 0$ such that for all $h \in (0, h^*]$ the semi-discrete problem (3.4.5a)–(3.4.5c) has the following error bounds*

$$\sup_{t \in [0, T]} \left[|\bar{x} - \bar{x}^h|_1^2 + |w - w^h|_0^2 \right] + \int_0^T \left[|\bar{x}_t - \bar{x}_t^h|_0^2 + |w - w^h|_0^2 \right] dt \leq C h^2, \quad (3.4.8)$$

for some $C > 0$ independent of h .

This is work presented in [110], but here we use more detail, if necessary, for the calculations. The proof of this theorem combines some of the techniques used in [6] and an extension of the techniques used in [42], as well as ideas from [40, 97]. Before we

begin with the proof of Theorem 3.23 we introduce some notation and the parameter that underpins the proof. We define

$$\begin{aligned}\vec{x} - \vec{x}^h &= (\vec{x} - I^h \vec{x}) + (I^h \vec{x} - \vec{x}^h) =: (I - I^h) \vec{x} + \vec{\theta}^h, \\ w - w^h &= (w - I^h w) + (I^h w - w^h) =: (I - I^h) w + \zeta^h,\end{aligned}$$

and we adapt arguments presented in [40] to define

$$\begin{aligned}T_h^* &:= \sup \left\{ t \in [0, T] : (\vec{x}^h, w^h) \text{ solves (3.4.5a), (3.4.5c) and (3.4.5b),} \right. \\ &\quad \frac{m}{2} \leq |\vec{x}_\rho^h| \leq 2M \quad \text{in } [0, 1] \times [0, t], \\ &\quad \|w^h\|_{C([0,t]; L^\infty(\mathcal{I}))} \leq 2C_w \|w\|_{C([0,T]; H^1(\mathcal{I}))}, \text{ and} \\ &\quad \left. \sup_{s \in [0,t]} e^{-\gamma s} \left[|\vec{\theta}_1^h|^2 + |\zeta^h|_0^2 \right] + \int_0^t e^{-\gamma s} \left[|\vec{\theta}_t^h|_0^2 + |\zeta^h|_1^2 \right] ds < 2C_1 h^2 \right\}.\end{aligned}$$

Moreover, we set

$$e^{\gamma T} (h^*)^{\frac{1}{2}} \leq \min \left\{ \frac{1}{2C_1}, \beta \right\} \quad \text{and} \quad \gamma \geq \max \left\{ 1, \frac{32C_2}{m^2 \alpha} \right\}. \quad (3.4.9)$$

In order to prove Theorem 3.23 we prove (3.4.12a)–(3.4.12c) on $[0, T_h^*]$, for C independent of T_h^* , thus enabling us to show that $T_h^* = T$ and hence proving the theorem. One can see this argument as a continuous version of an inductive proof. In order to do this we need to make sure the parameters are chosen carefully so that there are no hidden relations. First it is assumed that h^* and β can be chosen appropriately small independently of T_h^* , for the bound in (3.4.9) and (3.4.102), which puts a bound on h . We first define C_2 independently of T_h^* , h , β , h^* and γ , as a constant that depends on bounds on the true solutions \vec{x} and w and the function F , inverse estimates and interpolation results, and T . We use C_2 to find the bound on γ in (3.4.9) which is independent T_h^* , h and h^* . In a similar way to C_2 , we define C_3 as a constant that is independent T_h^* , h , β and γ . We use C_3 to find a bound on ω independent of T_h^* , h , β and γ , which enables us to combine the results in Lemmas 3.24 and 3.25. In a similar way to the proof of Theorem 3.13, we find C_1 independent of T_h^* , h and β . Finally, in order to prove that $T = T_h^*$, we choose β appropriately independently of T_h^* and h .

The main part of the proof of Theorem 3.23 is split into the following two lemmas:

Lemma 3.24.

For $t \in [0, T_h^*)$, we have

$$\begin{aligned}\frac{1}{4} e^{-\gamma t} |\vec{\theta}_1^h|^2 + \frac{m^2 \alpha}{16} \int_0^t e^{-\gamma s} |\vec{\theta}_t^h|_0^2 ds \\ \leq C_2 \int_0^t e^{-\gamma s} \left[h^2 + |\zeta^h|_0^2 + |\vec{\theta}_1^h|^2 + h^{-1} |\vec{\theta}_{0,\infty}^h|^4 \right] ds.\end{aligned} \quad (3.4.10)$$

Lemma 3.25.

For $h \in (0, h^*)$ and $t \in [0, T_h^*)$, we have

$$\frac{m}{4} e^{-\gamma t} |\zeta^h|_0^2 + \frac{1}{4M} \int_0^t e^{-\gamma s} |\zeta^h|_1^2 ds \leq C_3 \int_0^t e^{-\gamma s} \left[h^2 + |\bar{\theta}_t^h|_0^2 + |\zeta^h|_0^2 + |\bar{\theta}^h|_1^2 \right] ds. \quad (3.4.11)$$

Before proving Lemmas 3.24 and 3.25 and subsequently Theorem 3.23 we note some useful results. By the definition of T_h^* we have the following bounds

$$\frac{m}{2} \leq |\bar{x}^h| \leq 2M \quad \text{in } [0, 1] \times [0, T_h^*), \quad (3.4.12a)$$

$$\|w^h\|_{C([0, T_h^*]; L^\infty(\mathcal{I}))} \leq 2C_w \|w\|_{C([0, T]; H^1(\mathcal{I}))}, \quad (3.4.12b)$$

$$\sup_{s \in [0, T_h^*)} e^{-\gamma s} \left[|\bar{\theta}^h|_1^2 + |\zeta^h|_0^2 \right] + \int_0^{T_h^*} e^{-\gamma s} \left[|\bar{\theta}_t^h|_0^2 + |\zeta^h|_1^2 \right] ds < 2C_1 h^2. \quad (3.4.12c)$$

Using (3.1.5b) and (3.4.4a), we have

$$\begin{aligned} |\bar{x} - \bar{x}^h|_1 &\leq |(I - I^h)\bar{x}|_1 + |\bar{\theta}^h|_1 \\ &\leq C h |\bar{x}|_2 + |\bar{\theta}^h|_1 \leq C h \|\bar{x}\|_{W^{0, \infty}(0, T; [H^2(\mathcal{I}))^2)} + |\bar{\theta}^h|_1 \leq C \left[h + |\bar{\theta}^h|_1 \right], \end{aligned} \quad (3.4.13)$$

as well as

$$\begin{aligned} |\bar{x}_t - \bar{x}_t^h|_0 &\leq |(I - I^h)\bar{x}_t|_0 + |\bar{\theta}_t^h|_0 \\ &\leq C h |\bar{x}_t|_1 + |\bar{\theta}_t^h|_0 \leq C h \|\bar{x}\|_{W^{1, \infty}(0, T; [H^1(\mathcal{I}))^2)} + |\bar{\theta}_t^h|_0 \leq C \left[h + |\bar{\theta}_t^h|_0 \right]. \end{aligned} \quad (3.4.14)$$

Using (3.1.6a), (3.4.4a), (3.1.5a) and (3.1.4a), we have

$$\begin{aligned} |\bar{x}_t^h|_s &\leq |I^h \bar{x}_t|_s + |\bar{\theta}_t^h|_s \\ &\leq \|\bar{x}\|_{W^{1, \infty}(0, T; [H^s(\mathcal{I}))^2)} + C h^{-s} |\bar{\theta}_t^h|_0 \leq C \left[1 + h^{-s} |\bar{\theta}_t^h|_0 \right], \quad \text{for } s = 0, 1. \end{aligned} \quad (3.4.15)$$

Using (3.1.5b) and (3.4.4b), we have

$$\begin{aligned} |w - w^h|_0 &\leq |(I - I^h)w|_0 + |\zeta^h|_0 \\ &\leq C h |w|_1 + |\zeta^h|_0 \leq C h \|w\|_{C([0, T]; H^1(\mathcal{I}))} + |\zeta^h|_0 \leq C \left[h + |\zeta^h|_0 \right]. \end{aligned} \quad (3.4.16)$$

Using (3.1.6a), (3.4.4a), (3.1.5a) and (3.1.4a), we have

$$\begin{aligned} |w^h|_1 &\leq |I^h w|_1 + |\zeta^h|_1 \\ &\leq \|w\|_{C([0, T]; H^1(\mathcal{I}))} + C h^{-1} |\zeta^h|_0 \leq C h^{-1} \left[h + |\zeta^h|_0 \right]. \end{aligned} \quad (3.4.17)$$

Using (3.4.4e), (3.4.12a) and (3.4.13), we have

$$\left| \frac{1}{|\bar{x}_\rho|} - \frac{1}{|\bar{x}_\rho^h|} \right|_0 \leq \left| \frac{|\bar{x}_\rho| - |\bar{x}_\rho^h|}{|\bar{x}_\rho| |\bar{x}_\rho^h|} \right|_0 \leq \frac{4}{m^2} |\bar{x} - \bar{x}^h|_1 \leq C \left[h + |\bar{\theta}^h|_1 \right]. \quad (3.4.18)$$

Using (3.4.4e) and (3.4.13), we have

$$|\vec{\tau} - \vec{\tau}^h|_0 \leq \left| \vec{x}_\rho^h \frac{|\vec{x}_\rho^h| - |\vec{x}_\rho|}{|\vec{x}_\rho| |\vec{x}_\rho^h|} \right|_0 + \left| \frac{1}{|\vec{x}_\rho|} (\vec{x}_\rho - \vec{x}_\rho^h) \right|_0 \leq \frac{2}{m} |\vec{x} - \vec{x}^h|_1 \leq C [h + |\vec{\theta}^h|_1]$$

and hence it can be seen that

$$|\vec{\tau} - \vec{\tau}^h|_0 + |\vec{\nu} - \vec{\nu}^h|_0 \leq C [h + |\vec{\theta}^h|_1]. \quad (3.4.19)$$

Using (3.4.19), (3.4.14), (3.1.11) and (3.4.4a), we have

$$\begin{aligned} |\psi - \psi^h|_0 &= |\langle \vec{x}_t, \vec{\tau} \rangle - \langle \vec{x}_t^h, \vec{\tau}^h \rangle|_0 \\ &\leq |\langle \vec{x}_t, \vec{\tau} - \vec{\tau}^h \rangle|_0 + |\langle \vec{x}_t - \vec{x}_t^h, \vec{\tau}^h \rangle|_0 \\ &\leq |\vec{x}_t|_{0,\infty} |\vec{\tau} - \vec{\tau}^h|_0 + |\vec{x}_t - \vec{x}_t^h|_0 \\ &\leq C \|\vec{x}\|_{W^{1,\infty}(0,T;[H^1(\mathcal{I}))^2)} [h + |\vec{\theta}^h|_1] + C [h + |\vec{\theta}^h|_0] \leq C [h + |\vec{\theta}^h|_0 + |\vec{\theta}^h|_1] \end{aligned}$$

and hence it can be seen that

$$|\psi - \psi^h|_0 + |v - v^h|_0 \leq C [h + |\vec{\theta}^h|_0 + |\vec{\theta}^h|_1]. \quad (3.4.20)$$

Proof of Lemma 3.24: Taking $\vec{\xi} = \vec{\xi}^h$ and subtracting (3.4.5a) from (3.4.2a) we have

$$\begin{aligned} &\left[\left(|\vec{x}_\rho|^2 [\alpha \vec{x}_t + (1-\alpha) \langle \vec{x}_t, \vec{\nu} \rangle \vec{\nu}], \vec{\xi}^h \right) - \left(|\vec{x}_\rho^h|^2 [\alpha \vec{x}_t^h + (1-\alpha) \langle \vec{x}_t^h, \vec{\nu}^h \rangle \vec{\nu}^h], \vec{\xi}^h \right)^h \right] \\ &+ \left[\left(\vec{x}_\rho, \vec{\xi}_\rho^h \right) - \left(\vec{x}_\rho^h, \vec{\xi}_\rho^h \right) \right] = \left[\left(|\vec{x}_\rho|^2 f(w) \vec{\nu}, \vec{\xi}^h \right) - \left(|\vec{x}_\rho^h|^2 f(w^h) \vec{\nu}^h, \vec{\xi}^h \right)^h \right] \\ &+ \left[\langle \vec{x}_\rho, \nabla F(\vec{x}) \rangle \langle \vec{\xi}, \nabla F(\vec{x}) \rangle - \langle \vec{x}_\rho^h, \nabla F(\vec{x}^h) \rangle \langle \vec{\xi}^h, \nabla F(\vec{x}^h) \rangle \right]_0^1. \end{aligned}$$

Noting (3.3.20), which states that

$$\left(\vec{x}_\rho - I^h \vec{x}_\rho, \vec{\xi}_\rho^h \right) = 0,$$

by setting $\xi^h = \vec{\theta}_t^h$, we have

$$\begin{aligned} &\left(|\vec{x}_\rho^h|^2 [\alpha \vec{\theta}_t^h + (1-\alpha) \langle \vec{\theta}_t^h, \vec{\nu}^h \rangle \vec{\nu}^h], \vec{\theta}_t^h \right)^h + \left(\vec{\theta}_{\rho,t}^h, \vec{\theta}_t^h \right) \\ &= \left[\left(|\vec{x}_\rho^h|^2 [\alpha I^h \vec{x}_t + (1-\alpha) \langle I^h \vec{x}_t, \vec{\nu}^h \rangle \vec{\nu}^h], \vec{\theta}_t^h \right)^h \right. \\ &\quad \left. - \left(|\vec{x}_\rho|^2 [\alpha \vec{x}_t + (1-\alpha) \langle \vec{x}_t, \vec{\nu} \rangle \vec{\nu}], \vec{\theta}_t^h \right) \right] \\ &+ \left[\left(|\vec{x}_\rho|^2 f(w) \vec{\nu}, \vec{\theta}_t^h \right) - \left(|\vec{x}_\rho^h|^2 f(w^h) \vec{\nu}^h, \vec{\theta}_t^h \right)^h \right] \\ &+ \left[\langle \vec{x}_\rho, \nabla F(\vec{x}) \rangle \langle \vec{\theta}_t^h, \nabla F(\vec{x}) \rangle - \langle \vec{x}_\rho^h, \nabla F(\vec{x}^h) \rangle \langle \vec{\theta}_t^h, \nabla F(\vec{x}^h) \rangle \right]_0^1 =: \sum_{i=1}^3 T_i. \quad (3.4.21) \end{aligned}$$

It is easy to see that, using (3.4.12a) and (3.1.6a), we have

$$\begin{aligned} & \left(|\bar{x}_\rho^h|^2 \left[\alpha \bar{\theta}_t^h + (1 - \alpha) \langle \bar{\theta}_t^h, \bar{v}^h \rangle \bar{v}^h \right], \bar{\theta}_t^h \right)^h + \left(\bar{\theta}_{\rho,t}^h, \bar{\theta}_t^h \right) \\ & \geq \frac{m^2}{4} \left[\alpha \|\bar{\theta}_t^h\|_h^2 + (1 - \alpha) \|\langle \bar{\theta}_t^h, \bar{v}^h \rangle\|_h^2 \right] + \frac{1}{2} \frac{d}{dt} |\bar{\theta}^h|_1^2 \geq \frac{m^2 \alpha}{4} |\bar{\theta}_t^h|_0^2 + \frac{1}{2} \frac{d}{dt} |\bar{\theta}^h|_1^2. \end{aligned} \quad (3.4.22)$$

We now proceed to bound T_1 , T_2 and T_3 in (3.4.21), beginning with T_1 .

$$\begin{aligned} T_1 &= \left(|\bar{x}_\rho^h|^2 \left[\alpha I^h \bar{x}_t + (1 - \alpha) \langle I^h \bar{x}_t, \bar{v}^h \rangle \bar{v}^h \right], \bar{\theta}_t^h \right)^h - \left(|\bar{x}_\rho|^2 \left[\alpha \bar{x}_t + (1 - \alpha) \langle \bar{x}_t, \bar{v} \rangle \bar{v} \right], \bar{\theta}_t^h \right) \\ &= \left[\left(\left[|\bar{x}_\rho^h|^2 - |\bar{x}_\rho|^2 \right] \left[\alpha \bar{x}_t + (1 - \alpha) \langle \bar{x}_t, \bar{v} \rangle \bar{v} \right], \bar{\theta}_t^h \right) \right. \\ &\quad \left. + (1 - \alpha) \left(|\bar{x}_\rho^h|^2 \left[\langle \bar{x}_t, \bar{v}^h - \bar{v} \rangle \bar{v} + \langle \bar{x}_t, \bar{v}^h \rangle (\bar{v}^h - \bar{v}) \right], \bar{\theta}_t^h \right) \right] \\ &\quad + \left[\left(|\bar{x}_\rho^h|^2 \left[\alpha I^h \bar{x}_t + (1 - \alpha) \langle I^h \bar{x}_t, \bar{v}^h \rangle \bar{v}^h \right], \bar{\theta}_t^h \right)^h \right. \\ &\quad \left. - \left(|\bar{x}_\rho^h|^2 \left[\alpha I^h \bar{x}_t + (1 - \alpha) \langle I^h \bar{x}_t, \bar{v}^h \rangle \bar{v}^h \right], \bar{\theta}_t^h \right) \right] \\ &\quad + \left(|\bar{x}_\rho^h|^2 \left[\alpha (I^h - I) \bar{x}_t + (1 - \alpha) \langle (I^h - I) \bar{x}_t, \bar{v}^h \rangle \bar{v}^h \right], \bar{\theta}_t^h \right) =: \sum_{i=1}^3 T_{1,i}. \end{aligned} \quad (3.4.23)$$

Using (3.4.4a), (3.4.4e), (3.4.12a), (3.4.13), (3.1.11) and (3.4.19), we see that

$$\begin{aligned} T_{1,1} &= \left(\left[|\bar{x}_\rho^h|^2 - |\bar{x}_\rho|^2 \right] \left[\alpha \bar{x}_t + (1 - \alpha) \langle \bar{x}_t, \bar{v} \rangle \bar{v} \right], \bar{\theta}_t^h \right) \\ &\quad + (1 - \alpha) \left(|\bar{x}_\rho^h|^2 \left[\langle \bar{x}_t, \bar{v}^h - \bar{v} \rangle \bar{v} + \langle \bar{x}_t, \bar{v}^h \rangle (\bar{v}^h - \bar{v}) \right], \bar{\theta}_t^h \right) \\ &\leq |\bar{x}_t|_{0,\infty} \left[\left| |\bar{x}_\rho| + |\bar{x}_\rho^h| \right|_{0,\infty} |\bar{x} - \bar{x}^h|_1 + 8M^2(1 - \alpha) |\bar{v} - \bar{v}^h|_0 \right] |\bar{\theta}_t^h|_0 \\ &\leq C \|\bar{x}\|_{W^{1,\infty}(0,T;[H^1(\mathcal{I})]^2)} \left[h + |\bar{\theta}^h|_1 \right] \leq C \left[h + |\bar{\theta}^h|_1 \right] |\bar{\theta}_t^h|_0. \end{aligned} \quad (3.4.24)$$

Using (3.1.6b), (3.1.5d), (3.4.12a) and (3.4.4a), we see that

$$\begin{aligned} T_{1,2} &= \left(|\bar{x}_\rho^h|^2 \left[\alpha I^h \bar{x}_t + (1 - \alpha) \langle I^h \bar{x}_t, \bar{v}^h \rangle \bar{v}^h \right], \bar{\theta}_t^h \right)^h \\ &\quad - \left(|\bar{x}_\rho^h|^2 \left[\alpha I^h \bar{x}_t + (1 - \alpha) \langle I^h \bar{x}_t, \bar{v}^h \rangle \bar{v}^h \right], \bar{\theta}_t^h \right) \\ &\leq C h \sum_{j=1}^J \left| I_j^h \bar{x}_t \right|_{1,\sigma_j} \left| |\bar{x}_\rho^h|^2 \left[\bar{\theta}_t^h + \langle \bar{\theta}_t^h, \bar{v}^h \rangle \bar{v}^h \right] \right|_{0,\sigma_j} \\ &\leq C h |\bar{x}_t|_1 |\bar{\theta}_t^h|_0 \leq C h \|\bar{x}\|_{W^{1,\infty}(0,T;[H^1(\mathcal{I})]^2)} |\bar{\theta}_t^h|_0 \leq C h |\bar{\theta}_t^h|_0, \end{aligned} \quad (3.4.25)$$

where $|\eta|_{1,\sigma_j}$ is the seminorm of the space $H^1(\sigma_j)$. Using (3.4.12a), (3.1.5b) and (3.4.4a), we see that

$$\begin{aligned} T_{1,3} &= \left(|\bar{x}_\rho^h|^2 \left[\alpha (I^h - I) \bar{x}_t + (1 - \alpha) \langle (I^h - I) \bar{x}_t, \bar{v}^h \rangle \bar{v}^h \right], \bar{\theta}_t^h \right) \\ &\leq C h |\bar{x}_t|_1 |\bar{\theta}_t^h|_0 \leq C h \|\bar{x}\|_{W^{1,\infty}(0,T;[H^1(\mathcal{I})]^2)} |\bar{\theta}_t^h|_0 \leq C h |\bar{\theta}_t^h|_0. \end{aligned} \quad (3.4.26)$$

Combining (3.4.23)–(3.4.26) and using (3.1.8) we have

$$|T_1| \leq \frac{m^2 \alpha}{24} |\bar{\theta}_t^h|_0^2 + C \left[h^2 + |\bar{\theta}^h|_1^2 \right]. \quad (3.4.27)$$

We now bound T_2 .

$$\begin{aligned} T_2 &= \left(|\bar{x}_\rho|^2 f(w) \bar{v}, \bar{\theta}_t^h \right) - \left(|\bar{x}_\rho^h|^2 f(w^h) \bar{v}^h, \bar{\theta}_t^h \right)^h \\ &= \left(\left[|\bar{x}_\rho|^2 - |\bar{x}_\rho^h|^2 \right] f(w) \bar{v} + |\bar{x}_\rho^h|^2 f(w) \left[\bar{v} - \bar{v}^h \right], \bar{\theta}_t^h \right) + \left(|\bar{x}_\rho^h|^2 \left[f(w) - f(w^h) \right] \bar{v}^h, \bar{\theta}_t^h \right) \\ &\quad + \left[\left(|\bar{x}_\rho^h|^2 \left[(I - I^h) f(w^h) \right] \bar{v}^h, \bar{\theta}_t^h \right) + \left(|\bar{x}_\rho^h|^2 \left[(I^h - I) f(w^h) \right] \bar{v}^h, \bar{\theta}_t^h \right)^h \right] \\ &\quad + \left[\left(|\bar{x}_\rho^h|^2 I^h(f(w^h)) \bar{v}^h, \bar{\theta}_t^h \right) - \left(|\bar{x}_\rho^h|^2 I^h(f(w^h)) \bar{v}^h, \bar{\theta}_t^h \right)^h \right] =: \sum_{i=1}^4 T_{2,i}. \end{aligned} \quad (3.4.28)$$

Using (3.4.4e), (3.4.12a), (3.4.13), (3.4.4c), (3.4.19) and (3.4.16), we see that

$$\begin{aligned} T_{2,1} &= \left(\left[|\bar{x}_\rho|^2 - |\bar{x}_\rho^h|^2 \right] f(w) \bar{v} + |\bar{x}_\rho^h|^2 f(w) \left[\bar{v} - \bar{v}^h \right], \bar{\theta}_t^h \right) \\ &\leq |f|_{0,\infty} \left[\left| |\bar{x}_\rho| + |\bar{x}_\rho^h| \right|_{0,\infty} |\bar{x} - \bar{x}^h|_1 + 4M^2 |\bar{v} - \bar{v}^h|_0 \right] |\bar{\theta}_t^h|_0 \\ &\leq C \left[h + |\bar{\theta}^h|_1 \right] |\bar{\theta}_t^h|_0, \end{aligned} \quad (3.4.29)$$

and

$$\begin{aligned} T_{2,2} &= \left(|\bar{x}_\rho^h|^2 \left[f(w) - f(w^h) \right] \bar{v}^h, \bar{\theta}_t^h \right) \\ &\leq 4M^2 L_f |w - w^h|_0 |\bar{\theta}_t^h|_0 \leq C \left[h + |\zeta^h|_0 \right] |\bar{\theta}_t^h|_0. \end{aligned} \quad (3.4.30)$$

Using (3.4.12a), (3.1.6a), (3.1.6b), (3.1.5b), (3.4.12b), (3.4.4c), and (3.4.17), we see that

$$\begin{aligned} T_{2,3} &= \left(|\bar{x}_\rho^h|^2 \left[(I - I^h) f(w^h) \right] \bar{v}^h, \bar{\theta}_t^h \right) + \left(|\bar{x}_\rho^h|^2 \left[(I^h - I) f(w^h) \right] \bar{v}^h, \bar{\theta}_t^h \right)^h \\ &\leq C h |f(w^h)|_1 |\bar{\theta}_t^h|_0 \leq C h |f'(w^h)|_{0,\infty} |w^h|_1 |\bar{\theta}_t^h|_0 \leq C \left[h + |\zeta^h|_0 \right] |\bar{\theta}_t^h|_0. \end{aligned} \quad (3.4.31)$$

and

$$\begin{aligned} T_{2,4} &= \left(|\bar{x}_\rho^h|^2 I^h(f(w^h)) \bar{v}^h, \bar{\theta}_t^h \right) - \left(|\bar{x}_\rho^h|^2 I^h(f(w^h)) \bar{v}^h, \bar{\theta}_t^h \right)^h \\ &\leq C h \sum_{j=1}^J \left| I^h(f(w^h)) \right|_{1,\sigma_j} \left| |\bar{x}_\rho^h|^2 \langle \bar{\theta}_t^h, \bar{v}^h \rangle \right|_{0,\sigma_j} \\ &\leq C h |f(w^h)|_1 |\bar{\theta}_t^h|_0 \leq C \left[h + |\zeta^h|_0 \right] |\bar{\theta}_t^h|_0. \end{aligned} \quad (3.4.32)$$

Combining (3.4.28)–(3.4.32) and using (3.1.8), we have

$$|T_2| \leq \frac{m^2 \alpha}{24} |\bar{\theta}_t^h|_0^2 + C \left[h^2 + |\zeta^h|_0^2 + |\bar{\theta}^h|_1^2 \right]. \quad (3.4.33)$$

We now bound T_3 , to this end we set

$$b := \langle \bar{x}_\rho, \nabla F(\bar{x}) \rangle, \quad b^h := \langle \bar{x}_\rho^h, \nabla F(\bar{x}^h) \rangle$$

and thus, using (3.4.3), (3.4.7) and (3.1.7), we see that

$$\begin{aligned}
T_3 &= \left[b \langle \bar{\theta}_t^h, \nabla F(\bar{x}) \rangle - b^h \langle \bar{\theta}_t^h, \nabla F(\bar{x}^h) \rangle \right]_0^1 \\
&= \left[b \langle \bar{\theta}_t^h, \nabla F(\bar{x}) - \nabla F(\bar{x}^h) \rangle \right]_0^1 + \left[(b - b^h) \langle \bar{x}_t, \nabla F(\bar{x}^h) - \nabla F(\bar{x}) \rangle \right]_0^1 \\
&=: T_{3,1} + T_{3,2}.
\end{aligned} \tag{3.4.34}$$

Using (3.4.4a), (3.4.4e)–(3.4.4g), and noting (3.1.7), for $\rho \in \{0, 1\}$ and $t \in [0, T]$, we obtain

$$|b(\rho, t)| \leq M, \tag{3.4.35a}$$

$$|b_t(\rho, t)| \leq |\bar{x}_{\rho,t}(\rho, t)| + M |D^2 F(\bar{x}(\rho, t)) \bar{x}_t(\rho, t)| \leq C \|\bar{x}\|_{W^{1,\infty}(0,T;[H^1(\mathcal{X})]^2)} \leq C, \tag{3.4.35b}$$

as well as

$$|\nabla F(\bar{x}(\rho, t)) - \nabla F(\bar{x}^h(\rho, t))| \leq L_{\nabla F} |\bar{x}(\rho, t) - \bar{x}^h(\rho, t)| \leq C |\bar{\theta}^h(\cdot, t)|_{0,\infty}. \tag{3.4.35c}$$

We now bound $T_{3,1}$. Using (3.1.13), (3.4.35a), (3.4.35b), (3.4.4f), (3.1.5a) and (3.1.4a), we see that

$$\begin{aligned}
T_{3,1} &= \left[b \langle \bar{\theta}_t^h, \nabla F(\bar{x}) - \nabla F(\bar{x}^h) \rangle \right]_0^1 \\
&= \left[b \langle \bar{\theta}_t^h, D^2 F(\bar{x}) \bar{\theta}^h \rangle + b \int_0^1 \langle \bar{\theta}_t^h, (D^2 F(s\bar{x} + (1-s)\bar{x}^h) - D^2 F(\bar{x})) \bar{\theta}^h \rangle ds \right]_0^1 \\
&= \left[\frac{1}{2} \frac{d}{dt} \left(b \langle \bar{\theta}^h, D^2 F(\bar{x}) \bar{\theta}^h \rangle \right) - \frac{1}{2} b_t \langle \bar{\theta}^h, D^2 F(\bar{x}) \bar{\theta}^h \rangle - \frac{1}{2} b \langle \bar{\theta}^h, \frac{d}{dt} (D^2 F(\bar{x})) \bar{\theta}^h \right. \\
&\quad \left. + b \int_0^1 \langle \bar{\theta}_t^h, (D^2 F(s\bar{x} + (1-s)\bar{x}^h) - D^2 F(\bar{x})) \bar{\theta}^h \rangle ds \right]_0^1 \\
&\leq \frac{1}{2} \frac{d}{dt} \left[b \langle \bar{\theta}^h, D^2 F(\bar{x}) \bar{\theta}^h \rangle \right]_0^1 + C |\bar{\theta}^h|_{0,\infty}^2 \left[1 + |\bar{\theta}_t^h|_{0,\infty} \right] \\
&\leq \frac{1}{2} \frac{d}{dt} \left[b \langle \bar{\theta}^h, D^2 F(\bar{x}) \bar{\theta}^h \rangle \right]_0^1 + C |\bar{\theta}^h|_{0,\infty}^2 \left[1 + h^{-\frac{1}{2}} |\bar{\theta}_t^h|_0 \right].
\end{aligned} \tag{3.4.36}$$

Denoting $\bar{x}(0, t) := \bar{x}_0(t)$, taking $\bar{\xi} = (1 - \rho) \nabla F(\bar{x}_0)$ in (3.4.2a) and using (3.4.4g), we have

$$\begin{aligned}
&(|\bar{x}_\rho|^2 [\alpha \bar{x}_t + (1 - \alpha) \langle \bar{x}_t, \bar{\nu} \rangle \bar{\nu}], (1 - \rho) \nabla F(\bar{x}_0)) - (\bar{x}_\rho, \nabla F(\bar{x}_0)) \\
&= (|\bar{x}_\rho|^2 f(w) \bar{\nu}, (1 - \rho) \nabla F(\bar{x}_0)) + [(1 - \rho) \langle \bar{x}_\rho, \nabla F(\bar{x}) \rangle \langle \nabla F(\bar{x}_0), \nabla F(\bar{x}) \rangle]_0^1 \\
&= (|\bar{x}_\rho|^2 f(w) \bar{\nu}, (1 - \rho) \nabla F(\bar{x}_0)) - b(0, t),
\end{aligned}$$

and hence

$$\begin{aligned}
b(0, t) &= (\bar{x}_\rho, \nabla F(\bar{x}_0)) + (|\bar{x}_\rho|^2 f(w) \bar{\nu}, (1 - \rho) \nabla F(\bar{x}_0)) \\
&\quad - (|\bar{x}_\rho|^2 [\alpha \bar{x}_t + (1 - \alpha) \langle \bar{x}_t, \bar{\nu} \rangle \bar{\nu}], (1 - \rho) \nabla F(\bar{x}_0)).
\end{aligned} \tag{3.4.37}$$

Similarly, denoting $\bar{x}^h(0, t) := \bar{x}_0^h(t)$ and taking $\bar{\xi}^h = (1 - \rho) \nabla F(\bar{x}_0^h)$ in (3.4.5a), using (3.4.6), we see that

$$b^h(0, t) = \left(\bar{x}_\rho^h, \nabla F(\bar{x}_0^h) \right) + \left(|\bar{x}_\rho^h|^2 f(w^h) \bar{\nu}^h, (1 - \rho) \nabla F(\bar{x}_0^h) \right)^h$$

$$- \left(|\vec{x}_\rho^h|^2 \left[\alpha \vec{x}_t^h + (1 - \alpha) \langle \vec{x}_t^h, \vec{v}^h \rangle \vec{v}^h \right], (1 - \rho) \nabla F(\vec{x}_0^h) \right)^h. \quad (3.4.38)$$

Hence, we have

$$\begin{aligned} b(0, t) - b^h(0, t) &= \left[(\vec{x}_\rho, \nabla F(\vec{x}_0)) - (\vec{x}_\rho^h, \nabla F(\vec{x}_0^h)) \right] \\ &+ \left[\left(|\vec{x}_\rho|^2 f(w) \vec{v}, (1 - \rho) \nabla F(\vec{x}_0) \right) - \left(|\vec{x}_\rho^h|^2 f(w^h) \vec{v}^h, (1 - \rho) \nabla F(\vec{x}_0^h) \right)^h \right] \\ &+ \left[\left(|\vec{x}_\rho^h|^2 \left[\alpha \vec{x}_t^h + (1 - \alpha) \langle \vec{x}_t^h, \vec{v}^h \rangle \vec{v}^h \right], (1 - \rho) \nabla F(\vec{x}_0^h) \right)^h \right. \\ &\quad \left. - \left(|\vec{x}_\rho|^2 \left[\alpha \vec{x}_t + (1 - \alpha) \langle \vec{x}_t, \vec{v} \rangle \vec{v} \right], (1 - \rho) \nabla F(\vec{x}_0) \right) \right] =: \sum_{i=1}^3 B_i. \end{aligned} \quad (3.4.39)$$

Starting with B_1 , using (3.3.20), (3.4.4a), (3.4.35c) and (3.4.6), we have

$$\begin{aligned} B_1 &= (\vec{x}_\rho, \nabla F(\vec{x}_0)) - (\vec{x}_\rho^h, \nabla F(\vec{x}_0^h)) \\ &= (\vec{x}_\rho, \nabla F(\vec{x}_0) - \nabla F(\vec{x}_0^h)) + (\vec{\theta}_\rho^h, \nabla F(\vec{x}_0^h)) \\ &\leq C |\vec{x}|_1 |\vec{\theta}^h|_{0, \infty} + |\vec{\theta}^h|_1 \\ &\leq C \|\vec{x}\|_{W^{0, \infty}(0, T; [H^1(\mathcal{X})]^2)} |\vec{\theta}^h|_{0, \infty} + |\vec{\theta}^h|_1 \leq C \left[|\vec{\theta}^h|_{0, \infty} + |\vec{\theta}^h|_1 \right]. \end{aligned} \quad (3.4.40)$$

We now bound B_2 .

$$\begin{aligned} B_2 &= \left(|\vec{x}_\rho|^2 f(w) \vec{v}, (1 - \rho) \nabla F(\vec{x}_0) \right) - \left(|\vec{x}_\rho^h|^2 f(w^h) \vec{v}^h, (1 - \rho) \nabla F(\vec{x}_0^h) \right)^h \\ &= \left(|\vec{x}_\rho|^2 f(w) \vec{v}, (1 - \rho) \left[\nabla F(\vec{x}_0) - \nabla F(\vec{x}_0^h) \right] \right) \\ &+ \left(|\vec{x}_\rho^h|^2 \left[f(w) - f(w^h) \right] \vec{v}^h, (1 - \rho) \nabla F(\vec{x}_0^h) \right) \\ &+ \left(\left[|\vec{x}_\rho|^2 - |\vec{x}_\rho^h|^2 \right] f(w) \vec{v} + |\vec{x}_\rho^h|^2 f(w) \left[\vec{v} - \vec{v}^h \right], (1 - \rho) \nabla F(\vec{x}_0^h) \right) \\ &+ \left[\left(|\vec{x}_\rho^h|^2 \left[(I - I^h) f(w^h) \right] \vec{v}^h, (1 - \rho) \nabla F(\vec{x}_0^h) \right) \right. \\ &\quad \left. + \left(|\vec{x}_\rho^h|^2 \left[(I^h - I) f(w^h) \right] \vec{v}^h, (1 - \rho) \nabla F(\vec{x}_0^h) \right)^h \right] \\ &+ \left[\left(|\vec{x}_\rho^h|^2 I^h(f(w^h)) \vec{v}^h, (1 - \rho) \nabla F(\vec{x}_0^h) \right) \right. \\ &\quad \left. - \left(|\vec{x}_\rho^h|^2 I^h(f(w^h)) \vec{v}^h, (1 - \rho) \nabla F(\vec{x}_0^h) \right)^h \right] =: \sum_{i=1}^5 B_{2,i}. \end{aligned} \quad (3.4.41)$$

Using (3.4.4e), (3.4.4c), (3.4.4a) and (3.4.35c), we have

$$\begin{aligned} B_{2,1} &= \left(|\vec{x}_\rho|^2 f(w) \vec{v}, (1 - \rho) \left[\nabla F(\vec{x}_0) - \nabla F(\vec{x}_0^h) \right] \right) \\ &\leq M^2 |f(w)|_0 |1 - \rho|_0 \left| \nabla F(\vec{x}_0) - \nabla F(\vec{x}_0^h) \right| \leq C |\vec{\theta}^h|_{0, \infty}. \end{aligned} \quad (3.4.42)$$

Using similar arguments to prove (3.4.29)–(3.4.32), and using (3.4.6), we have

$$B_{2,2} = \left(|\vec{x}_\rho^h|^2 \left[f(w) - f(w^h) \right] \vec{v}^h, (1 - \rho) \nabla F(\vec{x}_0^h) \right)$$

$$\leq C |f(w) - f(w^h)|_0 |1 - \rho|_0 \leq C \left[h + |\zeta^h|_0 \right], \quad (3.4.43)$$

$$\begin{aligned} B_{2,3} &= \left(\left[|\vec{x}_\rho|^2 - |\vec{x}_\rho^h|^2 \right] f(w) \vec{v} + |\vec{x}_\rho^h|^2 f(w) \left[\vec{v} - \vec{v}^h \right], (1 - \rho) \nabla F(\vec{x}_0^h) \right) \\ &\leq C \left[|\vec{x}_\rho - \vec{x}_\rho^h|_0 + |\vec{v} - \vec{v}^h|_0 \right] |1 - \rho|_0 \leq C \left[h + |\vec{\theta}^h|_1 \right], \end{aligned} \quad (3.4.44)$$

$$\begin{aligned} B_{2,4} &= \left(|\vec{x}_\rho^h|^2 \left[(I - I^h) f(w^h) \right] \vec{v}^h, (1 - \rho) \nabla F(\vec{x}_0^h) \right) \\ &\quad + \left(|\vec{x}_\rho^h|^2 \left[(I^h - I) f(w^h) \right] \vec{v}^h, (1 - \rho) \nabla F(\vec{x}_0^h) \right)^h \\ &\leq C \left| (I - I^h) f(w^h) \right|_0 |1 - \rho|_0 \leq C \left[h + |\zeta^h|_0 \right], \end{aligned} \quad (3.4.45)$$

$$\begin{aligned} B_{2,5} &= \left(|\vec{x}_\rho^h|^2 I^h(f(w^h)) \vec{v}^h, (1 - \rho) \nabla F(\vec{x}_0^h) \right) - \left(|\vec{x}_\rho^h|^2 I^h(f(w^h)) \vec{v}^h, (1 - \rho) \nabla F(\vec{x}_0^h) \right)^h \\ &\leq C h |f(w^h)|_1 |1 - \rho|_0 \leq C \left[h + |\zeta^h|_0 \right]. \end{aligned} \quad (3.4.46)$$

Now we bound B_3 .

$$\begin{aligned} B_3 &= \left(|\vec{x}_\rho^h|^2 \left[\alpha \vec{x}_t^h + (1 - \alpha) \langle \vec{x}_t^h, \vec{v}^h \rangle \vec{v}^h \right], (1 - \rho) \nabla F(\vec{x}_0^h) \right)^h \\ &\quad - \left(|\vec{x}_\rho|^2 \left[\alpha \vec{x}_t + (1 - \alpha) \langle \vec{x}_t, \vec{v} \rangle \vec{v} \right], (1 - \rho) \nabla F(\vec{x}_0) \right) \\ &= \left(|\vec{x}_\rho|^2 \left[\alpha \vec{x}_t + (1 - \alpha) \langle \vec{x}_t, \vec{v} \rangle \vec{v} \right], (1 - \rho) \left[\nabla F(\vec{x}_0^h) - \nabla F(\vec{x}_0) \right] \right) \\ &\quad + \left(|\vec{x}_\rho^h|^2 \left[\alpha \left(\vec{x}_t^h - I^h \vec{x}_t \right) + (1 - \alpha) \langle \vec{x}_t^h - I^h \vec{x}_t, \vec{v}^h \rangle \vec{v}^h \right], (1 - \rho) \nabla F(\vec{x}_0^h) \right)^h \\ &\quad + \left[\left(\left[|\vec{x}_\rho^h|^2 - |\vec{x}_\rho|^2 \right] \left[\alpha \vec{x}_t + (1 - \alpha) \langle \vec{x}_t, \vec{v} \rangle \vec{v} \right], (1 - \rho) \nabla F(\vec{x}_0^h) \right) \right. \\ &\quad \left. + (1 - \alpha) \left(|\vec{x}_\rho^h|^2 \left[\langle \vec{x}_t, \vec{v}^h - \vec{v} \rangle \vec{v} + \langle \vec{x}_t, \vec{v}^h \rangle \left(\vec{v}^h - \vec{v} \right) \right], (1 - \rho) \nabla F(\vec{x}_0^h) \right) \right] \\ &\quad + \left(|\vec{x}_\rho^h|^2 \left[\alpha (I^h - I) \vec{x}_t + (1 - \alpha) \langle (I^h - I) \vec{x}_t, \vec{v}^h \rangle \vec{v}^h \right], (1 - \rho) \nabla F(\vec{x}_0^h) \right) \\ &\quad + \left[\left(|\vec{x}_\rho^h|^2 \left[\alpha I^h \vec{x}_t + (1 - \alpha) \langle I^h \vec{x}_t, \vec{v}^h \rangle \vec{v}^h \right], (1 - \rho) \nabla F(\vec{x}_0^h) \right)^h \right. \\ &\quad \left. - \left(|\vec{x}_\rho^h|^2 \left[\alpha I^h \vec{x}_t + (1 - \alpha) \langle I^h \vec{x}_t, \vec{v}^h \rangle \vec{v}^h \right], (1 - \rho) \nabla F(\vec{x}_0^h) \right) \right] \\ &=: \sum_{i=1}^5 B_{3,i}. \end{aligned} \quad (3.4.47)$$

Using (3.4.4e), (3.4.4a) and (3.4.35c), we have

$$\begin{aligned} B_{3,1} &= \left(|\vec{x}_\rho|^2 \left[\alpha \vec{x}_t + (1 - \alpha) \langle \vec{x}_t, \vec{v} \rangle \vec{v} \right], (1 - \rho) \left[\nabla F(\vec{x}_0^h) - \nabla F(\vec{x}_0) \right] \right) \\ &\leq M^2 |\vec{x}_t|_0 |1 - \rho|_0 \left| \nabla F(\vec{x}_0^h) - \nabla F(\vec{x}_0) \right| \leq C |\vec{\theta}^h|_{0,\infty}. \end{aligned} \quad (3.4.48)$$

Using (3.4.12a), (3.4.6) and (3.1.6a), we have

$$\begin{aligned} B_{3,2} &= \left(|\vec{x}_\rho^h|^2 \left[\alpha \left[\vec{x}_t^h - I^h \vec{x}_t \right] + (1 - \alpha) \langle \vec{x}_t^h - I^h \vec{x}_t, \vec{v}^h \rangle \vec{v}^h \right], (1 - \rho) \nabla F(\vec{x}_0^h) \right)^h \\ &\leq C \|\vec{\theta}_t^h\|_h \|1 - \rho\|_h \leq C |\vec{\theta}_t^h|_0. \end{aligned} \quad (3.4.49)$$

Using similar arguments to prove (3.4.24)–(3.4.26), and using (3.4.6), we have

$$\begin{aligned} B_{3,3} &= \left(\left[|\vec{x}_\rho^h|^2 - |\vec{x}_\rho|^2 \right] \left[\alpha \vec{x}_t + (1 - \alpha) \langle \vec{x}_t, \vec{v} \rangle \vec{v} \right], (1 - \rho) \nabla F(\vec{x}_0^h) \right) \\ &\quad + (1 - \alpha) \left(|\vec{x}_\rho^h|^2 \left[\langle x_t, \vec{v}^h - \vec{v} \rangle \vec{v} + \langle x_t, \vec{v}^h \rangle (\vec{v}^h - \vec{v}) \right], (1 - \rho) \nabla F(\vec{x}_0^h) \right) \\ &\leq C \left[|\vec{x}_\rho - \vec{x}_\rho^h|_0 + |\vec{v} - \vec{v}^h|_0 \right] |1 - \rho|_0 \leq C \left[h + |\vec{\theta}^h|_1 \right], \end{aligned} \quad (3.4.50)$$

$$\begin{aligned} B_{3,4} &= \left(|\vec{x}_\rho^h|^2 \left[\alpha (I^h - I) \vec{x}_t + (1 - \alpha) \langle (I^h - I) \vec{x}_t, \vec{v}^h \rangle \vec{v}^h \right], (1 - \rho) \nabla F(\vec{x}_0^h) \right) \\ &\leq C |(I - I^h) \vec{x}_t|_0 |1 - \rho|_0 \leq C h, \end{aligned} \quad (3.4.51)$$

$$\begin{aligned} B_{3,5} &= \left(|\vec{x}_\rho^h|^2 \left[\alpha I^h \vec{x}_t + (1 - \alpha) \langle I^h \vec{x}_t, \vec{v}^h \rangle \vec{v}^h \right], (1 - \rho) \nabla F(\vec{x}_0^h) \right)^h \\ &\quad - \left(|\vec{x}_\rho^h|^2 \left[\alpha I^h \vec{x}_t + (1 - \alpha) \langle I^h \vec{x}_t, \vec{v}^h \rangle \vec{v}^h \right], (1 - \rho) \nabla F(\vec{x}_0^h) \right) \\ &\leq C h |\vec{x}_t|_1 |1 - \rho|_0 \leq C h. \end{aligned} \quad (3.4.52)$$

Combining (3.4.39) with (3.4.40)–(3.4.52), for $t \in [0, T_h^*)$, we have

$$|b(0, t) - b^h(0, t)| \leq C \left[h + |\vec{\theta}^h|_{0, \infty} + |\vec{\theta}_t^h|_0 + |\zeta^h|_0 + |\vec{\theta}^h|_1 \right].$$

We remark that this bound does not depend on ρ and so also holds for $\rho = 1$ and hence, for $t \in [0, T_h^*)$, we have

$$|b(0, t) - b^h(0, t)| + |b(1, t) - b^h(1, t)| \leq C \left[h + |\vec{\theta}^h|_{0, \infty} + |\vec{\theta}_t^h|_0 + |\zeta^h|_0 + |\vec{\theta}^h|_1 \right]. \quad (3.4.53)$$

Hence, using (3.1.11), (3.4.35c), (3.4.53) and (3.4.4a), we have

$$\begin{aligned} T_{3,2} &= \left[(b - b^h) \langle \vec{x}_t, \nabla F(\vec{x}) - \nabla F(\vec{x}^h) \rangle \right]_0^1 \\ &\leq C \|w\|_{W^{1, \infty}(0, T; [H^1(X)]^2)} |\vec{\theta}^h|_{0, \infty} \left[|b(0, t) - b^h(0, t)| + |b(1, t) - b^h(1, t)| \right] \\ &\leq C |\vec{\theta}^h|_{0, \infty} \left[h + |\vec{\theta}^h|_{0, \infty} + |\vec{\theta}_t^h|_0 + |\zeta^h|_0 + |\vec{\theta}^h|_1 \right]. \end{aligned} \quad (3.4.54)$$

Hence, combining (3.4.34) with (3.4.36) and (3.4.54), and using (3.1.8), we have

$$\begin{aligned} T_3 &\leq \frac{1}{2} \frac{d}{dt} \left[\langle \vec{x}_\rho, \nabla F(\vec{x}) \rangle \langle \vec{\theta}^h, D^2 F(\vec{x}) \vec{\theta}^h \rangle \right]_0^1 + \frac{m^2 \alpha}{24} |\vec{\theta}_t^h|_0^2 \\ &\quad + C \left[h^2 + |\vec{\theta}^h|_{0, \infty}^2 + |\zeta^h|_0^2 + |\vec{\theta}^h|_1^2 + h^{-1} |\vec{\theta}^h|_{0, \infty}^4 \right]. \end{aligned} \quad (3.4.55)$$

Combining (3.4.22), (3.4.27), (3.4.33) and (3.4.55), we have

$$\begin{aligned} \frac{1}{2} \frac{d}{dt} |\vec{\theta}^h|_1^2 + \frac{m^2 \alpha}{8} |\vec{\theta}_t^h|_0^2 &\leq \frac{1}{2} \frac{d}{dt} \left[\langle \vec{x}_\rho, \nabla F(\vec{x}) \rangle \langle \vec{\theta}^h, D^2 F(\vec{x}) \vec{\theta}^h \rangle \right]_0^1 \\ &\quad + C \left[h^2 + |\vec{\theta}^h|_{0, \infty}^2 + |\zeta^h|_0^2 + |\vec{\theta}^h|_1^2 + h^{-1} |\vec{\theta}^h|_{0, \infty}^4 \right]. \end{aligned} \quad (3.4.56)$$

Multiplying (3.4.56) by $e^{-\gamma s}$, for $\gamma \geq 1$ and integrating with respect to $s \in (0, t)$ with $t \leq T_h^*$, and noting $|\vec{\theta}^h(\cdot, 0)| = 0$, we have

$$\frac{1}{2} e^{-\gamma t} |\vec{\theta}^h|_1^2 + \frac{\gamma}{2} \int_0^t e^{-\gamma s} |\vec{\theta}^h|_1^2 ds + \frac{m^2 \alpha}{8} \int_0^t e^{-\gamma s} |\vec{\theta}_t^h|_0^2 ds$$

$$\begin{aligned}
&\leq \frac{1}{2}e^{-\gamma t} \left[\langle \vec{x}_\rho, \nabla F(\vec{x}) \rangle \langle \vec{\theta}^h, D^2 F(\vec{x}) \vec{\theta}^h \rangle \right]_0^1 + \frac{\gamma}{2} \int_0^t e^{-\gamma s} \left[\langle \vec{x}_\rho, \nabla F(\vec{x}) \rangle \langle \vec{\theta}^h, D^2 F(\vec{x}) \vec{\theta}^h \rangle \right]_0^1 ds \\
&\quad + C \int_0^t e^{-\gamma s} \left[h^2 + |\vec{\theta}^h|_{0,\infty}^2 + |\zeta^h|_0^2 + |\vec{\theta}^h|_1^2 + h^{-1} |\vec{\theta}^h|_{0,\infty}^4 \right] ds \\
&=: (I_1 + I_2) + C \int_0^t e^{-\gamma s} \left[h^2 + |\vec{\theta}^h|_{0,\infty}^2 + |\zeta^h|_0^2 + |\vec{\theta}^h|_1^2 + h^{-1} |\vec{\theta}^h|_{0,\infty}^4 \right] ds. \tag{3.4.57}
\end{aligned}$$

Using (3.4.35a), (3.4.4f) and (3.1.9b), we see that

$$\begin{aligned}
I_1 + I_2 &= \frac{1}{2}e^{-\gamma t} \left[\langle \vec{x}_\rho, \nabla F(\vec{x}) \rangle \langle \vec{\theta}^h, D^2 F(\vec{x}) \vec{\theta}^h \rangle \right]_0^1 \\
&\quad + \frac{\gamma}{2} \int_0^t e^{-\gamma s} \left[\langle \vec{x}_\rho, \nabla F(\vec{x}) \rangle \langle \vec{\theta}^h, D^2 F(\vec{x}) \vec{\theta}^h \rangle \right]_0^1 ds \\
&\leq M e^{-\gamma t} |D^2 F|_{0,\infty} |\vec{\theta}^h|_{0,\infty}^2 + M \gamma \int_0^t e^{-\gamma s} |D^2 F|_{0,\infty} |\vec{\theta}^h|_{0,\infty}^2 ds \\
&\leq \frac{1}{4}e^{-\gamma t} |\vec{\theta}^h|_1^2 + C e^{-\gamma t} |\vec{\theta}^h|_0^2 + \frac{\gamma}{4} \int_0^t e^{-\gamma s} |\vec{\theta}^h|_1^2 ds + C \gamma \int_0^t e^{-\gamma s} |\vec{\theta}^h|_0^2 ds. \tag{3.4.58}
\end{aligned}$$

Substituting (3.4.58) into (3.4.57), and using (3.1.9b), gives

$$\begin{aligned}
&\frac{1}{4}e^{-\gamma t} |\vec{\theta}^h|_1^2 + \frac{\gamma}{4} \int_0^t e^{-\gamma s} |\vec{\theta}^h|_1^2 ds + \frac{m^2 \alpha}{8} \int_0^t e^{-\gamma s} |\vec{\theta}_t^h|_0^2 ds \\
&\leq C e^{-\gamma t} |\vec{\theta}^h|_0^2 + \frac{C \gamma}{2} \int_0^t e^{-\gamma s} |\vec{\theta}^h|_0^2 ds \\
&\quad + C_2 \int_0^t e^{-\gamma s} \left[h^2 + |\zeta^h|_0^2 + |\vec{\theta}^h|_1^2 + h^{-1} |\vec{\theta}^h|_{0,\infty}^4 \right] ds. \tag{3.4.59}
\end{aligned}$$

Since $|\vec{\theta}^h(\cdot, 0)| = 0$, we have

$$\begin{aligned}
e^{-\gamma t} |\vec{\theta}^h(\cdot, t)|_0^2 &= \int_0^t \frac{d}{ds} \left(e^{-\gamma s} |\vec{\theta}^h|_0^2 \right) ds \\
&\leq -\gamma \int_0^t e^{-\gamma s} |\vec{\theta}^h|_0^2 ds + 2 \int_0^t e^{-\gamma s} |\vec{\theta}^h|_0 |\vec{\theta}_t^h|_0 ds \\
&\leq -\frac{\gamma}{2} \int_0^t e^{-\gamma s} |\vec{\theta}^h|_0^2 ds + \frac{2}{\gamma} \int_0^t e^{-\gamma s} |\vec{\theta}_t^h|_0^2 ds,
\end{aligned}$$

and hence the first two terms on the right hand side of (3.4.59) can be bounded as follows

$$C e^{-\gamma t} |\vec{\theta}^h(\cdot, t)|_0^2 + \frac{C \gamma}{2} \int_0^t e^{-\gamma s} |\vec{\theta}^h|_0^2 ds \leq \frac{2C_2}{\gamma} \int_0^t e^{-\gamma s} |\vec{\theta}_t^h|_0^2 ds. \tag{3.4.60}$$

Combining (3.4.59) and (3.4.60), with γ chosen large enough such that $\gamma \geq \max \left\{ 1, \frac{32C_2}{m^2 \alpha} \right\}$, yields the desired result. \square

Proof of Lemma 3.25: In the proof of this lemma we follow the techniques used in [6].

We first start with a useful estimate specifically for the proof of this lemma. Using (3.4.9) and (3.4.12c), for $h \in (0, h^*]$ and $t \in [0, T_h^*)$, we have

$$|\vec{\theta}^h|_1^2 + |\zeta^h|_0^2 \leq 2C_1 h^2 e^{\gamma t} \leq 2C_1 (h^*)^{\frac{1}{2}} h^{\frac{3}{2}} e^{\gamma T} \leq h^{\frac{3}{2}}, \tag{3.4.61}$$

while (3.1.11), (3.4.4b) and (3.4.12b) yield

$$|\zeta^h|_{0,\infty} \leq |I^h w|_{0,\infty} + |w^h|_{0,\infty} \leq C \|w\|_{C([0,T];H^1(\mathcal{I}))} \leq C. \quad (3.4.62)$$

Taking $\eta = \eta^h$ and subtracting (3.4.5b) from (3.4.2b) we have

$$\begin{aligned} & \left[\left(\frac{\partial}{\partial t} (|\bar{x}_\rho| w), \eta^h \right) - \left(\frac{\partial}{\partial t} (|\bar{x}_\rho^h| w^h), \eta^h \right)^h \right] + d \left[\left(\frac{w_\rho}{|\bar{x}_\rho|}, \eta_\rho^h \right) - \left(\frac{w_\rho^h}{|\bar{x}_\rho^h|}, \eta_\rho^h \right) \right] \\ & + \left[\left(\psi w, \eta_\rho^h \right) - \left(\psi^h w^h, \eta_\rho^h \right)^h \right] = \left[(|\bar{x}_\rho| g(v, w), \eta) - (|\bar{x}_\rho^h| g(v^h, w^h), \eta^h)^h \right]. \end{aligned}$$

Using the identity

$$\frac{d}{dt} (fg) g = \frac{1}{2} \frac{d}{dt} (fg^2) + \frac{1}{2} \frac{df}{dt} g^2,$$

noting (3.3.20), setting $\eta^h = \zeta^h$, we have

$$\begin{aligned} & \frac{1}{2} \frac{d}{dt} (|\bar{x}_\rho^h| \zeta^h, \zeta^h)^h + d \left(\frac{1}{|\bar{x}_\rho^h|} \zeta_\rho^h, \zeta_\rho^h \right) \\ & = -\frac{1}{2} (|\bar{x}_\rho^h|_t \zeta^h, \zeta^h)^h + \left[\left((|\bar{x}_\rho^h| I^h w)_t, \zeta^h \right)^h - \left((|\bar{x}_\rho| w)_t, \zeta^h \right) \right] \\ & + d \left(w_\rho \left[\frac{1}{|\bar{x}_\rho^h|} - \frac{1}{|\bar{x}_\rho|} \right], \zeta_\rho^h \right) + \left[\left(\psi^h w^h, \zeta_\rho^h \right)^h - \left(\psi w, \zeta_\rho^h \right) \right] \\ & + \left[(|\bar{x}_\rho| g(v, w), \zeta^h) - (|\bar{x}_\rho^h| g(v^h, w^h), \zeta^h)^h \right] =: \sum_{i=4}^8 T_i. \end{aligned} \quad (3.4.63)$$

Using (3.4.12a) we see that the left hand side of (3.4.63) is bounded below by

$$\frac{d}{dt} (|\bar{x}_\rho^h| \zeta^h, \zeta^h)^h + d \left(\frac{1}{|\bar{x}_\rho^h|} \zeta_\rho^h, \zeta_\rho^h \right) \geq \frac{d}{dt} (|\bar{x}_\rho^h| \zeta^h, \zeta^h)^h + \frac{d}{2M} |\zeta^h|_1^2. \quad (3.4.64)$$

Now we bound T_i , $i = 4, \dots, 8$. Noting that $|\bar{x}_\rho^h|_t = \langle \bar{x}_{\rho,t}^h, \bar{\tau}^h \rangle$ and $\zeta^h \in S_0^h$, using integration by parts we have

$$\begin{aligned} T_4 & = -\frac{1}{2} (|\bar{x}_\rho^h|_t \zeta^h, \zeta^h)^h \\ & = \frac{1}{2} (\langle \bar{x}_{\rho,t}^h, \tau - \bar{\tau}^h \rangle \zeta^h, \zeta^h) + \left[\frac{1}{2} (\langle \bar{x}_t^h, \bar{\tau}_\rho \rangle \zeta^h, \zeta^h) + (\langle \bar{x}_t^h, \bar{\tau} \rangle \zeta^h, \zeta_\rho^h) \right] \\ & + \frac{1}{2} \left[(\langle \bar{x}_{\rho,t}^h, \bar{\tau}^h \rangle \zeta^h, \zeta^h) - (\langle \bar{x}_{\rho,t}^h, \bar{\tau}^h \rangle \zeta^h, \zeta^h)^h \right] =: \sum_{i=1}^3 T_{4,i}. \end{aligned} \quad (3.4.65)$$

Using (3.4.4a), (3.4.15), (3.4.19), (3.4.61) and (3.1.9a), we see that

$$\begin{aligned} T_{4,1} & = \frac{1}{2} (\langle \bar{x}_{\rho,t}^h, \tau - \bar{\tau}^h \rangle \zeta^h, \zeta^h) \\ & \leq \frac{1}{2} |\zeta^h|_{0,\infty}^2 |\bar{x}_t^h|_1 |\bar{\tau} - \bar{\tau}^h|_0 \\ & \leq C \|\bar{x}\|_{W^{1,\infty}(0,T;[H^1(\mathcal{I})]^2)} |\zeta^h|_{0,\infty}^2 \left[1 + h^{-1} |\bar{\theta}_t^h|_0 \right] \left[h + |\bar{\theta}^h|_1 \right] \\ & \leq C h^{\frac{3}{4}} |\zeta^h|_{0,\infty}^2 + C h^{-\frac{1}{4}} |\zeta^h|_0 \|\zeta^h\|_1 |\bar{\theta}_t^h|_0 \leq C h^{\frac{3}{4}} |\zeta^h|_{0,\infty}^2 + C h^{\frac{1}{2}} \|\zeta^h\|_1 |\bar{\theta}_t^h|_0. \end{aligned} \quad (3.4.66)$$

Using (3.4.4a) and (3.4.15), we have

$$\begin{aligned}
T_{4,2} &= \frac{1}{2} \left(\langle \vec{x}_t^h, \vec{\tau}_\rho \rangle \zeta^h, \zeta^h \right) + \left(\langle \vec{x}_t^h, \vec{\tau} \rangle \zeta^h, \zeta_\rho^h \right) \\
&\leq \left[\frac{1}{2} |\vec{\tau}|_1 |\zeta^h|_{0,\infty}^2 + |\zeta^h|_{0,\infty} |\zeta^h|_1 \right] |\vec{x}_t^h|_0 \\
&\leq C \|\vec{x}\|_{W^{0,\infty}(0,T;[H^2(\mathcal{I})]^2)} \left[1 + |\vec{\theta}_t^h|_0 \right] \left[|\zeta^h|_{0,\infty}^2 + |\zeta^h|_{0,\infty} |\zeta^h|_1 \right] \\
&\leq C \left[1 + |\vec{\theta}_t^h|_0 \right] \left[|\zeta^h|_{0,\infty}^2 + |\zeta^h|_{0,\infty} |\zeta^h|_1 \right], \tag{3.4.67}
\end{aligned}$$

while (3.1.6b), (3.4.62) and (3.4.15) yield

$$\begin{aligned}
2T_{4,3} &= \left(\langle \vec{x}_{\rho,t}^h, \vec{\tau}^h \rangle \zeta^h, \zeta^h \right) - \left(\langle \vec{x}_{\rho,t}^h, \vec{\tau}^h \rangle \zeta^h, \zeta^h \right)^h \\
&\leq C h \sum_{j=1}^J |\zeta^h|_{1,\sigma_j} |\langle \vec{x}_{\rho,t}^h, \vec{\tau}^h \rangle \zeta^h|_{0,\sigma_j} \\
&\leq C h |\zeta^h|_{0,\infty} |\vec{x}_t^h|_1 |\zeta^h|_1 \leq C \left[h + |\vec{\theta}_t^h|_0 \right] |\zeta^h|_1. \tag{3.4.68}
\end{aligned}$$

Thus, noting (3.4.62), combining (3.4.65) with (3.4.66)–(3.4.68), and using (3.1.9b), we have

$$|T_4| \leq \frac{d}{16M} |\zeta^h|_1^2 + C \left[h^2 + |\vec{\theta}_t^h|_0^2 + |\zeta^h|_0^2 \right]. \tag{3.4.69}$$

We prove two useful identities to be able to bound T_5 . Namely, noting $|\vec{x}_\rho^h| = \langle \vec{x}_\rho^h, \vec{\tau} \rangle$, we have

$$\langle \vec{\tau}^h, \vec{\tau}_t^h \rangle = \frac{1}{2} \frac{d}{dt} |\vec{\tau}^h|^2 = 0, \tag{3.4.70a}$$

as well as

$$\begin{aligned}
\frac{1}{2} |\vec{x}_\rho^h| |\vec{\tau} - \vec{\tau}^h|^2 &= \frac{1}{2} |\vec{x}_\rho^h| \langle \vec{\tau} - \vec{\tau}^h, \vec{\tau} - \vec{\tau}^h \rangle \\
&= \langle \vec{x}_\rho^h, \vec{\tau}^h \rangle \left(1 - \langle \vec{\tau}, \vec{\tau}^h \rangle \right) = \langle \vec{x}_\rho^h - \langle \vec{x}_\rho^h, \vec{\tau}^h \rangle \vec{\tau}, \vec{\tau}^h \rangle = \langle \vec{\tau}^h - \vec{\tau}, \vec{x}_\rho^h \rangle. \tag{3.4.70b}
\end{aligned}$$

Hence, using (3.4.70a)–(3.4.70b), as well as noting that $|\vec{x}_\rho| = \langle \vec{x}_\rho, \vec{\tau} \rangle$, we have

$$\begin{aligned}
\left(w \left(|\vec{x}_\rho^h| - |\vec{x}_\rho| \right)_t, \zeta^h \right) &= \left(w \left(\langle \vec{x}_\rho^h - \vec{x}_\rho, \vec{\tau} \rangle \right)_t, \zeta^h \right) + \left(w \left(\langle \vec{x}_\rho^h, \vec{\tau}^h - \vec{\tau} \rangle \right)_t, \zeta^h \right) \\
&= \left(w \langle \vec{x}_\rho^h - \vec{x}_\rho, \vec{\tau}_t \rangle, \zeta^h \right) + \left(w \langle (\vec{x}_\rho^h - \vec{x}_\rho)_t, \vec{\tau} \rangle, \zeta^h \right) \\
&\quad + \frac{1}{2} \left(w \left(|\vec{x}_\rho^h| |\vec{\tau} - \vec{\tau}^h|^2 \right)_t, \zeta^h \right) \\
&= \left(w \langle \vec{x}_\rho^h - \vec{x}_\rho, \vec{\tau}_t \rangle, \zeta^h \right) + \left(w \langle (\vec{x}_\rho^h - \vec{x}_\rho)_t, \vec{\tau} \rangle, \zeta^h \right) \\
&\quad + \frac{1}{2} \left(w |\vec{x}_\rho^h|_t |\vec{\tau} - \vec{\tau}^h|^2, \zeta^h \right) + \left(w |\vec{x}_\rho^h| \langle \vec{\tau} - \vec{\tau}^h, \vec{\tau}_t - \vec{\tau}_t^h \rangle, \zeta^h \right) \\
&= \left(w \langle \vec{x}_\rho^h - \vec{x}_\rho, \vec{\tau}_t \rangle, \zeta^h \right) + \left(w \langle (\vec{x}_\rho^h - \vec{x}_\rho)_t, \vec{\tau} \rangle, \zeta^h \right) \\
&\quad + \frac{1}{2} \left(w |\vec{x}_\rho^h|_t |\vec{\tau} - \vec{\tau}^h|^2, \zeta^h \right) + \left(w |\vec{x}_\rho^h| \langle \vec{\tau} - \vec{\tau}^h, \vec{\tau}_t \rangle, \zeta^h \right)
\end{aligned}$$

$$- \left(w |\bar{x}_\rho^h | \langle \bar{\tau}, \bar{\tau}^h \rangle, \zeta^h \right) \quad (3.4.71)$$

and hence

$$\begin{aligned} T_5 &= \left(\left(|\bar{x}_\rho^h | I^h w \right)_t, \zeta^h \right)^h - \left((|\bar{x}_\rho | w)_t, \zeta^h \right) \\ &= \left(w_t \left[|\bar{x}_\rho^h | - |\bar{x}_\rho | \right], \zeta^h \right) + \left(w \left(|\bar{x}_\rho^h | - |\bar{x}_\rho | \right)_t, \zeta^h \right) \\ &\quad + \left[\left(|\bar{x}_\rho^h | (I^h - I) w_t, \zeta^h \right) + \left(|\bar{x}_\rho^h |_t (I^h - I) w, \zeta^h \right) \right] \\ &\quad + \left[\left(\left(|\bar{x}_\rho^h | I^h w \right)_t, \zeta^h \right)^h - \left(\left(|\bar{x}_\rho^h | I^h w \right)_t, \zeta^h \right) \right] \\ &= \left(w_t \left[|\bar{x}_\rho^h | - |\bar{x}_\rho | \right], \zeta^h \right) + \left[\left(w \langle \bar{x}_\rho^h - \bar{x}_\rho, \bar{\tau}_t \rangle, \zeta^h \right) + \left(w \langle (\bar{x}_\rho^h - \bar{x}_\rho)_t, \bar{\tau} \rangle, \zeta^h \right) \right] \\ &\quad + \frac{1}{2} \left(w |\bar{x}_\rho^h |_t |\bar{\tau} - \bar{\tau}^h|^2, \zeta^h \right) + \left(w |\bar{x}_\rho^h | \langle \bar{\tau} - \bar{\tau}^h, \bar{\tau}_t \rangle, \zeta^h \right) - \left(w |\bar{x}_\rho^h | \langle \bar{\tau}, \bar{\tau}^h \rangle, \zeta^h \right) \\ &\quad + \left[\left(|\bar{x}_\rho^h | (I^h - I) w_t, \zeta^h \right) + \left(|\bar{x}_\rho^h |_t (I^h - I) w, \zeta^h \right) \right] \\ &\quad + \left[\left(\left(|\bar{x}_\rho^h | I^h w \right)_t, \zeta^h \right)^h - \left(\left(|\bar{x}_\rho^h | I^h w \right)_t, \zeta^h \right) \right] =: \sum_{i=1}^7 T_{5,i}. \end{aligned} \quad (3.4.72)$$

Using (3.1.11), (3.4.4b) and (3.4.13), we have

$$\begin{aligned} T_{5,1} &= \left(w_t \left[|\bar{x}_\rho^h | - |\bar{x}_\rho | \right], \zeta^h \right) \\ &\leq |w_t|_{0,\infty} |\bar{x} - \bar{x}^h|_1 |\zeta^h|_0 \\ &\leq C \|w\|_{W^{1,\infty}(0,T;H^1(\mathcal{I}))} \left[h + |\bar{\theta}^h|_1 \right] |\zeta^h|_0 \leq C \left[h + |\bar{\theta}^h|_1 \right] |\zeta^h|_0. \end{aligned} \quad (3.4.73)$$

Using integration by parts with (3.1.11), (3.4.4a), (3.4.4b), (3.4.14), (3.4.13), and noting that $\zeta^h \in S_0^h$, we have

$$\begin{aligned} T_{5,2} &= \left(w \langle \bar{x}_\rho^h - \bar{x}_\rho, \bar{\tau}_t \rangle, \zeta^h \right) + \left(w \langle (\bar{x}_\rho^h - \bar{x}_\rho)_t, \bar{\tau} \rangle, \zeta^h \right) \\ &= \left(w \langle \bar{x}_\rho^h - \bar{x}_\rho, \bar{\tau}_t \rangle, \zeta^h \right) + \left(\langle (\bar{x} - \bar{x}^h)_t, (\bar{\tau} w)_\rho \rangle, \zeta^h \right) + \left(w \langle (\bar{x} - \bar{x}^h)_t, \bar{\tau} \rangle, \zeta^h \right) \\ &\leq |w|_{0,\infty} |\bar{\tau}_t|_0 |\bar{x} - \bar{x}^h|_1 |\zeta^h|_{0,\infty} + |\bar{x}_t - \bar{x}_t^h|_0 |\bar{\tau} w|_1 |\zeta^h|_{0,\infty} + |w|_{0,\infty} |\bar{x}_t - \bar{x}_t^h|_0 |\zeta^h|_1 \\ &\leq C_{\bar{x}} \|w\|_{C([0,T];H^1(\mathcal{I}))} \left[h + |\bar{\theta}_t^h|_0 + |\bar{\theta}^h|_1 \right] \left[|\zeta^h|_{0,\infty} + |\zeta^h|_1 \right] \\ &\leq C \left[h + |\bar{\theta}_t^h|_0 + |\bar{\theta}^h|_1 \right] \left[|\zeta^h|_{0,\infty} + |\zeta^h|_1 \right], \end{aligned} \quad (3.4.74)$$

where $C_{\bar{x}} := 1 + \|\bar{x}\|_{W^{1,\infty}(0,T;[H^1(\mathcal{I})]^2)} + \|\bar{x}\|_{W^{0,\infty}(0,T;[H^2(\mathcal{I})]^2)}$. From (3.1.11), (3.4.4b), (3.1.5a), (3.1.4a), (3.4.19), (3.4.15) and (3.4.61), we have that

$$\begin{aligned} T_{5,3} &= \frac{1}{2} \left(w |\bar{x}_\rho^h | |\bar{\tau} - \bar{\tau}^h|^2, \zeta^h \right) \\ &\leq \frac{1}{2} |w|_{0,\infty} |\bar{\tau} - \bar{\tau}^h|_{0,\infty} |\bar{x}_t^h|_1 |\bar{\tau} - \bar{\tau}^h|_0 |\zeta^h|_{0,\infty} \\ &\leq C \|w\|_{C([0,T];H^1(\mathcal{I}))} \left[h^{\frac{1}{2}} + h^{-\frac{1}{2}} |\bar{\theta}^h|_1 \right] \left[1 + h^{-1} |\bar{\theta}_t^h|_0 \right] \left[h + |\bar{\theta}^h|_1 \right] |\zeta^h|_{0,\infty} \end{aligned}$$

$$\leq C \left[h + |\bar{\theta}_t^h|_0 \right] |\zeta^h|_{0,\infty}, \quad (3.4.75)$$

while, with the addition of (3.4.12a),

$$\begin{aligned} T_{5,4} &= \left(w |\bar{x}_\rho^h| \langle \bar{\tau} - \bar{\tau}^h, \bar{\tau}_t \rangle, \zeta^h \right) \\ &\leq C |w|_{0,\infty} |\bar{\tau} - \bar{\tau}^h|_0 |\bar{\tau}_t|_0 |\zeta^h|_{0,\infty} \\ &\leq C \|w\|_{C([0,T];H^1(\mathcal{I}))} \|\bar{x}\|_{W^{1,\infty}(0,T;[H^1(\mathcal{I})]^2)} \left[h + |\bar{\theta}^h|_1 \right] |\zeta^h|_{0,\infty} \\ &\leq C \left[h + |\bar{\theta}^h|_1 \right] |\zeta^h|_{0,\infty}. \end{aligned} \quad (3.4.76)$$

Setting $P^h := I - \bar{\tau}^h \otimes \bar{\tau}^h$ and noting

$$|\bar{x}_\rho^h| \bar{\tau}_t^h = \bar{x}_{\rho,t}^h - \langle \bar{x}_{\rho,t}^h, \bar{\tau}^h \rangle \bar{\tau}^h = P^h \bar{x}_{\rho,t}^h$$

yields

$$\begin{aligned} T_{5,5} &= - \left(w |\bar{x}_\rho^h| \langle \bar{\tau}, \bar{\tau}^h \rangle, \zeta^h \right) \\ &= - \left(w \langle \bar{\tau}, P^h \bar{x}_{\rho,t}^h \rangle, \zeta^h \right) \\ &= \left(w \langle \bar{\tau}, P^h \bar{\theta}_{\rho,t}^h \rangle, \zeta^h \right) - \left(w \langle \bar{\tau}, P^h I^h \bar{x}_{\rho,t}^h \rangle, \zeta^h \right) =: T_{5,5,1} + T_{5,5,2}. \end{aligned} \quad (3.4.77)$$

By definition P^h is constant each sub-interval σ_j , so, using integration by parts over each sub-interval and noting that $\zeta^h \in S_0^h$, we have

$$\begin{aligned} T_{5,5,1} &= \left(w \langle \bar{\tau}, P^h \bar{\theta}_{\rho,t}^h \rangle, \zeta^h \right) \\ &= \sum_{j=1}^J \int_{\sigma_j} w \langle \bar{\tau}, P^h \bar{\theta}_{\rho,t}^h \rangle \zeta^h d\rho \\ &= \sum_{j=1}^J \left[w \langle \bar{\tau}, P^h \bar{\theta}_t^h \rangle \zeta^h \right]_{\rho_{j-1}}^{\rho_j} - \sum_{j=1}^J \int_{\sigma_j} \langle (w \bar{\tau} \zeta^h)_\rho, P^h \bar{\theta}_t^h \rangle d\rho \\ &= - \sum_{j=1}^{J-1} \left[w(\rho_j, t) \langle \bar{\tau}(\rho_j, t), (P^h|_{\sigma_{j+1}} - P^h|_{\sigma_j}) \bar{\theta}_t^h(\rho_j, t) \rangle \zeta^h(\rho_j, t) \right] \\ &\quad - \left[\langle (w \bar{\tau})_\rho, P^h \bar{\theta}_t^h \rangle, \zeta^h \right] + \left(w \langle \bar{\tau}, P^h \bar{\theta}_t^h \rangle, \zeta^h \right) =: T_{5,5,1,1} + T_{5,5,1,2}. \end{aligned} \quad (3.4.78)$$

To bound the first term in (3.4.78) we note

$$\begin{aligned} P^h|_{\sigma_{j+1}} - P^h|_{\sigma_j} &= (I - \bar{\tau}_{|\sigma_{j+1}}^h \otimes \bar{\tau}_{|\sigma_{j+1}}^h) - (I - \bar{\tau}_{|\sigma_j}^h \otimes \bar{\tau}_{|\sigma_j}^h) \\ &= \bar{\tau}_{|\sigma_{j+1}}^h \otimes (\bar{\tau}_{|\sigma_j}^h - \bar{\tau}_{|\sigma_{j+1}}^h) + (\bar{\tau}_{|\sigma_j}^h - \bar{\tau}_{|\sigma_{j+1}}^h) \otimes \bar{\tau}_{|\sigma_j}^h, \end{aligned}$$

and

$$\bar{\tau}_{|\sigma_{j+1}}^h - \bar{\tau}_{|\sigma_j}^h = \frac{(\bar{x}_\rho^h)|_{\sigma_{j+1}}}{|(\bar{x}_\rho^h)|_{\sigma_{j+1}}} - \frac{(\bar{x}_\rho^h)|_{\sigma_j}}{|(\bar{x}_\rho^h)|_{\sigma_j}}$$

$$= \frac{1}{|(\vec{x}_\rho^h)_{\sigma_{j+1}}|} \left((\vec{x}_\rho^h)_{\sigma_{j+1}} - (\vec{x}_\rho^h)_{\sigma_j} \right) + \frac{\vec{\tau}_{|\sigma_j}^h}{|(\vec{x}_\rho^h)_{\sigma_{j+1}}|} \left(|(\vec{x}_\rho^h)_{\sigma_j}| - |(\vec{x}_\rho^h)_{\sigma_{j+1}}| \right).$$

For any $\vec{p} \in \mathbb{R}^2$, for $j = 1, \dots, J-1$, we set $\xi^h = \chi_j \vec{p}$ in (3.4.5a) to obtain

$$\begin{aligned} \langle (\vec{x}_\rho^h)_{\sigma_{j+1}} - (\vec{x}_\rho^h)_{\sigma_j}, \vec{p} \rangle &= - \left(h_{j+1} |(\vec{x}_\rho^h)_{\sigma_{j+1}}|^2 \langle \vec{v}_{|\sigma_{j+1}}^h, \vec{p} \rangle + h_j |(\vec{x}_\rho^h)_{\sigma_j}|^2 \langle \vec{v}_{|\sigma_j}^h, \vec{p} \rangle \right) f(w^h(\rho_j, t)) \\ &\quad + \alpha \left(h_{j+1} |(\vec{x}_\rho^h)_{\sigma_{j+1}}|^2 + h_j |(\vec{x}_\rho^h)_{\sigma_j}|^2 \right) \langle \vec{x}_t^h(\rho_j, t), \vec{p} \rangle \\ &\quad + (1 - \alpha) \left[h_{j+1} |(\vec{x}_\rho^h)_{\sigma_{j+1}}|^2 \langle \vec{x}_t^h(\rho_j, t), \vec{v}_{|\sigma_{j+1}}^h \rangle \langle \vec{v}_{|\sigma_{j+1}}^h, \vec{p} \rangle \right. \\ &\quad \left. + h_j |(\vec{x}_\rho^h)_{\sigma_j}|^2 \langle \vec{x}_t^h(\rho_j, t), \vec{v}_{|\sigma_j}^h \rangle \langle \vec{v}_{|\sigma_j}^h, \vec{p} \rangle \right]. \end{aligned}$$

Combining the three equations above and using (3.4.12a), (3.1.4a), (3.4.12b), (3.4.4c) and (3.4.4a), we have

$$\begin{aligned} |P_{|\sigma_{j+1}}^h - P_{|\sigma_j}^h| &\leq C |(\vec{x}_\rho^h)_{\sigma_{j+1}} - (\vec{x}_\rho^h)_{\sigma_j}| \\ &\leq C h \left[|f(w^h)|_{0,\infty} + |\vec{x}_t^h(\rho_j, t)| \right] \\ &\leq C h \left[|f(w^h)|_{0,\infty} + |I^h \vec{x}_t|_{0,\infty} + |\vec{\theta}_t^h(\rho_j, t)| \right] \\ &\leq C h \left[1 + |\vec{\theta}_t^h(\rho_j, t)| \right]. \end{aligned} \tag{3.4.79}$$

Hence, using (3.4.79), (3.1.4a), (3.1.11), (3.4.4b), (3.1.5a) and (3.4.61), we have

$$\begin{aligned} T_{5,5,1,1} &= - \sum_{j=1}^{J-1} \left[w(\rho_j, t) \langle \vec{\tau}(\rho_j, t), (P_{|\sigma_{j+1}}^h - P_{|\sigma_j}^h) \vec{\theta}_t^h(\rho_j, t) \rangle \zeta^h(\rho_j, t) \right] \\ &\leq C h |w|_{0,\infty} |\zeta^h|_{0,\infty} \sum_{j=1}^{J-1} \left[1 + |\vec{\theta}_t^h(\rho_j, t)| \right] |\vec{\theta}_t^h(\rho_j, t)| \\ &\leq C \|w\|_{C([0,T];H^1(\mathcal{I}))} |\zeta^h|_{0,\infty} \left[\sum_{j=1}^{J-1} h_j |\vec{\theta}_t^h(\rho_j, t)| + \sum_{j=1}^{J-1} h_j |\vec{\theta}_t^h(\rho_j, t)|^2 \right] \\ &\leq C |\zeta^h|_{0,\infty} \left[|\vec{\theta}_t^h|_{0,1} + |\vec{\theta}_t^h|_0^2 \right] \\ &\leq C |\vec{\theta}_t^h|_0 |\zeta^h|_{0,\infty} + C h^{-\frac{1}{2}} |\vec{\theta}_t^h|_0^2 |\zeta^h|_0 \leq C |\vec{\theta}_t^h|_0 |\zeta^h|_{0,\infty} + C |\vec{\theta}_t^h|_0^2. \end{aligned} \tag{3.4.80}$$

Using (3.4.12a), (3.1.11), (3.4.4b) and (3.4.4a), we have

$$\begin{aligned} T_{5,5,1,2} &= - \left(\langle (w \vec{\tau})_\rho, P^h \vec{\theta}_t^h \rangle, \zeta^h \right) - \left(w \langle \vec{\tau}, P^h \vec{\theta}_t^h \rangle, \zeta^h \right) \\ &\leq |P^h|_{0,\infty} |w \vec{\tau}|_1 |\vec{\theta}_t^h|_0 |\zeta^h|_{0,\infty} + |w|_{0,\infty} |P^h|_{0,\infty} |\vec{\theta}_t^h|_0 |\zeta^h|_1 \\ &\leq C \|w\|_{C([0,T];H^1(\mathcal{I}))} \left[1 + \|\vec{x}\|_{W^{0,\infty}(0,T;[H^2(\mathcal{I})]^2)} \right] \left[|\zeta^h|_{0,\infty} + |\zeta^h|_1 \right] |\vec{\theta}_t^h|_0 \\ &\leq C \left[|\zeta^h|_{0,\infty} + |\zeta^h|_1 \right] |\vec{\theta}_t^h|_0. \end{aligned} \tag{3.4.81}$$

To bound $T_{5,5,2}$, noting (3.4.70b), we utilise the following bound

$$P^h \vec{\tau} = \vec{\tau} - \langle \vec{\tau}, \vec{\tau}^h \rangle \vec{\tau}^h = \vec{\tau} - \left(1 - \frac{1}{2} |\vec{\tau} - \vec{\tau}^h|^2 \right) \vec{\tau}^h = \vec{\tau} - \vec{\tau}^h + \frac{1}{2} |\vec{\tau} - \vec{\tau}^h|^2 \vec{\tau}^h$$

as well as noting that P^h is symmetric and using (3.1.11), (3.4.4b), (3.1.5d), (3.4.4a), (3.4.19) and the fact that $|\bar{\tau} - \bar{\tau}^h| \leq |\bar{\tau}| + |\bar{\tau}^h| = 2$ to give

$$\begin{aligned}
T_{5,5,2} &= - \left(w \langle \bar{\tau}, P^h I^h \bar{x}_{\rho,t} \rangle, \zeta^h \right) \\
&= - \left(w \langle P^h \bar{\tau}, I^h \bar{x}_{\rho,t} \rangle, \zeta^h \right) \\
&= \left(w \langle \bar{\tau}^h - \bar{\tau}, I^h \bar{x}_{\rho,t} \rangle, \zeta^h \right) - \frac{1}{2} \left(w |\bar{\tau} - \bar{\tau}^h|^2 \langle \bar{\tau}^h, I^h \bar{x}_{\rho,t} \rangle, \zeta^h \right) \\
&\leq 2 \|w\|_{0,\infty} |\bar{\tau} - \bar{\tau}^h|_0 |I^h \bar{x}_t|_1 |\zeta^h|_{0,\infty} \\
&\leq C \|w\|_{C([0,T];H^1(\mathcal{I}))} \|\bar{x}\|_{W^{1,\infty}(0,T;[H^1(\mathcal{I})]^2)} \left[h + |\bar{\theta}^h|_1 \right] |\zeta^h|_{0,\infty} \\
&\leq C \left[h + |\bar{\theta}^h|_1 \right] |\zeta^h|_{0,\infty}.
\end{aligned} \tag{3.4.82}$$

Thus, combining (3.4.77) with (3.4.80)–(3.4.82), we have

$$T_{5,5} \leq C \left[h + |\bar{\theta}_t^h|_0 + |\bar{\theta}^h|_1 \right] \left[|\zeta^h|_{0,\infty} + |\zeta^h|_0 + |\zeta^h|_1 \right] + C |\bar{\theta}_t^h|_0^2. \tag{3.4.83}$$

Using (3.4.12a), (3.1.11), (3.1.5b), (3.4.4b) and (3.4.15), we have

$$\begin{aligned}
T_{5,6} &= \left(|\bar{x}_\rho^h| (I^h - I) w_t, \zeta^h \right) + \left(|\bar{x}_\rho^h|_t (I^h - I) w, \zeta^h \right) \\
&\leq C \left[h |w_t|_1 + |(I - I^h) w|_1 |\bar{x}_t^h|_1 \right] |\zeta^h|_0 \\
&\leq C \left[h \|w\|_{W^{1,\infty}(0,T;H^1(\mathcal{I}))} + h |w|_2 \left[1 + h^{-1} |\bar{\theta}_t^h|_0 \right] \right] |\zeta^h|_0 \\
&\leq C \left[h + \|w\|_{C([0,T];H^2(\mathcal{I}))} \left[h + |\bar{\theta}_t^h|_0 \right] \right] |\zeta^h|_0 \leq C \left[h + |\bar{\theta}_t^h|_0 \right] |\zeta^h|_0.
\end{aligned} \tag{3.4.84}$$

Using (3.1.6b), (3.4.12a), (3.1.5d), (3.1.11), (3.4.4b) and (3.4.15), we have

$$\begin{aligned}
T_{5,7} &= \left(\left(|\bar{x}_\rho^h| I^h w \right)_t, \zeta^h \right)^h - \left(\left(|\bar{x}_\rho^h| I^h w \right)_t, \zeta^h \right) \\
&\leq C h \sum_{j=1}^J |\zeta^h|_{1,\sigma_j} |(|\bar{x}_\rho^h| I^h w)_t|_{0,\sigma_j} \\
&\leq C h \left[|I^h w|_{0,\infty} |\bar{x}_t^h|_1 + |I^h w_t|_0 \right] |\zeta^h|_1 \\
&\leq C h \left[\|w\|_{C([0,T];H^1(\mathcal{I}))} \left[1 + h^{-1} |\bar{\theta}_t^h|_0 \right] + \|w\|_{W^{1,\infty}(0,T;L^2(\mathcal{I}))} \right] |\zeta^h|_1 \\
&\leq C \left[h + |\bar{\theta}_t^h|_0 \right] |\zeta^h|_1.
\end{aligned} \tag{3.4.85}$$

Combining (3.4.72) with (3.4.73)–(3.4.76) and (3.4.83)–(3.4.85), using (3.1.8) and (3.1.9b), we have

$$|T_5| \leq \frac{d}{16M} |\zeta^h|_1^2 + C \left[h^2 + |\bar{\theta}_t^h|_0^2 + |\zeta^h|_0^2 + |\bar{\theta}^h|_1^2 \right]. \tag{3.4.86}$$

Using (3.1.11), (3.4.4b), (3.4.18) and (3.1.8), we have

$$T_6 = d \left(w_\rho \left[\frac{1}{|\bar{x}_\rho^h|} - \frac{1}{|\bar{x}_\rho|} \right], \zeta_\rho^h \right)$$

$$\begin{aligned}
&\leq d |w|_{1,\infty} \left| \frac{1}{|\bar{x}_\rho|} - \frac{1}{|\bar{x}_\rho^h|} \right|_0 |\zeta^h|_1 \\
&\leq C d \|w\|_{C([0,T];H^2(\mathcal{I}))} \left[h + |\bar{\theta}^h|_1 \right] |\zeta^h|_1 \leq \frac{d}{16M} |\zeta^h|_1^2 + C \left[h^2 + |\bar{\theta}^h|_1^2 \right]. \quad (3.4.87)
\end{aligned}$$

We now bound T_7 .

$$\begin{aligned}
T_7 &= \left(\psi^h w^h, \zeta_\rho^h \right)^h - \left(\psi w, \zeta_\rho^h \right) \\
&= \left(\left[\psi^h - I^h \psi \right] w^h + I^h(\psi) \left[w^h - I^h w \right], \zeta_\rho^h \right)^h \\
&\quad + \left[\left(I^h(\psi) I^h(w), \zeta_\rho^h \right)^h - \left(I^h(\psi) I^h(w), \zeta_\rho^h \right) \right] \\
&\quad + \left[\left(\left[(I^h - I) \psi \right] I^h(w), \zeta_\rho^h \right) + \left(\psi \left[(I^h - I) w \right], \zeta_\rho^h \right) \right] =: \sum_{i=1}^3 T_{7,i}. \quad (3.4.88)
\end{aligned}$$

From (3.1.11), (3.4.12b), (3.4.4b), (3.4.4a), (3.1.6a), (3.1.5b) and (3.4.20) we have

$$\begin{aligned}
T_{7,1} &= \left(\left[\psi^h - I^h \psi \right] w^h + I^h(\psi) \left[w^h - I^h w \right], \zeta_\rho^h \right)^h \\
&\leq \max \left\{ |w^h|_{0,\infty}, |I^h \psi|_{0,\infty} \right\} \left[\|(I - I^h) \psi\|_h + \|\psi - \psi^h\|_h + \|\zeta^h\|_h \right] \|\zeta_\rho^h\|_h \\
&\leq C \max \left\{ \|w\|_{C([0,T];H^1(\mathcal{I}))}, \|\bar{x}\|_{W^{1,\infty}(0,T;[H^1(\mathcal{I})]^2)} \right\} \left[C_{\bar{x}} h + |\bar{\theta}_t^h|_0 + |\zeta^h|_0 + |\bar{\theta}^h|_1 \right] |\zeta^h|_1 \\
&\leq C \left[h + |\bar{\theta}_t^h|_0 + |\zeta^h|_0 + |\bar{\theta}^h|_1 \right] |\zeta^h|_1, \quad (3.4.89)
\end{aligned}$$

where $C_{\bar{x}} := 1 + \sqrt{2}(\|\bar{x}\|_{W^{1,\infty}(0,T;[H^1(\mathcal{I})]^2)} + \|\bar{x}\|_{W^{1,\infty}(0,T;[L^\infty(\mathcal{I})]^2)} \|\bar{x}\|_{W^{0,\infty}(0,T;[H^2(\mathcal{I})]^2)})$. Using (3.1.6b), (3.1.5d), (3.4.4b) and (3.4.4a), we have

$$\begin{aligned}
T_{7,2} &= \left(I^h(\psi) I^h(w), \zeta_\rho^h \right)^h - \left(I^h(\psi) I^h(w), \zeta_\rho^h \right) \\
&\leq C h \sum_{j=1}^J |I_j^h(\psi) I_j^h(w)|_{1,\sigma_j} |\zeta_\rho^h|_{0,\sigma_j} \\
&\leq C h \left[C_{\bar{x}} \|w\|_{C([0,T];L^\infty(\mathcal{I}))} + \|\bar{x}\|_{W^{1,\infty}(0,T;[L^\infty(\mathcal{I})]^2)} \|w\|_{C([0,T];H^1(\mathcal{I}))} \right] |\zeta^h|_1 \\
&\leq C h |\zeta^h|_1, \quad (3.4.90)
\end{aligned}$$

while with the addition of (3.1.5b) we obtain

$$\begin{aligned}
T_{7,3} &= \left[\left(\left[(I^h - I) \psi \right] I^h(w), \zeta_\rho^h \right) + \left(\psi \left[(I^h - I) w \right], \zeta_\rho^h \right) \right] \\
&\leq \max \left\{ |I^h w|_{0,\infty}, |\psi|_{0,\infty} \right\} \left[|(I - I^h) \psi|_0 + |(I - I^h) w|_0 \right] |\zeta^h|_1 \\
&\leq C \max \left\{ \|w\|_{C([0,T];H^1(\mathcal{I}))}, \|\bar{x}\|_{W^{1,\infty}(0,T;[H^1(\mathcal{I})]^2)} \right\} \left[C_{\bar{x}} + \|w\|_{C([0,T];H^1(\mathcal{I}))} \right] |\zeta^h|_1 \\
&\leq C h |\zeta^h|_1, \quad (3.4.91)
\end{aligned}$$

where $C_{\bar{x}} := \|\bar{x}\|_{W^{1,\infty}(0,T;[H^1(\mathcal{I})]^2)} + \|\bar{x}\|_{W^{1,\infty}(0,T;[L^\infty(\mathcal{I})]^2)} \|\bar{x}\|_{W^{0,\infty}(0,T;[H^2(\mathcal{I})]^2)}$. Combining (3.4.88) with (3.4.89)–(3.4.91) and using (3.1.8), we have

$$|T_7| \leq \frac{d}{16M} |\zeta^h|_1^2 + C \left[h^2 + |\bar{\theta}_t^h|_0^2 + |\zeta^h|_0^2 + |\bar{\theta}^h|_1^2 \right]. \quad (3.4.92)$$

We now bound T_8 . Using the continuity of g we have

$$\begin{aligned}
T_8 &= \left(|\bar{x}_\rho| g(v, w), \zeta^h \right) - \left(|\bar{x}_\rho^h| g(v^h, w^h), \zeta^h \right)^h \\
&= \left(\left[|\bar{x}_\rho| - |\bar{x}_\rho^h| \right] g(v, w), \zeta^h \right) + \left(|\bar{x}_\rho^h| (I - I^h) g(v, w), \zeta^h \right) \\
&\quad + \left[\left(|\bar{x}_\rho^h| I^h g(v, w), \zeta^h \right) - \left(|\bar{x}_\rho^h| I^h g(v, w), \zeta^h \right)^h \right] \\
&\quad + \left(|\bar{x}_\rho^h| \left(\left[g(I^h v, I^h w) - g(I^h v, w^h) \right] + \left[g(I^h v, w^h) - g(v^h, w^h) \right] \right), \zeta^h \right)^h \\
&=: \sum_{i=1}^4 T_{8,i}. \tag{3.4.93}
\end{aligned}$$

Using (3.4.4d) and (3.4.13), gives

$$T_{8,1} = \left(\left[|\bar{x}_\rho| - |\bar{x}_\rho^h| \right] g(v, w), \zeta^h \right) \leq |g|_{0,\infty} |\bar{x} - \bar{x}^h|_1 |\zeta^h|_0 \leq C \left[h + |\bar{\theta}^h|_1 \right] |\zeta^h|_0. \tag{3.4.94}$$

Using (3.4.12a), (3.1.5b), (3.4.4d), (3.4.4a) and (3.4.4b), we have

$$\begin{aligned}
T_{8,2} &= \left(|\bar{x}_\rho^h| (I - I^h) g(v, w), \zeta^h \right) \\
&\leq C h |g(v, w)|_1 |\zeta^h|_0 \leq C h |g(v, w)|_{0,\infty} \left[C_{\bar{x}} + \|w\|_{C([0,T];H^1(\mathcal{X}))} \right] |\zeta^h|_0 \\
&\leq C h |\zeta^h|_0, \tag{3.4.95}
\end{aligned}$$

whilst with the addition of (3.1.6b) and (3.1.5d) we obtain

$$\begin{aligned}
T_{8,3} &= \left[\left(|\bar{x}_\rho^h| I^h g(v, w), \zeta^h \right) - \left(|\bar{x}_\rho^h| I^h g(v, w), \zeta^h \right)^h \right] \\
&\leq C h \sum_{j=1}^J |g(v, w)|_{1,\sigma_j} \left| |\bar{x}_\rho^h| \zeta^h \right|_{0,\sigma_j} \leq C h |I^h g(v, w)|_1 |\zeta^h|_0 \leq C h |\zeta^h|_0, \tag{3.4.96}
\end{aligned}$$

where $C_{\bar{x}} := \|\bar{x}\|_{W^{1,\infty}(0,T;[H^1(\mathcal{X})]^2)} + \|\bar{x}\|_{W^{1,\infty}(0,T;[L^\infty(\mathcal{X})]^2)} \|\bar{x}\|_{W^{0,\infty}(0,T;[H^2(\mathcal{X})]^2)}$. Using (3.4.12a), (3.4.4d), (3.4.4a), (3.4.12b), (3.1.5b), (3.1.6b), (3.4.20) and (3.4.16), we have

$$\begin{aligned}
T_{8,4} &= \left(|\bar{x}_\rho^h| \left(\left[g(I^h v, I^h w) - g(I^h v, w^h) \right] + \left[g(I^h v, w^h) - g(v^h, w^h) \right] \right), \zeta^h \right)^h \\
&\leq 2ML_g \left[\|\zeta^h\|_h + \|I^h v - v^h\|_h \right] \|\zeta^h\|_h \\
&\leq C \left[|\zeta^h|_0 + |(I - I^h)v|_0 + |v - v^h|_0 \right] |\zeta^h|_0 \\
&\leq C \left[h + |\bar{\theta}_t^h|_0 + |\zeta^h|_0 + |\bar{\theta}^h|_1 \right] |\zeta^h|_0. \tag{3.4.97}
\end{aligned}$$

Combining (3.4.93) with (3.4.94)–(3.4.97) and using (3.1.8), we have

$$|T_8| \leq C \left[h^2 + |\bar{\theta}_t^h|_0^2 + |\zeta^h|_0^2 + |\bar{\theta}^h|_1^2 \right]. \tag{3.4.98}$$

We now combine (3.4.63) with (3.4.64), (3.4.69), (3.4.86), (3.4.87), (3.4.92) and (3.4.98) to obtain

$$\frac{1}{2} \frac{d}{dt} \left(|\bar{x}_\rho^h| \zeta^h, \zeta^h \right)^h + \frac{d}{4M} |\zeta^h|_1^2 \leq C \left[h^2 + |\bar{\theta}_t^h|_0^2 + |\zeta^h|_0^2 + |\bar{\theta}^h|_1^2 \right]. \tag{3.4.99}$$

Multiplying (3.4.99) by $e^{-\gamma s}$, for $\gamma \geq 1$ and integrating with respect to $s \in (0, t)$ with $t \leq T_h^*$, and noting $|\zeta^h(\cdot, 0)| = 0$, we have

$$\begin{aligned} & \frac{1}{2}e^{-\gamma t} \left(|\bar{x}_\rho^h | \zeta^h, \zeta^h \right)^h + \frac{\gamma}{2} \int_0^t e^{-\gamma s} \left(|\bar{x}_\rho^h | \zeta^h, \zeta^h \right)^h ds + \frac{d}{4M} \int_0^t e^{-\gamma s} |\zeta^h|_1^2 ds \\ & \leq C_3 \int_0^t e^{-\gamma s} \left[h^2 + |\bar{\theta}_t^h|_0^2 + |\zeta^h|_0^2 + |\bar{\theta}^h|_1^2 \right] ds. \end{aligned} \quad (3.4.100)$$

From (3.4.12a) and (3.1.6a), we have

$$\frac{1}{2}e^{-\gamma t} \left(|\bar{x}_\rho^h | \zeta^h, \zeta^h \right)^h + \frac{\gamma}{2} \int_0^t e^{-\gamma s} \left(|\bar{x}_\rho^h | \zeta^h, \zeta^h \right)^h ds \geq \frac{m}{4}e^{-\gamma t} |\zeta^h|_0^2 + \frac{\gamma m}{4} \int_0^t e^{-\gamma s} |\zeta^h|_0^2 ds,$$

which, together with (3.4.100), yields the desired result. \square

Proof of Theorem 3.23: Multiplying (3.4.11) by ω , where ω is chosen such that $C_3\omega \leq \frac{m^2\alpha}{32}$, and adding the resulting inequality to (3.4.10), for $t \in [0, T_h^*)$, we have

$$\begin{aligned} & \frac{1}{4}e^{-\gamma t} |\bar{\theta}^h|_1^2 + \frac{m\omega}{4}e^{-\gamma t} |\zeta^h|_0^2 + \frac{m^2\alpha}{32} \int_0^t e^{-\gamma s} |\bar{\theta}_t^h|_0^2 ds + \frac{d\omega}{4M} \int_0^t e^{-\gamma s} |\zeta^h|_1^2 ds \\ & \leq C(1 + \omega) \int_0^t e^{-\gamma s} \left[h^2 + |\zeta^h|_0^2 + |\bar{\theta}^h|_1^2 + h^{-1}|\bar{\theta}^h|_{0,\infty}^4 \right] ds. \end{aligned}$$

An application of Gronwall's lemma then gives

$$\begin{aligned} \sup_{s \in [0, T_h^*]} & \left[\frac{1}{4}e^{-\gamma s} |\bar{\theta}^h|_1^2 + \frac{m\omega}{4}e^{-\gamma s} |\zeta^h|_0^2 \right] + \frac{m^2\alpha}{32} \int_0^{T_h^*} e^{-\gamma s} |\bar{\theta}_t^h|_0^2 ds + \frac{d\omega}{4M} \int_0^{T_h^*} e^{-\gamma s} |\zeta^h|_1^2 ds \\ & \leq C_{\omega, \gamma, T} \int_0^{T_h^*} e^{-\gamma s} \left[h^2 + h^{-1}|\bar{\theta}^h|_{0,\infty}^4 \right] ds, \end{aligned}$$

where $C_{\omega, \gamma, T}$ depends on ω , γ and T but not on T_h^* . Dividing by $\min\{\frac{1}{4}, \frac{m\omega}{4}, \frac{m^2\alpha}{32}, \frac{d\omega}{4M}\}$ gives

$$\begin{aligned} \sup_{s \in [0, T_h^*]} & \left[e^{-\gamma s} |\bar{\theta}^h|_1^2 + e^{-\gamma s} |\zeta^h|_0^2 \right] + \int_0^{T_h^*} e^{-\gamma s} \left[|\bar{\theta}_t^h|_0^2 + |\zeta^h|_1^2 \right] ds \\ & \leq C_1 h^2 + C h^{-1} \int_0^{T_h^*} e^{-\gamma s} |\bar{\theta}^h|_{0,\infty}^4 ds. \end{aligned} \quad (3.4.101)$$

Using (3.1.9b), (3.4.60) and (3.4.12c), for $t \in [0, T_h^*)$, we have

$$e^{-\gamma t} |\bar{\theta}^h|_{0,\infty}^2 \leq e^{-\gamma t} |\bar{\theta}^h|_1^2 + C e^{-\gamma t} |\bar{\theta}^h|_0^2 \leq C C_1 h^2,$$

and hence, for $t \in [0, T_h^*)$, we have

$$C h^{-1} \int_0^t e^{-\gamma s} |\bar{\theta}^h|_{0,\infty}^4 ds \leq C h^{-1} e^{\gamma T} \int_0^t \left(e^{-\gamma s} |\bar{\theta}^h|_{0,\infty}^2 \right)^2 ds \leq C(C_1)^2 T e^{\gamma T} h^3,$$

which, together with (3.3.78), and on noting (3.4.9), yields

$$\sup_{s \in [0, T_h^*]} \left[e^{-\gamma s} |\bar{\theta}^h|_1^2 + e^{-\gamma s} |\zeta^h|_0^2 \right] + \int_0^{T_h^*} e^{-\gamma s} \left[|\bar{\theta}_t^h|_0^2 + |\zeta^h|_1^2 \right] ds$$

$$\leq C_1 h^2 + C(C_1)^2 T e^{\gamma T} h^3 \leq C_1 h^2 + C C_1 T h^{\frac{5}{2}} \leq C_1 h^2 + \frac{1}{2} C_1 h^2 \leq \frac{3}{2} C_1 h^2. \quad (3.4.102)$$

We now follow the argument in [40] to show that $T_h^* = T$. If it were not the case that $T_h^* = T$, we would have $T_h^* < T$, and using (3.4.4e), (3.1.5c), (3.1.5a), (3.1.4a), (3.4.4a), (3.4.102) and (3.4.9), for $\rho \in \mathcal{I}$, we would have

$$\begin{aligned} |\vec{x}_\rho^h(\rho, T_h^*)| &\leq |\vec{x}_\rho(\rho, T_h^*)| + |\vec{x}_\rho(\rho, T_h^*) - \vec{x}_\rho^h(\rho, T_h^*)| \\ &\leq M + |(I - I^h)\vec{x}(\cdot, T_h^*)|_{1,\infty} + |\vec{\theta}^h(\cdot, T_h^*)|_{1,\infty} \\ &\leq M + C h^{\frac{1}{2}} |\vec{x}(\cdot, T_h^*)|_2 + C h^{-\frac{1}{2}} |\vec{\theta}^h(\cdot, T_h^*)|_1 \\ &\leq M + C h^{\frac{1}{2}} \left[\|\vec{x}\|_{W^{0,\infty}(0,T;[H^2(\mathcal{I})]^2)} + e^{\frac{\gamma}{2}T} \right] \leq M + C\beta \leq \frac{3}{2}M, \end{aligned}$$

provided β is chosen small enough, and similarly

$$|\vec{x}_\rho^h(\rho, T_h^*)| \geq |\vec{x}_\rho(\rho, T_h^*)| - |\vec{x}_\rho(\rho, T_h^*) - \vec{x}_\rho^h(\rho, T_h^*)| \geq \frac{3m}{4}.$$

Using (3.1.5d), (3.1.5c), (3.4.4b), (3.1.5b), (3.1.4a), (3.4.102), (3.1.11) and (3.4.9), we see that

$$\begin{aligned} |w^h(\cdot, T_h^*)|_{0,\infty} &\leq |I^h w(\cdot, T_h^*)|_{0,\infty} + |I^h w(\cdot, T_h^*) - w^h(\cdot, T_h^*)|_{0,\infty} \\ &\leq \|w\|_{C([0,T];L^\infty(\mathcal{I}))} + C h^{-\frac{1}{2}} |\zeta^h(\cdot, T_h^*)|_0 \\ &\leq C_w \|w\|_{C([0,T];H^1(\mathcal{I}))} + C h^{\frac{1}{2}} e^{\frac{\gamma}{2}T} \\ &\leq (C_w + C\beta) \|w\|_{C([0,T];H^1(\mathcal{I}))} \leq \frac{3}{2} C_w \|w\|_{C([0,T];H^1(\mathcal{I}))}, \end{aligned}$$

provided β is chosen small enough. Thus we could then extend the discrete solution to an interval $[0, T_h^* + \delta]$, for some $\delta > 0$, with

$$\begin{aligned} \frac{m}{2} &\leq |\vec{x}_\rho^h| \leq 2M \quad \text{in } \mathcal{I} \times [0, T_h^* + \delta] \\ \|w^h\|_{C([0, T_h^* + \delta]; L^\infty(\mathcal{I}))} &\leq 2C_w \|w\|_{C([0, T]; H^1(\mathcal{I}))} \\ \sup_{s \in [0, T_h^* + \delta]} e^{-\gamma s} \left[|\vec{\theta}^h|_1^2 + |\zeta^h|_0^2 \right] &+ \int_0^{T_h^* + \delta} e^{-\gamma s} \left[|\vec{\theta}_t^h|_0^2 + |\zeta_t^h|_1^2 \right] ds < 2C_1 h^2 \end{aligned}$$

which contradicts the definition of T_h^* . Therefore $T_h^* = T$ and from (3.1.5b), (3.4.4a), (3.4.4b), (3.4.9) and (3.4.12c), for $t \in [0, T]$, we have

$$\begin{aligned} \sup_{t \in [0, T]} \left[|\vec{x} - \vec{x}_t^h|_1^2 + |w - w^h|_0^2 \right] &\leq 2 \sup_{t \in [0, T]} \left[|(I - I^h)\vec{x}|_1^2 + |\vec{\theta}_t^h|_1^2 + |(I - I^h)w|_0^2 + |\zeta^h|_0^2 \right] \\ &\leq C h^2 \left[\|\vec{x}\|_{W^{0,\infty}(0,T;[H^2(\mathcal{I})]^2)}^2 + \|w\|_{C([0,T];H^1(\mathcal{I}))}^2 \right] + 4C_1 h^2 e^{\gamma T} \\ &\leq C h^2, \end{aligned}$$

and

$$\int_0^T \left[|\vec{x}_t - \vec{x}_t^h|_0^2 + |w - w^h|_1^2 \right] ds \leq 2 \int_0^T \left[|(I - I^h)\vec{x}_t|_0^2 + |\vec{\theta}_t^h|_0^2 + |(I - I^h)w|_1^2 + |\zeta^h|_1^2 \right] ds$$

$$\begin{aligned} &\leq CT h^2 \left[\|\bar{x}\|_{W^{1,\infty}(0,T;[H^1(\mathcal{I})]^2)}^2 + \|w\|_{C([0,T];H^2(\mathcal{I}))}^2 \right] \\ &\quad + 4C_1 h^2 e^{\gamma T} \leq Ch^2. \end{aligned}$$

□

Remark 3.26. We note that the progression from the bound on the sums in (3.4.80) comes about from utilising the fact that the rectangle rule underestimates the $L^1(\mathcal{I})$ integral because $|\bar{\theta}_t^h(\cdot, t)|$ is positive, and also that it underestimates the $L^2(\mathcal{I})$ integral because $|\bar{\theta}_t^h(\cdot, t)|^2$ is convex.

Remark 3.27. We note here the unconventional approach to splitting (3.4.71) used to bound T_5 , specifically the reason why we split this bound into five parts. Without splitting the bound this way, the terms needed to be bound would be

$$\left(w \left(|\bar{x}_\rho^h| - |\bar{x}_\rho| \right)_t, \zeta^h \right) = \left(w \langle \bar{x}_{\rho,t}^h - \bar{x}_{\rho,t}, \bar{\tau} \rangle, \zeta^h \right) + \left(w \langle \bar{x}_{\rho,t}^h, \bar{\tau}^h - \bar{\tau} \rangle, \zeta^h \right).$$

The first term is part of $T_{5,2}$; however, using (3.1.11), (3.4.4b), (3.4.15), (3.4.19) and (3.4.61), the second term would yield

$$\begin{aligned} \left(w \langle \bar{x}_{\rho,t}^h, \bar{\tau}^h - \bar{\tau} \rangle, \zeta^h \right) &\leq |w|_{0,\infty} |\bar{x}_t^h|_1 |\bar{\tau} - \bar{\tau}^h|_0 |\zeta^h|_{0,\infty} \\ &\leq C \left[h + |\bar{\theta}_t^h|_0 + |\bar{\theta}_t^h|_1 + h^{-\frac{1}{4}} |\bar{\theta}_t^h|_0 \right] |\zeta^h|_{0,\infty}, \end{aligned}$$

which would not result in the desired power of h we require for the result.

3.5 Numerical results for Model \mathcal{M}_1 and Model \mathcal{M}_2

In this section we look to computationally analyse **Model \mathcal{M}_1** and **Model \mathcal{M}_2** . We first concentrate on **Model \mathcal{M}_1** and compare it to the numerical scheme introduced in [42]. Namely the authors in [42] chose to approximate $F(\bar{x}) = 0$ by using a slight variant on (3.3.7). They don't use $F(\bar{X}^n(\rho)) = 0$, for $\rho \in \{0, 1\}$, but rather assume that

$$\langle D_t \bar{X}_j^n, \nabla F(\bar{X}_j^{n-1}) \rangle = 0, \quad \text{for } j = 0, J,$$

as part of their approximation. This leads to a first order approximation of both (3.3.3) and $F(\bar{X}^n) = 0$, such that for their scheme

$$|F(\bar{X}^n)| \leq C \Delta t_n. \tag{3.5.1}$$

This means that Δt_n needs to be chosen appropriately small for the approximation \bar{X}^n to stay close to the boundary for long time simulations. Although we do not prove fully

discrete finite element error bounds using the α parameter, see Remark 3.11, we nevertheless derive the numerical scheme of **Model** \mathcal{M}_1 with the α parameter used and a forcing term on the right hand side. We shall still refer to this as **Model** \mathcal{M}_1 though. In the settings of closed curves, typically one chooses $\vec{\xi}^h = \chi_j \vec{e}_k$ to derive the finite element numerical scheme, where \vec{e}_k , for $k = 0, 1$, provides the standard basis for \mathbb{R}^2 ; however, due to the boundary conditions, considering the restrictions on (3.3.2), we choose to use $\vec{\xi}^h = \nabla^\perp F(\vec{X}_j^n) \chi_j$ for $j = 0, J$ and $\vec{\xi}^h = \chi_j \vec{e}_k$ for $j = 1, \dots, J-1$. Thus, by considering a uniform spatial mesh, the finite element numerical scheme for **Model** \mathcal{M}_1 is

$$\begin{aligned} & \frac{\alpha}{2} \left((q_j^{n-1})^2 + (q_{j+1}^{n-1})^2 \right) \frac{1}{\Delta t_n} \left(\vec{X}_j^n - \vec{X}_j^{n-1} \right) + \left(-\vec{X}_{j+1}^n + 2\vec{X}_j^n - \vec{X}_{j-1}^n \right) \\ & + \frac{1-\alpha}{2} \frac{1}{\Delta t_n} \left(\left\langle \vec{X}_j^n - \vec{X}_j^{n-1}, \vec{\mathcal{N}}_{j-1}^{n-1} \right\rangle \vec{\mathcal{N}}_{j-1}^{n-1} + \left\langle \vec{X}_j^n - \vec{X}_j^{n-1}, \vec{\mathcal{N}}_j^{n-1} \right\rangle \vec{\mathcal{N}}_j^{n-1} \right) \\ & = \frac{1}{2} \left(q_j^{n-1} \vec{\mathcal{N}}_{j-1}^{n-1} + q_{j+1}^{n-1} \vec{\mathcal{N}}_j^{n-1} \right) f_j^n \end{aligned} \quad (3.5.2a)$$

$$\begin{aligned} & \frac{\alpha}{2} (q_0^{n-1})^2 \frac{1}{\Delta t_n} \left\langle \vec{X}_0^n - \vec{X}_0^{n-1}, \nabla^\perp F(\vec{X}_0^n) \right\rangle + \left\langle \vec{X}_0^n - \vec{X}_1^n, \nabla^\perp F(\vec{X}_0^n) \right\rangle \\ & + \frac{1-\alpha}{2} \frac{1}{\Delta t_n} \left\langle \vec{X}_0^n - \vec{X}_0^{n-1}, \vec{\mathcal{N}}_0^{n-1} \right\rangle \left\langle \vec{\mathcal{N}}_0^{n-1}, \nabla^\perp F(\vec{X}_0^n) \right\rangle \\ & = \frac{1}{2} q_0^{n-1} f_0^n \left\langle \vec{\mathcal{N}}_0^{n-1}, \nabla^\perp F(\vec{X}_0^n) \right\rangle \end{aligned} \quad (3.5.2b)$$

$$\begin{aligned} & \frac{\alpha}{2} (q_{J-1}^{n-1})^2 \frac{1}{\Delta t_n} \left\langle \vec{X}_J^n - \vec{X}_J^{n-1}, \nabla^\perp F(\vec{X}_J^n) \right\rangle + \left\langle \vec{X}_J^n - \vec{X}_{J-1}^n, \nabla^\perp F(\vec{X}_J^n) \right\rangle \\ & + \frac{1-\alpha}{2} \frac{1}{\Delta t_n} \left\langle \vec{X}_J^n - \vec{X}_J^{n-1}, \vec{\mathcal{N}}_{J-1}^{n-1} \right\rangle \left\langle \vec{\mathcal{N}}_{J-1}^{n-1}, \nabla^\perp F(\vec{X}_J^n) \right\rangle \\ & = \frac{1}{2} q_{J-1}^{n-1} f_J^n \left\langle \vec{\mathcal{N}}_{J-1}^{n-1}, \nabla^\perp F(\vec{X}_J^n) \right\rangle \end{aligned} \quad (3.5.2c)$$

$$F(\vec{X}_0^n) = 0, \quad F(\vec{X}_J^n) = 0, \quad (3.5.2d)$$

where $q_j^n = |\vec{X}_j^n - \vec{X}_{j-1}^n|$ for $j = 1, \dots, J$ and $\vec{\mathcal{N}}_j^n = \left(\vec{X}_{j+1}^n - \vec{X}_j^n \right)^\perp$ for $j = 0, \dots, J-1$. We use a Newton's scheme to attend to the non-linear components in the following manner. By setting $\vec{X}^{n,i+1} := \vec{X}^{n,i} + \vec{\delta}^i$, with $\vec{X}^{n,0} := \vec{X}^{n-1}$, we replace all occurrences of \vec{X}^n with $\vec{X}^{n,i+1}$ and rearrange to solve for $\vec{\delta}^i$. We neglect terms which have more than one $\vec{\delta}^i$ term, hence gaining the name quadratic approximation, and we then iteratively solve until $|F(\vec{X}^{n,i+1})| < \tau$, for some predetermined tolerance τ . Thus, (3.5.2a)–(3.5.2d) become

$$\begin{aligned} & \frac{\alpha}{2} \left((q_j^{n-1})^2 + (q_{j+1}^{n-1})^2 \right) \frac{1}{\Delta t_n} \vec{\delta}_j^i + \left(-\vec{\delta}_{j+1}^i + 2\vec{\delta}_j^i - \vec{\delta}_{j-1}^i \right) \\ & + \frac{1-\alpha}{2} \frac{1}{\Delta t_n} \left(\left\langle \vec{\delta}_j^i, \vec{\mathcal{N}}_{j-1}^{n-1} \right\rangle \vec{\mathcal{N}}_{j-1}^{n-1} + \left\langle \vec{\delta}_j^i, \vec{\mathcal{N}}_j^{n-1} \right\rangle \vec{\mathcal{N}}_j^{n-1} \right) \\ & = \frac{1}{2} \left(q_j^{n-1} \vec{\mathcal{N}}_{j-1}^{n-1} + q_{j+1}^{n-1} \vec{\mathcal{N}}_j^{n-1} \right) f_j^n - \left(-\vec{X}_{j+1}^{n,i} + 2\vec{X}_j^{n,i} - \vec{X}_{j-1}^{n,i} \right) \\ & - \frac{1-\alpha}{2} \frac{1}{\Delta t_n} \left(\left\langle \vec{X}_j^{n,i} - \vec{X}_j^{n-1}, \vec{\mathcal{N}}_{j-1}^{n-1} \right\rangle \vec{\mathcal{N}}_{j-1}^{n-1} + \left\langle \vec{X}_j^{n,i} - \vec{X}_j^{n-1}, \vec{\mathcal{N}}_j^{n-1} \right\rangle \vec{\mathcal{N}}_j^{n-1} \right) \\ & - \frac{\alpha}{2} \left((q_j^{n-1})^2 + (q_{j+1}^{n-1})^2 \right) \frac{1}{\Delta t_n} \left(\vec{X}_j^{n,i} - \vec{X}_j^{n-1} \right) \end{aligned} \quad (3.5.3a)$$

$$\begin{aligned}
& \frac{\alpha}{2} (q_0^{n-1})^2 \frac{1}{\Delta t_n} \left\langle \vec{\delta}_0^i, \nabla^\perp F(\vec{X}_0^{n,i}) \right\rangle \\
& + \frac{\alpha}{2} (q_0^{n-1})^2 \frac{1}{\Delta t_n} \left\langle \vec{X}_0^{n,i} - \vec{X}_0^{n-1}, D_\perp^2 F(\vec{X}_0^{n,i}) \vec{\delta}_0^i \right\rangle + \left\langle \vec{\delta}_0^i - \vec{\delta}_1^i, \nabla^\perp F(\vec{X}_0^{n,i}) \right\rangle \\
& + \left\langle \vec{X}_0^{n,i} - \vec{X}_1^{n,i}, D_\perp^2 F(\vec{X}_0^{n,i}) \vec{\delta}_0^i \right\rangle \\
& + \frac{1-\alpha}{2} \frac{1}{\Delta t_n} \left\langle \vec{\delta}_0^i, \vec{\mathcal{N}}_0^{n-1} \right\rangle \left\langle \vec{\mathcal{N}}_0^{n-1}, \nabla^\perp F(\vec{X}_0^{n,i}) \right\rangle \\
& + \frac{1-\alpha}{2} \frac{1}{\Delta t_n} \left\langle \vec{X}_0^{n,i} - \vec{X}_0^{n-1}, \vec{\mathcal{N}}_0^{n-1} \right\rangle \left\langle \vec{\mathcal{N}}_0^{n-1}, D_\perp^2 F(\vec{X}_0^{n,i}) \vec{\delta}_0^i \right\rangle \\
& - \frac{1}{2} q_0^{n-1} f_0^n \left\langle \vec{\mathcal{N}}_0^{n-1}, D_\perp^2 F(\vec{X}_0^{n,i}) \vec{\delta}_0^i \right\rangle \\
& = \frac{1}{2} q_0^{n-1} f_0^n \left\langle \vec{\mathcal{N}}_0^{n-1}, \nabla^\perp F(\vec{X}_0^{n,i}) \right\rangle - \left\langle \vec{X}_0^{n,i} - \vec{X}_1^{n,i}, \nabla^\perp F(\vec{X}_0^{n,i}) \right\rangle \\
& - \frac{\alpha}{2} (q_0^{n-1})^2 \frac{1}{\Delta t_n} \left\langle \vec{X}_0^{n,i} - \vec{X}_0^{n-1}, \nabla^\perp F(\vec{X}_0^{n,i}) \right\rangle \\
& - \frac{1-\alpha}{2} \frac{1}{\Delta t_n} \left\langle \vec{X}_0^{n,i} - \vec{X}_0^{n-1}, \vec{\mathcal{N}}_0^{n-1} \right\rangle \left\langle \vec{\mathcal{N}}_0^{n-1}, \nabla^\perp F(\vec{X}_0^{n,i}) \right\rangle \tag{3.5.3b}
\end{aligned}$$

$$\begin{aligned}
& \frac{\alpha}{2} (q_{J-1}^{n-1})^2 \frac{1}{\Delta t_n} \left\langle \vec{\delta}_J^i, \nabla^\perp F(\vec{X}_J^{n,i}) \right\rangle + \left\langle \vec{\delta}_J^i - \vec{\delta}_{J-1}^i, \nabla^\perp F(\vec{X}_J^{n,i}) \right\rangle \\
& + \frac{\alpha}{2} (q_{J-1}^{n-1})^2 \frac{1}{\Delta t_n} \left\langle \vec{X}_J^{n,i} - \vec{X}_J^{n-1}, D_\perp^2 F(\vec{X}_J^{n,i}) \vec{\delta}_J^i \right\rangle \\
& + \left\langle \vec{X}_J^{n,i} - \vec{X}_{J-1}^{n,i}, D_\perp^2 F(\vec{X}_J^{n,i}) \vec{\delta}_J^i \right\rangle \\
& + \frac{1-\alpha}{2} \frac{1}{\Delta t_n} \left\langle \vec{\delta}_J^i, \vec{\mathcal{N}}_{J-1}^{n-1} \right\rangle \left\langle \vec{\mathcal{N}}_{J-1}^{n-1}, \nabla^\perp F(\vec{X}_J^{n,i}) \right\rangle \\
& + \frac{1-\alpha}{2} \frac{1}{\Delta t_n} \left\langle \vec{X}_J^{n,i} - \vec{X}_J^{n-1}, \vec{\mathcal{N}}_{J-1}^{n-1} \right\rangle \left\langle \vec{\mathcal{N}}_{J-1}^{n-1}, D_\perp^2 F(\vec{X}_J^{n,i}) \vec{\delta}_J^i \right\rangle \\
& - \frac{1}{2} q_{J-1}^{n-1} f_J^n \left\langle \vec{\mathcal{N}}_{J-1}^{n-1}, D_\perp^2 F(\vec{X}_J^{n,i}) \vec{\delta}_J^i \right\rangle \\
& = \frac{1}{2} q_{J-1}^{n-1} f_J^n \left\langle \vec{\mathcal{N}}_{J-1}^{n-1}, \nabla^\perp F(\vec{X}_J^{n,i}) \right\rangle - \left\langle \vec{X}_J^{n,i} - \vec{X}_{J-1}^{n,i}, \nabla^\perp F(\vec{X}_J^{n,i}) \right\rangle \\
& - \frac{\alpha}{2} (q_{J-1}^{n-1})^2 \frac{1}{\Delta t_n} \left\langle \vec{X}_J^{n,i} - \vec{X}_J^{n-1}, \nabla^\perp F(\vec{X}_J^{n,i}) \right\rangle \\
& - \frac{1-\alpha}{2} \frac{1}{\Delta t_n} \left\langle \vec{X}_J^{n,i} - \vec{X}_J^{n-1}, \vec{\mathcal{N}}_{J-1}^{n-1} \right\rangle \left\langle \vec{\mathcal{N}}_{J-1}^{n-1}, \nabla^\perp F(\vec{X}_J^{n,i}) \right\rangle \tag{3.5.3c}
\end{aligned}$$

$$F(\vec{X}_0^{n,i}) = -\langle \nabla F(\vec{X}_0^{n,i}), \vec{\delta}_0^i \rangle, \quad F(\vec{X}_J^{n,i}) = -\langle \nabla F(\vec{X}_J^{n,i}), \vec{\delta}_J^i \rangle, \tag{3.5.3d}$$

where $D_\perp^2 = RD^2$, with R being the anti-clockwise rotation matrix around $\frac{\pi}{2}$ and D being the second order differential operator. We state that this is work already conducted in [109], in which α is set to 1 for easy of presentation. We begin our numerical computations with two examples, one showing the benefit of the α parameter and the other showing the benefit of the Newton's scheme. In these two examples we monitor the following errors:

$$\mathcal{E}_1 := \sup_{n=0, \dots, N} |I^h(\vec{x}^n) - \vec{X}^n|_0^2, \quad \mathcal{E}_2 := \sum_{n=1}^N \Delta t_n |I^h(\vec{x}^n) - \vec{X}^n|_1^2, \tag{3.5.4}$$

$$\mathcal{E}_3 := \sup_{n=0, \dots, N} |I^h(\vec{x}^n) - \vec{X}^n|_1^2, \quad \mathcal{E}_4 := \sum_{n=1}^N \Delta t_n |D_t(I^h(\vec{x}^n) - \vec{X}^n)|_0^2, \tag{3.5.5}$$

and quantify them using

$$eoc_{i,j} := \frac{\ln(\mathcal{E}_{i,j+1}) - \ln(\mathcal{E}_{i,j})}{\ln(h_{i,j+1}) - \ln(h_{i,j})}. \quad (3.5.6)$$

Example 1

For our first example we consider a shrinking *semi* circle. Indeed setting $\Omega := \mathbb{R} \times \mathbb{R}_{>0}$ and taking $\Gamma(0)$ to be a semi-circle with radius one centred at 0, with $f(\rho, t) = 0$, the explicit solution to **Model** \mathcal{M}_1 is given by

$$\vec{x}(\rho, t) = \sqrt{1 - 2t} (\cos(\pi\rho), \sin(\pi\rho))^T, \quad \rho \in [0, 1], t \in [0, T].$$

We set $T = 0.4$ and consider a uniform time discretisation. The following Tables 3.1–3.6 were produced using MATLAB R2019a [92] installed on a 2015 Apple iMac 21.5” with an i5-3.1 GHz processor which has 4 cores. Typically MATLAB uses only one core when executing user developed code.

Tables 3.1–3.4 display the errors for the Newton’s scheme (3.5.3a)–(3.5.3d). The errors obtained by taking $\Delta t = h^2$ and $\alpha = 1$ are displayed in Table 3.1 while the errors obtained by taking $\Delta t = h^2$ and $\alpha = 0.5$ are displayed in Table 3.2. Tables 3.3 and 3.4 display the errors obtained by taking $\Delta t = 0.1h$ and $\alpha = 1$ and $\Delta t = 0.1h$ and $\alpha = 0.5$ respectively. Tables 3.5 and 3.6 display the errors for the numerical scheme presented in [42], the results in Table 3.5 were obtained by setting $\Delta t = h^2$ while the results in Table 3.6 were obtained by setting $\Delta t = 0.1h$. For \mathcal{E}_3 and \mathcal{E}_4 we see a similar experimental order of convergence for both $\alpha = 1$ and $\alpha < 1$, for both cases of $\Delta t = Ch$ and $\Delta t = Ch^2$. Indeed, we see eocs of close to 4 for both $\alpha = 1$ and $\alpha < 1$ with $\Delta t = Ch^2$, and we see eocs of close to 2 for both $\alpha = 1$ and $\alpha < 1$ with $\Delta t = Ch$. Considering $\Delta t = Ch$, all the errors are exhibiting the eocs expected from [6] however not proven in our setting in which the closed curve setting of [42] has been replaced by a curve attached orthogonally to a fixed boundary. Numerically, we see that both attain the desired convergence. We also see that \mathcal{E}_1 and \mathcal{E}_2 exhibit eocs of close to 4 for both $\alpha = 1$ and $\alpha < 1$ with $\Delta t = Ch^2$, and exhibit eocs close to 2 for both $\alpha = 1$ and $\alpha < 1$ with $\Delta t = Ch$. Considering $\Delta t = Ch^2$, all of the errors are exhibiting greater levels of convergence than what Theorems 3.13 and 3.18 predict. As described in Example 1 in Section 2.4.1, one might expect an eoc of 4 for \mathcal{E}_1 and \mathcal{E}_4 since they are L^2 type errors. Similarly, as described in Example 1 in Section 2.4.1 and [6], \mathcal{E}_2 and \mathcal{E}_3 are exhibiting superconvergence since they are H^1 type errors. Interestingly, we still see superconvergence when using a non-uniform mesh in this example, but we didn’t investigate this property further.

Next, we look at how α effects the errors. Comparing Tables 3.1 and 3.2 we can that the results in Table 3.2 give three to four times the amount of precision opposed to the results presented in Table 3.1. Another interesting result to note is that the finite element scheme presented in [42] and (3.5.3a)–(3.5.3d) give identical errors. Indeed we remark that the Newton’s step only requires one solve and so the schemes are actually identical for this example. The reason for the one step convergence is because the (important) boundary term is solved exactly. In particular, noting that in this example $\nabla F(\vec{p}) = (0, 1)^T$, for $\vec{p} \in \mathbb{R}^2$, equations (3.5.3b) and (3.5.3d) decouple and (3.5.3d) gives

$$F(\vec{X}_0^{n,i}) = -(\delta_0^i)_0$$

which, due to the initial condition, will always be 0. Since the stopping criteria for the Newton’s scheme is $|F(\vec{X}^{n,i+1})| \leq \tau$, and since in this case $|F(\vec{X}^{n,1})| = 0$, the iteration will stop after one step. Thus, since $\vec{X}^{n,0} = \vec{X}^{n-1}$ and F is linear, the schemes are the same.

Finally, we look at the computational time of some of the results. Considering the setting of $\alpha = 1$, taking $J = 10$ and $M = 40$ and using (3.5.3a)–(3.5.3d) results in approximately 0.011 seconds of execution time whilst using the scheme presented in [42] results in approximately 0.004 seconds of execution time. Taking $J = 160$ and $M = 10240$ and using (3.5.3a)–(3.5.3d) results in approximately 21.4 seconds of execution time whilst using the scheme presented in [42] results in approximately 23.6 seconds of execution time. Considering the setting of $\alpha = 0.5$, taking $J = 10$ and $M = 40$ and using (3.5.3a)–(3.5.3d) results in approximately 0.012 seconds of execution time whilst taking $J = 160$ and $M = 10240$ and using (3.5.3a)–(3.5.3d) results in approximately 25.1 seconds of execution time. Given what is discussed in the previous paragraph, it makes sense that the execution time for the scheme presented in [42] and (3.5.3a)–(3.5.3d) with $\alpha = 1$ solve at almost the same speed, the slightly greater execution time when considering $\alpha < 1$ is likely due to the extra terms which need to be computed for the system matrix.

J	M	$\mathcal{E}_1 \times 10^5$	eoc_1	$\mathcal{E}_2 \times 10^6$	eoc_2	$\mathcal{E}_3 \times 10^4$	eoc_3	$\mathcal{E}_4 \times 10^5$	eoc_4
10	40	46.95	-	299.3	-	46.72	-	201.6	-
20	160	4.042	3.54	2.255	3.73	39.97	3.55	18.59	3.44
40	640	0.2760	3.87	0.1481	3.93	2.726	3.87	1.298	3.84
80	2560	0.01765	3.97	0.009377	3.98	0.1742	3.97	0.08347	3.96
160	10240	0.001110	3.99	0.0005880	4.00	0.01095	3.99	0.005254	3.99

Table 3.1: Errors for (3.5.3a)–(3.5.3d), with $\Delta t = h^2$ and $\alpha = 1$, for Example 1.

J	M	$\mathcal{E}_1 \times 10^5$	eoc_1	$\mathcal{E}_2 \times 10^6$	eoc_2	$\mathcal{E}_3 \times 10^4$	eoc_3	$\mathcal{E}_4 \times 10^5$	eoc_4
10	40	15.97	-	79.91	-	15.89	-	88.84	-
20	160	1.405	3.51	6.093	3.71	1.389	3.52	8.302	3.42
40	640	0.09635	3.87	0.4013	3.92	0.09514	3.87	0.5798	3.84
80	2560	0.006167	3.97	0.02542	3.98	0.006087	3.97	0.03729	3.96
160	10240	0.0003877	3.99	0.001594	4.00	0.0003827	3.99	0.002348	3.99

Table 3.2: Errors for (3.5.3a)–(3.5.3d), with $\Delta t = h^2$ and $\alpha = 0.5$, for Example 1.

J	M	$\mathcal{E}_1 \times 10^5$	eoc_1	$\mathcal{E}_2 \times 10^6$	eoc_2	$\mathcal{E}_3 \times 10^4$	eoc_3	$\mathcal{E}_4 \times 10^5$	eoc_4
10	40	46.95	-	299.3	-	46.72	-	201.6	-
20	80	14.51	1.69	84.74	1.82	14.35	1.70	65.05	1.63
40	160	4.054	1.84	22.58	1.91	4.003	1.84	18.65	1.80
80	320	1.073	1.92	5.832	1.95	1.060	1.92	5.009	1.90
160	640	0.2763	1.96	1.482	1.98	0.2727	1.96	1.299	1.95

Table 3.3: Errors for (3.5.3a)–(3.5.3d), with $\Delta t = 0.1h$ and $\alpha = 1$, for Example 1.

J	M	$\mathcal{E}_1 \times 10^5$	eoc_1	$\mathcal{E}_2 \times 10^6$	eoc_2	$\mathcal{E}_3 \times 10^4$	eoc_3	$\mathcal{E}_4 \times 10^5$	eoc_4
10	40	15.97	-	79.91	-	15.89	-	88.84	-
20	80	9.159	0.80	48.77	0.71	9.058	0.81	45.11	0.98
40	160	3.267	1.49	17.46	1.48	3.226	1.49	15.66	1.53
80	320	0.9664	1.76	5.149	1.76	0.9540	1.76	4.598	1.77
160	640	0.2624	1.88	1.394	1.89	0.2589	1.88	1.245	1.88

Table 3.4: Errors for (3.5.3a)–(3.5.3d), with $\Delta t = 0.1h$ and $\alpha = 0.5$, for Example 1.

J	M	$\mathcal{E}_1 \times 10^5$	eoc_1	$\mathcal{E}_2 \times 10^6$	eoc_2	$\mathcal{E}_3 \times 10^4$	eoc_3	$\mathcal{E}_4 \times 10^5$	eoc_4
10	40	46.95	-	299.3	-	46.72	-	201.6	-
20	160	4.042	3.54	22.55	3.73	3.997	3.55	18.59	3.44
40	640	0.2760	3.87	1.481	3.93	0.2726	3.87	1.298	3.84
80	2560	0.01765	3.97	0.09377	3.98	0.01742	3.97	0.08347	3.96
160	10240	0.001110	3.99	0.005880	4.00	0.001095	3.99	0.005254	3.99

Table 3.5: Errors for the numerical scheme presented in [42], with $\Delta t = h^2$, for Example 1.

J	M	$\mathcal{E}_1 \times 10^5$	eoc_1	$\mathcal{E}_2 \times 10^6$	eoc_2	$\mathcal{E}_3 \times 10^4$	eoc_3	$\mathcal{E}_4 \times 10^5$	eoc_4
10	40	46.95	-	299.3	-	46.72	-	201.6	-
20	80	14.51	1.69	84.74	1.82	14.35	1.70	65.05	1.63
40	160	4.054	1.84	22.58	1.91	4.003	1.84	18.65	1.80
80	320	1.073	1.92	5.832	1.95	1.060	1.92	5.009	1.90
160	640	0.2763	1.96	1.482	1.98	0.2727	1.96	1.299	1.95

Table 3.6: Errors for the numerical scheme presented in [42], with $\Delta t = 0.1h$, for Example 1.

Example 2

Considering

$$\Omega := \{\vec{p} \in \mathbb{R}^2 : |\vec{p}|^2 < 1\}$$

and taking $\Gamma(0)$ to be the line $\vec{p}_1 = \vec{p}_0$, such that $\Gamma(0)$ is the diameter of the circle produced by Ω , as well as

$$f(\rho, t) = \frac{4(\rho - \frac{1}{2})}{(1 - 2t)^2 + 1},$$

gives rise to the explicit solution of **Model** \mathcal{M}_1 to be

$$\vec{x}(\rho, t) = \frac{2(\rho - \frac{1}{2})}{\sqrt{(1 - 2t)^2 + 1}}(1 - 2t, 1)^T, \quad \rho \in [0, 1], t \in [0, T].$$

Given the result of (3.5.1) we also monitor the error

$$\mathcal{E}_5 := \sup_{n=0, \dots, N} \sup_{j=0, J} |F(\vec{X}_j^n)|, \quad \text{with} \quad eoc_{5,j} = \frac{\ln(\mathcal{E}_{5,j+1}) - \ln(\mathcal{E}_{5,j})}{\ln(\Delta t_{j+1}) - \ln(\Delta t_j)}. \quad (3.5.7)$$

This example does not automatically satisfy $|\nabla F(\vec{p})| = 1$, for $\vec{p} \in \mathbb{R}^2$, nor is F linear, and hence enables the superiority of the Newton's scheme (3.5.2a)–(3.5.2d) to be observed.

Similarly to Example 1, we produce the results in Tables 3.7–3.14 and Figure 3.9 using MATLAB on the iMac computer.

We consider $T = 0.5$. We see (3.5.3a)–(3.5.3d) is significantly more precise than the numerical scheme presented in [42] regardless of the choice of α . Tables 3.7–3.10 display the errors for the Newton’s scheme. We note that we don’t demonstrate (3.5.7) for the Newton’s scheme (3.5.3a)–(3.5.3d) since the stopping criteria is set to be $\sup_{j=0,J} |F(\vec{X}_j^n)| < \tau$. The errors obtained by taking $\Delta t = h^2$ and $\alpha = 1$ are displayed in Table 3.7 whilst the errors obtained by taking $\Delta t = h^2$ and $\alpha = 0.5$ are displayed in Table 3.8. Tables 3.9 and 3.10 display the errors obtained by taking $\Delta t = 0.1h$ and $\alpha = 1$ and $\Delta t = 0.1h$ and $\alpha = 0.5$ respectively. Tables 3.11–3.14 display the errors for the numerical scheme presented in [42], the results in Tables 3.11 and 3.13 were obtained by setting $\Delta t = h^2$ while the results in Tables 3.12 and 3.14 were obtained by setting $\Delta t = 0.1h$. We see practically the same convergence results for this example as in Example 1. One can easily see the difference in magnitudes for all the errors comparing (3.5.3a)–(3.5.3d) to the numerical scheme presented in [42]. Indeed comparing Table 3.7 to Tables 3.11 and 3.13 and comparing Table 3.9 to Tables 3.12 and 3.14 we see that Tables 3.7 and 3.9 are between twenty to thirty times the precision of the errors in the respective tables for the numerical scheme presented in [42]. In Figure 3.9 we see the effect that (3.5.1) has on the numerical scheme produced in [42], in particular there is a noticeable gap between the end points of the curve \vec{X}^n and the boundary. Considering the setting of $\alpha = 1$, taking $J = 10$ and $M = 50$ and using (3.5.3a)–(3.5.3d) results in approximately 0.024 seconds of execution time whilst using the scheme presented in [42] results in approximately 0.005 seconds of execution time. Taking $J = 160$ and $M = 12800$ and using (3.5.3a)–(3.5.3d) results in approximately 71.8 seconds of execution time whilst using the scheme presented in [42] results in approximately 31.5 seconds of execution time. As one can see, the Newton’s scheme takes over twice as long to complete the computation but gains a significant increase in precision. Similarly to Example 1, taking $\alpha < 1$ doesn’t change the computational time much.

Remark 3.28. *We note that the choice of F hardly changes the errors from each scheme, further highlighting that the choice of linear F is what resulted in the errors being the same for each scheme rather than $|\nabla F| = 1$. Indeed taking*

$$F(\vec{p}) = |\vec{p}| - 1 \quad \text{or} \quad F(\vec{p}) = |\vec{p}|^2 - 1$$

had next to no effect on the errors for both schemes considered.

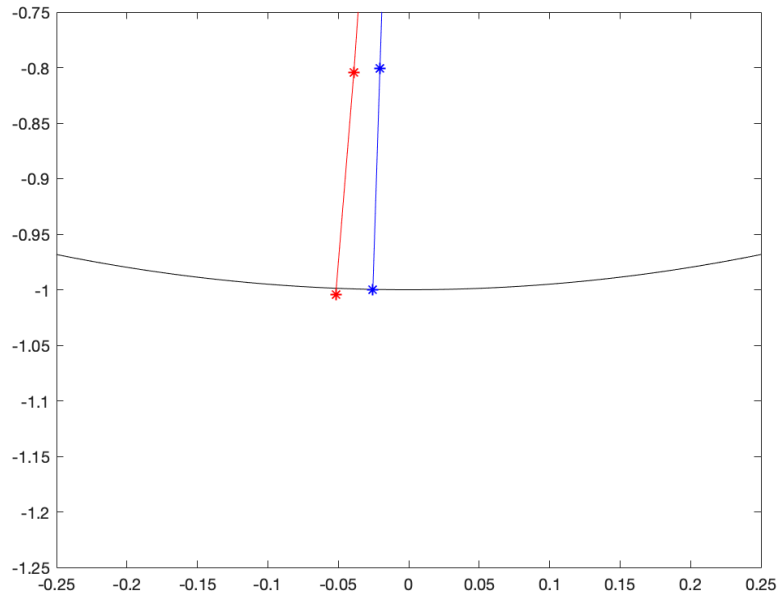


Figure 3.9: Demonstrating (3.5.1). The black line is the boundary, the red line is the numerical approximation from the numerical solution presented in [42] and the blue line is the approximation from (3.5.3a)–(3.5.3d).

J	M	$\mathcal{E}_1 \times 10^7$	eoc_1	$\mathcal{E}_2 \times 10^6$	eoc_2	$\mathcal{E}_3 \times 10^5$	eoc_3	$\mathcal{E}_4 \times 10^6$	eoc_4
10	50	107.9	-	27.70	-	14.40	-	30.40	-
20	200	6.797	3.99	1.796	3.95	0.9198	3.97	1.925	3.98
40	800	0.4256	4.00	0.1133	3.99	0.05780	3.99	0.1207	4.00
80	3200	0.02661	4.00	0.007100	4.00	0.003617	4.00	0.007552	4.00
160	12800	0.001664	4.00	0.000440	4.00	0.0002262	4.00	0.0004721	4.00

Table 3.7: Errors (3.5.4)–(3.5.5) for (3.5.3a)–(3.5.3d), with $\Delta t = h^2$ and $\alpha = 1$, for Example 2.

J	M	$\mathcal{E}_1 \times 10^7$	eoc_1	$\mathcal{E}_2 \times 10^6$	eoc_2	$\mathcal{E}_3 \times 10^5$	eoc_3	$\mathcal{E}_4 \times 10^6$	eoc_4
10	50	95.38	-	23.73	-	11.81	-	27.10	-
20	200	5.997	3.99	1.525	3.96	0.7459	3.98	1.716	3.98
40	800	0.3752	4.00	0.09596	3.99	0.04673	4.00	0.1076	4.00
80	3200	0.02346	4.00	0.006008	4.00	0.002923	4.00	0.006727	4.00
160	12800	0.001466	4.00	0.0003757	4.00	0.0001827	4.00	0.0004205	4.00

Table 3.8: Errors (3.5.4)–(3.5.5) for (3.5.3a)–(3.5.3d), with $\Delta t = h^2$ and $\alpha = 0.5$, for Example 2.

J	M	$\mathcal{E}_1 \times 10^7$	eoc_1	$\mathcal{E}_2 \times 10^6$	eoc_2	$\mathcal{E}_3 \times 10^5$	eoc_3	$\mathcal{E}_4 \times 10^6$	eoc_4
10	50	107.9	-	27.70	-	14.40	-	30.40	-
20	100	27.25	1.99	7.140	1.96	3.680	1.97	7.695	1.98
40	200	6.823	2.00	1.805	1.98	0.9250	1.99	1.931	1.99
80	400	1.705	2.00	0.4532	1.99	0.2316	2.00	0.4832	2.00
160	800	0.4261	2.00	0.1135	2.00	0.05790	2.00	0.1208	2.00

Table 3.9: Errors (3.5.4)–(3.5.5) for (3.5.3a)–(3.5.3d), with $\Delta t = 0.1h$ and $\alpha = 1$, for Example 2.

J	M	$\mathcal{E}_1 \times 10^7$	eoc_1	$\mathcal{E}_2 \times 10^6$	eoc_2	$\mathcal{E}_3 \times 10^5$	eoc_3	$\mathcal{E}_4 \times 10^6$	eoc_4
10	50	95.38	-	23.73	-	11.81	-	27.10	-
20	100	24.00	1.99	6.060	1.97	2.984	1.98	6.846	1.99
40	200	6.008	2.00	1.528	1.99	0.7480	2.00	1.718	1.99
80	400	1.502	2.00	0.3835	1.99	0.1871	2.00	0.4301	2.00
160	800	0.3755	2.00	0.09603	2.00	0.04678	2.00	0.1076	2.00

Table 3.10: Errors (3.5.4)–(3.5.5) for (3.5.3a)–(3.5.3d), with $\Delta t = 0.1h$ and $\alpha = 0.5$, for Example 2.

J	M	$\mathcal{E}_1 \times 10^7$	eoc_1	$\mathcal{E}_2 \times 10^6$	eoc_2
10	50	2839	-	71.71	-
20	200	203.4	3.80	51.83	3.79
40	800	13.24	3.94	3.379	3.94
80	3200	0.8383	3.98	0.2140	3.98
160	12800	0.05264	3.99	0.01343	3.99

Table 3.11: Errors (3.5.4) for the numerical scheme presented in [42], with $\Delta t = h^2$, for Example 2.

J	M	$\mathcal{E}_1 \times 10^7$	eoc_1	$\mathcal{E}_2 \times 10^6$	eoc_2
10	50	2839	-	717.1	-
20	100	788.9	1.85	201.7	1.83
40	200	206.9	1.93	52.94	1.93
80	400	52.91	1.97	13.53	1.97
160	800	13.38	1.98	3.416	1.99

Table 3.12: Errors (3.5.4) for the numerical scheme presented in [42], with $\Delta t = 0.1h$, for Example 2.

J	M	$\mathcal{E}_3 \times 10^5$	eoc_3	$\mathcal{E}_4 \times 10^6$	eoc_4	$\mathcal{E}_5 \times 10^4$	eoc_5
10	50	438.3	-	762.0	-	57.71	-
20	200	31.75	3.79	54.42	3.81	15.63	0.94
40	800	2.076	3.93	3.542	3.94	3.989	0.99
80	3200	0.1317	3.98	0.2243	3.98	1.003	1.00
160	12800	0.008275	3.99	0.01409	3.99	0.2509	1.00

Table 3.13: Errors (3.5.5) and (3.5.7) for the numerical scheme presented in [42], with $\Delta t = h^2$, for Example 2.

Now that we have demonstrated the effectiveness of taking $\alpha < 1$ and using our Newton's scheme we show the experimental order of convergence for the coupled system in **Model** \mathcal{M}_2 . The fully discrete finite element form of the reaction-diffusion equation takes the form

$$D_t \left[\left(|\vec{X}_\rho^n| W^n, \eta^h \right)^h \right] + \left(\Psi^n W^n, \eta_\rho^h \right)^h + d \left(\frac{W_\rho^n}{|\vec{X}_\rho^n|}, \eta_\rho^h \right)$$

J	M	$\mathcal{E}_3 \times 10^5$	eoc_3	$\mathcal{E}_4 \times 10^6$	eoc_4	$\mathcal{E}_5 \times 10^4$	eoc_5
10	50	438.3	-	762.0	-	57.71	-
20	100	123.4	1.83	211.2	1.85	30.41	0.92
40	200	32.49	1.93	55.34	1.93	15.63	0.96
80	400	8.319	1.97	14.15	1.97	7.923	0.98
160	800	2.104	1.98	3.577	1.98	3.989	0.99

Table 3.14: Errors (3.5.5) and (3.5.7) for the numerical scheme presented in [42], with $\Delta t = 0.1h$, for Example 2.

$$= \left(|\vec{X}_\rho^n| g(V^n, W^{n-1}), \eta^h \right)^h, \quad \forall \eta^h \in S_0^h, \quad (3.5.8a)$$

$$W_0^n = w_d, \quad W_J^n = w_d, \quad (3.5.8b)$$

where $\Psi^n(\cdot)$ and $V^n(\cdot)$ are the approximations to the tangential velocity $\psi(\cdot, t^n)$ and the normal velocity $v(\cdot, t^n)$ respectively, on each σ_j , which take the form

$$\Psi^n := \langle D_t \vec{X}^n, \vec{T}^n \rangle, \quad V^n := \langle D_t \vec{X}^n, \vec{V}^n \rangle, \quad \text{on } \sigma_j, j = 1, \dots, J.$$

For this coupled system as well as monitoring the errors in (3.5.5) we also monitor

$$\mathcal{E}_6 := \sup_{n=0, \dots, N} |I^h(w^n) - W^n|_0^2, \quad \mathcal{E}_7 := \sum_{n=1}^N \Delta t_n |I^h(w^n) - W^n|_1^2, \quad (3.5.9)$$

and quantify them using (3.5.6).

Example 3

Setting $\Omega := \mathbb{R} \times \mathbb{R}_{>0}$ and taking $\Gamma(0)$ to be a semi-circle with radius one centred around 0, with

$$f(w) = -\frac{1}{2} \frac{w^2}{(1-t)^{\frac{5}{2}}} - \frac{1}{2} \frac{\cos^2(\pi\rho)}{\sqrt{1-t}}, \quad g(v, w) = -\frac{1}{2} \frac{w}{1-t}$$

and $d = 1$, the explicit solutions to **Model** \mathcal{M}_2 are then given by

$$\vec{x}(\rho, t) = \sqrt{1-t} (\cos(\pi\rho), \sin(\pi\rho))^T, \quad w(\rho, t) = (1-t) \sin(\pi\rho), \quad \rho \in [0, 1], t \in [0, T].$$

As in Examples 1 and 2, we produce the results in Tables 3.15 – 3.18 using MATLAB on the iMac computer.

Table 3.15 displays the errors for $\Delta t = h^2$ and $\alpha = 1$ whilst Table 3.16 displays the errors for $\Delta t = h^2$ and $\alpha = 0.5$. Table 3.17 displays the errors for $\Delta t = 0.1h$ and $\alpha = 1$ whilst Table 3.18 displays the errors for $\Delta t = 0.1h$ and $\alpha = 0.5$. We see that \mathcal{E}_3 and

\mathcal{E}_4 are following the same convergence rate as in Examples 1 and 2 for both $\alpha = 1$ and $\alpha < 1$ with $\Delta t = Ch^2$ and $\Delta t = Ch$. We also see that \mathcal{E}_6 and \mathcal{E}_7 exhibit eocs of close to 4 for both $\alpha = 1$ and $\alpha < 1$ with $\Delta t = Ch^2$, and exhibit close to 2 for both $\alpha = 1$ and $\alpha < 1$ with $\Delta t = Ch$. Considering $\Delta t = Ch$, the errors \mathcal{E}_6 and \mathcal{E}_7 are exhibiting the eocs expected from [6] but again not proven in our setting. As with \mathcal{E}_4 , one expects the eoc of \mathcal{E}_6 to be 4 when $\Delta t = Ch^2$ since it is an L^2 type error. As with \mathcal{E}_3 , \mathcal{E}_7 is exhibiting superconvergence for $\Delta t = Ch^2$ since it is an H^1 type error. Considering the setting of $\alpha = 1$, taking $J = 10$ and $M = 80$ results in approximately 0.011 seconds of execution time whilst taking $J = 160$ and $M = 20480$ results in approximately 63.3 seconds of execution time.

J	M	$\mathcal{E}_3 \times 10^5$	eoc_3	$\mathcal{E}_4 \times 10^5$	eoc_4	$\mathcal{E}_6 \times 10^6$	eoc_6	$\mathcal{E}_7 \times 10^6$	eoc_7
10	80	445.4	-	147.0	-	11.23	-	55.22	-
20	320	37.90	3.55	13.34	3.46	0.6858	4.03	3.491	3.99
40	1280	2.577	3.88	0.9244	3.85	0.04296	4.00	0.2186	4.00
80	5120	0.1645	3.97	0.05933	3.96	0.002686	4.00	0.01367	4.00
160	20480	0.01034	3.99	0.003733	3.99	0.0001679	4.00	0.0008549	4.00

Table 3.15: Errors (3.5.5) and (3.5.9) for (3.5.3a)–(3.5.3d) and (3.5.8a)–(3.5.8b), with $\Delta t = h^2$ and $\alpha = 1$, for Example 3.

J	M	$\mathcal{E}_3 \times 10^5$	eoc_3	$\mathcal{E}_4 \times 10^5$	eoc_4	$\mathcal{E}_6 \times 10^6$	eoc_6	$\mathcal{E}_7 \times 10^6$	eoc_7
10	80	63.93	-	42.01	-	17.13	-	86.67	-
20	320	5.587	3.52	3.634	3.53	1.088	3.98	5.478	3.98
40	1280	0.3812	3.87	0.2478	3.87	0.06828	3.99	0.3433	4.00
80	5120	0.02436	3.97	0.01584	3.97	0.004272	4.00	0.02147	4.00
160	20480	0.001531	3.99	0.0009954	3.99	0.0002670	4.00	0.001342	4.00

Table 3.16: Errors (3.5.5) and (3.5.9) for (3.5.3a)–(3.5.3d) and (3.5.8a)–(3.5.8b), with $\Delta t = h^2$ and $\alpha = 0.5$, for Example 3.

J	M	$\mathcal{E}_3 \times 10^5$	eoc_3	$\mathcal{E}_4 \times 10^5$	eoc_4	$\mathcal{E}_6 \times 10^6$	eoc_6	$\mathcal{E}_7 \times 10^6$	eoc_7
10	80	445.4	-	147.0	-	11.23	-	55.22	-
20	160	182.5	1.29	56.70	1.37	1.197	3.23	3.353	4.04
40	320	57.53	1.67	17.61	1.69	0.1544	2.95	0.2024	4.05
80	640	16.11	1.84	4.911	1.84	0.02446	2.66	0.01592	3.67
160	1280	4.259	1.92	1.297	1.92	0.004616	2.41	0.002560	2.64

Table 3.17: Errors (3.5.5) and (3.5.9) for (3.5.3a)–(3.5.3d) and (3.5.8a)–(3.5.8b), with $\Delta t = 0.1h$ and $\alpha = 1$, for Example 3.

J	M	$\mathcal{E}_3 \times 10^5$	eoc_3	$\mathcal{E}_4 \times 10^5$	eoc_4	$\mathcal{E}_6 \times 10^6$	eoc_6	$\mathcal{E}_7 \times 10^6$	eoc_7
10	80	63.93	-	42.01	-	17.13	-	86.67	-
20	160	98.45	-0.63	34.68	0.28	1.141	3.91	5.145	4.07
40	320	44.07	1.16	14.08	1.30	0.1496	2.93	0.2967	4.12
80	640	14.21	1.63	4.411	1.67	0.02406	2.64	0.01948	3.93
160	1280	4.008	1.82	1.231	1.84	0.004587	2.39	0.002489	2.97

Table 3.18: Errors (3.5.5) and (3.5.9) for (3.5.3a)–(3.5.3d) and (3.5.8a)–(3.5.8b), with $\Delta t = 0.1h$ and $\alpha = 0.5$, for Example 3.

Chapter 4

Mathematical modelling and numerical discretisation of models focused on the rice blast fungus

In this chapter we review the mathematical model of the rice blast fungus derived in [102] and derive and discretise a diffuse interface approximation to this model. We chose to derive a diffuse interface approximation to this model purely for mathematical interest. There are mathematical elements in the sharp interface model described in [102] which don't have a clear representation in a phase field setting, such as the repulsion of two evolving surfaces. We only postulate ways to address the terms which don't have a clear representation in the phase field setting, rigorous mathematical proof is still required to show that the postulated terms do indeed approximate the sharp interface versions correctly such as by completing asymptotic analysis. First we briefly introduce the life cycle of the fungus.

The life cycle of the fungus can be broken up into seven stages in a fairly standard biological way, see [119]. Namely we have

1. Eruption: After consuming the plant, the fungus erupts out of a leaf and grows to infect more plants;
2. Spore tip mucilage¹: A spore finds a new plant (via a leaf) and begins the processing

¹Mucilage is a thin viscous pool of liquid that binds the tip of a spore, that has erupted from a fungus, to a surface, [121].

of infection;

3. Germ tube² formation: A germ tube is released by the spore and covers an area of the leaf;
4. Melanin-lined appressorium³ cell wall: Growth of the fungus puts pressure on the cell wall of the leaf;
5. Penetration peg: A part of the tumour penetrates the pressured leaf allowing for infection of the whole plant;
6. Primary invasive hyphae⁴: Upon puncturing through the cell wall, the fungus injects hyphae to infect the whole plant;
7. Tissue colonisation⁵: The fungus spreads around the plant until the majority of the leaf cells have been consumed.

Each of these stages matches an equivalent stage in Figure 4.1. The mathematical model in [102] focuses on stages four and five above. It describes the growth of the fungus and the penetration of the leaf as the result of the growth of the penetration peg.

The mathematical model presented in [102] comprises of six components. The fungus and leaf are each modelled as hypersurfaces in \mathbb{R}^3 . The mechanics describing the growth of the fungus and its peg are dependent on four molecular species living on the fungus surface. These species are Melanin, F-actin, Septins (a group of different Septin proteins) and a turgor sensor Sln1 (interchangeably referred to as TS). Initially, it is assumed that the fungus has grown to some given size before recruitment of the species begins. Each of the species satisfies a reaction-diffusion equation on the surface of the fungus. Moreover, each of the species is localised to specific parts of the surface of the fungus, detailed in Assumptions 4.1. The fungus can be split into two parts; the bulk and the appressorium. The bulk represents the interior of the fungus where the species are recruited from and the appressorium is the surface of the fungus. We interchangeably use fungus and appressorium to represent the same object. Furthermore we split the appressorium into two sections, the appressorium dome and the pore. The pore describes the part of the fungus

²A germ tube is an outgrowth in a spore produced by a fungus, [1].

³An appressorium is a pressing organ of a fungus from which an infection peg grows and punctures the host, [76].

⁴A hypha is a long, branching filamentous structure of a fungus, [90].

⁵In biology, colonisation is the process by which a species spreads to new areas, [106].

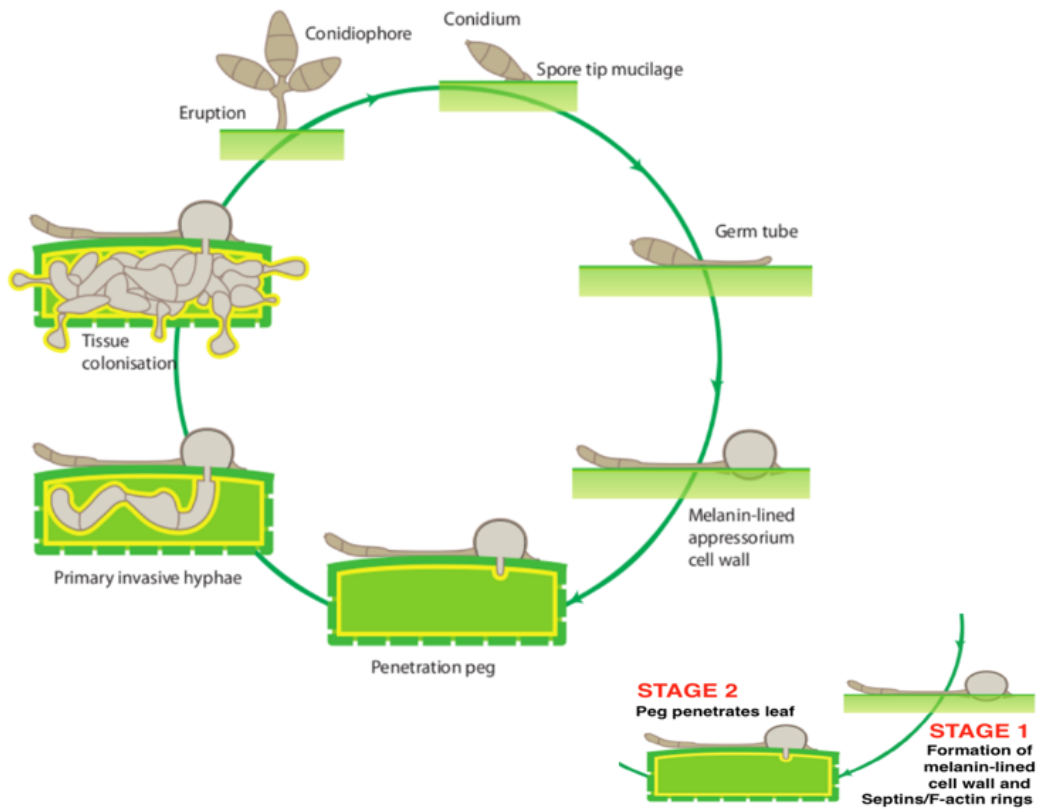


Figure 4.1: Life cycle of the rice blast fungus. Image created by Dr. George Littlejohn and Marian Littlejohn, University of Plymouth.

where the penetration peg will form. The assumptions of the model presented in [102] are defined in Assumptions 4.1.

Assumptions 4.1.

The authors in [102] assume the following when deriving the mathematical model:

1. Each molecular species is recruited to the surface from the bulk which is initially full; [102]
2. Bulk concentration of each species is taken to be spatially constant; [102]
3. The total amount, surface concentration and bulk concentration combined, of each species is conserved; [102]
4. Melanin is only recruited away from the pore; [21]
5. Melanin recruitment is positively correlated with increasing turgor pressure and is inhibited by the presence of Sln1 in the bulk; [31]

6. Sln1 recruitment to the surface is inhibited by the presence of Melanin in the bulk and can only be recruited once there is enough Melanin on the surface; [21]
7. F-actin and Sln1 are initially recruited to an annular region of the pore and diffuse into other parts of the pore over time; [35]
8. Significant recruitment of Septins and F-actin can only happen once there is a presence of Sln1; [35]
9. The Septins are recruited to a smaller, but further out from the centre, annular region of the pore to act as a diffusion barrier for the other species; [35]
10. The appressorium dome inflates due to turgor pressure, which is assumed to be an increasing function of the amount of Melanin on the surface; [36]
11. The interaction of the leaf and the fungus is in an annular region within the pore; [102]
12. F-actin is recruited to the pore to magnify turgor pressure; [35]
13. The Septins and Melanin are positively correlated with the rigidity of the appressorium; [35]
14. Once the leaf has formally been ruptured, it no longer resists penetration and no longer influences the motion of the fungus. [102]

4.1 Mathematical model introduced in [102]

This section will closely follow the supplementary information provided in [102]. The authors introduce the model with the biological values for parameters and then non-dimensionalise, here we give the non-dimensionalised values. They also consider two types of models, a wild type and a mutant type lacking the turgor sensor Sln1. In this setup, we only consider the wild type.

Let $\Gamma(t)$ be the evolving surface describing the fungus. The fungus is initially taken to be dome shaped with radius $R = 0.2$ that is cut off at a certain depth and made flat to model the pore area which has a diameter of $R_0 = 0.176$. Let $\Gamma_L(t)$ be the evolving surface describing the leaf. The leaf initially is taken to be a planar surface that is a square with sides of length 1. We first introduce the SRDEs satisfied by the concentrations of

the molecular species. The concentration of each of the molecular species is assumed to satisfy a mass conservation law, which is Assumption 3, and takes the following form

$$1 = B_i(t) + S_i(t), \quad t \in [0, T], \quad (4.1.1)$$

where $S_i(t)$ is the concentration of species i on the surface and $B_i(t)$ is the concentration of species i left in the bulk. Using the conservation law, denoting the species vector $\vec{u} := (u_m, u_{ts}, u_s, u_a)$ where u_m , u_{ts} , u_s and u_a denote the concentrations of Melanin, TS, the Septins, and F-Actin, respectively, with the velocity of the evolving fungus surface denoted by \vec{v} , from [58] each of the species satisfy an SRDE in the form of

$$\partial_t^\bullet u_i + u_i \operatorname{div}_\Gamma(\vec{v}) - \operatorname{div}_\Gamma(D_i(u_s) \nabla_\Gamma u_i) = f_i - k_i u_i, \quad \text{on } \Gamma(t), t \in (0, T], \quad (4.1.2a)$$

$$u_i(\cdot, 0) = 0, \quad \text{on } \Gamma(0), \quad (4.1.2b)$$

with each species having its own external forcing f_i and parameters D_i, k_i that affect the recruitment and mechanics of the molecular species. The initial condition for the molecular species coincide with Assumption 1. Indeed taking $t = 0$ in (4.1.1), and noting that $B_i(0) = 1$, we see that $S_i(0) = 0$, with $S_i(t)$ calculated in the following way

$$S_i(t) := \int_{\Gamma(t)} u_i(\cdot, t) dS, \quad t \in [0, T]. \quad (4.1.3)$$

The first term in the SRDEs is the material derivative $\partial_t^\bullet u_i = \partial_t u_i + \langle \vec{v}, \nabla u_i \rangle$ of the species u_i . An interpretation of the material derivative is the rate of change of a quantity as experienced by an observer that is moving along with the flow, [49]. It comprises of a local rate of change of concentration of a molecular species, represented by $\partial_t u_i$, and a non-local transportation of a molecular species from the growth of the fungus, represented by $\langle \vec{v}, \nabla u_i \rangle$. The second term of the SRDEs is the advection term of the molecular species u_i . An interpretation of the advection term is the flux of the concentration of the molecular species given the trajectory of the growth. In this model the velocity field $\vec{v} = v \vec{\nu}$ is the normal velocity of the surface. The third term of the SRDEs is the diffusion term of the molecular species u_i . An interpretation of the diffusion term is the change in concentration of the molecular species in comparison to the surrounding concentration of the molecular species. Here the diffusivity parameter is

$$D_i(u_s) := \begin{cases} d_s & \text{for } i = s \\ \frac{d_i}{2} \left(1 - H\left(\frac{u_s - s_3}{s_3}\right) \right) & \text{for } i = m, ts, a \end{cases}$$

where $H(\cdot)$ is the conventional Heaviside function, $(d_m, d_{ts}, d_s, d_a) = (0, 10^{-3}, 10^{-5}, 10^{-3})$ and $s_3 = 0.1$. Following Assumption 4, the diffusivity of Melanin is set to zero so that

it only present in the regions where it is recruited to which, as we will see, is everywhere except the pore. The diffusivity of Sln1 and F-actin are dependent on the concentration of Septins so that in areas of large amounts of Septins, there is no diffusion through those regions, per Assumption 9. The diffusivity values are small, but non zero, which follows Assumption 7. The parameter s_3 represents a threshold value for the concentration of Septins in certain regions. The first term on the right-hand side of the SRDEs is a source term. An interpretation of the source term is that it provides the system with the creation, and localisation, of each molecular species. Indeed, since the initial condition is zero, this term will define where on the surface the recruitment of each species takes place. Before we show the forms of the source terms we introduce components necessary to describe them. Firstly we describe the ring structure rs , which is used to represent the geometry of the pore and provide structure for the localisation of the molecular species. For $\vec{p} \in \Gamma(0)$, rs initially takes the form

$$rs(\vec{p}, 0) = \begin{cases} 0 & \text{if } \vec{p}_2 > 0, \\ 0 & \text{if } |(\vec{p}_0, \vec{p}_1)| > \frac{R_0}{2}, \\ r_1 + r_2 |(\vec{p}_0, \vec{p}_1)| & \text{otherwise.} \end{cases} \quad (4.1.4)$$

The parameters $r_1 = \frac{1}{3}$ and $r_2 = \frac{20}{3}$ correspond to initial reference values for the ring structure, and $R_0 = 0.176$ defines the initial diameter of the pore as above. The ring structure is assumed to not diffuse and is simply transported by the motion of the surface, and as such satisfies the following surface advection equation (SAE)

$$\partial_t^\bullet rs + rs \operatorname{div}_\Gamma(\vec{v}) = 0, \quad \text{on } \Gamma(t), t \in (0, T].$$

Next we introduce the turgor pressure

$$p(S_m(t), t) := p_1(t) + \mu S_m(t). \quad (4.1.5)$$

In this setting p_1 is the turgor pressure that increases linearly over time and then becomes constant. It takes the form

$$p_1(t) := \begin{cases} Pt + p_I & \text{for } t < \bar{t} \\ P\bar{t} + p_I & \text{for } \bar{t} \leq t \leq T \end{cases}$$

where $P = 5$ is the time pressure coupling constant, $p_I = 1$ is the initial pressure and \bar{t} is time period for turgor generation. Since S_m is the surface concentration of Melanin, $\mu = 2$ is the Melanin recruitment coupling constant, and the whole term provides extra turgor pressure proportional to the concentration of Melanin, which follows Assumption 5. Finally we introduce some sets which are the localisation regions for the recruitment of the molecular species, namely we have:

- \mathbb{S}_m defines the set of the surface where the pore is not, and hence where Melanin will be recruited to, and takes the form

$$\mathbb{S}_m(t) := \{\vec{p} \in \Gamma(t) : rs(\vec{p}, t) = 0\}$$

since rs represents the ring structure describing the pore;

- \mathbb{S}_{rs} defines the set of the surface where the pore is and takes the form

$$\mathbb{S}_{rs}(t) := \{\vec{p} \in \Gamma(t) : rs(\vec{p}, t) > 0\};$$

- $\mathbb{S}_{ts}, \mathbb{S}_s, \mathbb{S}_a$ define the annular sets on the surface where Sln1, the Septins and F-actin will be recruited to, and take the form

$$\mathbb{S}_i(t) := \{\vec{p} \in \Gamma(t) : rs(\vec{p}, t) > \alpha_i\}$$

for $i = ts, s, a$, where α_i defines the inner annulus radius for each species. Here $\alpha_s = 0.6$, $\alpha_{ts} = 0.3$ and $\alpha_a = 0.3$, which follows Assumption 9, since $\alpha_s > \max\{\alpha_a, \alpha_{ts}\}$, and Assumption 7;

- \mathbb{T} defines the set whereby enough Melanin has been recruited to the surface to allow for the turgor sensor to be recruited to the surface, and takes the form

$$\mathbb{T} := \{t \in [0, T] : S_m(t) > q_m B_m(t)\}$$

where $q_m = \frac{1}{19}$ defines the ratio of concentration of Melanin on the surface to the concentration in the bulk.

We can now describe the forcing functions of the SRDEs for each of the molecular species as follows:

- the forcing for Melanin f_m takes the form

$$f_m(t) := l_m \chi_{\mathbb{S}_m(t)} \frac{B_m(t) - q_b}{c_m + B_m(t) - q_b} (p(S_m(t), t) - p_I)$$

where $l_m = 30$ represents the coefficient of recruitment of Melanin from the bulk, $q_b = 0.55$ represents the proportion of Melanin and Sln1 that is unavailable for recruitment, $c_m = 10$ is the saturation level of Melanin which comes from a Michaelis-Menten formulation of the forcing, see [34], and χ_A is the characteristic function of the set A . It is noted in [102] that linear recruitment of Melanin was insufficient to differentiate between differences in behaviour between the wild type and mutant type, and so the authors chose to use the Michaelis-Menten term. The use of q_b acts per Assumption 5;

- the forcing for Sln1 f_{ts} takes the form

$$f_{ts}(t) := l_{ts}\chi_{\mathbb{S}_{ts}(t)}(B_{ts}(t) - q_b)\chi_{\mathbb{T}}$$

where $l_{ts} = 1$ represents the coefficient of recruitment of the turgor sensor from the bulk. The use of q_b and $\chi_{\mathbb{T}}$ acts per Assumption 6;

- the forcing for the Septins f_s takes the form for $\vec{p} \in \Gamma(t)$

$$f_s(\vec{p}, t) := (l_s\chi_{\mathbb{S}_s(t)}\chi_{u_{ts}(\vec{p}, t) > 0} + \beta_s\chi_{\mathbb{S}_{rs}(t)})B_s(t)$$

where $l_s = 1$ represents the coefficient of recruitment of the Septins from the bulk, and $\beta_s = 0.1$ is the uniform recruitment coefficient of the Septins. Since $l_s > \beta_s$, large amounts of recruitment are only initiated when there is a presence of turgor sensor, per Assumption 8;

- the forcing for F-actin f_a takes the form for $\vec{p} \in \Gamma(t)$

$$f_a(\vec{p}, t) := (l_a\chi_{\mathbb{S}_a(t)}\chi_{u_{ts}(\vec{p}, t) > 0} + \beta_a\chi_{\mathbb{S}_{rs}(t)})B_a(t)$$

where $l_a = 1$ represents the coefficient of recruitment of F-actin from the bulk, and $\beta_a = 0.1$ is the uniform recruitment coefficient of F-actin. Since $l_a > \beta_a$, large amounts of recruitment are only initiated when there is a presence of turgor sensor, per Assumption 8.

The final term on the right hand side of the SRDE is the degradation (or destruction) rate of each of the species. An interpretation of the degradation term is that it represents the re-absorption of each species from the fungus surface to the bulk. We have that $(k_m, k_{ts}, k_s, k_a) = (0, 0.1, 0.1, 0.1)$, whereby it is evident that no Melanin is re-absorbed.

We now describe the velocity laws for the motion of the fungus and leaf, both of which will take the form of forced mean curvature flow. We first introduce the velocity law for the fungus, namely

$$\omega v = \sigma \kappa + p(1 + g^p) + g^r, \quad \text{on } \Gamma(t), \quad t \in (0, T]. \quad (4.1.6)$$

Here the coefficient ω on the left-hand side of velocity law models the rigidity of the fungus and takes the form

$$\omega(u_m, u_a) := \omega_0(\lambda_{m_1, m_2}(u_m) + \lambda_{s_1, s_2}(u_s)), \quad (4.1.7)$$

where $\omega_0 = 1$ is the magnification factor of the rigidity and

$$\lambda_{i_1, i_2}(u_i) := 1 + \frac{i_1}{2} \left(1 + H \left(\frac{u_i - i_2}{i_2} \right) \right)$$

represents the magnification function for both Melanin and Septins, as per Assumption 13. In this setting $m_1 = s_1 = 1000$ are the rigidity magnification factors due to Melanin and Septins respectively, and $m_2 = 0.25$, $s_2 = 0.2$ are the reference values for the initiation of the magnification of the rigidity from Melanin and Septins respectively. We now briefly discuss why this term represents rigidity. Consider

$$\omega v = \kappa \quad \text{and} \quad v = \kappa$$

then, by fixing κ , if ω is significantly large, the velocity will be significantly smaller as the amount of curvature is being divided by this factor. Thus the factor ω will be restricting the movement of the surface. Similarly, we can see this by considering $\Gamma(t)$ to be a circle, as each law satisfies

$$r(t) = \sqrt{r(0)^2 - \frac{2}{\omega}t} \quad \text{and} \quad r(t) = \sqrt{r(0)^2 - 2t},$$

where $r(t)$ is the radius of $\Gamma(t)$. It can easily be seen that with a large value of ω , the reduction of the radius of the circle is impeded, and thus can be interpreted as rigidity. The coefficient $\sigma = 0.1$ in (4.1.6) acts as surface tension. This term can be interpreted as the resistance of the fungus to stretching. Mathematically σ is called the kinetic coefficient. The external forcing on the right-hand side of the velocity law consists of two parts, one which is a protrusive force $p(1 + g^p)$ and the other which is repulsion \vec{g} . First, we look at the protrusive force which takes the form

$$p(S_m(t), t)(1 + g^p(u_a)).$$

The function p describes the turgor pressure and has already been described in (4.1.5). Its inclusion into the velocity law for the fungus coincides with Assumption 10. The function g^p describes the magnification of the turgor from the presence of F-actin and takes the form

$$g^p(u_a) := \frac{a_1}{2} \left(1 + H \left(\frac{u_a - a_2}{a_2} \right) \right).$$

Here $a_1 = 5$ is the protrusive force magnification factor and $a_2 = 0.25$ is the reference value for the initiation of magnification due to the F-actin concentration. We notice that due to the forcing term for F-actin this pressure will be localised on the surface in an annulus in the pore, as per Assumption 12. For some $\vec{p} \in \Gamma(t)$, the repulsion force g^r in (4.1.6) takes the form

$$g^r(\kappa_L, \vec{p}, t) := \begin{cases} 0 & \|\kappa_L(\cdot, t)\|_{L^\infty(\Gamma_L(t))} > \bar{\kappa}_L, \\ \langle \vec{r}(\vec{p}, t), \vec{\nu}(\vec{p}, t) \rangle & \text{otherwise,} \end{cases} \quad (4.1.8)$$

where $\bar{\kappa}_L = 0.4$ is the maximum mean curvature of the leaf before rupturing, \vec{r} defines an obstacle potential and $\vec{\nu}$ represents the inward pointing unit normal vector to $\Gamma(t)$. The presence of $\bar{\kappa}_L$ provides the maximum threshold of pressure the leaf can withstand and once it has been breached the repulsion term is set to zero which signals that the leaf has been punctured, following Assumption 14. Before the threshold is breached an obstacle potential is considered that takes the form

$$\vec{r}(\vec{p}, t) := r_0 k \left(\frac{d_0}{d(\vec{p}, t)} \right)^k \frac{1}{d(\vec{p}, t)} \nabla d(\vec{p}, t) \quad (4.1.9)$$

where $r_0 = 1$ is the reference force per unit associated to the potential, $k = 12$ is a power factor, $d_0 = 0.05$ is the reference distance such that for $d(\vec{p}, t) > d_0$ the force becomes negligible and $d(\vec{p}, t)$ defined as

$$d(\vec{p}, t) := \min_{\vec{q} \in \Gamma_L(t)} |\vec{p} - \vec{q}|$$

is the minimum distance of a fixed point \vec{p} on the fungus to a point \vec{q} on the leaf. We note that the name obstacle potential is an abuse of notation and is not the same as the double obstacle potential described for the phase field approach to mean curvature flow. If $d(\vec{p}, t) > d_0$ then the contribution of this repulsive force is incredibly small but once we have $d(\vec{p}, t) < d_0$ the force quickly becomes large. Although by itself the repulsion term does not necessarily abide by Assumption 11, the added fact that the turgor pressure, and more importantly magnification due to F-actin, only happens where the concentration of F-actin is present and reached a certain threshold, which will be in an annular region in the pore area, means that with these combined we can say that this term is in accordance to Assumption 11.

Now that we have introduced the evolution law for the fungus, let us now introduce the evolution law for leaf, which takes the form

$$\omega_L v_L = \sigma_L \kappa_L + g_L^r, \quad \text{on } \Gamma_L(t), t \in (0, T]. \quad (4.1.10)$$

In (4.1.10) ω_L models the rigidity of the leaf and is taken to be constant with $\omega_L = 10^6$. Similarly σ_L is the resistance to stretching and takes the constant value $\sigma_L = 10^6$. These are both fixed contributions coming from the fact that the leaf is significantly larger than the fungus and that its material doesn't change in the life cycle of the fungus. The forcing term g_L^r is the repulsion term, which is similar to (4.1.8), and, for some $\vec{q} \in \Gamma_L(t)$, takes the form

$$g_L^r(\kappa_L, \vec{q}, t) := \begin{cases} 0 & \|\kappa_L(\cdot, t)\|_{L^\infty(\Gamma_L(t))} > \bar{\kappa}_L \\ -\langle \vec{r}(\vec{q}, t), \vec{\nu}_L(\vec{q}, t) \rangle & \text{otherwise} \end{cases}$$

where \vec{r} is the same obstacle potential described in (4.1.9), whereby

$$d(\vec{q}, t) := \min_{\vec{p} \in \Gamma(t)} |\vec{p} - \vec{q}|$$

describes the minimum distance from a fixed point \vec{q} on the leaf to a point \vec{q} on the fungus, and $\vec{\nu}_L$ is the upward pointing unit normal to Γ_L . Since the leaf is flat and hence has no curvature, the only movement will happen from the repulsion term. However the force from the repulsion has to be of a large magnitude due to the order of the coefficients of the velocity and curvature terms. This models the fact that the leaf is significantly larger than the fungus and that it will take a huge protrusive force from the fungus to start to bend the leaf.

4.2 Parametric formulation of a simplified model for curves

In [102] the authors solve a finite element approximation of the mathematical model that they derive and they present numerical simulations in which $\Gamma(t)$ and $\Gamma_L(t)$ are taken to be hypersurfaces in \mathbb{R}^3 , see [64]. In this section we reduce the spatial dimension of the problem and model the fungus and leaf as curves in \mathbb{R}^2 . We consider two setups, the first, presented in Section 4.2.1, describes the simulation of the full model in [102] reduced in dimension from surface to curves and the second, presented in Section 4.2.2, describes a reduction of the model in Section 4.2.1 which ties into the analysis conducted in Chapter 3.

4.2.1 Full model from [102] reduced from surfaces in \mathbb{R}^3 to curves in \mathbb{R}^2

Here we consider a vertical cross section of the geometry considered in [102] in which the appressorium from [102] is modelled by a closed curve in \mathbb{R}^2 , with a semi-circular dome and a flat pore section, and the leaf is modelled as a flat curve. We set $\Gamma(t)$ to denote the curve that represents the evolving fungus and initially we take it to be a circle cut off at a certain depth which we describe as

$$\Gamma(0) := \Gamma_1 \cup \Gamma_2, \tag{4.2.1}$$

where Γ_1 describes the circular part

$$\Gamma_1 := \{ \vec{p} \in \mathbb{R}^2 : -\theta_f \leq \tan^{-1}(\vec{p}_1/\vec{p}_0) \leq \pi + \theta_f, |\vec{p}| = R \}$$

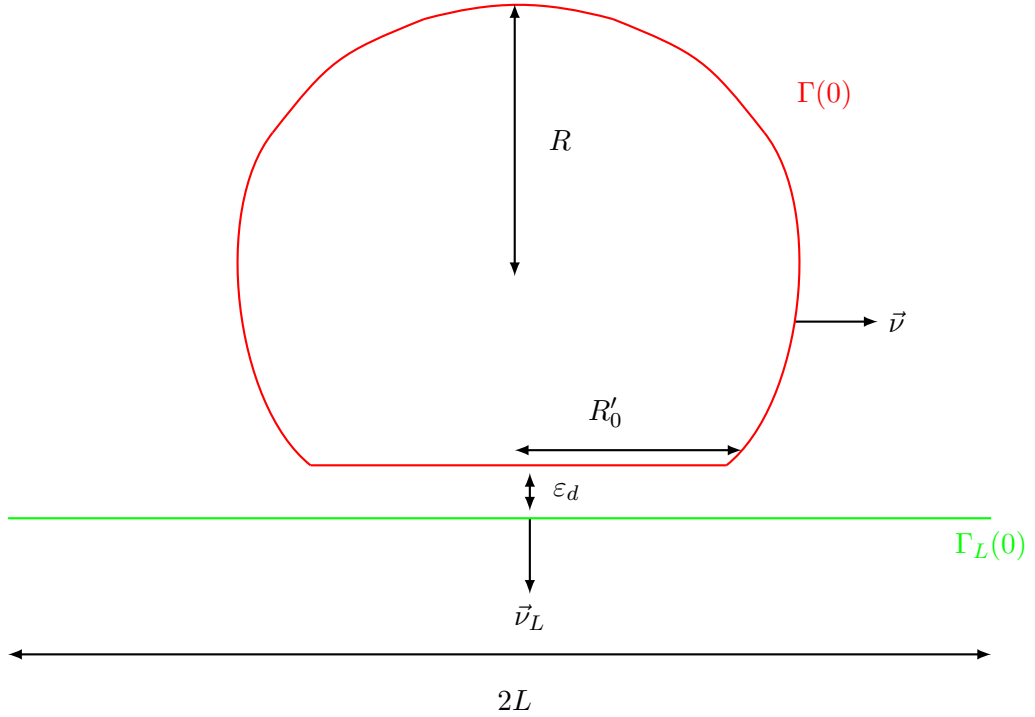


Figure 4.2: Initial rice blast schematic. The red line is the initial fungus curve and the green line is the initial leaf curve.

and Γ_2 describes the flat part

$$\Gamma_2 := \left\{ \vec{p} \in \mathbb{R}^2 : \pi + \theta_f \leq \tan^{-1}(\vec{p}_1/\vec{p}_0) \leq 2\pi - \theta_f, \vec{p}_1 = -\sqrt{R^2 - (R'_0)^2}, |\vec{p}_0| \leq R'_0 \right\}$$

where $\theta_f = \tan^{-1}(\sqrt{R^2 - (R'_0)^2}/R'_0)$ is the polar angle where Γ_1 and Γ_2 meet, $R = 0.2$ is the initial radius of the circle, and $2R'_0 = R_0$ with $R_0 = 0.176$ being the diameter of the pore, see Figure 4.2. Similarly we set $\Gamma_L(t)$ to denote the curve that represents the evolving leaf and initially we take it to be a bounded flat curve

$$\Gamma_L(0) = \{ \vec{p} \in \mathbb{R}^2 : \vec{p}_1 = -\sqrt{R^2 - (R'_0)^2} - \varepsilon_d, \vec{p}_0 \in [-L, L] \}. \quad (4.2.2)$$

We set $2L = 1$ to be the length of the $\Gamma_L(t)$ and define ε_d to be some threshold that ensures initially the leaf is sufficiently far away from the fungus, thus not invoking a reaction from the repulsion terms in the velocity laws immediately.

Let \vec{x} denote a parametrisation of $\Gamma(t)$ and \vec{y} denote a parametrisation of $\Gamma_L(t)$. Then the velocity laws (4.1.6) and (4.1.10) take the form

$$(\omega \vec{x})_t - \sigma \frac{\vec{x}_{\rho\rho}}{|\vec{x}_\rho|^2} = (p(1 + g^p) + g^r) \vec{v}, \quad (\rho, t) \in \mathbb{I} \times (0, T], \quad (4.2.3a)$$

$$\omega_L \vec{y}_t - \sigma_L \frac{\vec{y}_{\rho\rho}}{|\vec{y}_\rho|^2} = g_L^r \vec{v}_L, \quad (\rho, t) \in \mathcal{I} \times (0, T], \quad (4.2.3b)$$

$$\vec{x}(0, t) = \vec{x}(1, t), \quad t \in (0, T], \quad (4.2.3c)$$

$$F(\vec{y}(\rho, t)) = 0, \quad \langle \vec{y}_\rho(\rho, t), \nabla^\perp F(\vec{y}(\rho, t)) \rangle = 0, \quad (\rho, t) \in \{0, 1\} \times (0, T], \quad (4.2.3d)$$

$$\vec{x}(\rho, 0) = \vec{x}^0(\rho), \quad \rho \in \mathbb{I}, \quad \vec{y}(\rho, 0) = \vec{y}^0(\rho), \quad \rho \in [0, 1], \quad (4.2.3e)$$

where $\vec{\nu}$ denotes the outward pointing unit normal to $\Gamma(t)$, $\vec{\nu}_L$ denotes the downward pointing unit normal to $\Gamma_L(t)$, and, for some $\vec{p} \in \mathbb{R}^2$, F is defined as

$$F(\vec{p}) = |\vec{p}_0| - L.$$

In an abuse of notation we define the parametrisation of the arc-length of both curves \vec{x} and \vec{y} by ρ . The parameterisation in (4.2.3a)-(4.2.3e), noting (1.2.3) and (3.2.23b), leads to the following SRDEs for each of the species (u_m, u_{ts}, u_s, u_a)

$$(|\vec{x}_\rho| \tilde{u}_i)_t - (\psi \tilde{u}_i)_\rho - \left(D_i(\tilde{u}_s) \frac{(\tilde{u}_i)_\rho}{|\vec{x}_\rho|} \right)_\rho = |\vec{x}_\rho| (f_i - k_i \tilde{u}_i), \quad (\rho, t) \in \mathbb{I} \times (0, T], \quad (4.2.4a)$$

$$\tilde{u}_i(0, t) = \tilde{u}_i(1, t), \quad t \in (0, T], \quad (4.2.4b)$$

$$\tilde{u}_i(\rho, 0) = 0, \quad \rho \in \mathbb{I}, \quad (4.2.4c)$$

where $\tilde{u}_i(\rho, t) = u_i(\vec{x}(\rho, t), t)$ and $\psi = \langle \vec{x}_t, \vec{\nu}^\perp \rangle$ denotes the tangential velocity \vec{x} . For the remainder of this subsection we drop the tilde on u_i , and also rs , for ease of presentation. Initially we see that the concentration of each molecular species is set to zero, whereby we calculate the total amount of each species on the surface by

$$S_i(t) := \int_{\mathbb{I}} |\vec{x}_\rho(\cdot, t)| u_i(\cdot, t) d\rho, \quad t \in [0, T].$$

The diffusivity parameters we choose are

$$D_i(u_s) := \begin{cases} d_s & \text{for } i = s \\ \frac{d_i}{2} \left(1 - H^\delta \left(\frac{u_s - s_3}{s_3} \right) \right) & \text{for } i = m, ts, a \end{cases}$$

where, for $r \in \mathbb{R}$,

$$H^\delta(r) = \tanh(r \delta^{-1})$$

is a smooth approximation to the Heaviside function H for some positive $\delta \gg 1$, as taken in [102]. We take $(d_m, d_{ts}, d_s, d_a) = (0, 10^{-2}, 10^{-5}, 10^{-2})$ and $s_3 = 0.1$, which are the same values as in [102]. Since we consider a curve rather than a surface, we redefine the ring structure, which initially, for some $\vec{p} \in \Gamma(0)$, is given by

$$rs(\vec{p}, 0) := \begin{cases} 0 & \text{if } \vec{p}_1 > -\sqrt{R^2 - (R'_0)^2} \\ 0 & \text{if } |\vec{p}_0| > R'_0 \\ r_1 + r_2 |\vec{p}_0| & \text{otherwise,} \end{cases}$$

where $R = 0.2$, $R'_0 = 0.088$, $r_1 = \frac{1}{3}$ and $r_2 = \frac{20}{3}$ as in [102], and satisfies the following SAE

$$\begin{aligned} (|\vec{x}_\rho| rs)_t - (\psi rs)_\rho &= 0, & (\rho, t) \in \mathbb{I} \times (0, T], \\ rs(0, t) &= rs(1, t), & t \in (0, T]. \end{aligned}$$

The turgor pressure takes the form

$$p(S_m(t), t) := p_1(t) + \mu S_m(t), \quad (4.2.5)$$

where $\mu = 0.5$ is the Melanin coupling constant which has been reduced from $\mu = 2$ in [102] and $p_1(t)$ takes the form

$$p_1(t) := \begin{cases} Pt + p_I & \text{for } t < \bar{t} \\ P\bar{t} + p_I & \text{for } \bar{t} \leq t \leq T \end{cases}$$

with the time pressure constant $P = 1$ being reduced from $P = 5$ in [102], and $p_I = 1$ and $\bar{t} = 0.25$ as in [102]. We chose to reduce these parameters as computationally in our reduced model we found $\mu = 2$ caused the appressorium dome to grow too quickly in comparison to the simulations in [102] and, once the leaf has ruptured, $P = 5$ caused the penetration peg to grow too rapidly due to the too large pressure. The activation and recruitment sets follow the structure set in [102] and take the form

- \mathbb{S}_m defines the set of the surface where the pore is not, and takes the form

$$\mathbb{S}_m(t) := \{\vec{p} \in \Gamma(t) : rs(\vec{p}, t) = 0\};$$

- \mathbb{S}_{rs} defines the set of the surface where the pore is and takes the form

$$\mathbb{S}_{rs}(t) := \{\vec{p} \in \Gamma(t) : rs(\vec{p}, t) > 0\};$$

- \mathbb{S}_{ts} , \mathbb{S}_s , \mathbb{S}_a define the annular sets on the surface where Sln1, the Septins and F-actin will be recruited to, and take the form

$$\mathbb{S}_i(t) := \{\vec{p} \in \Gamma(t) : rs(\vec{p}, t) > \alpha_i\}$$

for $i = ts, s, a$, where $\alpha_s = 0.6$, $\alpha_{ts} = 0.3$ and $\alpha_a = 0.3$ as in [102];

- \mathbb{T} defines the set whereby enough Melanin has been recruited to the surface to allow for the turgor sensor to be recruited to the surface, and takes the form

$$\mathbb{T} := \{t \in [0, T] : S_m(t) > q_m B_m(t)\}$$

where $q_m = \frac{1}{19}$ as in [102].

The description of each forcing function f_i then follows as:

- the forcing for Melanin f_m takes the form

$$f_m(t) := l_m \chi_{\mathbb{S}_m(t)} \frac{B_m(t) - q_b}{c_m + B_m(t) - q_b} (p(\mathbb{S}_m(t), t) - p_I)$$

where $q_b = 0.55$ and $c_m = 10$, as in [102], and $l_m = 300$ which is increased from $l_m = 30$ in [102] to compensate for the reduction of the coupling constant in the turgor pressure;

- the forcing for Sln1 f_{ts} takes the form

$$f_{ts}(t) := l_{ts} \chi_{\mathbb{S}_{ts}(t)} (B_{ts}(t) - q_b) \chi_{\mathbb{T}}$$

where $l_{ts} = 1$ and $q_b = 0.55$ as in [102];

- the forcing for the Septins f_s takes the form for $\rho \in \mathbb{I}$

$$f_s(\rho, t) := (l_s \chi_{\mathbb{S}_s(t)} \chi_{u_{ts}(\rho, t) > 0} + \beta_s \chi_{\mathbb{S}_{rs}(t)}) B_s(t)$$

where $l_s = 1$ as in [102], and $\beta_s = 0.01$, which is decreased from $\beta_s = 0.1$ in [102] as in our setting the concentration throughout the pore became large enough to influence the evolution of the fungus in regions where it should not;

- the forcing for F-actin f_a takes the form for $\rho \in \mathbb{I}$

$$f_a(\rho, t) := (l_a \chi_{\mathbb{S}_a(t)} \chi_{u_{ts}(\rho, t) > 0} + \beta_a \chi_{\mathbb{S}_{rs}(t)}) B_a(t)$$

where $l_a = 1$ as in [102], and, for the same reason as above, $\beta_a = 0.01$ decreased from $\beta_a = 0.1$.

We kept the degradation rate of each species $(k_m, k_{ts}, k_s, k_a) = (0, 0.1, 0.1, 0.1)$ the same as in [102]. The rigidity, ω , takes the form

$$\omega(u_m, u_a) := \omega_0 (\lambda_{m_1, m_2}(\bar{u}_m) + \lambda_{s_1, s_2}(u_s)),$$

where $\omega_0 = 1$ as in [102], and

$$\lambda_{i_1, i_2}(u_i) := 1 + \frac{i_1}{2} \left(1 + H^\delta \left(\frac{u_i - i_2}{i_2} \right) \right)$$

with $m_1 = s_1 = 1000$ and $s_2 = 0.2$ as in [102], and $m_2 = 0.15$ which is reduced from $m_2 = 0.25$ in [102] because in our setup the concentration of Melanin increased much

faster than it did in to the simulations in [102]. For a similar reason we take $\lambda(\bar{u}_m)$, where \bar{u}_m is defined as for $\rho \in \mathbb{I}$

$$\bar{u}_m(\rho, t) := \begin{cases} \|u_m(\cdot, t)\|_{L^\infty(\mathbb{I})} & \text{if } u_m(\rho, t) > 0, \\ 0 & \text{otherwise,} \end{cases}$$

rather than $\lambda(u_m)$ as this gave rise to a more uniform distribution of Melanin than using $\lambda(u_m)$. The protrusive force takes the form

$$p(S_m(t), t)(1 + g^p(u_a))$$

with p defined as in (4.2.5), and the magnification function g^p defined as

$$g^p(u_a) := \frac{a_1}{2} \left(1 + H^\delta \left(\frac{u_a - a_2}{a_2} \right) \right),$$

where $a_2 = 0.25$ as in [102] and $a_1 = 1$ is reduced from $a_1 = 5$ in [102], as when we used $a_1 = 5$ once the leaf ruptured the penetration peg grew more rapidly than it did in the simulations in [102]. For some $\rho \in \mathbb{I}$, the repulsion force g^r takes the form

$$g^r(\kappa_L, \rho, t) := \begin{cases} 0 & \|\kappa_L(\cdot, t)\|_{L^\infty(\mathcal{I})} > \bar{\kappa}_L, \\ \langle -\vec{r}(\rho, t), \vec{\nu}(\rho, t) \rangle & \text{otherwise,} \end{cases} \quad (4.2.6)$$

where $\bar{\kappa}_L = 0.000604$ reduced from $\bar{\kappa}_L = 0.4$, the obstacle potential is defined as

$$\vec{r}(\rho, t) := r_0 k \left(\frac{d_0}{d(\rho, t)} \right)^k \frac{1}{d(\rho, t)} \nabla d(\rho, t) \quad (4.2.7)$$

with the distance function defined as

$$d(\rho, t) := \min_{\mathbf{p} \in [0, 1]} |\vec{x}(\rho, t) - \vec{y}(\mathbf{p}, t)|$$

to be the minimum distance of a fixed point $\vec{x}(\rho, t)$ on the fungus to a point $\vec{y}(\cdot, t)$ on the leaf. The parameters $r_0 = 1$, $k = 12$ and $d_0 = 0.05$ are as in [102], and $\bar{\kappa}_L$ was chosen experimentally to match the computational time the leaf ruptured in [102]. We also note that $\bar{\kappa}_L$ heavily relies on the choice of the surface tension on the leaf σ_L which was decreased from $\sigma_L = 10^6$ to $\sigma_L = 10^4$. Similarly we decreased the rigidity factor of the leaf from $\omega_L = 10^6$ to $\omega_L = 10^4$. Taking $\sigma_L = \omega_L = 10^6$ resulted in no noticeable penetration peg being formed before the rupture of the leaf. We keep the surface tension of the fungus to be $\sigma = 0.1$ as in [102]. The forcing term g_L^r , for some $\rho \in [0, 1]$, takes the form

$$g_L^r(\kappa_L, \rho, t) := \begin{cases} 0 & \|\kappa_L(\cdot, t)\|_{L^\infty(\mathcal{I})} > \bar{\kappa}_L, \\ \langle \vec{r}(\rho, t), \vec{\nu}_L(\rho, t) \rangle & \text{otherwise,} \end{cases}$$

where \vec{r} is the same obstacle potential described in (4.2.7), whereby

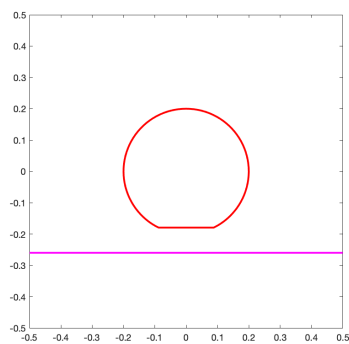
$$d(\rho, t) := \min_{\mathbf{p} \in \mathbb{I}} |\vec{x}(\mathbf{p}, t) - \vec{y}(\rho, t)|$$

describes the minimum distance of a fixed point $\vec{y}(\rho, t)$ on the leaf to a point $\vec{x}(\cdot, t)$ on the fungus. We note the changes of sign in comparison to Section 4.1 are due to the orientation of the two normal vectors $\vec{\nu}, \vec{\nu}_L$ from the setup.

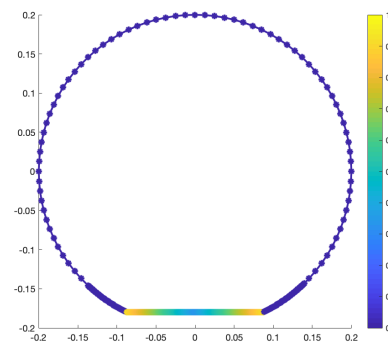
For a finite element approximation of this model, we used the numerical scheme presented in [6], with $\alpha = 1$, for the finite element approximation of (4.2.3a), (4.2.3c), (4.2.4a) and (4.2.4b), and we use the Newton's scheme (3.5.3a)-(3.5.3d) for the finite element approximation of (4.2.3b) and (4.2.3d). We take $T = 0.4$ as opposed to $T = 0.5$ in [102], $\delta = 10^2$ for the approximation to the Heaviside function and $\varepsilon_d = 0.1$ for the initial separation of the leaf and fungus curves. As in [102] we use a uniform mesh for the partition of the leaf \mathcal{I} but a non-uniform mesh for the partition of the fungus \mathbb{I} . Indeed we use a coarser mesh outside of the pore area and refine in the pore area, giving us a higher resolution for the penetration peg formation. This can be seen in Figure 4.3b. The simulations and visualisations were executed using MATLAB on the iMac computer, see Section 3.5, with 200 DOFs, $h_{min} = 10^{-3}$, $h_{max} = 10^{-2}$, and $\Delta t = 10^{-4}$ which resulted 180 seconds of execution time.

Figures 4.3–4.6 demonstrate the key parts of the simulation we want to compare to the simulation in [102]. Figure 4.3 shows the initial rice blast, leaf and ring structure, as well as the non-uniform mesh for the fungus. Figure 4.4 demonstrates the evolution of the fungus, Figure 4.5a–4.5d demonstrates the evolution of the Melanin concentration, Figure 4.5e–4.5h demonstrates the evolution of the Sln1 concentration, Figure 4.6a–4.6d demonstrates the evolution of the Septins concentration, and Figure 4.6e–4.6h demonstrates the evolution of the F-actin concentration. Figure 4.4a demonstrates the fungus growing, while Figures 4.4b and 4.5b show the largest the fungus will get as the Melanin rigidity threshold has been reached, as well as the annulus behaviour of the other three molecular species in Figures 4.5f, 4.6b and 4.6f. Figures 4.4c and 4.6g show that the threshold of the magnification of the turgor pressure has been reached and the pore area starts to push down on the leaf. Figure 4.4d shows the final time step of the simulation, whereby you can clearly see the peg has formed. Finally we demonstrate in Figure 4.7 that in fact although the fungus grows quite a lot, the ring structure doesn't move that much at all, which be important for our derivation of a phase field model in Section 4.3. An interesting behaviour that occurs here that may not be expected is that once the peg

starts to form the concentration of the molecular species on the surface of the peg start to deplete apart from right at the edge of the ring structure. This allows the peg to maintain its shape whilst not grow exceptionally large as the F-actin driven magnification of the pressure reduces.



(a) Initial rice blast and leaf.



(b) Initial ring structure demonstrating non-uniform mesh.

Figure 4.3: Initial conditions for full model simulation in the parametric framework.

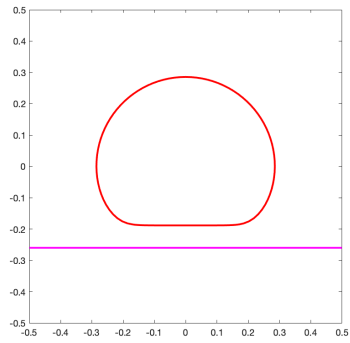
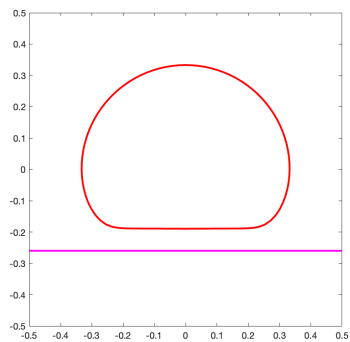
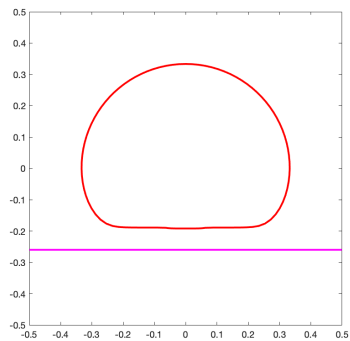
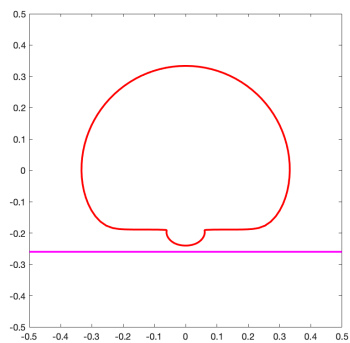
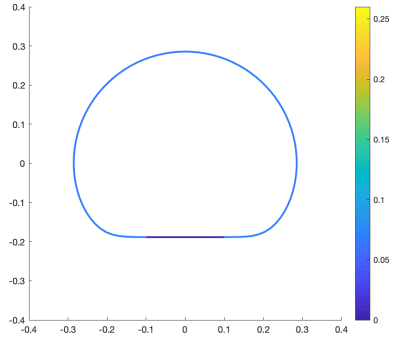
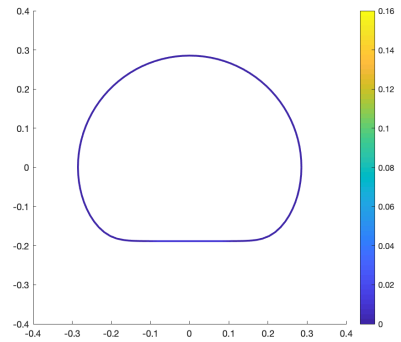
(a) Rice blast and leaf at $t = 0.1$.(b) Rice blast and leaf at $t = 0.2$.(c) Rice blast and leaf at $t = 0.3$.(d) Rice blast and leaf at $t = 0.4$.

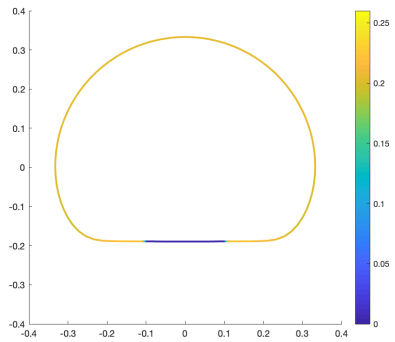
Figure 4.4: Full model simulation for parametric framework. Evolution of the rice blast.



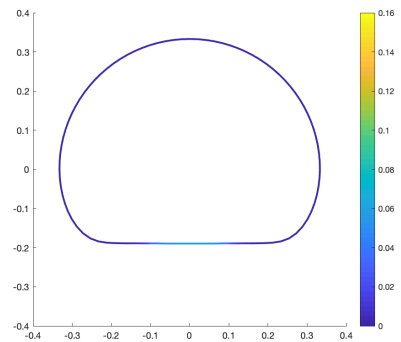
(a) Concentration of Melanin at $t = 0.1$.



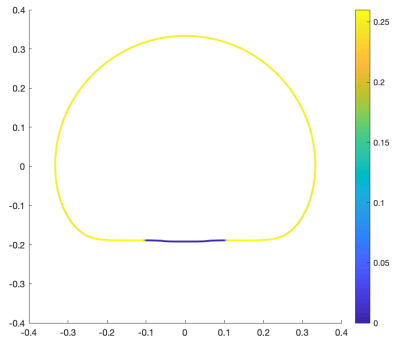
(e) Concentration of Sln1 at $t = 0.1$.



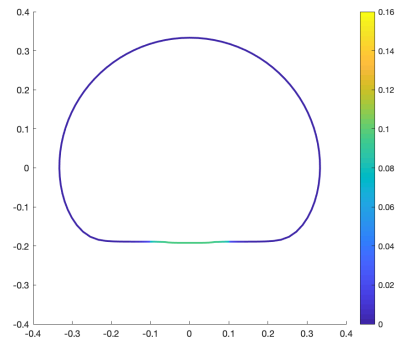
(b) Concentration of Melanin at $t = 0.2$.



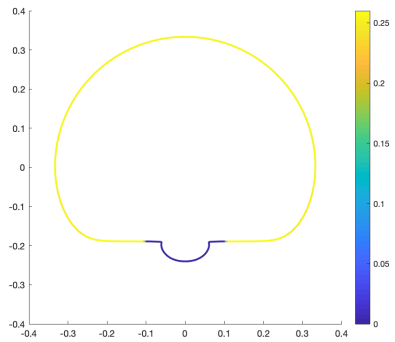
(f) Concentration of Sln1 at $t = 0.2$.



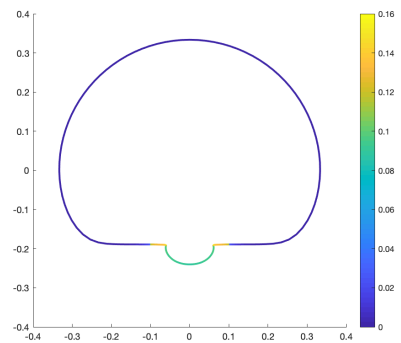
(c) Concentration of Melanin at $t = 0.3$.



(g) Concentration of Sln1 at $t = 0.3$.



(d) Concentration of Melanin at $t = 0.45$.



(h) Concentration of Sln1 at $t = 0.35$.

Figure 4.5: Full model simulation for parametric framework: Melanin and Sln1.

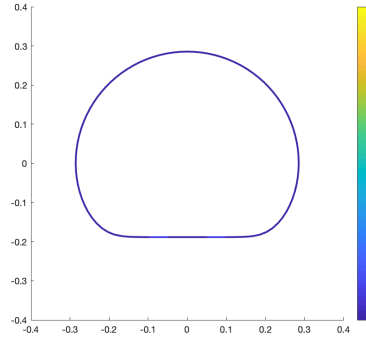
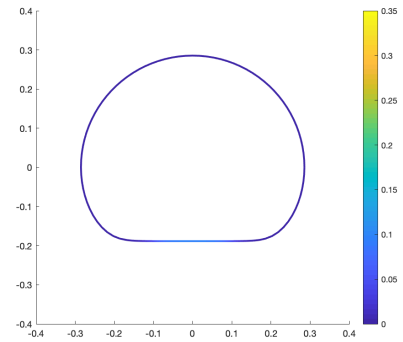
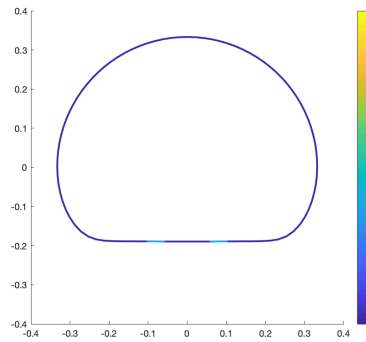
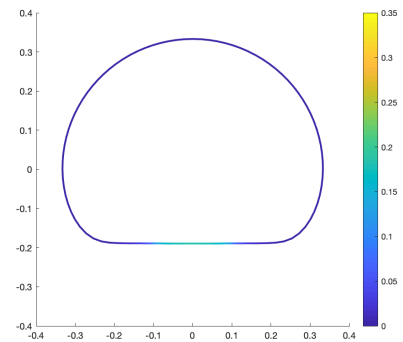
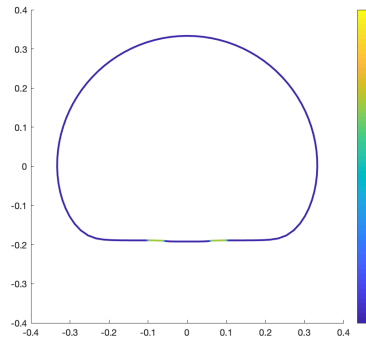
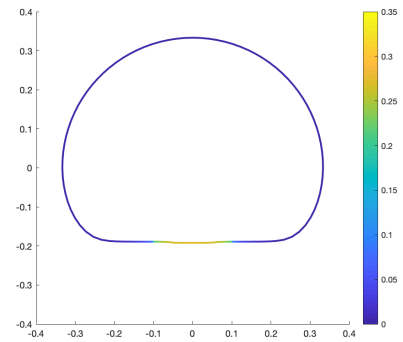
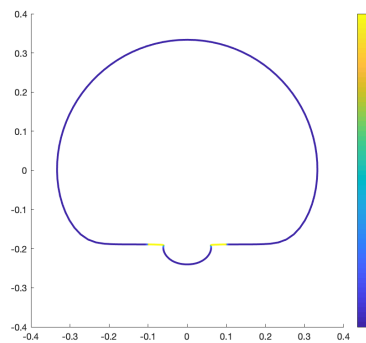
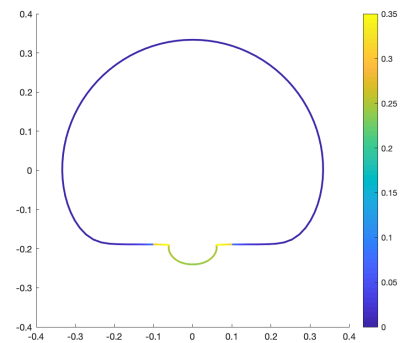
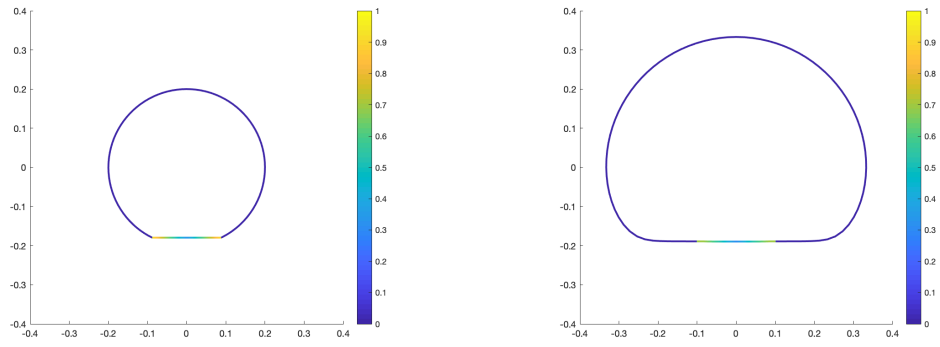
(a) Concentration of the Septins at $t = 0.1$.(e) Concentration of F-actin at $t = 0.1$.(b) Concentration of the Septins at $t = 0.2$.(f) Concentration of F-actin at $t = 0.2$.(c) Concentration of the Septins at $t = 0.3$.(g) Concentration of F-actin at $t = 0.3$.(d) Concentration of the Septins at $t = 0.35$.(h) Concentration of F-actin at $t = 0.35$.

Figure 4.6: Full model simulation for parametric framework: Septins and F-actin.

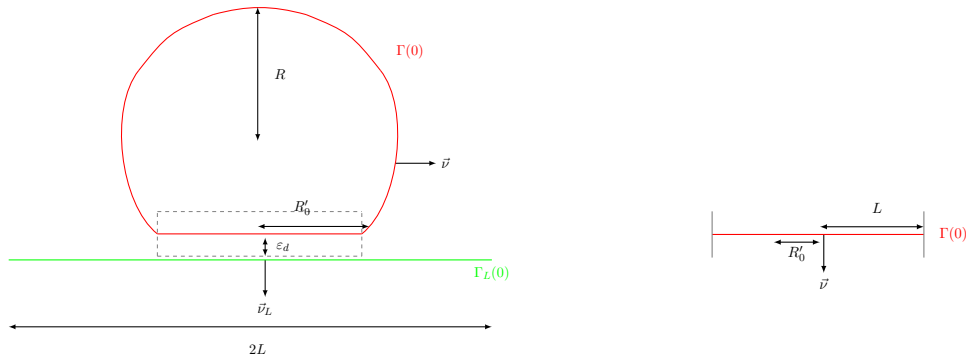


(a) Initial ring structure.

(b) Ring structure once fungus has stopped growing.

Figure 4.7: Demonstration of the movement of the ring structure in the full model simulation in the parametric framework.

4.2.2 Reduced model of the model presented in Section 4.2.1



(a) Initial rice blast schematic for full curve model.

(b) Initial rice blast schematic for reduced curve model.

Figure 4.8: Reduced model of the rice blast fungus. Here we consider only the pore area, the grey box in Figure 4.8a, and fix the remaining flat part of the fungus to a boundary far away from the pore, the grey lines in Figure 4.8b.

In this subsection we further simplify the model introduced in Section 4.2.1 by restricting $\Gamma(t)$ to the region around the pore area rather than considering the whole fungus in order to study only the penetration peg, as seen in Figure 4.8. With an abuse of notation, taking the curve $\Gamma(t)$ to represent the fungus (pore), we set

$$\Gamma(0) = \{ \vec{p} \in \mathbb{R}^2 : \vec{p}_0 \in [-L, L], \vec{p}_1 = 0 \},$$

where we consider $L = 0.5$ to be large enough to encompass the pore area. To be more specific, we assume that the support of the pore area is strictly contained within $\Gamma(t)$ throughout the evolution and is some positive distance away from the boundary $\partial\Omega$ during the evolution. We consider the evolution of $\Gamma(t)$ to be forced curve shortening flow fixed orthogonally to the boundary $\partial\Omega$, where

$$\Omega := \{\vec{p} \in \mathbb{R}^2 : \vec{p}_0 \in (-L, L)\},$$

and let \vec{x} be a parametrisation of $\Gamma(t)$. Thus, since we don't consider the leaf in this model, the reduced version of the velocity law (4.1.6) is

$$(\omega \vec{x})_t - \sigma \frac{\vec{x}_{\rho\rho}}{|\vec{x}_\rho|^2} = p(1 + g^p) \vec{\nu}, \quad (\rho, t) \in \mathcal{I} \times (0, T], \quad (4.2.8a)$$

$$F(\vec{x}(\rho, t)) = 0, \quad \langle \vec{x}_\rho(\rho, t), \nabla^\perp F(\vec{x}(\rho, t)) \rangle = 0, \quad (\rho, t) \in \{0, 1\} \times (0, T], \quad (4.2.8b)$$

$$\vec{x}(\rho, 0) = \vec{x}^0(\rho), \quad \rho \in [0, 1], \quad (4.2.8c)$$

where $\vec{\nu}$ denotes the downward pointing unit normal to $\Gamma(t)$, ρ denotes the parametrisation of the arc-length associated to $\Gamma(t)$, and, for some $\vec{p} \in \mathbb{R}^2$, F is defined as

$$F(\vec{p}) = |\vec{p}_0| - L.$$

By considering only the peg development we do not need to model Melanin or Sln1, since the primary role of Melanin is to increase the size of the fungus and the primary role of Sln1 is to act as a trigger for the Septins and F-actin upon a certain threshold of Melanin recruitment. Although it is primarily the role of F-actin to magnify the turgor pressure for the penetration peg, we still consider the Septins since its presence provides the enhancement of rigidity in the pore area, allowing the shape of the peg to form. This reduces the system of SRDEs from four to two, and so the parametrisation (4.2.8a)-(4.2.8b) leads to the following description of the SRDEs for the Septins and F-actin (u_s, u_a)

$$(|\vec{x}_\rho| \tilde{u}_i)_t - (\psi \tilde{u}_i)_\rho - \left(D_i(\tilde{u}_s) \frac{(\tilde{u}_i)_\rho}{|\vec{x}_\rho|} \right)_\rho = |\vec{x}_\rho| (f_i - k_i \tilde{u}_i), \quad (\rho, t) \in \mathcal{I} \times (0, T], \quad (4.2.9a)$$

$$\tilde{u}_i(0, t) = \tilde{u}_i(1, t) = 0, \quad t \in (0, T], \quad (4.2.9b)$$

$$\tilde{u}_i(\rho, 0) = 0, \quad \rho \in [0, 1], \quad (4.2.9c)$$

where $\tilde{u}_i(\rho, t) = u_i(\vec{x}(\rho, t), t)$ and $\psi = \langle \vec{x}_t, \vec{\nu}^\perp \rangle$ denotes the tangential velocity of \vec{x} . For the remainder of this subsection we drop the tilde from u_i , and rs , for ease of presentation. Since we make the assumption that the boundary $\partial\Omega$ is far enough away from the pore area, this leads us to taking (4.2.9b) since F-actin and the Septins are localised to the

pore. The diffusivity parameters we choose are

$$D_s(u_s) := 10^{-5}, \quad \text{and} \quad D_a(u_s) := \frac{10^{-2}}{2} \left(1 - H^\delta \left(\frac{u_s - s_3}{s_3} \right) \right)$$

with $s_3 = 0.1$ as in [102]. We redefine the ring structure and initially set it to be, for some $\vec{p} \in \Gamma(0)$,

$$rs(\vec{p}, 0) := \begin{cases} 0 & \text{if } \vec{p}_1 > 0 \\ 0 & \text{if } |\vec{p}_0| > \frac{R_0}{2} \\ r_1 + r_2 |\vec{p}_0| & \text{otherwise,} \end{cases}$$

where $R_0 = 0.176$, $r_1 = \frac{1}{3}$ and $r_2 = \frac{20}{3}$ as in [102], and it satisfies the following SAE

$$\begin{aligned} (|\vec{x}_\rho| rs)_t - (\psi rs)_\rho &= 0, & (\rho, t) \in \mathcal{I} \times (0, T], \\ rs(0, t) = rs(1, t) &= 0, & t \in (0, T], \end{aligned}$$

where the boundary condition is derived in a similar manner to (4.2.9b). Since we neglect Melanin, the turgor pressure p we use takes the form

$$p(t) := c_p p_1(t), \tag{4.2.10}$$

where $c_p = 0.05$ and $p_1(t)$ takes the form

$$p_1(t) := \begin{cases} Pt + p_I & \text{for } t < \bar{t} \\ P\bar{t} + p_I & \text{for } \bar{t} \leq t \leq T \end{cases}$$

with $P = 5$ and $\bar{t} = 0.25$ as in [102], and $p_I = 0$ reduced from $p_I = 1$ in [102] since there is no initial pressure in the pore area. We added c_p as a small multiplicative factor to reduce the turgor pressure generated by p over time. In the full model the repulsion function stops the peg growing until the magnification is large enough, however since we neglect repulsion in this reduced model we needed to reduce the magnitude of the pressure to allow enough recruitment of F-actin for magnification and enough recruitment of the Septins for the rigidity of the pore. By comparing (4.2.10) to (4.2.5) or (4.1.5), we notice the absence of the Melanin factor since its primary role in the pressure function is to increase the size of the appressorium dome. The activation and localisation are as in [102] and take the form

- \mathbb{S}_{rs} defines the set of the surface where the pore is and takes the form

$$\mathbb{S}_{rs}(t) := \{\vec{p} \in \Gamma(t) : rs(\vec{p}, t) > 0\};$$

- \mathbb{S}_s and \mathbb{S}_a define the annular sets on the surface where the Septins and F-actin will be recruited to, and take the form

$$\mathbb{S}_i(t) := \{\vec{p} \in \Gamma(t) : rs(\vec{p}, t) > \alpha_i\}$$

for $i = s, a$, where $\alpha_s = 0.6$ and $\alpha_a = 0.3$.

Then, the description of each forcing function f_i follows as:

- the forcing for the Septins f_s takes the form

$$f_s(t) := l_s \chi_{\mathbb{S}_s(t)} B_s(t)$$

with $l_s = 1$ as in [102] but with the absence of the uniform recruitment rate β_s ;

- the forcing for F-actin f_a takes the form

$$f_a(t) := l_a \chi_{\mathbb{S}_a(t)} B_a(t)$$

with $l_a = 1$ as in [102] but with the absence of the uniform recruitment rate β_a .

We keep the degradation rate of each species $(k_s, k_a) = (0.1, 0.1)$ the same as in [102].

Considering the rigidity, ω takes the form

$$\omega(u_s) := \omega_0(1 + \lambda(u_s)), \quad (4.2.11)$$

where $\omega_0 = 1$ as in [102], and

$$\lambda(u_s) := 1 + \frac{s_1}{2} \left(1 + H^\delta \left(\frac{u_s - s_2}{s_2} \right) \right)$$

with $s_1 = 1000$ and $s_2 = 0.2$ as in [102]. By comparing (4.2.11) to (4.1.7), we notice the absence of the rigidity caused by Melanin. Since the rigidity function considers the local concentration of Melanin on the surface rather than the total amount recruited to the surface of the fungus, it has no effect in the pore area, thus we take the contribution from Melanin to be the smallest value of λ_{m_1, m_2} . The protrusive force takes the form

$$p(t)(1 + g^p(u_a))$$

with p defined in (4.2.10), and the magnification factor g^p defined as

$$g^p(u_a) := \frac{a_1}{2} \left(1 + H^\delta \left(\frac{u_a - a_2}{a_2} \right) \right),$$

where $a_1 = 5$ and $a_2 = 0.25$ as in [102]. The surface tension of the pore area is taken to be $\sigma = 0.1$ as in [102].

For a finite element approximation of this model, we use the Newton's scheme (3.5.3a)-(3.5.3d) and (3.5.8a)-(3.5.8b) for the finite element approximation of (4.2.8a)-(4.2.8b), with $\alpha = 1$, and (4.2.9a)-(4.2.9b) respectively. We take $T = 0.3$ since the inception of the Septins and F-actin is not at $t = 0$ but much later in the simulation in [102], and we take $\delta = 10^2$ for the approximation of the Heaviside function. Similar to the full curve model, we use MATLAB for the simulation and visualisations on the iMac computer with 100 DOFs, $h = 10^{-2}$ and $\Delta t = 10^{-4}$ which resulted in 1.5 seconds of execution time.

We demonstrate the progression of the simulation in Figures 4.9 and 4.10. Figure 4.9 displays the evolution of the peg whilst Figure 4.10 displays the evolution of the concentration of the Septins and of F-actin. In each figure the boundary $\partial\Omega$ is depicted in black. We highlight noticeable mechanics. Figure 4.9b demonstrates the time-dependent forcing pushing down on the pore area. One can see that the whole pore area is moving. This wouldn't happen in the original model due to the repulsion term from the presence of the leaf as well as the rigidity from the concentration of Melanin. Figure 4.9c demonstrates the penetration peg starting to form due to the concentration of F-actin causing the magnification of the turgor pressure, see Figure 4.10g. One can see that annulus form of the Septins in Figure 4.10c and that the threshold for the the influx of rigidity has been reached. Finally, Figure 4.9d displays the clearly formed peg.

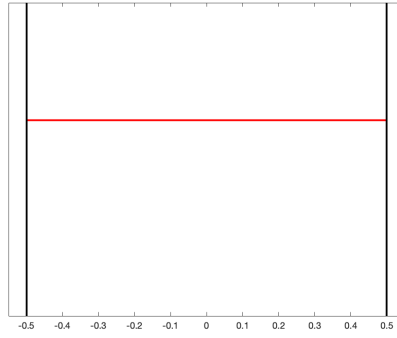
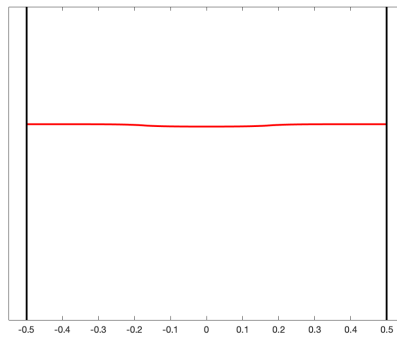
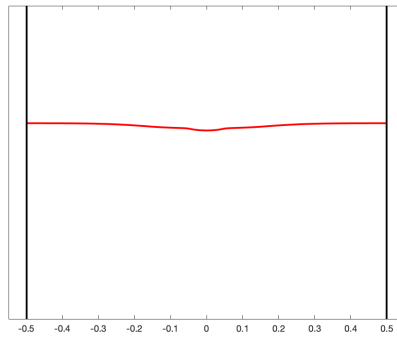
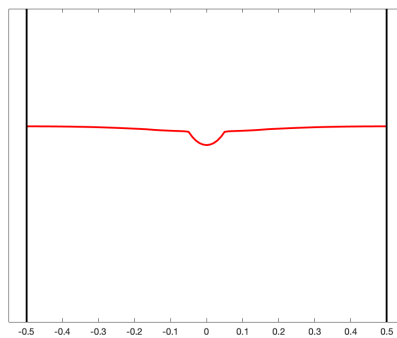
(a) Rice blast pore at $t = 0$.(b) Rice blast pore at $t = 0.1$.(c) Rice blast pore at $t = 0.2$.(d) Rice blast pore at $t = 0.3$.

Figure 4.9: Reduced model simulation for parametric framework. Evolution of rice blast pore.

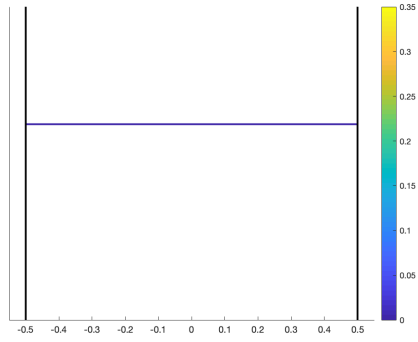
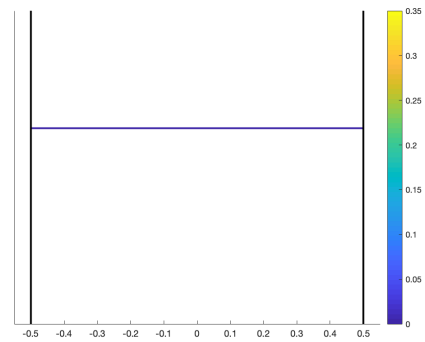
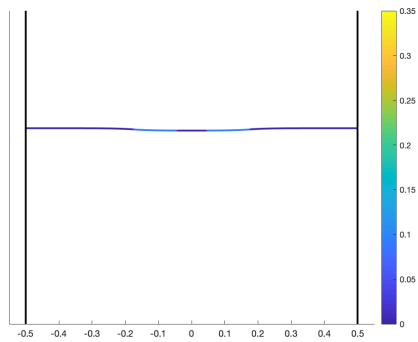
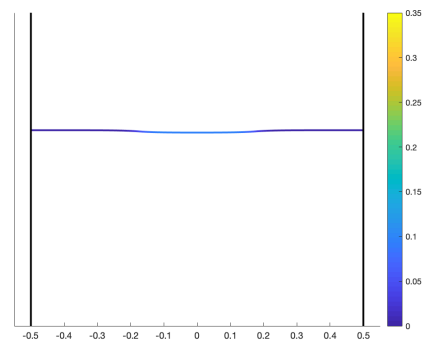
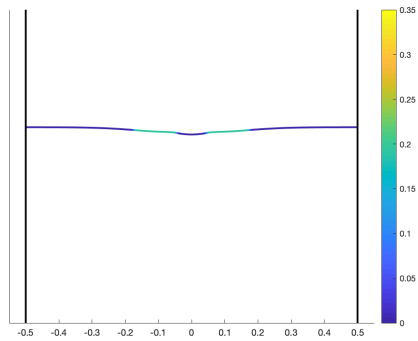
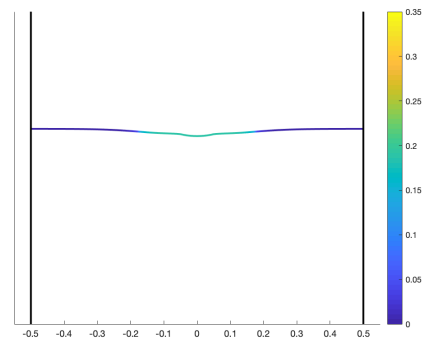
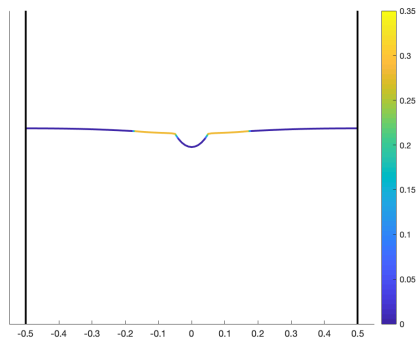
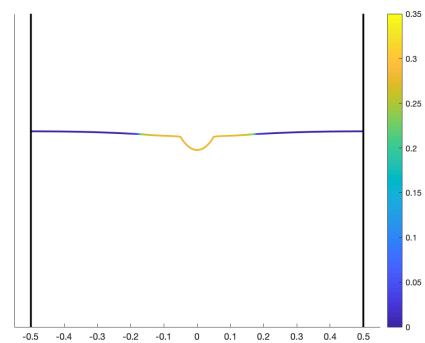
(a) Concentration of the Septins at $t = 0$.(e) Concentration of the F-actin at $t = 0$.(b) Concentration of the Septins at $t = 0.1$.(f) Concentration of the F-actin at $t = 0.1$.(c) Concentration of the Septins at $t = 0.2$.(g) Concentration of the F-actin at $t = 0.2$.(d) Concentration of the Septins at $t = 0.3$.(h) Concentration of the F-actin at $t = 0.3$.

Figure 4.10: Reduced model simulation for parametric framework: Septins and F-actin.

4.3 The phase field approach to approximating the model for the rice blast fungus

In this section we present a phase field approximation to the two dimensional model we developed in Section 4.2.1 as well as develop an approximation to a reduced version of the full three dimensional model proposed by [102]. We first present the phase field approximations of the velocity laws (4.1.6) and (4.1.10) as well as the diffuse interface approximations to the SRDE system (4.1.2a)-(4.1.2b). We continue to describe the fungus surface as $\Gamma(t)$ and the leaf surface as $\Gamma_L(t)$. For an approximation to the initial curve in the two dimensional model, we consider $\Gamma(0)$ and $\Gamma_L(0)$ defined by (4.2.1) and (4.2.2) respectively. For an approximation to the initial fungus surface in the three dimensional model, we define $\Gamma(0)$ as

$$\Gamma(0) = \Gamma_1 \cup \Gamma_2$$

where Γ_1 describes the dome part

$$\Gamma_1 = \left\{ \vec{p} \in \mathbb{R}^3 : 0 \leq \tan^{-1} \left(\frac{|(\vec{p}_0, \vec{p}_1)|}{\vec{p}_2} \right) \leq \theta_f, |\vec{p}| = R \right\}$$

and Γ_2 describes the pore area

$$\Gamma_2 = \left\{ \vec{p} \in \mathbb{R}^3 : \theta_f \leq \tan^{-1} \left(\frac{|(\vec{p}_0, \vec{p}_y)|}{\vec{p}_2} \right) \leq \pi, \vec{p}_2 = -\sqrt{R^2 - (R'_0)^2}, |(\vec{p}_0, \vec{p}_1)| \leq R'_0 \right\}$$

where $\theta_f = \pi - \tan^{-1}(R'_0/\sqrt{R^2 - (R'_0)^2})$ is the polar angle where Γ_1 and Γ_2 meet, $R = 0.2$ is the initial radius of the dome, and $2R'_0 = R_0$ with $R_0 = 0.176$ being the diameter of the pore. This initial data is shown in Figure 4.11. For the initial data for the leaf surface in the three dimensional model, we define $\Gamma_L(0)$ as

$$\Gamma_L(0) = \{ \vec{p} \in \mathbb{R}^3 : \vec{p}_2 = -\sqrt{R^2 - (R'_0)^2}, \vec{p}_0 \in [-L, L], \vec{p}_1 \in [-L, L] \},$$

where we set $L = 0.5$. Let $\Omega \subset \mathbb{R}^{n+1}$, where $n = 1, 2$, is a bounded domain such that $\Gamma(t) \cup \Gamma_L(t) \subset \Omega$, $\forall t \in [0, T]$. We denote, for some $\vec{p} \in \bar{\Omega}$, $\phi(\vec{p}, t) := d_\Gamma(\vec{p}, t)$ and $\phi_L(\vec{p}, t) := d_{\Gamma_L}(\vec{p}, t)$, where $d_\Gamma(\cdot, t)$ and $d_{\Gamma_L}(\cdot, t)$ are the signed distance functions corresponding to $\Gamma(t)$ and $\Gamma_L(t)$ respectively. By considering

$$\Gamma(t) = \{ \vec{p} \in \bar{\Omega} : \phi(\vec{p}, t) = 0 \} \quad \text{and} \quad \Gamma_L(t) = \{ \vec{p} \in \bar{\Omega} : \phi_L(\vec{p}, t) = 0 \},$$

the double obstacle phase field approximations to the velocity laws (4.1.6) and (4.1.10) satisfy the variational inequalities

$$\varepsilon((\omega \varphi)_t, \xi - \varphi) + \varepsilon \sigma(\nabla \varphi, \nabla \xi - \nabla \varphi) - \frac{\sigma}{\varepsilon}(\varphi, \xi - \varphi)$$

$$\geq \left(\frac{\pi}{4} p(1 + g^p) - \frac{1}{\varepsilon} \varphi(1 - \varphi_L^2), \xi - \varphi \right), \quad \forall \xi \in \mathcal{K}, \quad (4.3.1a)$$

$$\begin{aligned} \varepsilon_L \omega_L((\varphi_L)_t, \eta - \varphi_L) + \varepsilon_L \sigma_L(\nabla \varphi_L, \nabla \eta - \nabla \varphi_L) - \frac{\sigma_L}{\varepsilon_L}(\varphi_L, \eta - \varphi_L) \\ \geq -\frac{1}{\varepsilon_L}(\varphi_L(1 - \varphi^2), \eta - \varphi_L), \quad \forall \eta \in \mathcal{K}, \end{aligned} \quad (4.3.1b)$$

$$\varphi(\cdot, 0) = \varphi^0(\cdot), \quad \varphi_L(\cdot, 0) = \varphi_L^0(\cdot), \quad \text{in } \bar{\Omega}, \quad (4.3.1c)$$

where $\varphi(\cdot, t)$ and $\varphi_L(\cdot, t)$ are the phase field approximations to $\phi(\cdot, t)$ and $\phi_L(\cdot, t)$ respectively, φ^0 and φ_L^0 follow the same structure as (2.4.20), and

$$\mathcal{K} := \{\xi \in H^1(\Omega) : |\xi| \leq 1\}.$$

We set

$$\rho_\varphi(\cdot, t) := 1 - \varphi^2(\cdot, t), \quad \text{and} \quad \Gamma_\varepsilon(t) := \{\vec{p} \in \Omega : \rho_\varphi(\vec{p}, t) > 0\}, \quad (4.3.2)$$

to be the diffuse interface function and interfacial regions respectively. We also set the phase field approximations to the normal velocity v of $\Gamma(t)$, the outward pointing unit normal $\vec{\nu}$ to $\Gamma(t)$ and the material velocity \vec{v} of $\Gamma(t)$ to be

$$v_\varphi(\cdot, t) := -\frac{\varphi_t(\cdot, t)}{|\nabla \varphi(\cdot, t)|}, \quad \vec{v}_\varphi(\cdot, t) := \frac{\nabla \varphi(\cdot, t)}{|\nabla \varphi(\cdot, t)|}, \quad \vec{\nu}_\varphi(\cdot, t) := v_\varphi(\cdot, t) \vec{\nu}_\varphi(\cdot, t).$$

Then, neglecting the contribution from R , the diffuse interface approximation of the SRDE system (4.1.2a)-(4.1.2b) satisfies the following weak formulation

$$\begin{aligned} \frac{d}{dt} (\rho_\varphi u_i^e |\nabla \varphi|, \zeta) + d_i (\rho_\varphi \nabla u_i^e |\nabla \varphi|, \nabla \zeta) - (\rho_\varphi u_i^e \vec{v}_\varphi |\nabla \varphi|, \nabla \zeta) \\ = (\rho_\varphi (f_i^e - k_i u_i^e) |\nabla \varphi|, \zeta), \quad \forall \zeta \in H^1(\Omega), \end{aligned} \quad (4.3.3a)$$

$$u_i^e(\cdot, 0) = 0, \quad \text{in } \bar{\Omega}. \quad (4.3.3b)$$

The extensions u_i^e and f^e we use in (4.3.3a) are a projection of the function values on $\Gamma(t)$ in the (positive and negative) normal direction to $\Gamma(t)$ by $\frac{\pi\varepsilon}{2}$. Noting (2.3.7), we calculate the total surface amount of each species in the following way

$$S_i^e(t) := \frac{2}{\pi\varepsilon} \int_{\Omega} \rho_\varphi(\cdot, t) u_i^e(\cdot, t) dx,$$

and maintain that

$$1 = S_i^e(t) + B_i^e(t), \quad t \in [0, T].$$

4.3.1 Approximation to the curve model in Section 4.2.1

In this subsection we present the parameter choices and assumptions used for the phase field approximation of the curve model presented in Section 4.2.1.

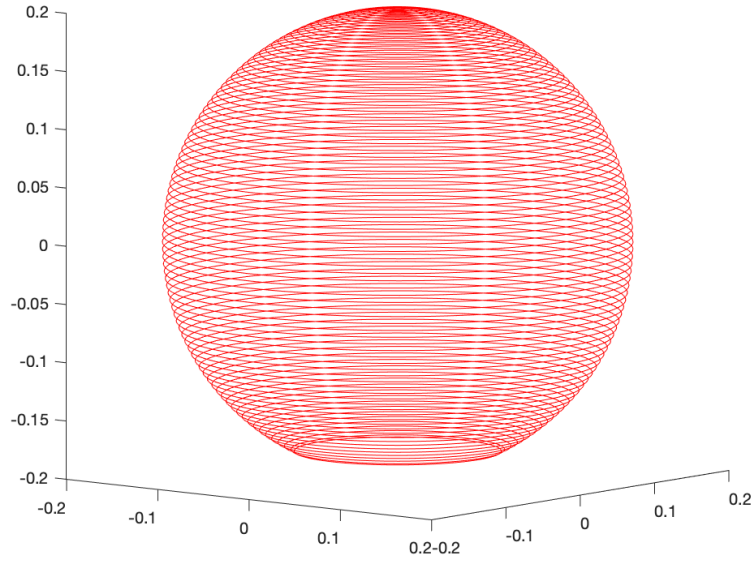


Figure 4.11: Initial surface $\Gamma(0)$ describing the rice blast.

In order to simplify the phase field model, noting the investigations in Sections 2.4.2 and 2.4.4, we choose to make the diffusivity constants independent on the concentration of the Septins and take $d_i = (1, 10, 1, 10) \times 10^{-3}$. In addition, given the movement of the ring structure when the fungus is growing in Figure 4.7b, we make rs^e constant in time, so that, for $\vec{p} \in \bar{\Omega}$, we have

$$rs^e(\vec{p}) := \begin{cases} 0 & \text{if } |\vec{p}_1 + \sqrt{R^2 - (R'_0)^2}| > \frac{\pi\varepsilon}{2} \\ 0 & \text{if } |\vec{p}_0| > R'_0 \\ r_1 + r_2|\vec{p}_0| & \text{otherwise,} \end{cases}$$

where $R = 0.2$, $R'_0 = 0.088$, $r_1 = \frac{1}{3}$ and $r_2 = \frac{20}{3}$ as in [102]. These simplifications could be addressed in subsequent models. We set the turgor pressure to be

$$p(S_m(t), t) := p_1(t) + \mu S_m(t), \quad (4.3.4)$$

where $\mu = 2$ as in [102] and $p_1(t)$ satisfies

$$p_1(t) := \begin{cases} Pt + p_I & \text{for } t < \bar{t} \\ P\bar{t} + p_I & \text{for } \bar{t} \leq t \leq T \end{cases}$$

with $p_I = 1$ and $\bar{t} = 0.25$ as in [102] and the time pressure constant $P = 1$ which is reduced from $P = 5$ in [102] since the value 5 caused the penetration peg to grow too rapidly once the leaf has been punctured. We take the recruitment sets for the molecular species to be:

- \mathbb{S}_{m^e} defines the (time independent) set on the curve where the pore is not:

$$\mathbb{S}_{m^e} := \{\vec{p} \in \overline{\Omega} : rs^e(\vec{p}) = 0\};$$

- \mathbb{S}_{rs^e} defines the set where the pore is:

$$\mathbb{S}_{rs^e} := \{\vec{p} \in \overline{\Omega} : rs^e(\vec{p}) > 0\};$$

- $\mathbb{S}_{ts^e}, \mathbb{S}_{s^e}, \mathbb{S}_{a^e}$ define the annular sets on the curve where Sln1, the Septins and F-actin will be recruited to:

$$\mathbb{S}_{i^e} := \{\vec{p} \in \overline{\Omega} : rs^e(\vec{p}) > \alpha_i\},$$

for $i = ts, s, a$, where $\alpha_{ts} = 0.3$, $\alpha_s = 0.6$ and $\alpha_a = 0.3$ as in [102];

- \mathbb{T}^e defines the set whereby enough Melanin has been recruited to the curve to allow for the turgor sensor to be recruited:

$$\mathbb{T}^e := \{t \in [0, T] : S_m^e(t) > q_m B_m^e(t)\},$$

where $q_m = \frac{1}{19}$ as in [102].

The description of each forcing function f_i^e then follow as:

- the forcing for Melanin f_m^e takes the form

$$f_m^e(t) := l_m \chi_{\mathbb{S}_{m^e}} \frac{B_m^e(t) - q_b}{c_m + B_m^e(t) - q_b} (p(S_m^e(t), t) - p_I)$$

where $q_b = 0.55$ and $c_m = 10$, as in [102], and $l_m = 300$ which is increased from $l_m = 30$ in [102] in order to compensate for the reduction of the coupling constant in the turgor pressure;

- the forcing for Sln1 f_{ts}^e takes the form

$$f_{ts}^e(t) := l_{ts} \chi_{\mathbb{S}_{ts^e}} (B_{ts}^e(t) - q_b) \chi_{\mathbb{T}^e}$$

where $l_{ts} = 1$ and $q_b = 0.55$ as in [102];

- the forcing for the Septins f_s^e takes the form for $\vec{p} \in \overline{\Omega}$

$$f_s^e(\vec{p}, t) := (l_s \chi_{\mathbb{S}_{s^e}} \chi_{u_{ts}^e(\vec{p}, t) > 0} + \beta_s \chi_{\mathbb{S}_{rs^e}}) B_s^e(t)$$

where $l_s = 1$ as in [102], and $\beta_s = 0.01$ which is decreased from $\beta_s = 0.1$ in [102] since setting $\beta_s = 0.1$ brought about a concentration throughout the pore was large enough to influence the evolution of the fungus in regions where it should not;

- the forcing for F-actin f_a^e takes the form for $\vec{p} \in \overline{\Omega}$

$$f_a^e(\vec{p}, t) := (l_a \chi_{\mathbb{S}_{a^e}} \chi_{u_{ts}(\vec{p}, t) > 0} + \beta_a \chi_{\mathbb{S}_{r,s^e}}) B_a^e(t)$$

where $l_a = 1$ as in [102], and, for the same reason as above, $\beta_a = 0.01$ decreased from $\beta_a = 0.1$.

We keep the degradation rate of each species $(k_m, k_{ts}, k_s, k_a) = (0, 0.1, 0.1, 0.1)$ the same as in [102]. Considering the rigidity, we approximate ω in (4.1.6) by

$$\omega(\rho_\varphi u_m^e, \rho_\varphi u_s^e) := \omega_0 (\lambda_{m_1, m_2}(\rho_\varphi u_m^e) + \lambda_{s_1, s_2}(\rho_\varphi u_s^e)),$$

where $\omega_0 = 1$ as in [102], and

$$\lambda_{i_1, i_2}(\rho_\varphi u_i^e) := 1 + \frac{i_1}{2} \left(1 + H^\delta \left(\frac{\rho_\varphi u_i^e - i_2}{i_2} \right) \right),$$

with $m_1 = s_1 = 1000$, $m_2 = 0.25$ and $s_2 = 0.2$ as in [102]. We approximate the protrusive force with

$$p(S_m^e(t), t)(1 + g^p(\rho_\varphi u_i^e))$$

with p defined in (4.3.4), where the approximation to the magnification function g^p in (4.1.6) takes the form

$$g^p(\rho_\varphi u_a^e) := \frac{a_1}{2} \left(1 + H^\delta \left(\frac{\rho_\varphi u_a^e - a_2}{a_2} \right) \right),$$

with $a_2 = 0.25$ as in [102] and $a_1 = 1$ reduced from $a_1 = 5$ in [102] due to the penetration peg growing too rapidly once the leaf had ruptured. We approximate the repulsion of the leaf from the fungus g^r in (4.1.8) by using

$$\frac{\kappa_\infty}{\varepsilon} \varphi(1 - \varphi_L^2), \tag{4.3.5}$$

where

$$\kappa_\infty := \begin{cases} 0 & \text{if } \|\kappa_L\|_{L^2(\Omega)} > \overline{\kappa_L} \\ 1 & \text{otherwise,} \end{cases}$$

with $\overline{\kappa_L} = 0.004$. This is an experimentally led figure to match the dynamics of the simulation in [102], and we chose to use the L^2 norm rather than the L^∞ as we found it produced more reliable readings to match against the model in [102]. From personal communications with Charles M. Elliott from the University of Warwick, the term in (4.3.5) comes from the addition of

$$\frac{1}{2\varepsilon} \int_\Omega (1 - \varphi(\cdot, t))^2 (1 - \varphi_L^2(\cdot, t)) dx$$

into the Ginzburg–Landau–Wilson functional (2.2.1) which heavily penalises having both $|\varphi| < 1$ and $|\varphi_L| < 1$ at any given point. Similarly we approximate the repulsion of the fungus from the leaf by using

$$\frac{\kappa_\infty}{\varepsilon} \varphi_L (1 - \varphi^2).$$

As explained previously, κ_L heavily relies on the choice of surface tension σ_L which we decreased from $\sigma_L = 10^6$ in [102] to $\sigma_L = 10^3$. Similarly we decreased the rigidity factor of the leaf from $\omega_L = 10^6$ to $\omega_L = 10^3$. We kept the fungus surface tension $\sigma = 0.1$ the same as in [102].

To solve the finite element approximation of this model, we use **Model: $\mathcal{ACFE}\varepsilon$** (2.4.17a)–(2.4.17b) with use of the projected SOR technique (2.4.19a)–(2.4.19b) for the solution to the algebraic system of equations arising from the phase field approximation to the velocity law as well as GMRES with diagonal preconditioning to solve the algebraic systems arising from the SRDE system. We set $T = 0.35$ and use the refinement procedure discussed in Section 2.4, whereby we increase refinement in the interfacial regions defined in a similar way to (2.4.15) with

$$\begin{aligned} \mathcal{N}_h^n &:= \{i \in \mathcal{N} : \exists j \in \omega_i \text{ such that } \rho_\Phi^n(\vec{p}_j) > 0\}, & \Gamma_\varepsilon^{h,n} &:= \{T^h \in \mathcal{T}^h : \mathcal{N}_{T^h} \subset \mathcal{N}_h^n\}, \\ \mathcal{N}_{L,h}^n &:= \{i \in \mathcal{N} : \exists j \in \omega_i \text{ such that } \rho_{\Phi_L}^n(\vec{p}_j) > 0\}, & \Gamma_{L,\varepsilon}^{h,n} &:= \{T^h \in \mathcal{T}^h : \mathcal{N}_{T^h} \subset \mathcal{N}_{L,h}^n\} \end{aligned}$$

and coarsen everywhere else, where here we have denoted Φ^n and Φ_L^n to be the finite element approximations to φ^n and φ_L^n respectively, and similar to (4.3.2) we denote $\rho_\Phi^n(\cdot) := 1 - (\Phi^n(\cdot))^2$ and $\rho_{\Phi_L}^n(\cdot) := 1 - (\Phi_L^n(\cdot))^2$. Further to this, once the leaf has ruptured, we increase the refinement of the triangles specifically in the pore area and coarsen the triangles in $\Gamma_{L,\varepsilon}^{h,n}$. We set $\varepsilon = \varepsilon_L$ for ease of mesh parameter choice and take $\delta = 10^2$ for the approximation of the Heaviside function. The following simulation was produced using ALBERTA using one core on the HPC and the visualisations were produced on MATLAB. Taking $\varepsilon = \frac{\sqrt{2}}{80}$, which equates initially to 12275 DOFs and finishes with 13125 DOFs, $h_{\mathcal{T}} = \frac{131}{30000}$ and $\Delta t = 10^{-5}$, results in approximately 540 minutes of execution.

As in the previous section we show figures that include interesting evolution properties and compare them to the figures produced in Section 4.2.1. Figure 4.12 depicts the initial fungus and leaf configurations whilst Figure 4.13 depicts the evolution of the fungus and leaf. Figures 4.14a–4.14d depict the evolution of the Melanin concentration, Figures 4.14e–4.14h depict the evolution of the Sln1 concentration, Figures 4.15a–4.15d depict the

evolution of the Septins concentrations, and Figures 4.15e–4.15h depict the evolution of the F-actin. We now compare the two simulations. We first note that there are two main driving forces of the differences between the simulations; the first is the different forcing and the second is the approximation to the repulsion term. The most noticeable difference between the simulations is the difference between the pointwise values of the molecular species. The different forcing for each species contribute to different pointwise values of the concentrations on each of the curves, which in turn causes certain fungus behaviour to occur at slightly different times and therefore a smaller simulation time T . More explicitly, although the notation and values are the same in the forcing functions for the both approaches, the forcing functions in the phase field approach are an approximation to the sharp interface approach due to the forcing functions being proportional to the surface concentration of each species. We believe the approximation to the surface integral using (2.3.7) is the main element which is contributing to the different recruitment rates and therefore the difference in pointwise values. More subtly, focusing on Melanin, in the absence of velocity once the dome has reached maximum size, diffusion and degradation, the SRDE is only driven by the forcing. Now, notice that the forcing function is monotonically decreasing to 0 as the bulk concentration decreases towards q_b , which means that the Melanin surface concentration will reach a steady state of $1 - q_b$. We postulate that, due to the approximation of the surface integral (2.3.7), the pointwise values of u_m^ϵ will be different to u_m in order to satisfy $S_m^\epsilon(t) \approx 1 - q_b$ and are causing the overestimation. Although there is diffusion, degradation and surface movement for the other three species, we postulate that if we were to run the simulation longer than $T = 0.35$, without the peg forming mechanism, we would see the same behaviour happen. That is, at the moment they seem to be underestimated using the phase field approach, and we postulate they will be overestimated in a similar way to Melanin if the simulation ran for long enough. The pointwise values also differ due to the simulation time T , although the recruitment of Sln1, the Septins and F-actin happens at roughly the same time in both approaches, the shorter simulation time will have an effect on the recruitment time. Moreover, we also note that, as shown in Section 2.4.4, the Allen-Cahn equation coupled to the diffuse interface approximation does not react well with a small diffusion coefficient. Even though we increased the diffusion coefficients significantly for Melanin and the Septins, $d = 10^{-2}$ and $d = 10^{-3}$ still cause reasonably large changes across the interface even with edges-smoothing, as can be seen in Figure 2.23. We believe these changes also have a knock-on effect to the interface pointwise values due to the surface integrals being approximated with an integral

of each of the molecular species over the whole domain Ω . Another noticeable difference is the distance between the fungus and the leaf. The repulsion term causes the fungus and leaf to be significantly closer, and caused the difference in the leaf surface tension.

We first compare the evolution of the fungus by comparing Figure 4.13 with Figure 4.4. We see that the fungus has reached maximum size by $t = 0.2$, demonstrated by Figures 4.4a and 4.13a, but the fungus in the phase field simulation is slightly larger and, as alluded to already, the fungus and leaf are closer. We also see that the peg is quite a bit larger in the phase field simulation by comparing Figures 4.13d, where $t = 0.35$, and 4.4d, where $t = 0.4$. Next we compare the evolution of the Melanin concentration by comparing Figure 4.14a–4.14d with Figure 4.5a–4.5d. We see that the Melanin is mostly localised in the same area of the fungus, whereby the Melanin has diffused slightly into the pore area in the phase field setting since the diffusion constant is non-zero. Next we compare the evolution of the Sln1 concentration by comparing Figure 4.14e–4.14h to Figure 4.5e–4.5h. We see that the Sln1 is localised to the pore area and that, once the peg grows, the concentration depletes on the peg’s surface. We notice that the increased diffusion in the phase field setting doesn’t visually effect the location of the presence of the Sln1 concentration on the fungus surface. Next we compare the evolution of the Septins concentration by comparing Figure 4.15a–4.15d to Figure 4.6a–4.6d. The Septins are localised in the same annular region of the pore however we can see that the Septins concentration in the phase field setting has diffused further. Moreover, by comparing Figure 4.6d with Figure 4.15d we can see that in the sharp interface simulation there is a large concentration of Septins still in the annular region whilst in the phase field simulation this doesn’t feature. We speculate that this is one of the main causes for the peg to grow faster in the phase field setting. We also speculate that this issue may be rectified by allowing the ring structure to move with the fungus. Finally, we compare the evolution of the F-actin concentrations by comparing Figure 4.15e–4.15h to Figure 4.6e–4.6h. Again, we see the concentration is localised to the pore area however, in Figure 4.15h, we see a large concentration of F-actin at the front of the peg in the phase field setting whilst in the sharp interface approach we see the concentration has depleted. We believe that this increase in concentration is the other main factor causing the peg to increase in size rapidly.

A more detailed investigation is needed to match the forcing terms in the phase field scenario to the sharp interface model, and to show that the repulsion term in the phase field setting does asymptotically match the repulsion term in the sharp interface setting. Doing

this analysis will also show the correct scaling needed. It is also evident that the diffusion constants do influence the fungus evolution, and some further work is needed to allow for smaller diffusion constants in the numerical schemes. This could be managed if the edge smoothing technique introduced in Section 2.4.3 could be applied to the finite volume approximation of the diffuse interface approach, or alternatively to use a discontinuous Galerkin approach [33, 79].

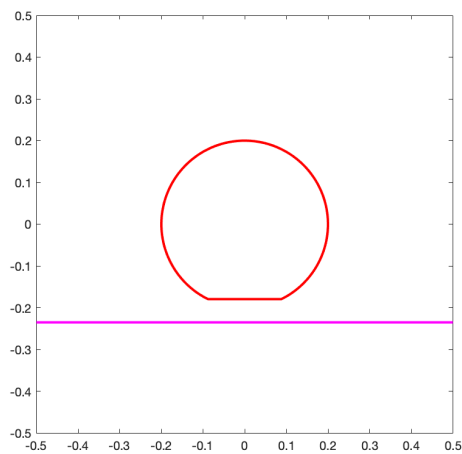


Figure 4.12: Initial rice blast and leaf on the $\Phi^0 = 0$ and $\Phi_L^0 = 0$ level sets for the phase field curve approximation.

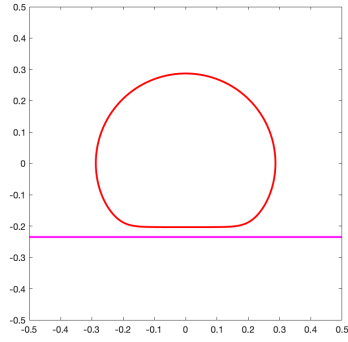
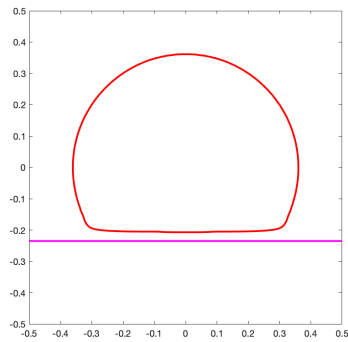
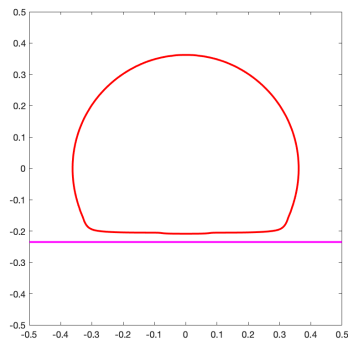
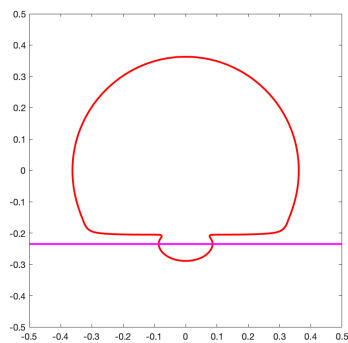
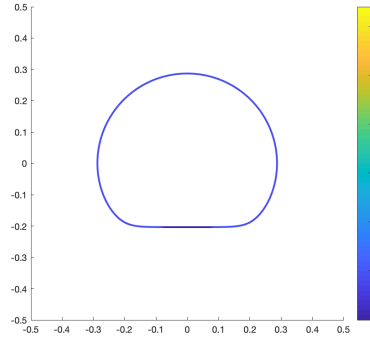
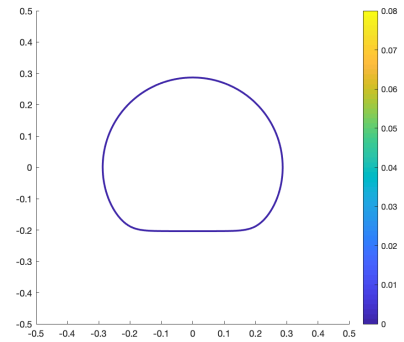
(a) Rice blast and leaf at $t = 0.1$.(b) Rice blast and leaf at $t = 0.2$.(c) Rice blast and leaf at $t = 0.3$.(d) Rice blast and leaf at $t = 0.35$.

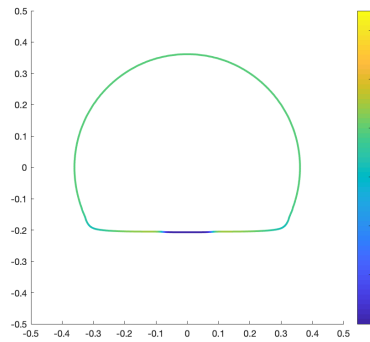
Figure 4.13: Curve simulation for phase field framework. Rice blast and leaf on the $\Phi^n = 0$ and $\Phi_L^n = 0$ level sets respectively at different times.



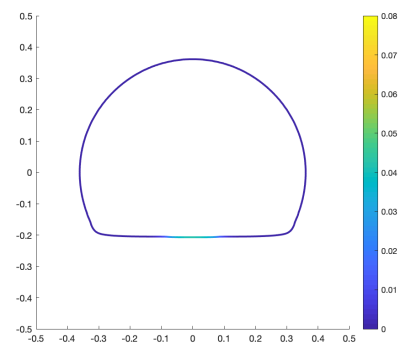
(a) Concentration of Melanin at $t = 0.1$.



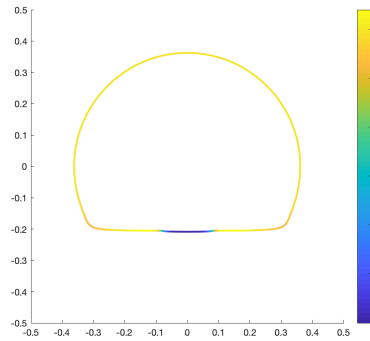
(e) Concentration of Sln1 at $t = 0.1$.



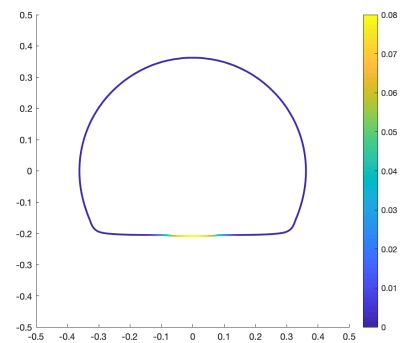
(b) Concentration of Melanin at $t = 0.2$.



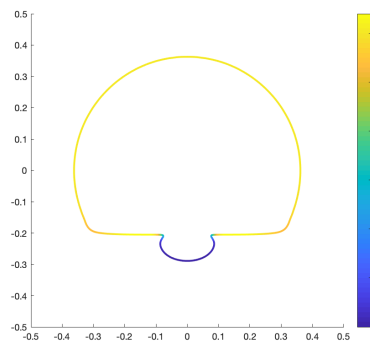
(f) Concentration of Sln1 at $t = 0.2$.



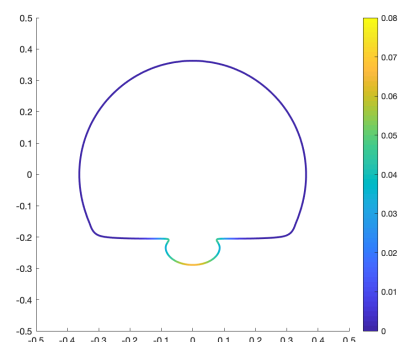
(c) Concentration of Melanin at $t = 0.3$.



(g) Concentration of Sln1 at $t = 0.3$.



(d) Concentration of Melanin at $t = 0.35$.



(h) Concentration of Sln1 at $t = 0.35$.

Figure 4.14: Curve simulation for phase field framework: Melanin and Sln1.

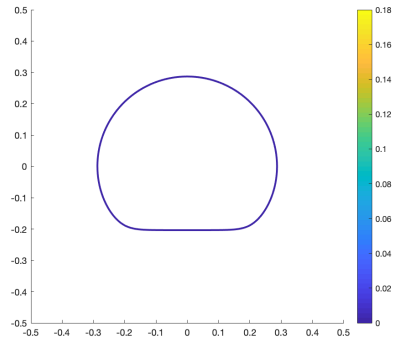
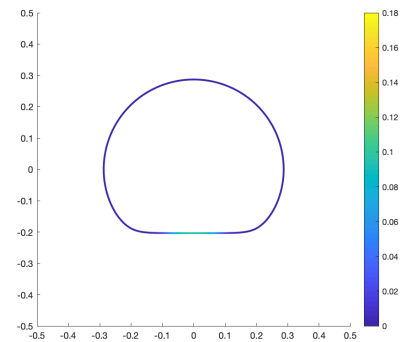
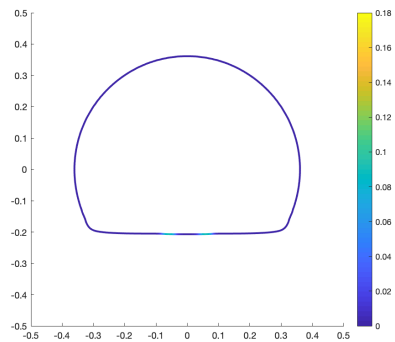
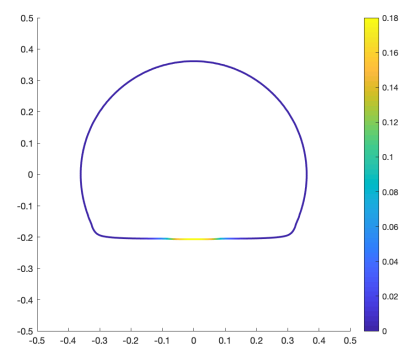
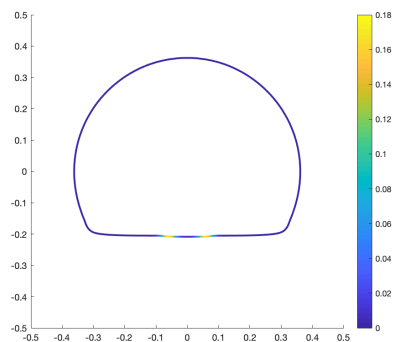
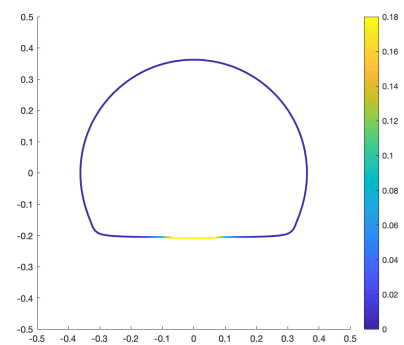
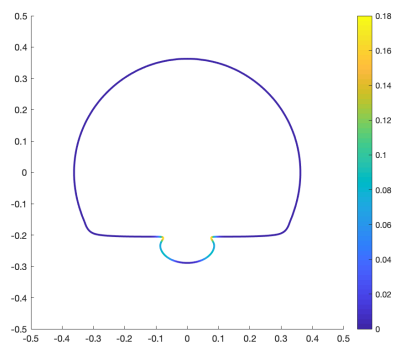
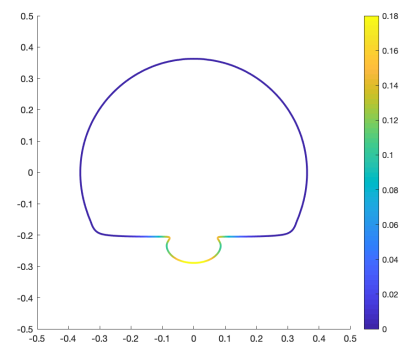
(a) Concentration of the Septins at $t = 0.1$.(e) Concentration of F-actin at $t = 0.1$.(b) Concentration of the Septins at $t = 0.2$.(f) Concentration of F-actin at $t = 0.2$.(c) Concentration of the Septins at $t = 0.3$.(g) Concentration of F-actin at $t = 0.3$.(d) Concentration of the Septins at $t = 0.35$.(h) Concentration of F-actin at $t = 0.35$.

Figure 4.15: Curve simulation for phase field framework: Septins and F-actin.

4.3.2 Approximation to the three dimensional surface model in [102]

The phase field versions of all the components that are derived in Section 4.3.1 naturally extend to three space dimensions and so can be used to approximate the three dimensional model in Section 4.1. We present simulations of this three dimensional setup using all the same parameters as the ones defined in Section 4.3.1, where we note that we redefine the initial ring structure rs^e to mirror the dimension of the model, so that, for $\vec{p} \in \bar{\Omega}$, we have

$$rs^e(\vec{p}) := \begin{cases} 0 & \text{if } \left| \vec{p}_2 + \sqrt{R^2 - (R'_0)^2} \right| > \frac{\pi\varepsilon}{2} \\ 0 & \text{if } |(\vec{p}_0, \vec{p}_1)| > R'_0 \\ r_1 + r_2 |(\vec{p}_0, \vec{p}_1)| & \text{otherwise,} \end{cases}$$

where $R = 0.2$, $R'_0 = 0.088$, $r_1 = \frac{1}{3}$ and $r_2 = \frac{20}{3}$ as in [102].

Using the same numerical procedure for the solution to the resulting systems of algebraic equations and the same refinement procedure we present the following figures of the three dimensional phase field approximation to the model in [102]. The following simulation was executed using ALBERTA using one core on the HPC, the visualisations in Figures 4.16 and 4.17 were produced in MATLAB, and the visualisations in Figures 4.18 to 4.21 were produced in ParaView [73]. Taking $\varepsilon = \frac{\sqrt{2}}{80}$, which equates initially to 251611 DOFs and finishes with 259804 DOFs, $h_{\mathcal{T}} = 2^{-6}$ and $\Delta t = 10^{-4}$, results in approximately 6240 minutes (4 days, 8 hours) of execution.

Figures 4.16–4.21 demonstrate the three dimensional simulation. Figure 4.16 depicts the initial fungus and leaf configuration, while Figure 4.17 depicts the evolution of the two surfaces, in both figures $x - z$ cross sections are displayed. In Figures 4.18 and 4.19 we display the pore area of the fungus by presented the results from the view point below the fungus. Figure 4.18a–4.18d depicts the evolution of the concentration of Melanin, while Figure 4.18e–4.18h depicts the evolution of the concentration of Sln1, Figure 4.19a–4.19d depicts the evolution of the concentration of the Septins, while Figure 4.19e–4.19h depicts the evolution of the concentration of the F-actin. Figure Figure 4.20 depicts the evolution of the peg from initial formation to full growth, while Figure 4.21 depicts all the molecular species at the final time from a side point of view. First we will compare the curve simulation to the surface simulation, and then compare the surface simulation to the figures in [102]. We begin by comparing the evolution of the fungus in Figure 4.17 to Figure 4.13. We see that the fungus is slightly bigger in the curve simulation in comparison to the surface simulation. We also see the leaf breaks early in the surface simulation, seen

by a peg form at $t = 0.3$ in Figure 4.17c whilst not appearing in Figure 4.13c at $t = 0.3$. Interestingly, we also see that the peg grows slower in the surface simulation in comparison to the curve simulation since the pegs are roughly similar sizes at $t = 0.35$ in Figures 4.17d and 4.13d. We speculate that this has something to do with the increase in dimension and thus the increase in surface area. We quite clearly see the localisation of all the molecular species are similar, and see the depletion of each of the species clearer in the surface simulation compared to the curve simulation. This is emphasised by Figure 4.21, where we can also see the diffusion of the Melanin into the seeded pore area in Figure 4.21a and the diffusion of the Septins into the peg in Figure 4.21c. Now we compare our results to the results in [102]. We first note that our peg is much larger than the one presented in Figure 2a in [102]. We believe this is due to the difference in concentration of the recruitment of the Septins to the surface. We see that the molecular species concentrations are mostly constant throughout their recruitment regions, with the exception of the turgor sensor, in [102] whilst in our simulations, since we have higher diffusion constants, we see it happen until we get close to the boundaries of the localisation regions.

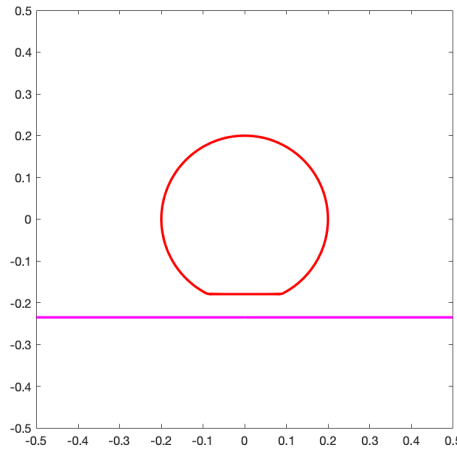


Figure 4.16: Initial rice blast and leaf on the $\Phi^0 = 0$ and $\Phi_L^0 = 0$ level sets for the phase field surface approximation, $x - z$ cross section.

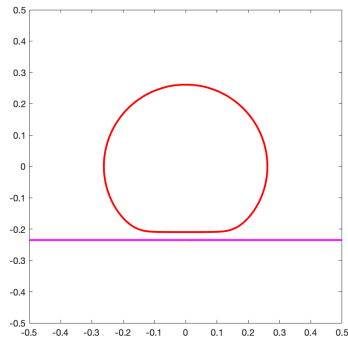
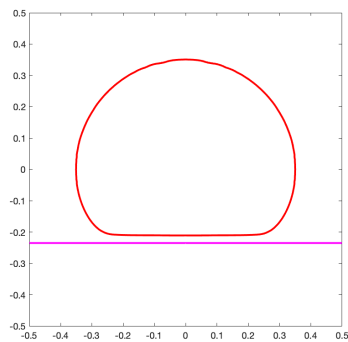
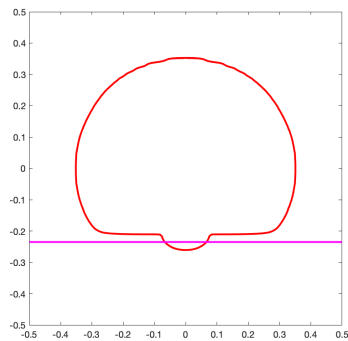
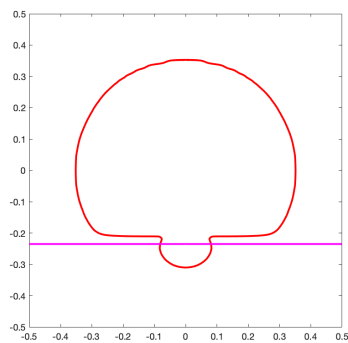
(a) Rice blast and leaf at $t = 0.1$.(b) Rice blast and leaf at $t = 0.2$.(c) Rice blast and leaf at $t = 0.3$.(d) Rice blast and leaf at $t = 0.35$.

Figure 4.17: Surface simulation for phase field framework, $x - z$ cross section. Rice blast and leaf on the $\Phi^n = 0$ and $\Phi_L^n = 0$ level sets respectively at different times.

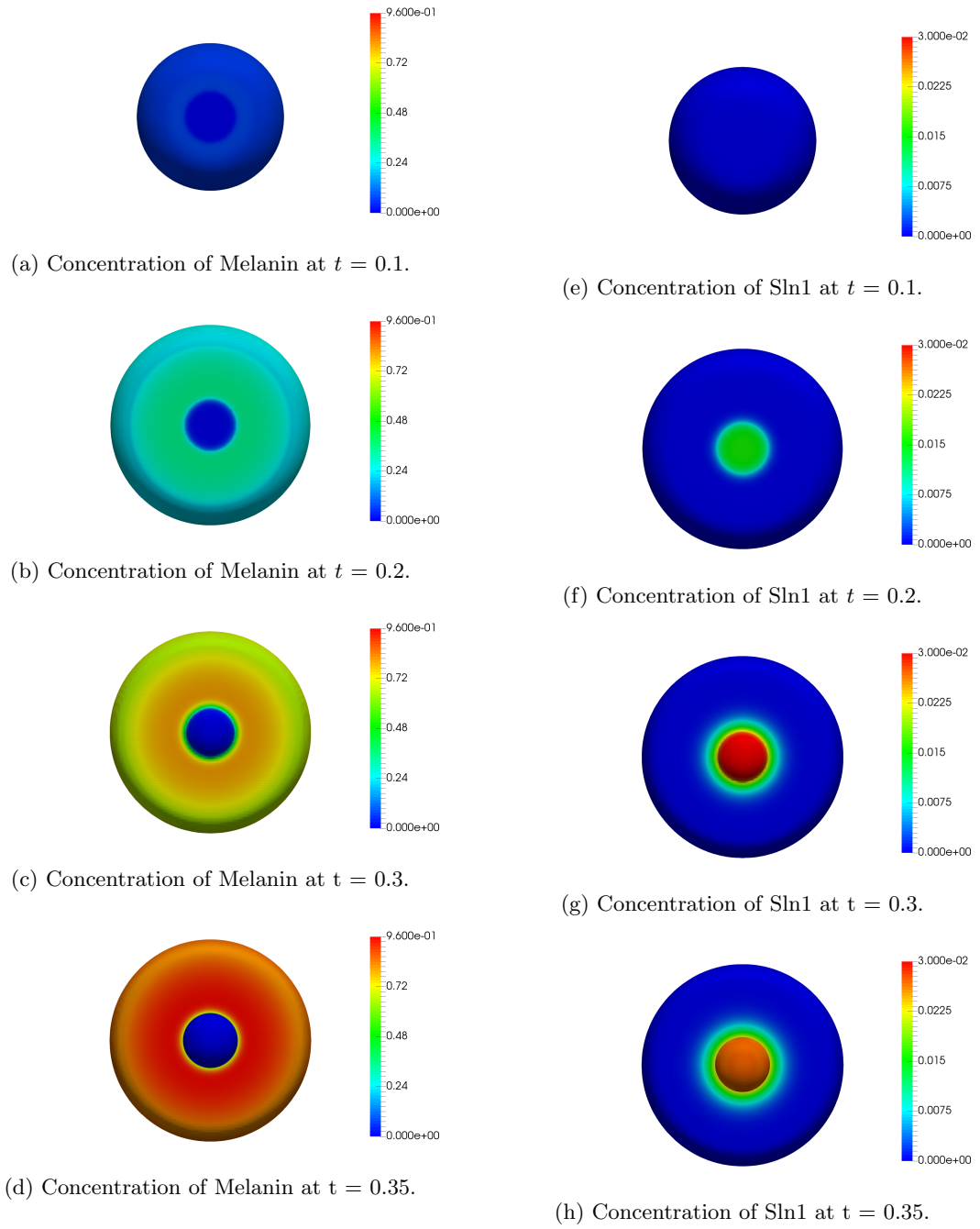


Figure 4.18: Surface simulation for phase field framework, pore area: Melanin and Sln1.

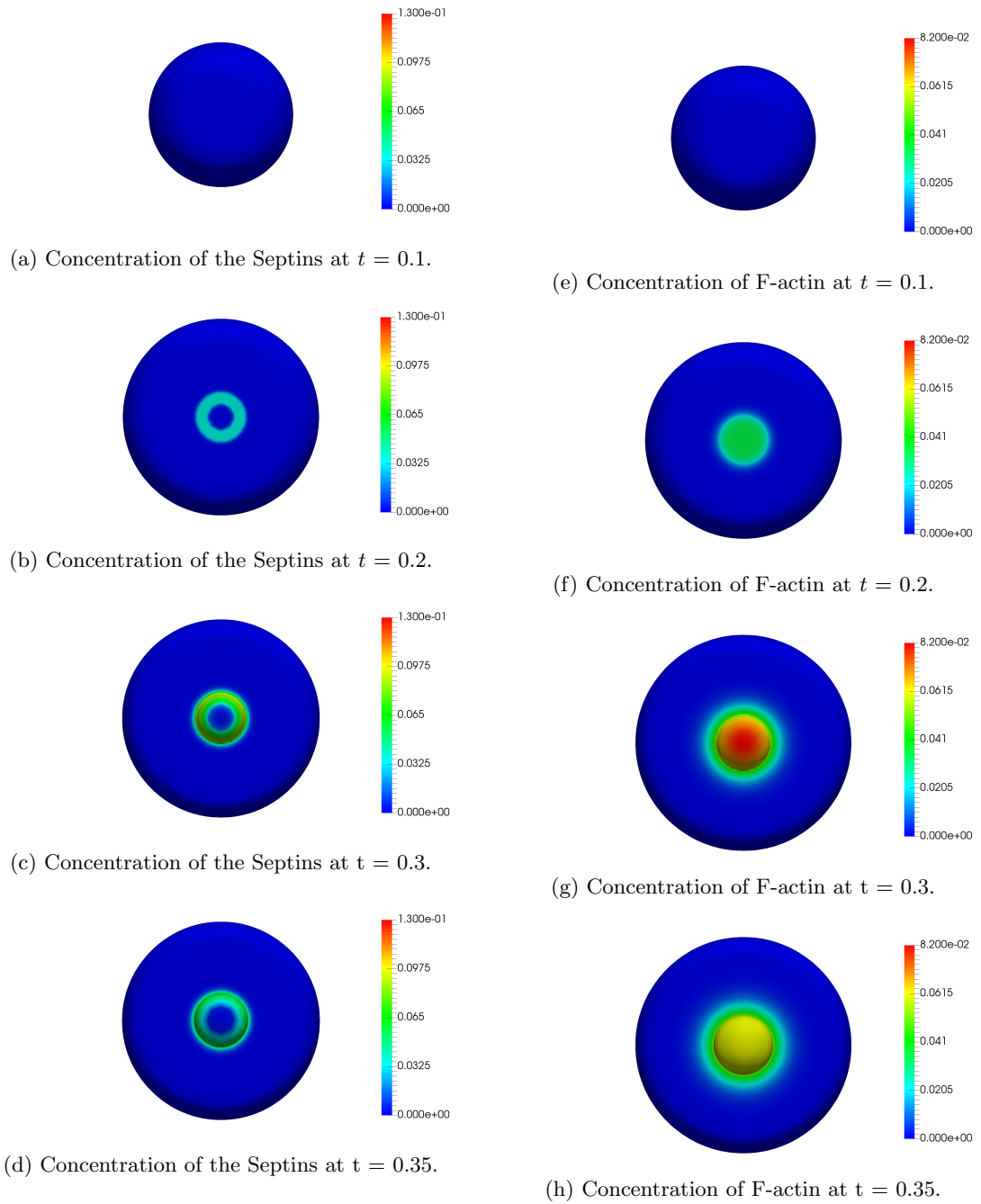


Figure 4.19: Surface simulation for phase field framework, pore area: Septins and F-actin.



(a) Fungus at $t = 0.25$.



(b) Fungus at $t = 0.275$.



(c) Fungus at $t = 0.3$.



(d) Fungus at $t = 0.35$.

Figure 4.20: Surface simulation for phase field framework. Fungus peg formation $\Phi^n = 0$ level set surface at times around the leaf breaking and peg forming.

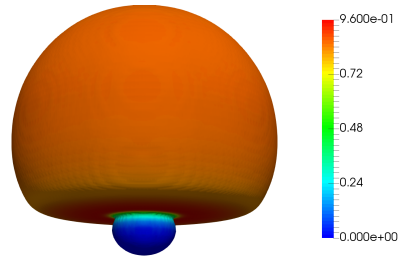
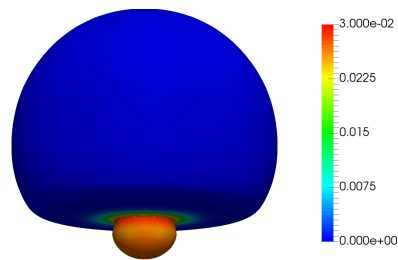
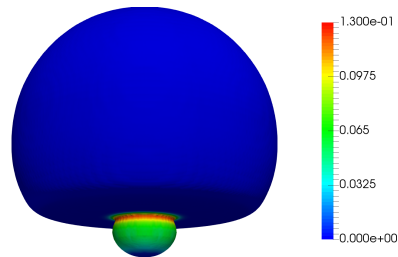
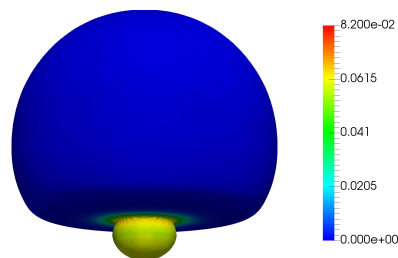
(a) Concentration of Melanin at $t = 0.35$.(b) Concentration of Sln1 at $t = 0.35$.(c) Concentration of the Septins at $t = 0.35$.(d) Concentration of F-actin at $t = 0.35$.

Figure 4.21: Full simulation for phase field framework, $x-z$ cross section. Concentrations of the molecular species on the $\Phi^n = 0$ level set at $t = 0.35$.

Chapter 5

Conclusion

5.1 Summary

In this thesis we began by introducing topics on the mean curvature flow of hypersurfaces and partial differential equations defined on hypersurfaces. In Chapter 2 we introduced the phase field approximation to mean curvature flow, specifically the introduction of the double obstacle potential, and the finite element discretisation of the phase field approach. We then followed [44, 63] and state a diffuse interface approximation to SADEs together with a finite element approximation. We showed experimental order of convergence for a diffusion-dominated example and then explored an advection-dominated example. In doing this we saw that, as the diffusion constant became smaller, instabilities occurred across the profile of the finite element diffuse interface numerical solution. This motivated us to introduce and derive a finite volume approximation to the diffuse interface approach with upwinding and we demonstrated that, for advection-dominated equations, the finite volume approximation errors were an improvement on the equivalent errors resulting from the finite element approximation. As the diffusion constant became smaller both approximations suffered from profile spiking near the edge of the interfacial region, and so we followed the authors in [63] and introduced edge smoothing in the form of streamline diffusion for the finite element approximation. This solved the profile spiking problem for the finite element approximation but did not solve the appearance of instabilities, and, although the profile looks better, the errors were worse. As in [63] we then considered an application where the velocity law of the surface satisfied mean curvature flow and so coupled the diffuse interface approximation to SADEs to the double obstacle phase

field approximation to mean curvature flow. We again considered a advection-dominant example to demonstrate that even when the surface is a finite element approximation, the finite element approximation to the SADE still has bad instabilities and the finite volume approximation performed much better but also still has large profile spiking.

In Chapter 3 we introduced curve shortening flow for closed curves and for curves attached to some fixed boundary orthogonally. We extended the semi-discrete finite element bounds for curve shortening flow attached to some fixed boundary orthogonally in [42] to the fully discrete setting in Theorems 3.13 and 3.18.

Theorem.

Let $\vec{X}^0 = I^h \vec{x}^0 \in [S^h]^2$. There exists $h^* > 0$ and $\Delta t^* > 0$ such that for all $h \in (0, h^*]$ and $\Delta t \in (0, \Delta t^*]$, with $\Delta t \leq Ch^2$, the fully-discrete problem (3.3.5a)-(3.3.5b) has the following error bounds

$$\sup_{n=0, \dots, N} |\vec{x}^n - \vec{X}^n|_1^2 + \sum_{n=1}^N \Delta t_n |\vec{x}_t^n - D_t \vec{X}^n|_0^2 \leq Ch^2,$$

$$\sup_{n=0, \dots, N} |\vec{x}^n - \vec{X}^n|_0^2 \leq Ch^4,$$

for some $C > 0$ independent of h and Δt .

We also extended the same semi-discrete finite element bounds in [42] for curve shortening flow attached to some fixed boundary orthogonally to be coupled to a reaction-diffusion equation on the curve in Theorem 3.23.

Theorem.

Let $\vec{x}^h(\cdot, 0) = I^h \vec{x}^0(\cdot) \in [S^h]^2$ and $w^h(\cdot, 0) = I^h w^0(\cdot) \in S^h$. There exists $h^* > 0$ such that for all $h \in (0, h^*]$, the semi-discrete problem (3.4.5a)-(3.4.5c) has the following error bounds

$$\sup_{t \in [0, T]} \left[|\vec{x}(\cdot, t) - \vec{x}^h(\cdot, t)|_1^2 + |w(\cdot, t) - w^h(\cdot, t)|_0^2 \right]$$

$$+ \int_0^T |\vec{x}_t(\cdot, t) - \vec{x}_t^h(\cdot, t)|_0^2 + |w(\cdot, t) - w^h(\cdot, t)|_1^2 dt \leq Ch^2,$$

for some $C > 0$ independent of h .

We closed this chapter by deriving a Newton's scheme for the non-linear implicit boundary conditions and demonstrated its superiority compared to the scheme introduced in [42] for a similar problem.

In Chapter 4 we introduced the rice blast model as presented in [102]. We simplified the model from an evolving surface to an evolving curve and used the parametric framework to

produce a simulation matching [102]. We made further simplifications to only consider the pore area of the fungus and used the Newton's scheme derived in the Chapter 3. We then derived a diffuse interface approximation of the SRDEs the molecular species satisfied for a curve approximation and the surface approximation and showed two dimensional simulations which matched our parametric model for curves as well as three dimensional simulations that matched the surface model in [102].

5.2 Future work

We finalise this thesis with possible directions for future research. This list is by no means exhaustive of the possibilities arising from the research conducted, but rather those that follow as a simple continuation.

- Investigate the edge smoothing analysis for the finite volume approximation of the diffuse interface approach;
- Prove stability results and error bounds for the finite volume approximation of the diffuse interface approach;
- Extend the finite volume approximation of the diffuse interface approximation of SPDEs on evolving curves to evolving surfaces;
- Investigate other numerical tools for advection-dominated PDEs, like the discontinuous Galerkin method, in the diffuse interface approximation setting;
- Extend the finite element error analysis used to prove Theorem 3.13 and Theorem 3.23 to prove fully discrete finite element error bounds for **Model** \mathcal{M}_2 , similar to those obtained in [6];
- Generalise the fixed boundary conditions to hold on surfaces;
- Generalise the fixed boundary conditions so that one can consider an evolving curve attached orthogonally to an evolving boundary;
- Retract the assumption that the diffusion constants in the diffuse interface approximation to the rice blast model in Section 4.3 are independent of the Septins and reduce their values closer to the values set in [102];

- Retract the assumption that the ring structure in the diffuse interface approximation to the rice blast model in Section 4.3 is stationary.

This work has been difficult but very rewarding. I look forward to continuing to do research for as long as is admissable. I gratefully acknowledge the support of the EPSRC grant 1805391. This concludes the thesis.

Appendix A

Geometric definitions and operators

We follow the definitions introduced in [14, 41].

Definition A.1 ($C^{2,1}$ -family of hypersurfaces).

A family $(\Gamma(t))_{t \in (0, T)}$ is called a $C^{2,1}$ -family of hypersurfaces if, for each $(\vec{p}, t) \in \mathbb{R}^{n+1} \times (0, T)$ with $\vec{p} \in \Gamma(t)$, there exists an open set $U \subset \mathbb{R}^{n+1}$, $\delta > 0$ and a function $u \in C^{2,1}(U \times (t - \delta, t + \delta))$ such that

$$U \cap \Gamma(t) = \{\vec{p} \in U : u(\vec{p}, t) = 0\} \quad \text{and} \quad \nabla u(\vec{p}, t) \neq 0 \quad \forall \vec{p} \in U \cap \Gamma(t).$$

Note. $C^{2,1}$ -family of hypersurfaces will be referred to as a family of hypersurfaces or simply hypersurface, depending on the context.

Definition A.2 (Tangent space).

The *tangent space* to a hypersurface Γ is the n -dimensional linear subspace of \mathbb{R}^{n+1} that is orthogonal to $\nabla u(\vec{p})$, denoted $T_x \Gamma$.

Definition A.3 (Orientable hypersurface).

A hyperspace $\Gamma \subset \mathbb{R}^{n+1}$ is called *orientable* if there exists a vector field $\vec{\nu} \in C^1(\mathbb{R}^{n+1})$ such that

$$\vec{\nu}(\vec{p}) \perp T_x \Gamma \quad \text{and} \quad |\vec{\nu}(\vec{p})| = 1, \quad \forall \vec{p} \in \Gamma.$$

Definition A.4 (Tangential derivative).

Let f be a function that is differentiable in an open neighbourhood of a hypersurface Γ . Then, for $\vec{p} \in \Gamma$, the *tangential derivative* of f is characterised as

$$\nabla_{\Gamma} f(\vec{p}) = \nabla f(\vec{p}) - \langle \nabla f(\vec{p}), \vec{\nu}(\vec{p}) \rangle \vec{\nu}(\vec{p})$$

where ∇ is the standard derivative in \mathbb{R}^{n+1} , $\langle \cdot, \cdot \rangle$ is the standard scalar product in \mathbb{R}^{n+1} and $\vec{\nu}$ is the outward pointing unit normal to Γ .

Note. If $n = 1$ then this can also be written as $\nabla_{\Gamma} f(\vec{p}) = \langle \nabla f(\vec{p}), \vec{\tau} \rangle \vec{\tau}$, if $\vec{\tau} := \vec{\nu}^{\perp}$.

Definition A.5 (Tangential divergence).

Let \vec{v} be a vector function whereby its components v_i are differentiable in an open neighbourhood of a hypersurface Γ . Then, for $\vec{p} \in \Gamma$, the *tangential divergence* of \vec{v} is characterised as

$$\operatorname{div}_{\Gamma} \vec{v}(\vec{p}) = \operatorname{div} \vec{v}(\vec{p}) - \langle \nabla \langle \vec{v}(\vec{p}), \vec{\nu}(\vec{p}) \rangle, \vec{\nu}(\vec{p}) \rangle.$$

Note. If $n = 1$ then this can also be written as $\operatorname{div}_{\Gamma} \vec{v}(\vec{p}) = \langle (\vec{\tau}(\vec{p}) \otimes \vec{\tau}(\vec{p})) \nabla, \vec{v}(\vec{p}) \rangle$.

Definition A.6 (Mean curvature).

Let Γ be a hypersurface with outward pointing unit normal $\vec{\nu}$. Then, for $\vec{p} \in \Gamma$, the mean curvature of Γ at a point \vec{p} is defined as

$$\kappa(\vec{p}) = -\operatorname{div}_{\Gamma} \vec{\nu}(\vec{p}).$$

Definition A.7 (Laplace-Beltrami operator).

Let f be a function that is twice differentiable in an open neighbourhood of a hypersurface Γ . Then, for $\vec{p} \in \Gamma$, the *Laplace-Beltrami* of f is characterised as

$$\Delta_{\Gamma} f(\vec{p}) = \operatorname{div}_{\Gamma}(\nabla_{\Gamma} f(\vec{p})).$$

Note. It is easy to show that Δ_{Γ} can also be computed by $\Delta_{\Gamma} f(\vec{p}) = \operatorname{div}(\nabla_{\Gamma} f(\vec{p}))$.

Appendix B

Notable analysis results

B.1 Informal derivation of (2.2.9)

In this section we look to derive the weak form of (2.2.2a) with (2.2.7) in an informal manner using the subdifferential

$$B(s) := \begin{cases} (-\infty, 0] & s = -1, \\ 0 & |s| < 1, \\ [0, \infty) & s = 1. \end{cases}$$

First we prove the formula for the subdifferential is indeed the one above, and then we proceed with the informal derivation of the weak form of (2.2.2a) with (2.2.7).

B.1.1 Derivation of subdifferential B

We first begin with the definition of a subdifferential of a function and a useful property [68].

Definition B.1 (Subdifferential).

A *subgradient* of a function $f : \mathbb{R} \rightarrow (-\infty, \infty]$, $f \not\equiv \infty$, at the point $x_0 \in \mathbb{R}$ is a value $\xi \in \mathbb{R}$ such that

$$f(x) \geq f(x_0) + \xi(x - x_0), \quad \forall x \in \mathbb{R}. \quad (\text{B.1.1})$$

The set $\partial f(x_0)$ of all such values is called the *subdifferential* of f at the point x_0 .

Proposition B.2.

Let $f : \mathbb{R} \rightarrow (-\infty, \infty]$ be a convex function that is differentiable at the point $x_0 \in$

int dom(f). Then $\partial f(x_0) = \{f'(x_0)\}$.

We now look to derive the subdifferential B . Consider

$$f(x) = \frac{1}{2}(1 - x^2) + \mathbb{I}_{[-1,1]}(x)$$

where

$$\mathbb{I}_{[-1,1]}(x) := \begin{cases} 0 & |x| \leq 1, \\ \infty & |x| > 1. \end{cases}$$

We see that $\text{dom}(f) = [-1, 1]$ and $\text{int dom}(f) = (-1, 1)$. We split the calculation of the subdifferential into three cases:

Case 1: Consider $x_0 \in (-1, 1)$. Since f is convex and differentiable, using Proposition B.2 we see that $\partial f(x_0) = \{-x_0\}$.

Case 2: Consider $x_0 = 1$, then for $x \in [-1, 1]$, using (B.1.1), we have

$$\frac{1}{2}(1 - x^2) \geq \xi(x - 1) \quad \Leftrightarrow \quad \xi \geq \frac{1}{2} \frac{(1 - x^2)}{x - 1} = -\frac{1}{2}(1 + x) \quad \forall x \in [-1, 1].$$

This implies that $\partial f(1) = [-1, \infty)$.

Case 3: Consider $x_0 = -1$, then for $x \in [-1, 1]$, using (B.1.1), we have

$$\frac{1}{2}(1 - x^2) \geq \xi(x + 1) \quad \Leftrightarrow \quad \xi \leq \frac{1}{2} \frac{(1 - x^2)}{x + 1} = \frac{1}{2}(1 - x) \quad \forall x \in [-1, 1].$$

This implies that $\partial f(-1) = (-\infty, 1]$.

Hence, $\forall x_0 \in \mathbb{R}$ we have that

$$\partial f(x_0) = \begin{cases} -x_0 & |x_0| < 1, \\ [-1, \infty) & x_0 = 1, \\ [-\infty, 1] & x_0 = -1, \\ \emptyset & |x_0| > 1, \end{cases}$$

and so it not hard to deduce, with $\partial f(x_0) := W'(x_0) = -x_0 + B(x_0)$, the definition of B from here.

B.1.2 Derivation of variational inequality (2.2.9)

Now that we have derived B , we can continue with the informal derivation of (2.2.9). Indeed, multiplying (2.2.2a) by $\xi - \varphi$, where $\xi \in \mathcal{K}$, and using integration by parts as well

as (2.2.2b), noting informally that $W'(s) = -s + B(s)$, we have

$$\varepsilon(\varphi_t, \xi - \varphi) + \varepsilon(\nabla\varphi, \nabla\xi - \nabla\varphi) - \frac{1}{\varepsilon}(\varphi, \xi - \varphi) = -\frac{1}{\varepsilon}(B(\varphi), \xi - \varphi), \quad \forall \xi \in \mathcal{K}.$$

We can split the integral on the right-hand side into three cases:

Case 1: Set $\varphi = 1$.

- (a) Set $\xi = 1$. Then $\xi - \varphi = 0$ and therefore $B(\varphi)(\xi - \varphi) = 0$.
- (b) Set $-1 \leq \xi < 1$. Since $\xi - \varphi < 0$ and $B(\varphi) \geq 0$ then $B(\varphi)(\xi - \varphi) \leq 0$.

Case 2: Set $\varphi = -1$.

- (a) Set $\xi = -1$. Then $\xi - \varphi = 0$ and therefore $B(\varphi)(\xi - \varphi) = 0$.
- (b) Set $-1 < \xi \leq 1$. Since $\xi - \varphi > 0$ and $B(\varphi) \leq 0$ then $B(\varphi)(\xi - \varphi) \leq 0$.

Case 3: set $|\varphi| < 1$. Then $B(\varphi) = 0$ and therefore $B(\varphi)(\xi - \varphi) = 0$.

Thus, since $B(\varphi)(\xi - \varphi) \leq 0, \forall \xi \in \mathcal{K}$, we arrive at (2.2.9).

B.2 Proof of coarea approximation (2.3.7)

In this section we look to derive the approximation (2.3.7). We first begin with the definition of the coarea from [68].

Definition B.3 (Coarea formula).

Let $u : \mathbb{R}^n \rightarrow \mathbb{R}$ be Lipschitz continuous and assume that for a.e. $r \in \mathbb{R}$ the level set

$$\{x \in \mathbb{R}^n : u(x) = r\}$$

is a smooth, $(n - 1)$ dimensional hypersurface in \mathbb{R}^n . Suppose also that $f : \mathbb{R}^n \rightarrow \mathbb{R}$ is continuous and $f \in L^1(\mathbb{R}^n)$. Then,

$$\int_{\mathbb{R}^n} f |\nabla u| dx = \int_{-\infty}^{\infty} \left(\int_{\{u=r\}} f dS \right) dr. \quad (\text{B.2.1})$$

From the definition, we set $f := \xi \rho_\varepsilon$ and $u := \phi$, where $\xi \in L^1(\Omega)$, $\phi \in C^{2,1}(\Omega \times [0, T])$ and $\rho_\varepsilon \in C^{1,1}(\Omega \times [0, T])$. Noting that $\rho_\varepsilon(\cdot, t) = 0$ in $\mathbb{R}^n \setminus \Omega$ and (2.3.3), we have

$$\int_{\Omega} \xi(\cdot) \rho_\varepsilon(\cdot, t) |\nabla \phi(\cdot, t)| dx = \int_{\mathbb{R}^n} \xi(\cdot) \rho_\varepsilon(\cdot, t) |\nabla \phi(\cdot, t)| dx$$

$$\begin{aligned}
&= \int_{-\infty}^{\infty} \left(\int_{\{\phi(\cdot, t)=r\}} \xi(\cdot) \rho_{\varepsilon}(\cdot, t) dS \right) dr \\
&= \int_{-\frac{\varepsilon\pi}{2}}^{\frac{\varepsilon\pi}{2}} \left(\int_{\{\phi(\cdot, t)=r\}} \xi(\cdot) g\left(\frac{r}{\varepsilon}\right) dS \right) dr \\
&= \int_{-\frac{\varepsilon\pi}{2}}^{\frac{\varepsilon\pi}{2}} g\left(\frac{r}{\varepsilon}\right) I(r) dr,
\end{aligned}$$

where

$$I(r) := \int_{\{\phi(\cdot, t)=r\}} \xi(\cdot) dS.$$

Using a standard trapezium quadrature rule

$$\int_a^b f(x) dx \approx \frac{1}{2}(b-a)f(x),$$

for some $x \in (a, b)$, we conclude that

$$\int_{\Omega} \xi(\cdot) \rho_{\varepsilon}(\cdot, t) |\nabla \phi(\cdot, t)| dx \approx \frac{1}{2} \left(\frac{\varepsilon\pi}{2} + \frac{\varepsilon\pi}{2} \right) g(0) I(0) = \frac{\varepsilon\pi}{2} \int_{\{\phi(\cdot, t)=0\}} \xi(\cdot) dS.$$

B.3 Useful theorems

Theorem B.4 (Cayley-Hamilton Theorem in $\mathbb{R}^{2 \times 2}$, [16]).

Given $M \in \mathbb{R}^{2 \times 2}$ and let $I \in \mathbb{R}^{2 \times 2}$ be the identity matrix. Given λ that satisfies

$$\det(M - \lambda I) = \lambda^2 - \text{Tr}(M)\lambda + \det(M) = 0,$$

then M satisfies

$$M^2 - \text{Tr}(M)M + \det(M)I = \underline{0},$$

where $\underline{0} = 0I$.

Theorem B.5.

Let $T \in \mathbb{R}^{2 \times 2}$ be idempotent and let $M \in \mathbb{R}^{2 \times 2}$ satisfy $I + \beta T = M$, for $\beta \in \mathbb{R} \setminus \{-1\}$.

Then the inverse of M is

$$M^{-1} = I - \frac{\beta}{1 + \beta} T.$$

Proof: Utilising the fact that T is idempotent, we see that

$$\frac{1}{\beta}(M - I) = T = T^2 = \frac{1}{\beta^2}(M - I)^2 = \frac{1}{\beta^2}(M^2 - 2M + I)$$

Rearranging we see that

$$I = \frac{1}{1 + \beta} M((2 + \beta)I - M).$$

Hence, due to the definition of an inverse, we see that

$$M^{-1} = \frac{1}{1+\beta}((2+\beta)I - M) = \frac{1}{1+\beta}(2I + \beta I - I - \beta T) = I - \frac{\beta}{1+\beta}T.$$

□

Theorem B.6 (Sobolev Embedding, [68]).

Let $U \subset \mathbb{R}^n$ be bounded and open, with a C^1 boundary. Assume $u \in W^{k,p}(U)$.

1. If $k < \frac{n}{p}$, then $u \in L^q(U)$ where $\frac{1}{q} = \frac{1}{p} - \frac{k}{n}$. In addition we have the estimate

$$\|u\|_{L^q(U)} \leq C\|u\|_{W^{k,p}(U)},$$

where C depends only on k, p, n and U , i.e. $W^{k,p}(U) \hookrightarrow L^q(U)$.

2. if $k > \frac{n}{p}$, then $u \in C^{k - [\frac{n}{p}] - 1, \gamma}(\bar{U})$, where

$$\gamma = \begin{cases} [\frac{n}{p}] + 1 - \frac{n}{p} & \text{if } \frac{n}{p} \text{ is not an integer} \\ \text{any positive number} < 1 & \text{if } \frac{n}{p} \text{ is an integer} \end{cases}$$

and

$$[x] = \begin{cases} [x] & \text{if the decimal digit is } \leq 5 \\ \lceil x \rceil & \text{if the decimal digit is } > 5. \end{cases}$$

In addition we have the estimate

$$\|u\|_{C^{k - [\frac{n}{p}] - 1, \gamma}(\bar{U})} \leq C\|u\|_{W^{k,p}(U)},$$

where C depends only on k, p, n, γ and U , i.e. $W^{k,p}(U) \hookrightarrow C^{k - [\frac{n}{p}] - 1, \gamma}(\bar{U})$.

B.4 Fully discrete results

Lemma B.1.

For some for $\mu > 0$, we have

$$\begin{aligned} e^{-\mu t_n} |\vec{E}^n|_0^2 + \frac{\mu}{2} \sum_{m=1}^n \Delta t_m e^{-\mu t_m} |\vec{E}^{m-1}|_0^2 \\ \leq \sum_{m=1}^n \left(\mu (\Delta t_m)^2 + \frac{4}{\mu} \right) \Delta t_m e^{-\mu t_m} |D_t \vec{E}^m|_0^2. \end{aligned} \quad (\text{B.4.1})$$

Furthermore, if $\mu \Delta t \leq \frac{1}{2}$, we have

$$\frac{\mu}{2} \sum_{m=1}^n \Delta t_m e^{-\mu t_{m-1}} |\vec{E}^{m-1}|_0^2 \leq 2 \sum_{m=1}^n \left(\mu (\Delta t_m)^2 + \frac{4}{\mu} \right) \Delta t_m e^{-\mu t_m} |D_t \vec{E}^m|_0^2. \quad (\text{B.4.2})$$

Proof: Firstly, we note that for $\mu > 0$

$$\Delta t_n D_t e^{-\mu t_n} = e^{-\mu t_n} - e^{-\mu t_{n-1}} = e^{-\mu t_n} (1 - e^{\mu \Delta t_n}) \leq -\mu \Delta t_n e^{-\mu t_n}, \quad (\text{B.4.3})$$

and

$$-\Delta t_m D_t e^{-\mu t_m} = e^{-\mu t_{m-1}} - e^{-\mu t_m} = e^{-\mu t_{m-1}} (1 - e^{-\mu \Delta t_m}) \leq \mu \Delta t_m e^{-\mu t_{m-1}}. \quad (\text{B.4.4})$$

Consequently, using (B.4.3), since $|E^0| = 0$, we have

$$\begin{aligned} e^{-\mu t_n} |\vec{E}^n|_0^2 &= \sum_{m=1}^n \Delta t_m D_t \left[e^{-\mu t_m} |\vec{E}^m|_0^2 \right] \\ &= \sum_{m=1}^n \left[\Delta t_m e^{-\mu t_m} D_t |\vec{E}^m|_0^2 + \Delta t_m |\vec{E}^{m-1}|_0^2 D_t e^{-\mu t_m} \right] \\ &\leq \sum_{m=1}^n \left[\Delta t_m e^{-\mu t_m} D_t |\vec{E}^m|_0^2 - \mu \Delta t_m e^{-\mu t_m} |\vec{E}^{m-1}|_0^2 \right]. \end{aligned} \quad (\text{B.4.5})$$

Using (3.1.10) we have

$$\begin{aligned} |\vec{E}^m|_0^2 - |\vec{E}^{m-1}|_0^2 &= \int_{\mathcal{I}} \left[|\vec{E}^m|^2 - |\vec{E}^{m-1}|^2 \right] d\rho \\ &\leq \int_{\mathcal{I}} 2 |\vec{E}^m| \left[|\vec{E}^m| - |\vec{E}^{m-1}| \right] d\rho \\ &\leq \int_{\mathcal{I}} \frac{\delta}{2} \Delta t_m |\vec{E}^m|^2 + \frac{2}{\delta} \Delta t_m |D_t \vec{E}^m|^2 d\rho \\ &\leq \frac{\delta}{2} \Delta t_m |\vec{E}^m|_0^2 + \frac{2}{\delta} \Delta t_m |D_t \vec{E}^m|_0^2. \end{aligned} \quad (\text{B.4.6})$$

Setting $\delta = \frac{1}{\Delta t_m}$ in (B.4.6) we see that

$$|\vec{E}^m|_0^2 \leq 2 |\vec{E}^{m-1}|_0^2 + 4 (\Delta t_m)^2 |D_t \vec{E}^m|_0^2, \quad (\text{B.4.7})$$

while setting $\delta = \frac{\mu}{2}$ in (B.4.6) and using (B.4.7) we have

$$\Delta t_m D_t |\vec{E}^m|_0^2 \leq \frac{\mu}{4} \Delta t_m |\vec{E}^m|_0^2 + \frac{4}{\mu} \Delta t_m |D_t \vec{E}^m|_0^2. \quad (\text{B.4.8})$$

Thus, from (B.4.5) and (B.4.8), we have that

$$e^{-\mu t_n} |\vec{E}^n|_0^2 + \frac{\mu}{2} \sum_{m=1}^n \Delta t_m e^{-\mu t_m} |\vec{E}^{m-1}|_0^2 \leq \sum_{m=1}^n \left(\mu (\Delta t_m)^2 + \frac{4}{\mu} \right) \Delta t_m e^{-\mu t_m} |D_t \vec{E}^m|_0^2.$$

Furthermore, using (B.4.4) and (B.4.1), we see that

$$\begin{aligned} \frac{\mu}{2} \sum_{m=1}^n \Delta t_m e^{-\mu t_{m-1}} |\vec{E}^{m-1}|_0^2 &= \frac{\mu}{2} \sum_{m=1}^n \Delta t_m e^{-\mu t_m} |\vec{E}^{m-1}|_0^2 \\ &\quad + \frac{\mu}{2} \sum_{m=1}^n \Delta t_m [e^{-\mu t_{m-1}} - e^{-\mu t_m}] |\vec{E}^{m-1}|_0^2 \\ &\leq \sum_{m=1}^n \left(\mu (\Delta t_m)^2 + \frac{4}{\mu} \right) \Delta t_m e^{-\mu t_m} |D_t \vec{E}^m|_0^2 \end{aligned}$$

$$+ \frac{\mu}{2} \sum_{m=1}^n \mu (\Delta t_m)^2 e^{-\mu t_{m-1}} |\vec{E}^{m-1}|_0^2.$$

Thus, provided $\mu \Delta t \leq \frac{1}{2}$, we have

$$\frac{\mu}{2} \sum_{m=1}^n \Delta t_m e^{-\mu t_{m-1}} |\vec{E}^{m-1}|_0^2 \leq 2 \sum_{m=1}^n \left(\mu (\Delta t_m)^2 + \frac{4}{\mu} \right) \Delta t_m e^{-\mu t_m} |D_t \vec{E}^m|_0^2.$$

□

Bibliography

- [1] C. J. Alexopoulos, C. W. Mims, and M. Blackwell. *Introductory mycology*. Number Ed. 4. John Wiley and Sons, 1996. [138](#)
- [2] S. M. Allen and J. W. Cahn. A microscopic theory for antiphase boundary motion and its application to antiphase domain coarsening. *Acta metallurgica*, 27(6):1085–1095, 1979. [17](#)
- [3] G. Aubert and P. Kornprobst. *Mathematical problems in image processing: partial differential equations and the calculus of variations*, volume 147. Springer Science & Business Media, 2006. [3](#)
- [4] R. Barreira, C. M. Elliott, and A. Madzvamuse. The surface finite element method for pattern formation on evolving biological surfaces. *Journal of mathematical biology*, 63(6):1095–1119, 2011. [11](#)
- [5] R. Barreira and A. Madzvamuse. Domain-growth-induced patterning for reaction-diffusion systems with linear cross-diffusion. *Discrete & Continuous Dynamical Systems-B*, 23(7):2775–2801, 2018. [11](#)
- [6] J. W. Barrett, K. Deckelnick, and V. Styles. Numerical analysis for a system coupling curve evolution to reaction diffusion on the curve. *SIAM Journal on Numerical Analysis*, 55(2):1080–1100, 2017. [12](#), [13](#), [78](#), [79](#), [83](#), [86](#), [102](#), [112](#), [126](#), [135](#), [153](#), [186](#)
- [7] J. W. Barrett, K. Deckelnick, and V. Styles. A practical phase field method for an elliptic surface pde. *arXiv preprint arXiv:2002.07504*, 2020. [28](#)
- [8] J. W. Barrett, H. Garcke, and R. Nürnberg. On the variational approximation of combined second and fourth order geometric evolution equations. *SIAM Journal on Scientific Computing*, 29(3):1006–1041, 2007. [71](#), [72](#)

- [9] J. W. Barrett, H. Garcke, and R. Nürnberg. A parametric finite element method for fourth order geometric evolution equations. *Journal of Computational Physics*, 222(1):441–467, 2007. [71](#)
- [10] J. W. Barrett, H. Garcke, and R. Nürnberg. On the parametric finite element approximation of evolving hypersurfaces in \mathbb{R}^3 . *Journal of Computational Physics*, 227(9):4281–4307, 2008. [71](#)
- [11] J. W. Barrett, H. Garcke, and R. Nürnberg. The approximation of planar curve evolutions by stable fully implicit finite element schemes that equidistribute. *Numerical Methods for Partial Differential Equations*, 27(1):1–30, 2011. [xii](#), [72](#), [73](#), [74](#), [75](#), [77](#), [82](#)
- [12] J. W. Barrett, H. Garcke, and R. Nürnberg. Phase field models versus parametric front tracking methods: Are they accurate and computationally efficient? *Communications in Computational Physics*, 15(2):506–555, 2014. [5](#)
- [13] J. W. Barrett, H. Garcke, and R. Nürnberg. On the stable numerical approximation of two-phase flow with insoluble surfactant. *ESAIM: Mathematical modelling and numerical analysis*, 49(2):421–458, 2015. [10](#)
- [14] J. W. Barrett, H. Garcke, and R. Nürnberg. Parametric finite element approximations of curvature driven interface evolutions. *Handbook of Numerical Analysis*, 21(4):275–424, 2020. [188](#)
- [15] G. Bellettini, M. Paolini, and C. Verdi. Γ -convergence of discrete approximations to interfaces with prescribed mean curvature. *Atti della Accademia Nazionale dei Lincei. Classe di Scienze Fisiche, Matematiche e Naturali. Rendiconti Lincei. Matematica e Applicazioni*, 1(4):317–328, 1990. [19](#)
- [16] R. Bhatia. *Matrix analysis*, volume 169. Springer Science & Business Media, 2013. [193](#)
- [17] K. N. Blazakis, A. Madzvamuse, C. C. Reyes-Aldasoro, V. Styles, and C. Venkataraman. An optimal control approach to cell tracking. 2014. [3](#)
- [18] J. F. Blowey and C. M. Elliott. The cahn–hilliard gradient theory for phase separation with non-smooth free energy part i: Mathematical analysis. *European Journal of Applied Mathematics*, 2(3):233–280, 1991. [21](#)

- [19] J. F. Blowey and C. M. Elliott. The cahn–hilliard gradient theory for phase separation with non-smooth free energy part ii: numerical analysis. *European Journal of Applied Mathematics*, 3(2):147–179, 1992. [22](#)
- [20] J. F. Blowey and C. M. Elliott. Curvature dependent phase boundary motion and parabolic double obstacle problems. In *Degenerate Diffusions*, pages 19–60. Springer, 1993. [18](#)
- [21] T. M. Bourett and R. J. Howard. In vitro development of penetration structures in the rice blast fungus magnaporthe grisea. *Canadian Journal of Botany*, 68(2):329–342, 1990. [139](#), [140](#)
- [22] Dietrich Braess. *Finite elements: Theory, fast solvers, and applications in solid mechanics*. Cambridge University Press, 2007. [33](#)
- [23] H. M. Byrne and M. A. J. Chaplain. Free boundary value problems associated with the growth and development of multicellular spheroids. *European Journal of Applied Mathematics*, 8(6):639–658, 1997. [11](#)
- [24] G. Caginalp. An analysis of a phase field model of a free boundary. *Archive for Rational Mechanics and Analysis*, 92(3):205–245, 1986. [17](#)
- [25] G. Caginalp and X. Chen. Convergence of the phase field model to its sharp interface limits. *European Journal of Applied Mathematics*, 9(4):417–445, 1998. [17](#)
- [26] J. W. Cahn, P. Fife, and O. Penrose. A phase-field model for diffusion-induced grain-boundary motion. *Acta Materialia*, 45(10):4397–4413, 1997. [3](#)
- [27] J. W. Cahn and J. E. Hilliard. Free energy of a nonuniform system. i. interfacial free energy. *The Journal of chemical physics*, 28(2):258–267, 1958. [17](#)
- [28] Zhiqiang Cai. On the finite volume element method. *Numerische Mathematik*, 58(1):713–735, 1990. [36](#)
- [29] X. Chen and C. M. Elliott. Asymptotics for a parabolic double obstacle problem. *Proceedings of the Royal Society of London. Series A: Mathematical and Physical Sciences*, 444(1922):429–445, 1994. [20](#)
- [30] X. Chen, C. M. Elliott, A. Gardiner, and J. Jing Zhao. Convergence of numerical solutions to the allen–cahn equation. *Applicable analysis*, 69(1-2):47–56, 1998. [19](#)

- [31] F. G. Chumley and B. Valent. Genetic analysis of melanin-deficient, nonpathogenic mutants of *magnaporthe grisea*. *Mol. Plant-Microbe Interact*, 3(3):135–143, 1990. [139](#)
- [32] P. G. Ciarlet. *The finite element method for elliptic problems*, volume 40. Siam, 2002. [29](#), [33](#), [64](#)
- [33] Bernardo Cockburn, George E Karniadakis, and Chi-Wang Shu. *Discontinuous Galerkin methods: theory, computation and applications*, volume 11. Springer Science & Business Media, 2012. [173](#)
- [34] M. M. Cox, A. L. Lehninger, and D. L. Nelson. *Lehninger principles of biochemistry*. Macmillan, 2008. [143](#)
- [35] Y. F. Dagdas, K. Yoshino, G. Dagdas, L. S. Ryder, E. Bielska, G. Steinberg, and N. J. Talbot. Septin-mediated plant cell invasion by the rice blast fungus, *magnaporthe oryzae*. *Science*, 336(6088):1590–1595, 2012. [140](#)
- [36] J. C. de Jong, B. J. McCormack, N. Smirnov, and N. J. Talbot. Glycerol generates turgor in rice blast. *Nature*, 389(6648):244, 1997. [140](#)
- [37] K. Deckelnick and G. Dziuk. On the approximation of the curve shortening flow. *Pitman Research Notes in Mathematics Series*, pages 100–108, 1995. [xii](#), [12](#), [67](#), [68](#), [69](#), [75](#), [77](#), [100](#)
- [38] K. Deckelnick and G. Dziuk. Error estimates for a semi-implicit fully discrete finite element scheme for the mean curvature flow of graphs. *Interfaces and Free Boundaries*, 2(4):341–359, 2000. [3](#)
- [39] K. Deckelnick and G. Dziuk. Convergence of numerical schemes for the approximation of level set solutions to mean curvature flow. *Series on Advances in Mathematics for Applied Sciences*, 59:77–94, 2001. [3](#)
- [40] K. Deckelnick and G. Dziuk. Error analysis for the elastic flow of parametrized curves. *Mathematics of computation*, 78(266):645–671, 2009. [12](#), [102](#), [103](#), [122](#)
- [41] K. Deckelnick, G. Dziuk, and C. M. Elliott. Computation of geometric partial differential equations and mean curvature flow. *Acta numerica*, 14:139–232, 2005. [2](#), [3](#), [18](#), [20](#), [22](#), [52](#), [53](#), [188](#)

- [42] K. Deckelnick and C. M. Elliott. Finite element error bounds for a curve shrinking with prescribed normal contact to a fixed boundary. *IMA journal of numerical analysis*, 18(4):635–654, 1998. [x](#), [12](#), [66](#), [69](#), [70](#), [71](#), [82](#), [83](#), [87](#), [94](#), [100](#), [102](#), [123](#), [126](#), [127](#), [129](#), [130](#), [131](#), [133](#), [134](#), [185](#)
- [43] K. Deckelnick, C. M. Elliott, and V. Styles. Numerical diffusion-induced grain boundary motion. *Interfaces and Free Boundaries*, 3(4):393–414, 2001. [3](#)
- [44] K. Deckelnick and V. Styles. Stability and error analysis for a diffuse interface approach to an advection–diffusion equation on a moving surface. *Numerische mathematik*, 139(3):709–741, 2018. [iii](#), [vi](#), [9](#), [10](#), [13](#), [15](#), [16](#), [23](#), [25](#), [26](#), [27](#), [28](#), [31](#), [32](#), [33](#), [52](#), [184](#)
- [45] D. M. DeTurck. Deforming metrics in the direction of their ricci tensors. *Journal of Differential Geometry*, 18(1):157–162, 1983. [73](#)
- [46] Paul Deuring. A finite element–finite volume discretization of convection-diffusion-reaction equations with nonhomogeneous mixedboundary conditions: Error estimates. *Numerical Methods for Partial Differential Equations*, 32(6):1591–1621, 2016. [37](#)
- [47] Paul Deuring and Marcus Mildner. Error estimates for a finite element–finite volume discretization of convection–diffusion equations. *Applied numerical mathematics*, 61(6):785–801, 2011. [37](#)
- [48] Q. Du and X. Feng. The phase field method for geometric moving interfaces and their numerical approximations. *Handbook of Numerical Analysis*, 21(5):425–508, 2020. [19](#)
- [49] D. R. Durran. *Numerical methods for fluid dynamics: With applications to geophysics*, volume 32. Springer Science & Business Media, 2010. [141](#)
- [50] G. Dziuk. Finite elements for the beltrami operator on arbitrary surfaces. In *Partial differential equations and calculus of variations*, pages 142–155. Springer, 1988. [8](#)
- [51] G. Dziuk. An algorithm for evolutionary surfaces. *Numerische Mathematik*, 58(1):603–611, 1990. [75](#)
- [52] G. Dziuk. Convergence of a semi-discrete scheme for the curve shortening flow. *Mathematical Models and Methods in Applied Sciences*, 4(04):589–606, 1994. [xii](#), [65](#), [66](#), [68](#), [69](#), [77](#)

- [53] G. Dziuk and C. M. Elliott. Finite elements on evolving surfaces. *IMA journal of numerical analysis*, 27(2):262–292, 2007. [8](#)
- [54] G. Dziuk and C. M. Elliott. Surface finite elements for parabolic equations. *Journal of Computational Mathematics*, pages 385–407, 2007. [8](#)
- [55] G. Dziuk and C. M. Elliott. Eulerian finite element method for parabolic pdes on implicit surfaces. *Interfaces and Free Boundaries*, 10(1):119–138, 2008. [8](#), [9](#)
- [56] G. Dziuk and C. M. Elliott. An eulerian approach to transport and diffusion on evolving implicit surfaces. *Computing and visualization in science*, 13(1):17–28, 2010. [8](#), [27](#)
- [57] G. Dziuk and C. M. Elliott. A fully discrete evolving surface finite element method. *SIAM Journal on Numerical Analysis*, 50(5):2677–2694, 2012. [8](#)
- [58] G. Dziuk and C. M. Elliott. Finite element methods for surface pdes. *Acta Numerica*, 22:289–396, 2013. [7](#), [8](#), [29](#), [141](#)
- [59] C. M. Elliott and H. Fritz. On approximations of the curve shortening flow and of the mean curvature flow based on the deturck trick. *IMA Journal of Numerical Analysis*, 37(2):543–603, 2016. [xii](#), [12](#), [71](#), [73](#), [74](#), [75](#), [76](#), [77](#), [82](#), [99](#), [100](#)
- [60] C. M. Elliott and J. R. Ockendon. *Weak and variational methods for moving boundary problems*, volume 59. Pitman Publishing, 1982. [22](#), [53](#)
- [61] C. M. Elliott and T. Ranner. A unified theory for continuous in time evolving finite element space approximations to partial differential equations in evolving domains. *arXiv preprint arXiv:1703.04679*, 2019. [6](#)
- [62] C. M. Elliott and B. Stinner. Analysis of a diffuse interface approach to an advection diffusion equation on a moving surface. *Mathematical Models and Methods in Applied Sciences*, 19(05):787–802, 2009. [24](#), [42](#)
- [63] C. M. Elliott, B. Stinner, V. Styles, and R. Welford. Numerical computation of advection and diffusion on evolving diffuse interfaces. *IMA Journal of Numerical Analysis*, 31(3):786–812, 2010. [iii](#), [vi](#), [13](#), [15](#), [16](#), [23](#), [24](#), [25](#), [29](#), [30](#), [31](#), [32](#), [35](#), [42](#), [43](#), [44](#), [51](#), [53](#), [60](#), [184](#)
- [64] C. M. Elliott, B. Stinner, and C. Venkataraman. Modelling cell motility and chemotaxis with evolving surface finite elements. *Journal of The Royal Society Interface*, 9(76):3027–3044, 2012. [147](#)

- [65] C. M. Elliott and A. M. Stuart. The global dynamics of discrete semilinear parabolic equations. *SIAM journal on numerical analysis*, 30(6):1622–1663, 1993. [19](#)
- [66] C. M. Elliott and V. Styles. Numerical analysis of a mean field model of superconducting vortices. *IMA journal of numerical analysis*, 21(1):1–51, 2001. [35](#), [36](#)
- [67] C. M. Elliott and V. Styles. An ale esfem for solving pdes on evolving surfaces. *Milan Journal of Mathematics*, 80(2):469–501, 2012. [8](#)
- [68] L. C. Evans. *Partial Differential Equations*, volume 19. American Mathematical Society, 2010. [6](#), [18](#), [21](#), [29](#), [190](#), [192](#), [194](#)
- [69] J. Eyles. *Numerical analysis and simulations of a tractable model for tumour growth*. PhD thesis, University of Sussex, 2019. [11](#)
- [70] M. Gage and R. S. Hamilton. The heat equation shrinking convex plane curves. *Journal of Differential Geometry*, 23(1):69–96, 1986. [5](#)
- [71] C. Gräser. *Convex minimization and phase field models*. PhD thesis, 2011. [22](#)
- [72] M. A. Grayson. The heat equation shrinks embedded plane curves to round points. *Journal of Differential geometry*, 26(2):285–314, 1987. [5](#), [20](#)
- [73] A. Henderson. *ParaView Guide: A Parallel Visualization Application*. Kitware Inc., 2007. [177](#)
- [74] C. Hirsch. *Numerical computation of internal and external flows: The fundamentals of computational fluid dynamics*. Elsevier, 2007. [37](#)
- [75] J. M. Holte. Discrete Gronwall lemma and applications. In *MAA-NCS meeting at the University of North Dakota*, volume 24, pages 1–7, 2009. [65](#)
- [76] R. J. Howard and B. Valent. Breaking and entering: host penetration by the fungal rice blast pathogen *Magnaporthe oryzae*. *Annual Reviews in Microbiology*, 50(1):491–512, 1996. [138](#)
- [77] G. Huisken. Flow by mean curvature of convex surfaces into spheres. *Journal of Differential Geometry*, 20(1):237–266, 1984. [75](#)
- [78] A. J. James and J. Lowengrub. A surfactant-conserving volume-of-fluid method for interfacial flows with insoluble surfactant. *Journal of computational physics*, 201(2):685–722, 2004. [10](#)

- [79] Claes Johnson. *Numerical solution of partial differential equations by the finite element method*. Courier Corporation, 2012. [173](#)
- [80] H. Kato and T. Yamaguchi. The perfect state of *pyricularia oryzae* cav. from rice plants in culture. *Japanese Journal of Phytopathology*, 48(5):607–612, 1982. [1](#)
- [81] J. R. King and S. J. Franks. Mathematical analysis of some multi-dimensional tissue-growth models. *European Journal of Applied Mathematics*, 15(3):273–295, 2004. [11](#)
- [82] B. Kovács, B. Li, and C. Lubich. A convergent algorithm for mean curvature flow driven by diffusion on the surface. *arXiv preprint arXiv:1912.05924*, 2019. [79](#)
- [83] B. Kovács, B. Li, and C. Lubich. A convergent evolving finite element algorithm for mean curvature flow of closed surfaces. *Numerische Mathematik*, 143(4):797–853, 2019. [75](#), [79](#)
- [84] K. F. Lam. *Diffuse interface models of soluble surfactants in two-phase fluid flows*. PhD thesis, University of Warwick, 2014. [10](#)
- [85] Raytcho D Lazarov and Ilya D Mishev. Finite volume methods for reaction diffusion problems in: F. *Finite volumes for complex applications, Problems and Perspectives (Hermes, Paris)*, pages 233–240, 1996. [36](#), [37](#)
- [86] S. Lee and D. Lee. The fractional allen–cahn equation with the sextic potential. *Applied Mathematics and Computation*, 351:176–192, 2019. [22](#)
- [87] X. Li, J. Lowengrub, K. E. Teigen, A. Voigt, and F. Wang. A diffuse-interface approach for modeling transport, diffusion and adsorption/desorption of material quantities on a deformable interface. *Communications in mathematical sciences*, 4(7):1009–1037, 2009. [23](#)
- [88] G. M. Lieberman. The first initial-boundary value problem for quasilinear second order parabolic equations. *Annali della Scuola Normale Superiore di Pisa-Classe di Scienze*, 13(3):347–387, 1986. [3](#)
- [89] J. A. Mackenzie, M. Nolan, and R. H. Insall. Local modulation of chemoattractant concentrations by single cells: dissection using a bulk-surface computational model. *Interface focus*, 6(5):2016.0036, 2016. [3](#)
- [90] M. T. Madigan, J. M. Martinko, and J. Parker. *Brock biology of microorganisms*, volume 11. Prentice hall Upper Saddle River, NJ, 1997. [138](#)

- [91] R. Malladi and J. A. Sethian. Image processing via level set curvature flow. *proceedings of the National Academy of sciences*, 92(15):7046–7050, 1995. [3](#)
- [92] Matlab. *Version 9.7.0 (R2019a)*. The MathWorks Inc., 2019. [38](#), [126](#)
- [93] U. F. Mayer and G. Simonett. Classical solutions for diffusion-induced grain-boundary motion. *Journal of mathematical analysis and applications*, 234(2):660–674, 1999. [3](#)
- [94] ID Mishev. *Finite volume and finite volume element methods for nonsymmetric problems*, Texas A&M University. PhD thesis, Ph. D. Thesis, 1997, Technical Report ISC-96-04-MATH. [36](#)
- [95] L. Murphy. *Mathematical studies of a mechanobiochemical model for 3D cell migration*. PhD thesis, University of Sussex, 2019. [11](#)
- [96] T. J. Penn, M. E. Wood, D. M. Soanes, M. Csukai, A. J. Corran, and N. J. Talbot. Protein kinase c is essential for viability of the rice blast fungus *magnaporthe oryzae*. *Molecular microbiology*, 98(3):403–419, 2015. [1](#)
- [97] P. Pozzi and B. Stinner. Curve shortening flow coupled to lateral diffusion. *Numerische Mathematik*, 135(4):1171–1205, 2017. [75](#), [77](#), [100](#), [102](#)
- [98] P. Pozzi and B. Stinner. A converging finite element scheme for motion by curvature of a network with a triple junction. *arXiv preprint arXiv:1911.09636*, 2019. [71](#)
- [99] A. Rätz and A. Voigt. Pde’s on surfaces—a diffuse interface approach. *Communications in Mathematical Sciences*, 4(3):575–590, 2006. [23](#)
- [100] R. T. Rockafellar and R. J. B. Wets. *Variational analysis*, volume 317. Springer Science & Business Media, 2009. [24](#)
- [101] B. M. H. Romeny. *Geometry-driven diffusion in computer vision*, volume 1. Springer Science & Business Media, 2013. [3](#)
- [102] L. S. Ryder, Y. F. Dagdas, M. J. Kershaw, C. Venkataraman, A. Madzvamuse, X. Yan, N. Cruz-Mireles, D. M. Soanes, M. Oses-Ruiz, V. Styles, J. Sklenar, F. L. H. Menke, and N. J. Talbot. A sensor kinase controls turgor-driven plant infection by the rice blast fungus. *Nature*, 574(7778):423–427, 2019. [ii](#), [iii](#), [vii](#), [1](#), [13](#), [14](#), [137](#), [138](#), [139](#), [140](#), [143](#), [147](#), [149](#), [150](#), [151](#), [152](#), [153](#), [160](#), [161](#), [162](#), [165](#), [167](#), [168](#), [169](#), [170](#), [177](#), [178](#), [185](#), [186](#)

- [103] A. Schmidt. Computation of three dimensional dendrites with finite elements. *Journal of Computational Physics*, 125(2):293–312, 1996. [5](#)
- [104] A. Schmidt and K. G. Siebert. *Design of Adaptive Finite Element Software: The Finite Element Toolbox ALBERTA*. Lecture Notes in Computational Science and Engineering 42. Springer-Verlag, Berlin, 2004. [32](#)
- [105] J. A. Sethian. *Level set methods and fast marching methods: evolving interfaces in computational geometry, fluid mechanics, computer vision, and materials science*, volume 3. Cambridge university press, 1999. [3](#)
- [106] S. E. Smith and D. Read. Mycorrhizas in achlorophyllous plants (mycoheterotrophs). *Smith, SE. and Read, D. Academic Press, 3rd Edition. San Diego*, pages 458–506, 2008. [138](#)
- [107] M. D. Spivak. *A comprehensive introduction to differential geometry*. Publish or perish, 1970. [66](#)
- [108] J. Steinhilber. *Numerical analysis for harmonic maps between hypersurfaces and grid improvement for computational parametric geometric flows*. PhD thesis, Verlag nicht ermittelbar, 2014. [99](#), [100](#)
- [109] V. Styles and J. Van Yperen. Finite element approximation of a system coupling curve evolution with prescribed normal contact to a fixed boundary to reaction-diffusion on the curve. In *European Conference on Numerical Mathematics and Advanced Applications*. Springer, 2019. [ii](#), [125](#)
- [110] V. Styles and J. Van Yperen. Numerical analysis of a system coupling curve evolution with prescribed normal contact to a fixed boundary to reaction-diffusion on the curve. *Submitted*, 2020. [ii](#), [102](#)
- [111] HPC Sysadmins. University of sussex high performance computer cluster documentation. <https://info.hpc.sussex.ac.uk/hpc-guide/index.html>. [32](#)
- [112] N. J. Talbot. On the trail of a cereal killer: exploring the biology of magnaporthe grisea. *Annual Reviews in Microbiology*, 57(1):177–202, 2003. [1](#)
- [113] N. J. Talbot and A. J. Foster. Genetics and genomics of the rice blast fungus magnaporthe grisea: developing an experimental model for understanding fungal diseases of cereals. 2001. [1](#)

- [114] X. Thinlay, M. R. Finckh, A. C. Bordeos, and R. S. Zeigler. Effects and possible causes of an unprecedented rice blast epidemic on the traditional farming system of bhutan. *Agriculture, Ecosystems & Environment*, 78(3):237–248, 2000. [1](#)
- [115] Vidar Thomée. *Galerkin finite element methods for parabolic problems*, volume 1054. Springer, 1984. [33](#)
- [116] L. W. Tu. *Differential geometry: connections, curvature, and characteristic classes*, volume 275. Springer, 2017. [65](#)
- [117] A. M. Turing. The chemical basis of morphogenesis. *Bulletin of mathematical biology*, 52(1-2):153–197, 1990. [11](#)
- [118] B. Valent and F. G. Chumley. Molecular genetic analysis of the rice blast fungus, magnaporthe grisea. *Annual review of phytopathology*, 29(1):443–467, 1991. [1](#)
- [119] R. A. Wilson and N. J. Talbot. Under pressure: investigating the biology of plant infection by magnaporthe oryzae. *Nature Reviews Microbiology*, 7(3):185–195, 2009. [1](#), [137](#)
- [120] F. W. Yang, C. Venkataraman, V. Styles, V. Kuttenger, E. Horn, Z. von Guttenberg, and A. Madzvamuse. A computational framework for particle and whole cell tracking applied to a real biological dataset. *Journal of biomechanics*, 49(8):1290–1304, 2016. [3](#)
- [121] R. S. Zeigler, S. A. Leong, and P. S. Teng. *Rice blast disease*. Int. Rice Res. Inst., 1994. [137](#)